

AD-A115 866

FOREIGN TECHNOLOGY DIV WRIGHT-PATTERSON AFB OH
RECENT SELECTED PAPERS OF NORTHWESTERN POLYTECHNICAL UNIVERSITY--ETC(U)
AUG 81

F/6 20/4

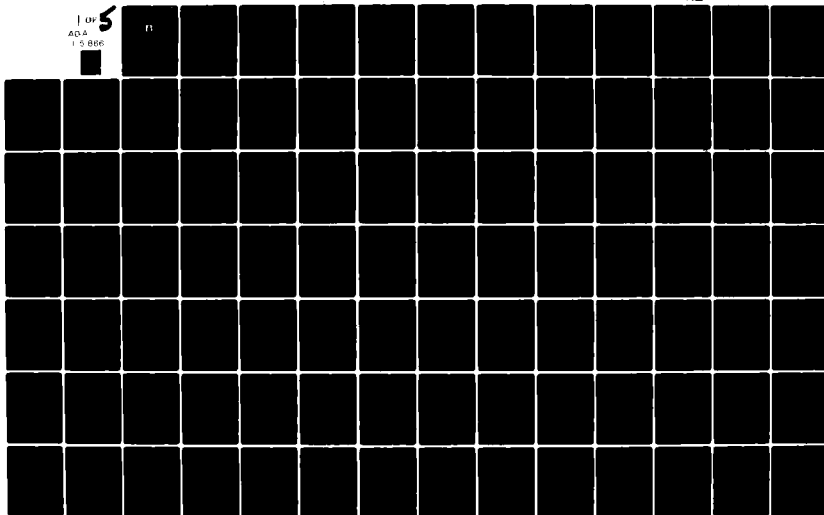
UNCLASSIFIED

FTD-ID(RS)T-0260-81-PT-2

NL

1 of 5
ADA
15 866

11



2

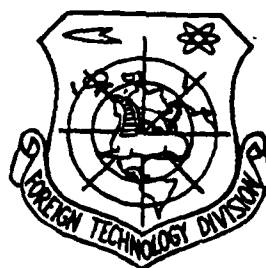
FTD-ID(RS)T-0260-81

AD A115866

FOREIGN TECHNOLOGY DIVISION



RECENT SELECTED PAPERS OF NORTHWESTERN POLYTECHNICAL
UNIVERSITY IN TWO PARTS
(PART II)



DTIC
JUN 24 1982
E

DTIC FILE COPY

Approved for public release;
distribution unlimited.



EDITED TRANSLATION

FTD-ID(RS)T-0260-81

28 August 1981

MICROFICHE NR: FTD-81-C-000812

RECENT SELECTED PAPERS OF NORTHWESTERN
POLYTECHNICAL UNIVERSITY IN TWO PARTS
(PART II)

English pages: 413

Source: Recent Selected Papers of Northwestern
Polytechnical University in Two Parts,
Part 2, Xi'an, Shaanxi, 1979,
pp. 1-137, 139-167, 169-185, 187- 1,
203-215, 217-240, pages 138, 168, 186,
202, 216 missing in original foreign
document

Country of origin: China

Translated by: SCITRAN

F33657-78-D-0619

Requester: FTD/TQTA

Approved for public release; distribution
unlimited.

THIS TRANSLATION IS A RENDITION OF THE ORIGINAL FOREIGN TEXT WITHOUT ANY ANALYTICAL OR EDITORIAL COMMENT. STATEMENTS OR THEORIES ADVOCATED OR IMPLIED ARE THOSE OF THE SOURCE AND DO NOT NECESSARILY REFLECT THE POSITION OR OPINION OF THE FOREIGN TECHNOLOGY DIVISION.

PREPARED BY:

TRANSLATION DIVISION
FOREIGN TECHNOLOGY DIVISION
WP-AFB, OHIO

FTD-ID(RS)T-0260-81

Date 28 Aug 19 81

RECENT SELECTED PAPERS OF NORTHWESTERN
POLYTECHNICAL UNIVERSITY IN TWO PARTS (PART II)

1979

Xi'an, Shaanxi
The People's Republic of China



| Accession For | |
|---------------|--|
| NTIS GRA&I | <input checked="checked" type="checkbox"/> |
| DTIC TAB | <input type="checkbox"/> |
| Unannounced | <input type="checkbox"/> |
| Justification | |
| | |
| Re | |
| By | |
| Codes | |
| or | |
| al | |
| A | |

TABLE OF CONTENTS

| | <u>Page</u> |
|---|-------------|
| Dual Properties of Elastic Structures | 1 |
| Matrix Analysis of Wings | 76 |
| On a Method for the Determination of Plane Stress Fracture Toughness K_{IC} of CrMnSiNi2A Steel and Some Related Problems | 112 |
| The Island Structure of (M-A) in Hardened Low Alloy High Strength Steels | 137 |
| A Study on Insulated Risers | 174 |
| The Study on Technological Fundamentals of Pulsed Spray Transfer Arc Welding (IV) -- Observations on Arc Phenomena in the Case of Stable Welding Conditions (Report I) | 197 |
| A Fast Fourier Transform Hardware Processor | 237 |
| Color Discrimination by a Color-Picture Reader | 253 |
| Uniqueness of the Solution to the Velocity Potential Integral Equation Established by Using Green's Theorem | 273 |
| Initial Experimental Research into the Response of Turbojet Engine Compressors to Distortion of Intake Pressure | 287 |
| Measurement and Analysis of Station Parameters of a Turbojet Engine | 319 |
| Experimental Investigation of the Rotating Stall, Surge and Wake Behind the Rotor for a Single Stage Axial Compressor | 347 |

Experimental Investigation of a Vaporizing
Combustion with Double Combustion Spaces

371

Combustion Instability in Solid Propellant
Rocket Motors with Tubular Grain

390

DUAL PROPERTIES OF ELASTIC STRUCTURES

Chen Baiping

SUMMARY

It does not make any difference if one is considering a one-dimensional, two-dimensional or three-dimensional problem in the statics of elastic bodies; any such consideration always involves four function vectors. These are displacement, strain, stress and distributed-load function vectors, i.e.,

$$\{\psi(x,y,z)\}, \{e(x,y,z)\}, \{\sigma(x,y,z)\}, \{\bar{\phi}(x,y,z)\}.$$

With the scope of the study of linear forces, the set of partial differential equations which is obtained is of a self-adjoint type. Because of this, elastic bodies are naturally self-adjoint systems (Section 1); they are built on the two foundation stones set out below:

(Assumption I) There exists the geometrical operator-matrix (a) which satisfies the geometrical relation

$$\{e(x,y,z)\} = [a] \{\psi(x,y,z)\}$$

$$l=1 \quad l=m \quad m=1$$

The equation above means that the displacement function vector determines the strain function vector.

(Assumption II) There exists an equilibrium operator matrix (b) which satisfies the equilibrium relationship

$$\{\bar{\phi}(x,y,z)\} = [k] \{\sigma(x,y,z)\}$$

$$m=1 \quad m=l \quad l=1$$

The equation above means that the distributed load function vector is determined by the stress function vector.

In Section 1, there was an analysis of a three-dimensional elastic body. In such a case, it is always possible to obtain a self-adjoint system; however, the solution required is difficult. Normally, one would use a finite element technique in order to obtain an approximate solution. This method can be further divided

into two stages. These stages have six steps in them all together and they run generally as shown below.

(Stage One) The Modeling Stage. This stage is further divided into steps (i, ii and iii).

(i) Take the elastic body and divide it up into finite elements. In the elastic body, choose a finite number of points (say J of them), and let all of them be called the nodal points. If one connects the nodal points, then, by doing so, he divides the elastic body into a finite number of elastic body elements.

Each of the elastic body elements will employ four function vectors. If we take a one-dimensional elastic body as an example, then, these function vectors are:

$$\{\psi(x)'\}_{m_i \times 1}, \{e(x)'\}_{l_i \times 1}, \{\sigma(x)'\}_{l_i \times 1}, \{\bar{\phi}(x)'\}_{m_i \times 1}.$$

Concerning the application of model analysis to these elements, the main thing is to cause the strain state or the stress state to approximate the real state or condition. It is best to begin from the estimate of the internal energy density $\frac{dU}{dx}$.

If we are dealing with the case in which

$$\frac{dU}{dx} = \frac{1}{2}(e_1(x) e_1(x) + \dots + e_n(x) e_n(x)),$$

then, we may assume the strain function vector, the elasticity moduli function square matrix and the stress function vector are

$$\begin{aligned} \{e(x)'\}_{l_i \times 1} &= \begin{Bmatrix} e_1(x) \\ \vdots \\ e_n(x) \end{Bmatrix}, \\ [e(x)']_{l_i \times l_i} &= \begin{bmatrix} e_1(x) & & \\ & \dots & \\ & & e_n(x) \end{bmatrix}, \\ \{\sigma(x)'\}_{l_i \times 1} &= \begin{Bmatrix} e_1(x) & e_1(x) \\ \vdots & \vdots \\ e_n(x) & e_n(x) \end{Bmatrix} = \begin{Bmatrix} \sigma_1(x) \\ \vdots \\ \sigma_n(x) \end{Bmatrix}. \end{aligned}$$

Or, if we assume that

$$\frac{dU'}{dx} = \frac{1}{2} (f_1(x) \sigma_1(x)^2 + \dots + f_n(x) \sigma_n(x)^2),$$

Then we may assume that

$$\{\sigma_i(x)\}_{i=1}^n = \begin{Bmatrix} \sigma_1(x) \\ \vdots \\ \sigma_n(x) \end{Bmatrix}, [f(x)']_{i=1}^n = \begin{bmatrix} f_1(x) & \dots & f_n(x) \end{bmatrix}, \{e(x)'\}_{i=1}^n = \begin{Bmatrix} f_1(x) \sigma_1(x) \\ \vdots \\ f_n(x) \sigma_n(x) \end{Bmatrix} = \begin{Bmatrix} e_1(x) \\ \vdots \\ e_n(x) \end{Bmatrix}.$$

To summarize, the l_i components in $\{e(x)'\}$ or $\{\sigma(x)'\}$ should be made linearly independent and they should also satisfy the relationship

$$\frac{dU'}{dx} = \frac{1}{2} [\sigma(x)'] [\{e(x)'\}],$$

moreover, they should embody the physical relationship

$$\{\sigma(x)'\}_{i=1}^n = [e(x)']_{l_i \times l_i} \{e(x)'\}_{l_i \times 1} \quad \text{or} \quad \{e(x)'\}_{i=1}^n = [f(x)']_{l_i \times l_i} \{\sigma(x)'\}_{l_i \times 1}.$$

(ii) Make sure whether or not (a) and (b) exist. Concerning the two foundation stones on which self-adjoint systems rest, that is to say, the assumptions concerning form and the forces involved, whether or not they are continuously existent and whether or not the two operator matrices, $[a^1]$ and $[h^1]$, which satisfy the geometrical relationship and equilibrium relationship set out below, i.e.,

$$\{e(x)'\}_{l_i \times 1} = [a^1]_{l_i \times m_i} \{\psi(x)'\}_{m_i \times 1}, \quad \{\bar{\phi}(x)'\}_{m_i \times 1} = [h^1]_{m_i \times l_i} \{\sigma(x)'\}_{l_i \times 1}$$

are continuously existent or not has a very large influence on the computational operations which follow.

At the end of step (ii), it is possible to take the distributed load $\{\bar{\phi}(x)'\}$, on the i th element and replace it at the nodal points with the equivalent structural load $\{\bar{\phi}(x)'\} = \{0\}$.

(iii) Take the i th element and convert it into the structural member i , that is to say, take the four function vectors and turn them into four definite-value vectors:

$$\begin{matrix} \{\psi^i\}, \{e^i\}, \{\sigma^i\}, \{\phi^i\}. \\ \mu^i \times 1 \quad \lambda^i \times 1 \quad \lambda^i \times 1 \quad \mu^i \times 1 \end{matrix}$$

Here, $\{\phi^i\}$ is the external force on the two ends of the member i . As far as effects on the four definite-value vectors go, the limits are also present in the form set out below

$$U^i = \frac{1}{2} \{e^i\} \{\sigma^i\}, \quad W^i = \frac{1}{2} \{\phi^i\} \{\psi^i\}.$$

Also, it is required that it be possible for corresponding function vectors and definite-value vectors to represent each other. This is very convenient for the derivation of formulae and for computations. For example, from $\{e(x)^i\}_{l_i \times 1}$ it is possible, by employing the operator matrix, to solve for $\{e^i\}_{\lambda^i \times 1}$; from $\{e^i\}_{\lambda^i \times 1}$, by employing auxiliary functions, it is possible to solve for $\{e(x)^i\}_{l_i \times 1}$, and so on. Moreover, this explains the following:

If $[a^i]$ holds, then the geometrical matrix $[a^i]$ which satisfies the geometrical relationship $\{e^i\} = [a^i] \{\phi^i\}$ also holds. If $[h^i]$ holds, then, the equilibrium matrix $[h^i]$, which satisfies the equilibrium relationship $\{\phi^i\} = [h^i] \{\sigma^i\}$, also holds. If $[a^i]$ and $[h^i]$ both hold, then, $[h^i] = [a^i]'$.

(Stage Two) The structural computation stage. This stage can also be broken down, this time into steps (iv, v and vi).

(iv) Take all the free structural members and assemble them together. In this way, we can obtain the assembled structure. Its four assembly vectors (which can also be called collection vectors) are

$$\begin{matrix} \{\psi\}, & \{e\}, & \{\sigma\}, & \{\phi\}. \\ \sum \mu \times 1 & \sum \lambda \times 1 & \sum \lambda \times 1 & \sum \mu \times 1 \end{matrix}$$

(v) Let us assume that the structure has N rigid roller joints all together. Cancel all zero displacements at rigid roller joints and cancel the unknown restraining forces at the rigid joints. If one does so, then it is possible to obtain the four generalized vectors $\{\psi\}$, $\{e\}$, $\{\sigma\}$ & $\{\phi\}$. In this case, the external or known load vector $\{\phi\}$ is a quantity which is already known.

(vi) Solve this elastic structure problem

It is easy to see that both one-dimensional beams and plane trusses are self-adjoint systems and can be easily solved. If we study these cases which are easily solved, then we can better understand the nature of self-adjoint systems.

This article points out that, through the analysis of one-dimensional beams, it is possible to reach the conclusion below. This conclusion is that, in the modeling analysis of the elements of elastic bodies, the observation of whether or not the two cornerstone assumptions, that is, Assumption I and Assumption II, remain in effect or not will influence the calculations which come later. In specific terms, one can say:

(i) If Assumption I remains in effect (that is, if $\begin{matrix} [\sigma'] \\ l_i \cdot m_i \end{matrix}$ exists), then all the various matrices in the steps which follow also exist, that is

$$\begin{matrix} [\sigma'], & [\sigma], & [\sigma] \\ \lambda' \cdot \mu' & \Sigma \lambda \cdot \Sigma \mu & \lambda \cdot \mu \end{matrix}$$

(This type of structure can be called a fixed-form structure).

(ii) If Assumption II remains in effect (that is, if $\begin{matrix} [h'] \\ m_i \cdot l_i \end{matrix}$ exists), then all the equilibrium matrices which occur in the steps that follow also exist, that is

$$\begin{matrix} [h'], & [h], & [h] \\ \mu' \cdot \lambda' & \Sigma \mu \cdot \Sigma \lambda & \mu \cdot \lambda \end{matrix}$$

(This structure may also be called a fixed-force structure).

On the basis of the discussion above, it is possible to divide elastic structures into four types:

Type A (fixed-form and fixed-force structures) $[a]_{nn}$ & $[h]_{nn}$ both exist.

Type B (fixed-form, non-fixed-force structures) $[a]_{nn}$ exists and $[h]_{nn}$ does not exist.

Type C (fixed-force, non-fixed form structures) $[h]_{nn}$ exists and $[a]_{nn}$ does not exist.

Type D (structures of a mixed type) $[a]_{nn}$ and $[h]_{nn}$ are both unclear. (Note) D-type structures are not within the scope of the discussion in this article.

This article also points out with great emphasis the fact that each of the three types of structures discussed above has one method of solution which suits it best, for example:

A-type structures use the direct rigidity or stiffness method [2];

B-type structures use the generalized strain method [3]. It is possible to overdo this method so that one ends up with the direct rigidity or stiffness method;

C-type structures use the generalized stress method [3].

If we utilize the general requirements for elastic structures, that is to say, structural assumptions (1), (2a), (2b), (3a) and (3b), then we can rigorously deduce these three types of methods. Moreover, if we take as an example a planar truss, then we can explain the computational process involved in the three methods mentioned above.

It is worth pointing out the fact that an A-type structure and a B-type structure, under conditions of full duality, possess a characteristic which is extremely convenient and fortunate. This characteristic is that, when one is using the generalized strain method, it is possible to deduce the full formula for the generalized stress method; this also works out the other way around. In other words, these three types of methods are very conveniently mutually related or interchangeable; the amount of work involved in each method is also generally equal.

If this is so, then which method is actually best? The feeling of the author is that this is strictly related to the physical quantities which are required in a particular problem; let me explain by means of two examples. (1) In a vibration problem, if one is looking for the mode (or displacement), then the direct rigidity or stiffness method is the best. (2) If one is finding the unknown design parameter values in a minimum weight problem, then it is relatively more convenient to employ the generalized strain method [4]. The reason for this is the fact that it is much easier to adjust the value of $[c']_{pp}$ than it is to adjust the value of $[k]_{pp}$.

It is unfortunate that most of the authors who write on the subject of finite element methods only consider the aspects of it which relate to the area of elasticity theory and almost completely ignore all aspects of these techniques which relate to the area of the mechanics of the structures. It is also true that these authors usually take the results they obtain and put them together into the form of standardized rigidity matrices (when, in fact, these results were obtained by converting back from other methods). Using this type of approach does not allow an opportunity to clearly explain the generalized strain and generalized stress methods; it also leaves no room for selecting the most appropriate method of solution to be used in the various different types of problems.

The author would like to express his thanks to Professor Hu Pei Yuan and Instructor Tang Xuan Chun for the help which they gave him during the process of compiling this article.

SECTION 1. ANY ELASTIC BODY IS BASICALLY A SELF-ADJOINT SYSTEM WITHIN THE REALM OF LINEAR DYNAMICS

According to the theory of homogeneous elastic dynamics, all three-dimensional elastic bodies have four types of physical quantities associated with them. These are distributed load (such as body force), stress, strain and displacement and they are all functions of x , y and z . Consequently, we will use four function vectors to represent them. These are

$$\{\vec{f}(x,y,z)\}, \{\sigma(x,y,z)\}, \{\epsilon(x,y,z)\}, \{\psi(x,y,z)\}. \quad (1.1)$$

Practically speaking, these vectors are

$$\begin{Bmatrix} \vec{f} \\ \sigma \\ \epsilon \end{Bmatrix}, \begin{Bmatrix} \sigma_x \\ \sigma_y \\ \sigma_z \\ \sigma_{yz} \\ \sigma_{zx} \\ \sigma_{xy} \end{Bmatrix}, \begin{Bmatrix} \epsilon_x \\ \epsilon_y \\ \epsilon_z \\ \gamma_{yz} \\ \gamma_{zx} \\ \gamma_{xy} \end{Bmatrix}, \begin{Bmatrix} u \\ v \\ w \end{Bmatrix}.$$

The units for the various component vectors are respectively kg/cm^3 , kg/cm^2 and 1 to the cm.

In order to prevent the selection and use of these vectors in an arbitrary manner, let us fix the ways in which they may be arranged together by twos as follows. In a differentiated body, the external load work is

$$dW = \frac{1}{2} [\vec{f}] \{\psi\} dx dy dz, \quad (1.2)$$

In a differentiated body, the internal energy is

$$dU = \frac{1}{2} [\sigma] \{ \epsilon \} dx dy dz. \quad (1.2)'$$

Between the four vectors, there are three relationships as set out below:

1° geometrical relationship

$$\begin{matrix} \{ \epsilon \} = [a] \{ \phi \}, \\ 6 \times 1 \quad 6 \times 3 \quad 3 \times 1 \end{matrix} \quad (1.3)$$

2° physical relationship

$$\begin{matrix} \{ \sigma \} = [e] \{ \epsilon \}, \\ 6 \times 1 \quad 6 \times 6 \quad 6 \times 1 \end{matrix} \quad (1.4)$$

3° equilibrium relationship

$$\begin{matrix} \{ \phi \} = [h] \{ \sigma \}, \\ 3 \times 1 \quad 3 \times 6 \quad 6 \times 1 \end{matrix} \quad (1.5)$$

In this case, [a] is called the geometrical computation matrix; [e] is called the square matrix for generalized elasticity modulus and [h] is called the equilibrium computation matrix.

Let us utilize the computations below

$$D_x = \frac{\partial}{\partial x}, \quad D_y = \frac{\partial}{\partial y}, \quad D_z = \frac{\partial}{\partial z}, \quad (1.6)$$

as well as these computational square matrices

$$[D_1]_{3 \times 3} = \begin{bmatrix} D_x & & \\ & D_y & \\ & & D_z \end{bmatrix}, \quad [D_2]_{3 \times 3} = \begin{bmatrix} 0 & D_x & D_y \\ D_x & 0 & D_z \\ D_y & D_z & 0 \end{bmatrix}, \quad (1.6')$$

If we give some consideration to the fact that

$$\epsilon_x = \frac{\partial u}{\partial x}, \quad \gamma_{yz} = \frac{\partial v}{\partial z} + \frac{\partial w}{\partial y}, \text{ etc...}$$

it then follows that the geometrical computational matrix

$$[a]_{6 \times 3} = \begin{bmatrix} D_1 \\ D_2 \end{bmatrix}. \quad (1.7)$$

In this case, the square matrix of the modulus of elasticity $(e)_{6 \times 6}$, becomes

$$[e]_{6 \times 6} = \begin{bmatrix} [e_1]_{3 \times 3} & \\ & [e_2]_{3 \times 3} \end{bmatrix}, \quad (1.8)$$

In this case, the square matrix for the modulus of homogeneous linear elasticity in various directions is (note that attention should be paid to the calculations which are not contained in these).

$$[e_1] = 2G \begin{bmatrix} 1 & & \\ & 1 & \\ & & 1 \end{bmatrix} + \frac{2G\nu}{1-2\nu} \begin{bmatrix} 1 & 1 & 1 \\ 1 & 1 & 1 \\ 1 & 1 & 1 \end{bmatrix}, \quad [e_2] = \begin{bmatrix} G & \\ & G \\ & & G \end{bmatrix}, \quad (1.8')$$

If we give some thought to the equilibrium equation for the differentiated body, then

$$\bar{x} = -\left(\frac{\partial \sigma_x}{\partial x} + \frac{\partial \sigma_{xy}}{\partial y} + \frac{\partial \sigma_{xz}}{\partial z}\right), \dots$$

and so on, and so on. It follows from this that the computational matrix for equilibrium is

$$[k]_{3 \times 6} = [-D_1, -D_2]. \quad (1.9)$$

From equations (1.3), (1.4) and (1.5), it is possible to obtain the partial differential equation of Lamé which relates to displacement

$$\{\bar{\phi}\}_{3 \times 1} = [k]_{3 \times 6} \{\phi\}_{6 \times 1}. \quad (1.10)$$

In this case, $[k]$ is the Lamé computational square matrix or, as it is also called, the computational matrix for "rigidity" in elastic bodies, that is

$$[k]_{3 \times 3} = [h]_{3 \times 6} [e]_{6 \times 6} [a]_{6 \times 3} = -[D_1]_{3 \times 6} [e_1]_{6 \times 3} [D_1]_{3 \times 6} - [D_2]_{3 \times 6} [e_2]_{6 \times 3} [D_2]_{3 \times 6}. \quad (1.11)$$

The actual form of the set of partial differential non-homogeneous linear equations of Lamé is

$$\begin{Bmatrix} \bar{u} \\ \bar{v} \\ \bar{z} \end{Bmatrix} = -G \begin{Bmatrix} \Delta u \\ \Delta v \\ \Delta w \end{Bmatrix} - \frac{G}{1-2\nu} \begin{Bmatrix} \frac{\partial \theta}{\partial x} \\ \frac{\partial \theta}{\partial y} \\ \frac{\partial \theta}{\partial z} \end{Bmatrix} \quad (1.10')$$

In this case, $\Delta = \frac{\partial^2}{\partial x^2} + \frac{\partial^2}{\partial y^2} + \frac{\partial^2}{\partial z^2}$, is the Laplacian result and θ is the divergence of the displacement vectors, $\theta = \frac{\partial u}{\partial x} + \frac{\partial v}{\partial y} + \frac{\partial w}{\partial z}$. Below we will explain the fact that $[k]$ is the computational matrix for a self-adjoint system.

As a starter, we will begin talking about the one-dimensional partial result $(D = \frac{\partial}{\partial x})$. A certain one-dimensional near result is

$$P = a_0(x) 1 + a_1(x) D + a_2(x) D^2 + \dots + a_n D^n,$$

The coefficient $a_1(x)$ possesses a derived continuity function between the limits of 0 and $(n-1)$. When this result is used in the function $v(x)$, then one obtains

$$P v(x) = a_0(x) v(x) + a_1(x) v'(x) + \dots + a_n(x) v^{(n)}(x).$$

When this is used in the function $u(x)$, then one obtains

$$\bar{P} u(x) = a_0(x) u(x) - (a_1 u)' + (a_2 u)'' + \dots + (-1)^n (a_n u)^{(n)}.$$

It is possible to verify the fact that the self-adjoint operator of \bar{P} is also fundamentally the same as P . It follows from this that P and \bar{P} are mutually adjoint. They are also similar to the linear operations whose forms are explained below:

$$q = e_0 1 - D(e_1 D) + D^2(e_2 D^2) - \dots, \quad (1.13)$$

$$(q W(x) = e_0 W - (e_1 W')' + (e_2 W'')'' - \dots)$$

If we can assume that $\bar{q} = q$, then the operation q is called a self-adjoint operator.

Concerning the two operator matrices $[a]$ and $[b]$, if their corresponding elements are mutually self-adjoint, that is to say that

$$b_{ji} = \overline{(a_{ij})}, \quad i=1,2,\dots, l, \quad j=1,2,\dots, m \quad (1.14)$$

then, they are called mutually self-adjoint operator matrices; it is possible to use

$$[b]_{mi} = \overline{([a]_{lm})}$$

to illustrate this. If an operator matrix is mutually adjoint with itself, then it is called a self-adjoint operator matrix. For example, if $[c]$ is a symmetrical function square matrix, then the three products

$$[\bar{a}][c][a]$$

are self-adjoint operator square matrices. The definitions and conclusions above make it possible to extend what has already been said to a situation in which one is dealing with many dimensions.

From equations (1.7) and (1.9), it is possible to see that geometrical operator matrices and equilibrium operator matrices $[h]$ are actually self-adjoint matrices; $[c]$ (see equation (1.8)) is a symmetrical function square matrix (non-inclusive operation). It follows from this that the Lamé square operator matrix, $[k]_{3 \times 3}$, is a self-adjoint square operator matrix.

In the general run of problems dealing with linear elastic bodies, the distributed load $\{f(x, y, z)\}$ is already known. If we are speaking in theoretical terms, then on the basis of the partial differential equations of Lamé as well as actual boundary conditions, it is possible to solve the displacement function $\{u(x, y, z)\}$. On the basis of this, it is possible to say that elastic bodies are self-adjoint systems. (Self-adjoint systems = self-adjoint partial differential equations + sufficiently good actual boundary conditions).

If we are speaking from a practical point of view, Lamé equations as well as other types of partial differential equations are all very difficult to solve for precise answers. The decade of the 1950's saw the emergence of the finite element method of

solution. The object of this method was to first set up a way to figure out the physical quantities associated with certain selected points (these points can be called "nodal points") (the most important of these physical quantities are displacement and stress). These quantities must be determined to a definite degree of exactitude. After this is done, then it is possible to figure out the physical quantities which are associated with other points. If we take these nodal points and consider them to be end points or peaks, then we will have divided the elastic body under study into finite elements; these finite elements can be called the elements of the elastic body. The other steps which can be taken will be seen in sections which follow.

SECTION 2. THE TWO STAGE FINITE ELEMENT METHOD

The measures which are taken as part of the finite element solution method can be generally included in two stages: 1° the modeling stage and 2° the structural computation stage. Each of these stages can be further divided into three steps, making six steps in all; each of these steps is dealt with separately below.

1° the modeling stage: (Step one) Take the i th elastic body element (i) and on the basis of its condition in terms of stress and strain, abstract it into the form of a dynamic model. By simplifying, we can clearly determine the four function vectors for the element of the elastic body under study, that is to say, displacement, strain, stress and distributed load as well as their various matrices. If we take a one-dimensional beam element as an example, these four function vectors would respectively be

$$\begin{matrix} \{\phi(x)\}, & \{e(x)\}, & \{\sigma(x)\}, & \{\bar{p}(x)\}. \\ m_i=1 & l_i=1 & l_i=1 & m_i=1 \end{matrix}$$

In this case, the one-dimensional variable is x , the independent displacement is $v(x)$, and the distributed load is $\bar{Y}(x)$, $m_i=1$.

The unit of length of strain energy is

$$\frac{dU}{dx} = \frac{1}{2} \{e_0 v^2 + e_1 (v')^2 + e_2 (v'')^2\}.$$

In this case, $e_0 = K(x)$ is the basic coefficient of rigidity or stiffness for the elastic body (kg/cm^2); $e_1 = N(x)$ is the internal axial force (kg/cm with a pull force being positive); $e_2 = EI(x)$ (kg/cm^2) is always positive. We can take the three quantities above to be the permanent characteristics of beams and these do not vary with changes in external loading or displacement.

The standard second-degree equation which can be written for the strain function vector $\{e(x)\}$ of $\frac{dU}{dx}$ is

$$\frac{dU}{dx} = \frac{1}{2} [e_{(x)}] [e_{(x)}] \{e_{(x)}\}, \quad (2.1)$$

If we carry out a comparison, we then obtain square matrices for the modulus of elasticity and the strain function vector of the beam element involved; the nature of these matrices is as follows:

$$\{e_{(x)}\}_{l,1} = \begin{Bmatrix} v(x) \\ v'(x) \\ v''(x) \end{Bmatrix}, \quad [e_{(x)}] = \begin{bmatrix} e_0(x) & & \\ & e_1(x) & \\ & & e_2(x) \end{bmatrix} = \begin{bmatrix} K(x) & & \\ & N(x) & \\ & & EI(x) \end{bmatrix}.$$

Let us also define it to be true that the stress function vector $\{\sigma_{(x)}\}_{l,1}$ and $\{e_{(x)}\}$ satisfies the corresponding relationship

$$\frac{dU}{dx} = \frac{1}{2} [\sigma_{(x)}] \{e_{(x)}\}, \quad (2.2)$$

Acting as a sort of limit on $\{\sigma_{(x)}\}$ and $\{e_{(x)}\}$, the physical relationship between the elements of these two is

$$\{\sigma_{(x)}\}_{l,1} = [e_{(x)}] \cdot \{e_{(x)}\}_{l,1}. \quad (2.3)$$

Acting as another type of limit, the displacement $\{\psi_{(x)}\}_{m,1}$ and the distributed load $\{\bar{p}_{(x)}\}_{m,1}$ satisfy the corresponding relationship

$$\frac{dW^e}{dx} = \frac{1}{2} \sum_{i=m_1}^l \{ \bar{f}_i^e \} \{ \psi_i^e \} \quad (2.4)$$

If, in the case of a one-dimensional beam element, we chose $\{ \bar{f}_i^e \} = \{ \bar{P}(x) \}$, $\{ \psi_i^e \} = \{ v(x) \}$, then the work done by the distributed load per unit of length is as shown in the solution set of equation (2.4).

(Step two) In a modeling analysis of the elastic body element, one should first pay attention to whether or not the assumptions listed below are in effect or not.

(i) The fixed-form assumption:

$$\{ e^e \} = [a^e] \{ \psi^e \} \quad (2.5)$$

$l_e \times 1 \quad l_e \times m_e \quad m_e \times 1$ geometrical relationship

(ii) The fixed-force assumption:

$$\{ f^e \} = [h^e] \{ \sigma^e \} \quad (2.6)$$

$m_e \times 1 \quad m_e \times l_e \quad l_e \times 1$ equilibrium relationship

It is also necessary to pay attention to whether or not the geometrical operator matrices for the element $[a]$ and the equilibrium operator matrices for the elements $[h]$ exist.

On the basis of what determination is made about this point, there are four different types of situations in which the elements of an elastic body can find themselves, that is

(i) $[a^e]$ and $[h^e]$ both exist (it is possible to demonstrate that the two of them are mutually adjoint); an element for which this is true is called a self-adjoint element. The three types of elements which follow are all not self-adjoint elements.

(ii) $[a^e]$ exists and $[h^e]$ does not exist. This type of element is called a fixed form-non-fixed force element.

$$\left\{ \begin{matrix} v \\ v' \\ v'' \end{matrix} \right\}_{l_i \times 1} = \left\{ \begin{matrix} v \\ v' \\ v'' \end{matrix} \right\} = [a'] \{v\}, \quad (2.5')$$

It can be seen that the geometrical operator matrix $[a]$ does exist: This establishes the geometrical relationship (the establishment of the fixed form assumption). $[a'] = \begin{bmatrix} 1 \\ D \\ D^2 \end{bmatrix}$.

From the physical relationship (2.3), it is possible to obtain the component vectors l_i of $\{\sigma(x)\}'$; moreover, this explains the physical significance of them, that is

$$\left\{ \begin{matrix} \sigma(x) \\ \sigma'(x) \\ \sigma''(x) \end{matrix} \right\}_{l_i \times 1} = \left\{ \begin{matrix} K(x) v(x) \\ N(x) v'(x) \\ EI(x) v''(x) \end{matrix} \right\} = \left\{ \begin{matrix} \bar{Y} + Q' \\ Q + M' \\ M \end{matrix} \right\} \begin{matrix} \text{(equilibrium element)} \\ \text{" " " (2.3')} \\ \text{(modeling analysis)} \end{matrix}$$

In this case, Q and M are the shear force and strain matrices (employing a beam standard).

By eliminating Q and M , one can then obtain the equilibrium relationship between the distributed load vector $\{\bar{Y}(x)\}'$ and the stress function vector $\{\sigma\}'$, that is

$$\left\{ \begin{matrix} \bar{Y}' \\ \sigma' \end{matrix} \right\}_{m_i \times 1} = [h'] \{\sigma\}', \quad m_i \times 1 \quad m_i \times l_i \quad l_i \times 1$$

In this case the equilibrium operator matrix is

$$[h'] = [1, -D, D^2],$$

it can be seen that the fixed-force assumption is in effect. Moreover, the two operator matrices $[a']$ and $[h']$ are mutually adjoint. The non-homogeneous linear differential equation for the beam elements is

$$\begin{aligned} \{\bar{Y}(x)\}' &= [k'] \{v(x)\}' \\ &= [1, -D, D^2] \begin{bmatrix} e_0(x) \\ e_1(x) \\ e_2(x) \end{bmatrix} \begin{Bmatrix} 1 \\ D \\ D^2 \end{Bmatrix} \{v(x)\}', \end{aligned}$$

If we simplify the standard 1 above, we can then write the differential equation for the curve of the beam elements, that is

$$\bar{Y}(x) = K(x) v(x) - (N(x) v'(x))' + (EI(x) v''(x))'', \quad (2.7)$$

And again, due to the actual nature of its boundary conditions, it follows that we can know that a one-dimensional beam element is a self-adjoint system.

Due to the fact that a one-dimensional beam is susceptible to solution, this article will discuss it in somewhat more detail as follows. Let us assume that its solution is

$$v(x) = v^*(x) + [\psi(x)]\{c\}, \quad (2.8)$$

In this case, $v^*(x)$ is a certain special solution to the non-homogeneous differential equation (2.7); it is also true that

$$[\psi(x)] = [\psi_1(x), \psi_2(x), \psi_3(x), \psi_4(x)],$$

are a set of linear independent auxiliary functions and they satisfy the homogeneous linear equation $[k]v(x) = 0$; moreover, $\{c\} = \begin{Bmatrix} c_1 \\ \vdots \\ c_4 \end{Bmatrix}$ is an integral constant vector; 4 equals the step function of the differential equation and $\{c\}$ is decided by four boundary conditions.

The two end boundary values for beam elements are organized from or consist of the displacement of the two end boundaries and the external forces of the two end boundaries. The displacement vectors of the two end boundaries include the degree of deflection or buckling of the two ends $v(o)$ and $v(L)$ as well as the deflection angles of the two ends $v'(o)$ and $v'(L)$; we can simplify matters by the use of $\{Bv\}$ for purposes of representation; $[B]$ is the boundary displacement operator for the elements concerned, that is

$$\begin{pmatrix} v_0 \\ v'_0 \\ v_L \\ v'_L \end{pmatrix} = \begin{pmatrix} 1_0 \\ D_0 \\ 1_L \\ D_L \end{pmatrix} v(x) = [B] \{v(x)\} = \{Bv\}_0.$$

$\mu_1=1$
 $\mu_1=4$

The external force vectors for the two end boundaries include the concentrated forces for the two ends $Y(0)$ and $Y(L)$ as well as the matching concentrated forces $m(0)$ and $m(L)$ (employ standard nodal points); we can simplify matters by using $\{Fv\}$ for purposes of demonstration; $\{F\}$ is the external force operator for the boundaries of the elements involved, that is,

$$\begin{pmatrix} Y_0 \\ m_0 \\ Y_L \\ m_L \end{pmatrix} = \begin{pmatrix} -Q_0 \\ -M_0 \\ Q_L \\ M_L \end{pmatrix} = \begin{pmatrix} -(Nv')_0 + (EIv'')'_0 \\ -(EIv'')'_0 \\ (Nv')_L - (EIv'')'_L \\ (EIv'')'_L \end{pmatrix} = [F] \{v(x)\} = \{Fv\},$$

$$[F] = \begin{pmatrix} -(ND)_0 + D(EID^2)_0 & \\ & -(EID^2)_0 \\ (ND)_L - D(EID^2)_L & \\ & (EID^2)_L \end{pmatrix}.$$

$\mu_1=1$
 $\mu_1=4$

In simple practical problems, for example, the hinge branches at the two ends of the elements involved, there are then four boundary conditions which prevail, those are $v_0 = v_L = m_0 = m_L = 0$, from these it is possible to figure out $\{c\}$.

However, if we are dealing with problems in which are included chain-type situations with many beam elements being involved, then the two end boundary values for the beam elements involved are still indeterminate; the solution method for this type of problem will be demonstrated in steps three to six.

(Step Three) Let us assume that the beam elements involved have distributed loads (as well as corresponding distributed forces or zero point concentrated load and concentrated corresponding forces, etc.); if we assume this, then let us solve and take the equivalent external structural forces and move them to places at the two ends (that is to say, a secondary system of forces opposite to the first which is created when the two ends do not move, see [1]); we can then substitute them for the original distributed load. After the substitution is made, the situation is as follows. The new distributed load is $\bar{Y}(x)=0$; in this case, equation (2.7) is changed to become a homogeneous equation; it is possible to pick out the special solution $v^*(x)=0$, and on the basis of this, the displacement function is

$$v(x) = [\psi(x)] \{c\}. \quad (2.12)$$

It is possible to change the procedure and use the boundary displacement $\{Bv\}$ to represent $\{c\}$ & $v(x)$ in order to make operations simpler. If we use the operator $[B]$ and first multiply it through equation (2.12), then it is possible to obtain

$$\{Bv\} = ([B] [\psi(x)]) \{c\},$$

$$\mu_i = 1 \quad \mu_i = \mu_i \quad \mu_i = 1$$

In this case, $([B] [\psi(x)])$ is a reversible square matrix (the only time it is irreversible is when the beam column element elasticity loses its stability [1]; we can write this simply as $[B\psi]$, and it follows from this that

$$\{c\}_i = [B\psi]^{-1} \{Bv\}_i,$$

as well as that

$$v(x) = [\psi(x)] [B\psi]^{-1} \{Bv\}. \quad (2.13)$$

It can be easily pointed out that $[\psi(x)] [B\psi]^{-1}$ has no relationship with the set of auxiliary functions which are selected; it is possible to call these functions standard auxiliary functions and

they can be represented by the expression $[\psi^s(x)]$; it follows from this that

$$v(x) = [\psi^s(x)] \{Bv\}. \quad (2.13')$$

If we take for an example the case in which an even cross-sectional beam element is acted upon by evenly distributed forces, then $K(x) = N(x) = 0$, EI equals a constant, and $\bar{Y}(x)$ equals a constant. The equivalent external structural load which is moved to the two ends are

$$Y_L^{Kq} = Y_L^{Kq} = \frac{1}{2} \bar{Y} L, \quad m_L^{Kq} = -m_L^{Kq} = \frac{1}{12} \bar{Y} L^2.$$

After the movement and substitution of these forces, the homogeneous differential equation is $EI v'''' = 0$; or will employ the non-dimensional auxiliary functions

$$\psi_1(x) = 1, \quad \psi_2(x) = \frac{x}{L}, \quad \psi_3(x) = \left(\frac{x}{L}\right)^2, \quad \psi_4(x) = \left(\frac{x}{L}\right)^3,$$

The stable square matrix is reversible to

$$[B\psi] = \begin{bmatrix} 1 & 0 & 0 & 0 \\ 0 & \frac{1}{L} & 0 & 0 \\ 1 & 1 & 1 & 1 \\ 0 & \frac{1}{L} & \frac{2}{L} & \frac{3}{L} \end{bmatrix}, \quad [B\psi]^{-1} = \begin{bmatrix} 1 & 0 & 0 & 0 \\ 0 & L & 0 & 0 \\ -3 & -2L & 3 & -L \\ 2 & L & -2 & L \end{bmatrix}.$$

If we solve for the standard auxiliary functions, then

$$[\psi^s(x)] = \left[1 - \frac{3x^2}{L^2} + \frac{2x^3}{L^3}, \quad x - \frac{2x^2}{L} + \frac{x^3}{L^2}, \right. \\ \left. \frac{3x^2}{L^2} - \frac{2x^3}{L^3}, \quad -\frac{x^2}{L} + \frac{x^3}{L^2} \right]. \quad (2.13'')$$

Moreover, the displacement function is also as shown in equation (2.13').

In the third step of the modeling phase, it is still necessary to take the i th free member of the elastic body and turn it into the i th free structural member; at the time that this is done, there is already no distributed load. It is necessary to take the four function vectors of the element i (we may still take a one-dimensional beam as an example) and we then obtain

$$\begin{matrix} \{v(x)\}' (=v(x)), & \{e(x)\}', & \{\sigma(x)\}', & \{\beta(x)\}' (= \bar{Y}(x)). \end{matrix} \quad (2.14)$$

$$\begin{matrix} m_i+1 & l_i+1 & l_i+1 & m_i+1 \end{matrix}$$

These quantities which satisfy the limitations of $\{\beta(x)\}' \{v(x)\}' = 2dW'/dx$ and $\{\sigma(x)\}' \{e(x)\}' = 2dU'/dx$ turn into the four generalized value vectors of element i , that is

$$\begin{matrix} \{\psi\}' (= \{Bv\}'), & \{e'\}', & \{\sigma'\}', & \{\phi'\}' (= \{Fv\}'). \end{matrix} \quad (2.15)$$

$$\begin{matrix} \mu_i+1 & l_i+1 & l_i+1 & \mu_i+1 \end{matrix}$$

This satisfies the limitations of $\{\phi'\}' \{\psi'\}' = 2W'$ $\{\sigma'\}' \{e'\}' = 2U'$

Moreover, in order to carry out the transformation operation and the resubstitution operation, the function vectors of the elements and the fixed value vectors of the members can be changed for each other in the following way

| | | | |
|-------------------------|---|---------------------------|--------|
| operation | | | |
| element function vector | ← | member fixed value vector | |
| (2.14) | → | (2.15) | (2.16) |
| auxiliary functions | | | |

For example, the displacement of the member i $\{v(x)\}'_{m_i+1}$ can be the operation B and yield the $\{Bv\}'_{\mu_i+1}$ of member i ; the $\{Bv\}'_{\mu_i+1}$ of member i can be solved for and, by that means, we can obtain the value of $\{e'\}'_{l_i+1}$ and further obtain the $v(x)'$ of element i (see equation 2.13). As far as other like vectors are concerned, such as $\{e(x)\}'_{l_i+1}$ and $\{e'\}'_{l_i+1}$ and so on, it is also necessary for them to be capable of mutual substitution.

If we now take a uniform cross-section beam ($K(x)=N(x)=0$, $EI(x)$ equal to a constant) as an example, we can explain the relationship between element strain and member strain.

Element strain $\{e(x)'\}_{l_i+1} = \{v''(x)\},$

If $2! \leq m_i$ (m_i is the step function of the displacement vector of a member), and $\{e(x)'\}$ is a linear function, then it is possible to select the two end strain values to act as the member strains:

the member strain

$$\{e'\}_{\lambda_i+1} = \begin{Bmatrix} e_0 \\ e_L \end{Bmatrix} = \begin{Bmatrix} v''(0) \\ v''(L) \end{Bmatrix} = \begin{bmatrix} 1_0 \\ 1_L \end{bmatrix}_{\lambda_i+1} \{v''(x)\}. \quad (2.17)$$

That is to say, let us use the $\begin{bmatrix} 1_0 \\ 1_L \end{bmatrix}$ operator to pre-multiply the element strain. Turning it around the other way, the formula for solving for $\{e(x)'\}$ from $\{e'\} = \begin{Bmatrix} e_0 \\ e_L \end{Bmatrix}$ is

$$\{e(x)'\}_{l_i+1} = \frac{L-x}{L} e_0 + \frac{x}{L} e_L = [p(x)]_{l_i+1, \lambda_i} \begin{Bmatrix} e_0 \\ e_L \end{Bmatrix}_{\lambda_i+1}, \quad (2.17')$$

In this case,

$$[p(x)] = \left[\frac{L-x}{L}, \frac{x}{L} \right]$$

is an interpolation function matrix. It is possible to see that the product of the two end value operator matrix $\begin{bmatrix} 1_0 \\ 1_L \end{bmatrix}$ and the interpolation function matrix is a unit square matrix

$$\begin{bmatrix} 1_0 \\ 1_L \end{bmatrix}_{\lambda_i+1, l_i} [p(x)]_{l_i+1, \lambda_i} = [I]_{m_i \times m_i}. \quad (2.17'')$$

We can use this example to explain the facts set out below:
 1° if the geometrical operator matrix of an element $[a']$ exists, then the member geometrical matrix $[a']$ also exists. (It is also possible to use $\{e(x)'\}$ to represent $\{e'\}$).
 2° if the equilibrium operator matrix of an element exists, then the member equilibrium $[h']$ also exists.
 3° if $[a']$ and $[h']$ both exist and

are mutually self-adjoint, then $[a']$ and $[h']$ both exist and are mutually transposed.

When one is dealing with a one-dimensional beam element,

$[a'] = \begin{bmatrix} 1 \\ D \\ D^2 \end{bmatrix}$, when one is dealing with a situation in which one has an even cross-section beam element, then $[a']$ breaks down to be $[D^2]$

$$\begin{aligned} \{e(x)'\} &= \{v''(x)\} = [D^2] v(x) = [a^2] \{v(x)\} \\ l_1 \times 1 & \qquad \qquad \qquad l_1 \times m_1 \quad m_1 \times 1 \\ &= [a'] [\psi^s(x)] \{Bv\}, \end{aligned}$$

In this case, even cross-section members then have

$$\{e'\} = \begin{bmatrix} 1_0 \\ 1_L \end{bmatrix} \{e(x)'\} = \begin{bmatrix} 1_0 \\ 1_L \end{bmatrix} [a^2] [\psi^s(x)] \{Bv\},$$

It follows from this that its geometrical relationship is

$$\begin{aligned} \{e'\} &= [a'] \{Bv\} \\ \lambda_1 \times 1 & \quad \lambda_1 \times \mu_1 \end{aligned}$$

and is also established, that is to say, that the member geometrical matrix $[a']$ also exists and is equal to

$$[a'] = \begin{bmatrix} 1_0 \\ 1_L \end{bmatrix} [a^2] [\psi^s(x)] \quad (2.18)$$

$\lambda_1 \times \mu_1 \quad \lambda_1 \times m_1 \quad m_1 \times \mu_1$

If, when we are engaged in the actual process of calculation, and we employ equation (2.13'), then we can obtain

$$\begin{aligned} [a'] [\psi^s(x)] &= \frac{2}{L^2} \left[-3 + 6 \frac{x}{L}, 2L + 3x, 3 - 6 \frac{x}{L}, -L + 3x \right] \\ &= \frac{2}{L^2} \begin{bmatrix} -2L + 3x, & -L + 3x \end{bmatrix} \begin{bmatrix} 1 & 1 & -1 & 0 \\ 1 & 0 & -1 & 1 \end{bmatrix}, \\ [a'] &= \frac{2}{L^2} \begin{bmatrix} -3 & -2L & 3 & -L \\ 3 & L & -3 & 2L \end{bmatrix} = \frac{2}{L^2} \begin{bmatrix} -2L & -L \\ L & 2L \end{bmatrix} \cdot \begin{bmatrix} 1 & 1 & -1 & 0 \\ 1 & 0 & -1 & 1 \end{bmatrix}. \end{aligned}$$

The square function matrices of the moduli of elasticity for elements and members, $[e(x)']$ and $[e']$ must satisfy the relationships that follow, that is, internal energies must be equal or, to say it another way,

$$2U' = \int_0^L [e(x)'] [e(x)'] \{e(x)\}' dx = [e'] [e'] \{e'\}. \quad (2.19)$$

The reason for this is that in a situation in which $[e(x)'] = [EI]$ is deteriorating and its value in kg-cm^2 is a constant, then it follows that we can obtain

$$EI \int_0^L \begin{bmatrix} -2L+3x \\ -L+3x \end{bmatrix} \begin{bmatrix} -2L+3x & -L+3x \end{bmatrix} dx = \begin{bmatrix} -2L & L \\ -L & 2L \end{bmatrix} [e'] \begin{bmatrix} -2L & -L \\ L & 2L \end{bmatrix}.$$

In turn, it follows from this that

$$[e'] = \frac{1}{6} EIL \begin{bmatrix} 2 & 1 \\ 1 & 2 \end{bmatrix}, \quad \text{kg-cm}^3. \quad (2.19')$$

When we are dealing with the situation in which $\{e(x)\}'$ is a linear function, then it is possible to deduce the following formula

$$[e'] = \int_0^L \begin{bmatrix} p(x)' \\ \lambda_i \cdot e_i \end{bmatrix} \begin{bmatrix} e(x)' \\ l_i \cdot l_i \end{bmatrix} [p(x)] dx, \quad (2.20)$$

If $[e(x)'] = [EI]$, then we obtain (2.19').

On the basis of physical relationships, we can arrive at the stress vectors for elements and members:

$$\text{Element} \quad \begin{bmatrix} \sigma(x)' \\ l_i \cdot l_i \end{bmatrix} = [e(x)'] \{e(x)\}' = \{E/v''(x)\},$$

and, on the basis of modeling analysis, it is nothing else but the bending moment $M(x)$;

$$\{\sigma(x)\}' = \{M(x)\} \quad . \quad (\text{Bending moment, kg-cm, beam model or standard})$$

Member

$$\begin{aligned}
 \{\sigma'\} &= [c'] \{e'\} = \frac{1}{6} EIL \begin{bmatrix} 2 & 1 \\ 1 & 2 \end{bmatrix} \begin{Bmatrix} v''_0 \\ v''_l \end{Bmatrix} \\
 &= \frac{L}{6} \begin{bmatrix} 2 & 1 \\ 1 & 2 \end{bmatrix} \begin{Bmatrix} M_0 \\ M_l \end{Bmatrix} \quad \text{kg cm}^2 \\
 &= \frac{L}{2} \begin{Bmatrix} M_0 \text{ at } x = \frac{1}{3} L \text{ the place where} \\ M_l \text{ at } x = \frac{2}{3} L \text{ the place where} \end{Bmatrix}
 \end{aligned}$$

1--where

(Translator's note: something missing in the text) the equilibrium relationship for the element 1. In the case of the general run of beam elements, these elements possess equilibrium matrices and equilibrium relationships as follows: $\{\beta\} = [h'] \{\sigma(x)\}$ that is,

$$\{\bar{Y}(x)\} = [1, -D, D^2] \begin{Bmatrix} K(x) v(x) \\ N(x) v'(x) \\ EI(x) v''(x) \end{Bmatrix}, \quad (l=3)$$

When one is dealing with the case of a beam element with an even cross-section, then $\{\sigma(x)\}$ and $[h']$ degenerate down to the limit of

$$\begin{aligned}
 \{\sigma(x)\} &= \{EI v''(x)\} = \{M(x)\}, \quad (l=1) \\
 [h'] &= [D^2] (= [\bar{\sigma}']), \quad (m_1=1)
 \end{aligned} \tag{2.21}$$

We are able from this to obtain the ordinary differential equation

$$EI v''''(x) = \bar{Y}(x).$$

It can be seen that the functioning of the degeneration certainly does not cause the disappearances of the equilibrium relationship. All it does is to cause yet another internal force, that is, the shear force $Q(x)$ to be included within the degenerated stream vector $\left(\frac{dM}{dx} = -Q\right)$ and nothing more than that.

The fixed form of the external forces on a member 1 is the external boundary forces on the two ends and the external force complement, that is,

$$\{\phi'\} = \{Fv\} = \begin{Bmatrix} Y_n \\ m_o \\ Y_L \\ m_L \end{Bmatrix}, \begin{array}{l} \text{use} \\ \text{standard} \\ \text{model parts } \mu_1 = 4 \end{array}$$

In this case, the stream vector is

$$\{\sigma'\} = \frac{L}{2} \begin{Bmatrix} M^1 x = \frac{1}{3} L^2 \\ M^2 x = \frac{2}{3} L^2 \end{Bmatrix}, \quad (\lambda_1 = 2)$$

1--where 2--the place where

Let us first figure out the bending moments for the two ends (beam model or standard):

$$\begin{Bmatrix} M_o \\ M_L \end{Bmatrix} = \frac{6}{L} \begin{bmatrix} 2 & 1 \\ 1 & 2 \end{bmatrix}^{-1} [\sigma'] = \frac{2}{L} \begin{bmatrix} 2 & -1 \\ -1 & 2 \end{bmatrix} \{\sigma'\},$$

When, if we change to the use of a nodal point model,

$$\begin{Bmatrix} m_o \\ m_L \end{Bmatrix} = \begin{Bmatrix} -M_o \\ +M_L \end{Bmatrix} = \frac{2}{L} \begin{bmatrix} -2 & 1 \\ -1 & 2 \end{bmatrix} \{\sigma'\}.$$

Due to the fact that this free beam member not only has no distributed load, that is, it has already been substituted for, but also has no basic elastic force or axial force, $\{\phi'\}_{\mu_1}$ is not an independent vector, and it has the relationship which follows:

$$Y_o = -Y_L = \frac{m_o + m_L}{L},$$

It follows from this that we can obtain

$$\{\phi'\}_{\mu_1=1} = \begin{bmatrix} \frac{1}{L} & \frac{1}{L} \\ 1 & 0 \\ -\frac{1}{L} & -\frac{1}{L} \\ 0 & 1 \end{bmatrix} \begin{Bmatrix} m_o \\ m_L \end{Bmatrix} = \left(\frac{2}{L^2} \right) \begin{bmatrix} -3 & 3 \\ -2L & L \\ 3 & -3 \\ -L & -2L \end{bmatrix} \{\sigma'\} \quad (2.22)$$

$$= [h'] \{\sigma'\}. \quad (2.22')$$

$$\mu_1 = \lambda_1, \lambda_1 = 1$$

It can be seen that the fixed force assumption for the member is also in effect, that $[h']$ exists and, moreover, that it is equal to the transposed form of $[a']$.

As far as the conclusions above go, it is possible to employ the principle of virtual work to demonstrate the following:

(Thesis) $[a']_{\lambda_i=\mu_i}$ and $[h']_{\mu_i=\lambda_i}$ for a certain member i which is already known both exist and if this is the case, then the two of them can be mutually transposed.

(Proof) Consider the virtual displacement $\{\psi_o\}$, if we do so, then the virtual strain is $[a']\{\psi_o\}$; the virtual potential energy which stored in virtual strain by the actual stress $\{\sigma'\}$ is $[\sigma'] [a']\{\psi_o\}$. The virtual work done by the actual external force $[h']\{\sigma'\}$ in the virtual displacement is

$$[\phi]\{\psi_o\} = ([h']\{\sigma'\})' \{\psi_o\} = [\sigma'] [h']' \{\psi_o\}.$$

The principle of virtual displacement gives us the fact that the virtual potential energy is equal to the virtual work, that is to say,

$$[\sigma'] [a'] \{\psi_o\} = [\sigma'] [h']' \{\psi_o\}$$

Due to the fact that $\{\psi_o\}$ is an independent vector which does not get out of control arbitrarily, it follows that it is possible to eliminate $\{\psi_o\}$ and obtain $[\sigma'] [a'] = [\sigma'] [h']'$.

In the general run of situation s , if we determine $[\sigma']$ to be an independent vector and, if we also decide that it varies with changes in the external loading, then it is also possible to eliminate $[\sigma']$, and arrive at a proof that way.

By induction, we can obtain the relationships below which pertain to a one-dimensional beam member of a fixed-form-force type:

$$\begin{aligned} \{Fv\}_{\mu_i=1} &= [h']_{\lambda_i=1} \{\sigma'\}_{\lambda_i=1}, & \{\sigma'\}_{\lambda_i=1} &= [e']_{\lambda_i=1} \{e'\}_{\lambda_i=1}, & \{e'\}_{\lambda_i=1} &= [a']_{\lambda_i=1} \{Bv\}_{\mu_i=1}, \\ \therefore \{Fv\}_{\mu_i=1} &= [h']_{\mu_i=\mu_i} \{Bv\}_{\mu_i=1}. \end{aligned} \quad (2.20)$$

In this case, $[k']_{\mu_i \times \mu_i}$ is the rigidity or stiffness matrix for the beam member, and its value is

$$[k']_{\mu_i \times \mu_i} = [k'] [e'] [a'] = [a']' [e'] [a'] . \quad (2.21)$$

$\mu_i \times \lambda_i \quad \lambda_i \times \lambda_i \quad \lambda_i \times \mu_i$

It follows from this that we can be certain that it is a symmetrical non-negative fixed matrix. Even in the case of the modeling stage, it is still possible to get a value for $[k']$; the formula for this is as follows: $\{Fv\}_{\mu_i \times 1} = [F]_{\mu_i \times 1} \{\psi^s\}_{1 \times \mu_i} \{Bv\}_{1 \times \mu_i}$,

If we employ the operator

$$\therefore [k']_{\mu_i \times \mu_i} = [F]_{\mu_i \times 1} \{\psi^s\}_{1 \times \mu_i} . \quad (2.21')$$

and give consideration to the relationship $W' = U'$, then it is possible to obtain

$$\{Bv\}_{1 \times \mu_i} [k']_{\mu_i \times \mu_i} \{Bv\}_{\mu_i \times 1} = \int_0^L [e(x)]_{1 \times l_i} [e(x)]_{l_i \times l_i} \{e(x)\}_{l_i \times 1} dx ,$$

Due to the fact that

$$\{e(x)\}_{l_i \times 1} = [a']_{l_i \times 1} v(x) = [a']_{l_i \times 1} \{\psi^s\}_{1 \times \mu_i} \{Bv\}_{\mu_i \times 1} ,$$

it follows that we can also obtain

$$[k']_{\mu_i \times \mu_i} = \int_0^L [a']_{\mu_i \times l_i} \{\psi^s\}'_{l_i \times l_i} [a']_{l_i \times \mu_i} \psi^s dx . \quad (2.21'')$$

As was the case with the even or homogeneous cross-section beam member, equations (21, 21', 21'') are all capable of giving us the result

$$[k'] = \frac{EI}{L^3} \begin{pmatrix} 12 & 6L & -12 & 6L \\ 6L & 4L^2 & -6L & 2L^2 \\ -12 & -6L & 12 & -6L \\ 6L & 2L^2 & -6L & 4L^2 \end{pmatrix} .$$

2° The structural computation stage

(Step 4) Structures composed entirely from free members are called assembly structures.

We can take chain-type beam structures as an example by which to explain this. Let us assume that we have all told I free members whose designation numbers are $1, 2, \dots, I$; let us also assume that we have all told J nodal points and that their designation numbers are $1, 2, \dots, I, J$; let us also assume that $J = I+1$.

The member i is the member which connects the nodal points i and j ($= i+1$). The displacements of the two ends are

$$[B v^i] = \begin{Bmatrix} \{\psi^i\} \\ \{\psi^j\} \end{Bmatrix}, \quad i=1, 2, \dots, I.$$

$\mu_i = 1$
 $(\mu^i + \mu^j) = 1$

The collected displacement vectors for a structure (also known as the assembly displacement vector) is defined to be

$$\begin{Bmatrix} \psi \\ \Sigma \mu \end{Bmatrix} = \begin{Bmatrix} \psi^1 \\ \psi^2 \\ \vdots \\ \psi^J \end{Bmatrix}, \quad \Sigma \mu = \mu^1 + \mu^2 + \dots + \mu^J.$$

If all the members are of a fixed-form type, then take $[a^i]$ and divide it into its component parts $[a^{ii}, a^{ij}]$, $\lambda^i = \mu^i$ $\lambda^i = \mu^j$ then we can get

$$\{e^i\} = [a^{ii}, a^{ij}] \begin{Bmatrix} \{\psi^i\} \\ \{\psi^j\} \end{Bmatrix}, \quad i=1, 2, \dots, I \quad (2.22)$$

By bringing things together, we can also obtain the combined geometrical relationship for fixed-form structures

$$\begin{Bmatrix} e^1 \\ e^2 \\ \vdots \\ e^J \\ \Sigma \lambda \end{Bmatrix} = \begin{pmatrix} a^{11} & a^{12} & & \\ & a^{22} & a^{23} & \\ & & \dots & \\ & & & a^{JJ} & a^{JJ'} \\ & & & & a^{JJ'} \end{pmatrix} \begin{Bmatrix} \psi^1 \\ \psi^2 \\ \vdots \\ \psi^J \\ \psi^J \end{Bmatrix} \Sigma \mu$$

This can be simplified to be

$$\{\epsilon\}_{\Sigma\lambda} = [a]_{\Sigma\lambda, \Sigma\lambda} \{\psi\}_{\Sigma\lambda}, \quad \Sigma\lambda = \lambda_1 + \lambda_2 + \dots + \lambda_I.$$

On the basis of this, it is possible to obtain the combined physical relationship for the structure involved, that is

$$\begin{pmatrix} \sigma^1 \\ \sigma^2 \\ \vdots \\ \sigma^I \end{pmatrix}_{\Sigma\lambda} = \begin{pmatrix} [e^1]_{\lambda_1\lambda_1} & & \\ & [e^2]_{\lambda_2\lambda_2} & \\ & & \dots \\ & & & [e^I]_{\lambda_I\lambda_I} \end{pmatrix} \begin{pmatrix} \epsilon^1 \\ \epsilon^2 \\ \vdots \\ \epsilon^I \end{pmatrix}_{\Sigma\lambda}$$

This can be simplified to be

$$\{\sigma\}_{\Sigma\lambda} = [e]_{\Sigma\lambda, \Sigma\lambda} \{\epsilon\}_{\Sigma\lambda} \quad (2.23)$$

If all of the members are of the fixed-force type, and if $\begin{pmatrix} h' \\ (\mu^i, \mu^j) \cdot \lambda^i \end{pmatrix}$ exists and we divide it up into $\begin{pmatrix} h'' \\ h'' \end{pmatrix}$, then the equilibrium equation for the i th member is

$$\begin{pmatrix} \delta'' \\ \delta'' \end{pmatrix} = \begin{pmatrix} h'' \\ h'' \end{pmatrix} \{\sigma^i\} \quad i = 1, 2, \dots, I$$

Therefore, the combined equilibrium equation for fixed-force structures is

$$\begin{pmatrix} \delta'' \\ \delta^{21} + \delta^{22} \\ \delta^{23} + \delta^{33} \\ \vdots \\ \delta^{IJ} \end{pmatrix}_{\Sigma\mu+1} = \begin{pmatrix} h^{11} & & \\ h^{21} & h^{22} & \\ & h^{30} & h^{33} \\ & & \dots & \\ & & & h^{IJ} \end{pmatrix}_{\Sigma\mu+1, \Sigma\lambda} \begin{pmatrix} \sigma^1 \\ \sigma^2 \\ \vdots \\ \sigma_I \end{pmatrix}_{\Sigma\lambda+1}$$

This can be simplified to be

$$\{\delta\}_{\Sigma\mu} = [h]_{\Sigma\mu, \Sigma\lambda} \{\sigma\}_{\Sigma\lambda}$$

$[h]_{\Sigma\mu, \Sigma\lambda}$ is the combined equilibrium matrix for fixed-force structures.

If all the members are of the fixed-form type and are also of the fixed-force type, then it follows from that basis that $[a'] = [h']$ in such a case, it is also true that the combined geometrical matrix $[a]_{\Sigma\lambda, \Sigma\lambda}$ and the combined equilibrium matrix $[h]_{\Sigma\lambda, \Sigma\mu}$ both exist and that

they are capable of being mutually transposed.

Between the combined vectors $\{\psi\}_{\Sigma\mu}$ and $\{\bar{\phi}\}_{\Sigma\mu}$ of fixed-form fixed-force structures there is also the rigidity or stiffness equation

$$\{\bar{\phi}\}_{\Sigma\mu} = [k]_{\Sigma\mu\Sigma\mu} \{\psi\}_{\Sigma\mu}, \quad (2.26)$$

In this case,

$$[k]_{\Sigma\mu\Sigma\mu} = [k][e][a] = [a]' [e] [a], \quad (2.25')$$

$$\Sigma^{\mu} \Sigma^{\lambda} \Sigma^{\lambda} \Sigma^{\mu}$$

This is also a symmetrical non-negative fixed matrix. After combining we have the internal energy of the structure:

$$U = U^1 + U^2 + \dots + U^r = \frac{1}{2} \begin{bmatrix} \sigma \end{bmatrix} \begin{bmatrix} e \end{bmatrix},$$

$$1 \cdot \Sigma^{\lambda} \Sigma^{\lambda} \cdot 1$$

the work done on the structure by external forces:

$$W = W^1 + W^2 + \dots + W^r = \frac{1}{2} \begin{bmatrix} \bar{\phi} \end{bmatrix} \begin{bmatrix} \psi \end{bmatrix}$$

$$1 \cdot \Sigma^{\mu} \Sigma^{\mu} \cdot 1$$

We also reach the result $U = W_0$. (Note) the external force at any given nodal point j is $\bar{\phi}_j = \phi_j + \bar{\phi}_j$; ϕ_j is the external load and $\bar{\phi}_j$ is the external constraining force.

In general, during the process of combining, the turning of the axis to the direction of the standard axis $0 \xi \eta \zeta$ makes it easier to the operations of addition and subtraction. The four combined vectors which are obtained are

$$\{\bar{\phi}\}_{\Sigma\mu}, \{\psi\}_{\Sigma\mu}, \{\sigma\}_{\Sigma\lambda}, \{e\}_{\Sigma\lambda}$$

(Step 5) Employ measures for making vectors independent so that each one becomes an independent vector. For example,

(1) let us assume that a certain nodal point j has the support of a rolling base in the direction of the ξ axis (a rigid external constraint); in such a case, $\psi_j^{\xi} = 0$; it follows from this that $\{\psi\}_{\Sigma\mu}$ is not an independent vector. It is possible to delete the zero-value displacement; moreover, we can also delete the value of $[\sigma']$, $[\sigma']$ and $[k]$ which correspond to ψ_j^{ξ} . For the time being, it is not necessary to solve for the value of the external constraining force, because of this, if we eliminate the

equation which relates to $\delta \{ \}$, we can then eliminate the corresponding horizontal row. This rigid external restraining force also does not do work and the fact that it is deleted does not have any effect on the value of W either.

(ii) if a body undergoes an elastic constraining force (such as that which would come from an external spring), that would do work and it would be possible to handle it as though it were an elastic member. On the basis of this idea, it is possible to obtain four independent vectors

$$\{\phi\}_\mu, \{\psi\}_\mu, \{\sigma\}_\lambda, \{\epsilon\}_\lambda$$

and they will satisfy the limitations set out below, that is

$$2U = \sum_{\lambda=1}^{\lambda} \{\sigma\} \{\epsilon\} = \sum_{\lambda=1}^{\lambda} \{\phi\} \{\psi\} = 2W. \quad (2.26)$$

Moreover, the fixed-form assumption and the fixed-force assumption can also be maintained. μ is called the effective limit of level and λ is called the limit or level of independence.

The matrix of structural elasticity moduli $[e]_{\lambda\lambda}$ which satisfies the structural physics relationships $\{\sigma\} = [e] \{\epsilon\}$ is always in existence; it is a symmetrical positive fixed reversible square matrix. The reverse of this matrix, that is, $[f]_{\lambda\lambda}$ is called a reverse elasticity modulus square matrix.

Whether or not the structural geometry matrix $[a]$ which satisfies the structural geometry relationship $\{\epsilon\} = [a] \{\psi\}$ exists or not is a question which is related to whether or not all the elements of an elastic body are of the fixed-force type or not. If $[a]$ exists, then the structure involved is called a fixed-force structure.

The question of whether or not the structural equilibrium matrix $[h]$, which satisfies the structural equilibrium relationship $\{\phi\} = [h] \{\sigma\}$, exists or not, is a question which is related to whether or not all the elements of the elastic bodies involved are of a fixed-force type.

Below we will enter the sixth stop; we will take for an example a plane truss and use this to make a complete explanation of the principles involved.

We will now explain the fact that free plane two force rod or bar members are of the fixed-form type as well as of the fixed-force type. If we take nodal point 1 to be the origin and bar or rod 12 to be the x axis, then all the coordinates and displacements of the nodal points as well as the external forces are as shown below:

$$\begin{matrix} \{x_1=0 \\ y_1=0 \end{matrix} \quad \begin{matrix} \{x_2=L \\ y_2=0 \end{matrix} \quad \begin{matrix} \{u_1 \\ v_1 \end{matrix} \quad \begin{matrix} \{u_2 \\ v_2 \end{matrix} \quad \begin{matrix} \{X_1 \\ Y_1 \end{matrix} \quad \begin{matrix} \{X_2 \\ Y_2 \end{matrix}$$

As far as $\lambda_1=1$ is concerned, one can use tensile displacement to represent it, and, by doing this one gets

$$\begin{matrix} \{e'\} = \{u_2 - u_1\} \\ \lambda_1 \cdot 1 \end{matrix} = \begin{matrix} [-1, 0, 1, 0] \\ \lambda_1 \cdot (\mu^1 + \mu^2) \end{matrix} \begin{matrix} \left\{ \begin{matrix} u_1 \\ v_1 \\ u_2 \\ v_2 \end{matrix} \right\} \\ \left\{ \begin{matrix} \psi^1 \\ \psi^2 \end{matrix} \right\} \end{matrix} = [a'] \begin{matrix} \left\{ \begin{matrix} \psi^1 \\ \psi^2 \end{matrix} \right\} \\ \left\{ \begin{matrix} \psi^1 \\ \psi^2 \end{matrix} \right\} \end{matrix}$$

Because of the fact that $[a']$ exists, two-force rods are of a fixed-form type.

If one determines precise values for the member modulus of elasticity square matrix $[e']$ and the generalized member stress $\{\sigma'\}$, and then, the internal member energy is $U_1 = \frac{1}{2} [e'] [c'] \{e'\}$, one gets the relationship $[e'] = \left[\frac{E_1 A_1}{L_1} \right]$.

In this case, the generalized member stress vector is

$$\{\sigma'\} = [c'] \{e\} = \frac{E_1 A_1}{L_1} (u_2 - u_1) = N^1$$

(Axial force, kg, Take an extension to be positive)

If we select the strain vector of the member $\{e'\}_L$ to be the amount of extension of the rod or bar (cm, take an extension of length to be positive) and when a two-force bar or rod member is at equilibrium, we have the relationships

$$-X_1 = X_2 = N, \quad Y_1 = Y_2 = 0$$

$$\therefore \{F\} = \begin{bmatrix} -1 \\ 0 \\ 1 \\ 0 \end{bmatrix} N = [h'] \{e'\},$$

It can be seen that $[h']$ exists; because of this fact, this member is of the fixed-force type. Moreover,

$$[e'] = [-1, 0, 1, 0] \text{ \& } [h'] = \begin{bmatrix} -1 \\ 0 \\ 1 \\ 0 \end{bmatrix} \text{ mutually transposed}$$

The rigidity of stiffness square matrix for a free bar or rod member, that is, $[k']$ is

$$[k']_{4 \times 4} = [h'] [e'] [e'] = \frac{EA}{L} \begin{bmatrix} 1 & 0 & -1 & 0 \\ 0 & 0 & 0 & 0 \\ -1 & 0 & 1 & 0 \\ 0 & 0 & 0 & 0 \end{bmatrix}.$$

Section 3. A detailed discussion on the structure of elastic bodies

Sec. 3.1 The three basic assumptions about structure

In order to narrow the scope of this discussion before we get into it, we will only consider questions of static linear strength and we will first of all bring out three common basic assumptions which appear below.

Assumption 1: For the parameters of cross-sections already selected, all the geometrical relationships, physical relationships and equilibrium relationships (if we are speaking of a case in which they exist) are all linear. For example, the cross-section parameters and so on are not changed by variations in the external load, do not exhibit the occurrence of elastic stability loss, do not exceed the limits of elasticity and so on and so on. These assumptions will guarantee that the limits stay within the scope of linear dynamics; given that we have this limitation to begin with, we can, whenever it is convenient, employ the principle of superposition or repeated addition.

Assumption 2: That structures have sufficient external constraints, that is, that not only do they (2a) have adequate strength to stop the production of rigid body displacement but that (2b) they also are adequate to balance out whatever external loading there is.

Assumption 3: Structures have adequate internal and external constraints. Moreover, (3a) if structures are of the fixed-form type, then it is required that they be geometrically invariable. (3b) If structures are of the fixed-force type, then it is required that they be able to undergo external loading on all of the members.

Assumptions 2 and 3 reflect the characteristics of structures with the exception of some minor problems relating to free structures and also with the exception of questions which fall into the category of institutional matters.

Sec. 3.2 Sufficient conditions for the rigid body displacement and balanced external loading of free plane structures

If we assume that all of the nodal points of a free plane structure have coordinates which are

$$\begin{Bmatrix} x_1 \\ y_1 \end{Bmatrix}, \begin{Bmatrix} x_2 \\ y_2 \end{Bmatrix}, \dots$$

then the amount of rigid body displacement (combined vector) which is produced by a planar displacement $u=1$, $v=1$ and a rotation of $\theta_0=1$ must consequently be

$$\begin{pmatrix} u=1 & v=1 & \theta_0=1 \end{pmatrix} \begin{pmatrix} 1 & 0 & -y_1 \\ 0 & 1 & x_1 \\ 1 & 0 & -y_2 \\ 0 & 1 & x_2 \\ \vdots & \vdots & \vdots \end{pmatrix}$$

Moreover, by combining, we can obtain the rigid body displacement matrix

$$[\Psi^0]_{\Sigma \mu \cdot 3} = \begin{pmatrix} 1 & 0 & -y_1 \\ 0 & 1 & x_1 \\ 1 & 0 & -y_2 \\ 0 & 1 & x_2 \\ \vdots & \vdots & \vdots \end{pmatrix}$$

The general run of rigid body displacements of free planar structures are, then, a combination of three linear ones; it is possible to represent this as

$$\{\phi^0\}_{\Sigma \mu \cdot 1} = [\Psi^0]_{\Sigma \mu \cdot 3} \{C\}_3 \quad (3.1)$$

In this case $\{C\}_3$ represents $\begin{Bmatrix} u \\ v \\ \theta_0 \end{Bmatrix}$. When $\{C\}_3 = \{0\}$ is the case, then it is possible to obtain $\{\phi\}_{\Sigma \mu} = \{0\}$; in certain sundry types of situations, habitually, we do not lay great stress on the fact that this is rigid body displacement.

The external loads which are taken on by free planar structures must satisfy the three equilibrium equations $\Sigma X = \Sigma Y = \Sigma M$, that is to say that $\{\phi\}$ satisfies

$$[\Psi^0]'_{3 \cdot \Sigma \mu} \cdot \{\phi\}_{\Sigma \mu \cdot 1} = \{0\}_{\Sigma \lambda \cdot 1} \quad (3.2)$$

If we are dealing with a case in which the structure under consideration is of the fixed-force type, then we have

$$\{\phi\}_{\Sigma \mu} = [h]_{\Sigma \mu \Sigma \lambda} \{\sigma\}_{\Sigma \lambda}$$

Moreover, if we assume that $\{\sigma\}_{\Sigma}$ is an independent vector, then it follows from this that $[h]$ itself also satisfies the relationship

$$\begin{aligned} [\Psi^0]' [h] &= [0] \\ 3 \cdot \Sigma \mu \quad \Sigma \mu \cdot \Sigma \lambda \quad 3 \cdot \Sigma \lambda \end{aligned} \quad (3.3)$$

The $[h^4]$ of a free member (raised to the level $\Sigma \mu \times \Sigma \lambda$) obviously also satisfies

$$\begin{aligned} [\Psi^0]' [h'] &= [0] \\ 3 \cdot \Sigma \mu \quad \Sigma \mu \cdot \lambda_i \quad 3 \cdot \lambda_i \end{aligned} \quad (3.3')$$

For example, the two-force bar or rod member 12 which we talked about before satisfies

$$\begin{bmatrix} 1 & 0 & 1 & 0 \\ 0 & 1 & 0 & 1 \\ 0 & 0 & 0 & L \end{bmatrix} \begin{bmatrix} -1 \\ 0 \\ 1 \\ 0 \end{bmatrix} = [0]_{3 \times 1},$$

Sec. 3.3 The functions which are given rise to by assumptions 2a, 3b, 2a, 3b and so on (sic)

1° Assumption 2a: When the external constraining force is not sufficient, it is possible to obtain the set or group number of the linear independent rigid body displacement.

If we assume that the planar structure has N roller bases or seats, then the number of the effective number of displacement is $\mu = \Sigma \mu - N$. It follows from this the combined displacement vector can be written as

$$\{\phi\}_{\Sigma \mu} = \begin{Bmatrix} \{\psi\}_{\mu} \\ \{0\}_N \end{Bmatrix},$$

Let us assume that if we are dealing with a rigid body displacement, then we will have the relationship

$$\begin{Bmatrix} \{\psi\}_{\mu} \\ \{0\}_N \end{Bmatrix} = \underset{\Sigma \mu \times 3}{[\Psi'']} \{C\}_3 = \begin{bmatrix} [\Psi'']_{\mu \times 3} \\ [\Psi'']_{N \times 3} \end{bmatrix} \{C\}_3$$

When $\{\phi\}_{\Sigma \mu}$ is a rigid body displacement, then it is possible to achieve a non-trivial solution $\{C\}_3 \neq \{0\}$; if we do a test solution

in the equation below (homogeneous equation), then we get

$$\{0\}_N = [\Psi'']_{N \times 3} \{C\}_3, \quad (3.4)$$

If the order of $[\Psi'']_{N \times 3}$ is $r < 3$, then it is possible to achieve a solution for the $(3-r)$ set of linear independent rigid body displacements.

(Example) Let us assume that we have a planar four-connected rod or bar structure ABCD, and that the coordinates and displacements for the four nodal points are

| | | | | | |
|--------------|----------|----------------------|----------------------|----------------------|----------------------|
| Nodal points | <i>J</i> | <i>x_J</i> | <i>y_J</i> | <i>u_J</i> | <i>v_J</i> |
| | A | 0 | 0 | <i>u_A</i> | <i>v_A</i> |
| | B | <i>L₁</i> | 0 | <i>u_B</i> | <i>v_B</i> |
| | C | 0 | <i>L₂</i> | <i>u_C</i> | <i>v_C</i> |
| | D | <i>L₁</i> | <i>L₂</i> | <i>u_D</i> | <i>v_D</i> |

If we consider the case in which there are at the points A and D a standard level roller point or seat ($N=2$) then let us ask the question, "which or how many sets or linear independent rigid body displacements are there in this structure?"

Let us first write out the rigid body displacement vectors which are

$$\{\psi''\} = \begin{Bmatrix} u_A \\ v_A \\ u_B \\ v_B \\ u_C \\ v_C \\ u_D \\ v_D \end{Bmatrix} = \begin{bmatrix} 1 & 0 & 0 \\ 0 & 1 & 0 \\ 1 & 0 & 0 \\ 0 & 1 & L_1 \\ 1 & 0 & -L_1 \\ 0 & 1 & 0 \\ 1 & 0 & -L_1 \\ 0 & 1 & L_1 \end{bmatrix} \{c\}_3,$$

The matrix which springs from and corresponds to u_A and u_D is

$$[\Psi'']_{N \times 3} = \begin{bmatrix} 1 & 0 & 0 \\ 1 & 0 & -L_1 \end{bmatrix}, \text{ its order } r=2.$$

It follows from this that there is only a $(3-r)$ 1 set of rigid body displacements (which correspond to $v=1$ planar movements), that is

$$\{\psi^0\}_{\Sigma_n} = [0, 1, 0, 1, 0, 1, 0, 1],$$

The lowered level is

$$\{\psi^0\}_n = [1, 0, 1, 0, 1, 1]. \quad (3.4')$$

If the $N(=2)$ standard level roller seats or bases which were discussed above are moved in their locations to the points A and B, then this will cause the condition $u_A = u_B = 0$.

$$[\psi^0]_{N \times 3} = \begin{bmatrix} 1 & 0 & 0 \\ 1 & 0 & 0 \end{bmatrix}, \quad \text{its order } r=1$$

That is to say, that there is a $(3-r)=2$ set of linear independent rigid body displacements such as the plane displacement $v=1$ and the rotational movement around the origin point of $\theta_0=1$.

It follows from this that the external constraining force is adequate to prevent rigid body displacement in the sufficient condition that $[\psi^0]_{N \times 3}$ its order $r=3$

(Note) If a structure does exhibit a rigidity displacement, then its strain $\{\epsilon\}_n$ is zero.

2° Assumption 3a: The geometry of fixed-form structures is invariable.

Definition: If all of the non-rigid body displacements cause the strain $\{\epsilon\}_n$ of a fixed-form structure to be something other than zero, then the fixed-form structure under consideration is geometrically invariable. If these are q linear independent non-rigid displacements in existence, and they all cause $\{\epsilon\}_n$ to be equal to zero, then the fixed-form structure under consideration is geometrically variable to the q th degree.

If we let the strain on a fixed-form structure be equal to zero, then

$$\{\epsilon\}_\lambda = [a]_{\lambda\mu} \{\psi\}_\mu = \{0\}, \quad (3.6)$$

Let us try to solve this homogeneous equation. Let us suppose that the order of $[a]_{\lambda\mu}$ is t ; if this is the case, then equation (3.6) has $(\mu - t)$ sets of linear independent non-zero solutions. However, there are $(3-r)$ sets of linear independent rigid body displacements $\{\psi''\}$ which can occur when they are allowed by the external constraining forces (roller seats or bases) on the body of the structure itself; the strains which are produced by these sets of rigid body displacements are also equal to zero, that is,

$[a]_{\lambda\mu} \{\psi''\} = \{0\}_\lambda$; they are all completely included in the solutions to equation (3.6). Besides these, the ones which are left over are

$$q = \mu - t - (3-r) \left(\begin{matrix} \text{r.s. } [\psi'']_{\lambda\mu} \text{ order} \\ \text{t.s. } [a]_{\lambda\mu} \text{ order} \end{matrix} \right) \quad (3.7)$$

If each set of linear independent non-rigid body displacement causes the strain on a structure to be zero, then it follows that we know that the fixed-form structure under consideration has a geometric variability number of q .

If the example which we previously gave of a planar four connected rod or bar figure ABCD receives support from $N=2$ standard level roller bases or seats, then this will cause the condition $u_1 = u_4 = 0$.

$$\{\epsilon\}_\lambda = \begin{Bmatrix} \epsilon_{AB} \\ \epsilon_{AC} \\ \epsilon_{CD} \\ \epsilon_{DB} \end{Bmatrix} = \begin{bmatrix} -1 & 0 & 1 & 0 \\ 0 & -1 & & 0 & 1 \\ & & -1 & 0 & 1 & 0 \\ & 0 & -1 & & 0 & 1 \end{bmatrix} \begin{Bmatrix} u_A \\ v_A \\ u_B \\ v_B \\ u_C \\ v_C \\ u_D \\ v_D \end{Bmatrix} \quad \begin{matrix} \Sigma \mu \\ \lambda \cdot \Sigma \mu \end{matrix}$$

If we get rid of the first and seventh values of $[a]_{\lambda\mu}$, then we can obtain

$$\{e\}_\lambda = [a]_{\lambda\mu} \{\psi\}_\mu = \begin{pmatrix} 0 & 1 & 0 \\ -1 & & 0 & 1 \\ & -1 & 0 & 0 \\ 0 & -1 & & 1 \end{pmatrix} \begin{pmatrix} v_A \\ u_B \\ v_B \\ u_C \\ v_C \\ v_D \end{pmatrix}.$$

If we let it be equal to zero, then the order of $[a]_{\lambda\mu}$ is $t=4$, and it follows from this that there are $2(=\mu - t)$ sets of linear independent non-zero solutions; due to the fact that the order of $[\psi]_{N \times 3}$ is $r=2$, the $(3-r =)$ 1 set of rigid body displacements which we obtain is as shown in (3.4'). The other left over ($q=$) 1 set of non-rigid body displacements are

$$[\psi] = [0, 0, 1, 0, 0, 1],$$

It follows from this that the geometrical invariability number of this fixed-form structure is $q = 1$.

3° The combined use of assumptions 2a and 3a

The function of assumption 2a is $r=3$; the function of assumption 3a is $q=0$. The combined action or functioning of assumption 2a and 3a is $t=\mu$, that is to say, the fixed-form structure under consideration has an order of $[a]_{\lambda\mu}$ which is μ . (3.8)

Besides this, yet another action or functioning of the combination of assumption 2a and assumption 3a is as follows. If a certain displacement which is exhibited in a fixed-form structure after it is acted upon by an external load is $\{\psi\}_\mu \neq \{0\}$, then these displacement is not a rigid body displacement (on the basis of 2a, rigid body displacements would have been prevented). Because of the invariable characteristics of the geometry, it follows that we can obtain $\{e\}_\lambda \neq \{0\}$; it would be best to assume that $[e]_{\lambda\mu}$ is a symmetrical positive fixed reversible diagonal square matrix, that is

$$[e]_{\lambda\lambda} = \begin{matrix} & e_1 & & \\ & & e_2 & \\ & & & \dots \\ & & & & e_n \end{matrix}, \quad \text{all } e_i > 0,$$

The conclusion in this case is that the strain on a structure is always kept at an energy level greater than zero, that is

$$U = \frac{1}{2} (e_1^2 e_1 + e_2^2 e_2 + \dots + e_n^2 e_n) > 0. \quad (3.8)'$$

The conclusion which was stated above is that when the displacement of a fixed-form structure is not equal to zero, then the strain energy in the structure is always positive. This conclusion will be useful in proving that the square rigidity matrix for a structure is a reversible square matrix (see Section 4.1).

4° Assumption 2b: The external constraints on a structure are adequate to balance the conditions of the external loading.

Let us assume that the external load is $\{\varphi\}_{\Sigma\mu}$; then let the external constraining force be $\{\bar{\varphi}\}_N$; let us then add a zero and raise it to the level Σ^μ so that it becomes $\{\bar{\varphi}\}_{\Sigma\mu}$; the equilibrium condition for these two is

$$\frac{[\Psi^0]'}{3 \cdot \Sigma\mu} (\{\varphi\}_{\Sigma\mu} + \{\bar{\varphi}\}_{\Sigma\mu}) = 0. \quad (3.9)$$

That is to say,

$$[\Psi^0]'\{\bar{\varphi}\}_{\Sigma\mu} = -[\Psi^0]'\{\varphi\}_{\Sigma\mu},$$

The right side is a combined force system or coefficient which we already knew and can be simplified to be written $\{R\}_\mu$.

If we take and separate out the left side, then we get

$$\frac{[\Psi^0]'}{3 \cdot \Sigma\mu} = \left[\frac{[\Psi^0]'}{3 \cdot \mu}, \frac{[\Psi^0]'}{3 \cdot N} \right], \quad \{\bar{\varphi}\}_{\Sigma\mu} = \begin{Bmatrix} \{0\}_\mu \\ \{\bar{\varphi}\}_N \end{Bmatrix},$$

It follows from this that in order to obtain the external restraining force it is necessary to satisfy the equilibrium equation

$$\frac{[\Psi^0]'}{3 \cdot N} \{ \bar{\varphi} \} = \{ R \}. \quad (3.9')$$

As far as the order r of $\begin{matrix} [\psi^a] \\ 3 \cdot N \end{matrix}$ is concerned, there are two types of situations:

(i) $r=3$: It makes no difference what value $\{R\}$ may have, it will still exist and $\{\bar{\varphi}\}_N$ will satisfy the equation above.

(ii) $r<3$: It is possible to take equation (3.9') and write it in the form of a successive product, that is

$$\begin{bmatrix} [I]_{rr} \\ [S]_{(3-r)r} \end{bmatrix} \cdot [\psi^a]_{rr}' \cdot \begin{bmatrix} [I]_{rr} & [T]_{r(N-r)} \end{bmatrix} \cdot \{\bar{\varphi}\}_N = \begin{Bmatrix} \{R\}_r \\ \{R\}_{(3-r)r} \end{Bmatrix},$$

If we look at the case in which the two vectors which come from the combined force system or coefficient $\{R\}_r$ do not satisfy the relationship

$$[S]_{(3-r)r} \{R\}_r = \{R\}_{(3-r)r},$$

then, equation (3.9') does not have a solution, that is to say, the external constraining force $\{\bar{\varphi}\}_N$ cannot balance out a given external loading. It follows from this that we know that the sufficient condition for an external constraining force which can balance out a given external loading is

$$\begin{matrix} [\psi^a]' \text{ order is } r=3 \\ 3 \cdot N \end{matrix} \quad (3.9'')$$

This condition is entirely identical to the conditions for Assumption 2a.

5° Assumption 3b: The internal and external constraining forces on a fixed force-type structure are capable of supporting or handling the given conditions of external loading.

Let us consider the case in which a fixed-force-type structure exhibits the equilibrium relationship $\{\varphi\}_n = [h]_{n\lambda} \{\sigma\}_\lambda$; now let us prove the fact that the sufficient condition for the internal and external constraining forces in the structure in question to be able to support or cope with a given external loading is

$[h]_{\mu\lambda}$ order is $S=\mu$

Let us use the method of proving the opposite of a proposition. Let us assume the case in which the order of $[h]_{\mu\lambda}$ is $S < \mu$. It is possible to take $[h]_{\mu\lambda}$ and write it in the form of a three element chain product

$$\begin{bmatrix} [I]_{ss} \\ [S]_{\bar{\mu}s} \end{bmatrix} \cdot [h]_{\mu\bar{s}} \cdot \begin{bmatrix} [I]_{ss}, [T]_{s\bar{\lambda}} \end{bmatrix} \quad \begin{aligned} \bar{\mu} &= \mu - S \geq 0, \\ \bar{\lambda} &= \lambda - S \geq 0. \end{aligned}$$

In this case, $[S]_{\bar{\mu}s} = [h]_{\bar{\mu}s} [h]_{s\bar{s}}^{-1}$, $[T]_{s\bar{\lambda}} = [h]_{s\bar{\lambda}}^{-1} [h]_{s\bar{s}}$.

Obviously, $[h]_{\mu\lambda}$ has with it an orthogonal matrix $[Z]_{\bar{\mu}\mu}$ that is,

$$[Z]_{\bar{\mu}\mu} = [-[S]_{\bar{\mu}s}, [I]_{\bar{\mu}\bar{\mu}}] (\neq [0]),$$

This relationship satisfies the condition $[Z]_{\bar{\mu}\mu} [h]_{\mu\lambda} = 0$.

On the basis of the equilibrium relationship for fixed-force-type structures, that is, $\{\varphi\}_{\mu} = [h]_{\mu\lambda} \{\sigma\}_{\lambda}$, use $[Z]_{\bar{\mu}\mu}$ to multiply and one can obtain $[Z]_{\bar{\mu}\mu} \{\varphi\}_{\mu} = [Z]_{\bar{\mu}\mu} [h]_{\mu\lambda} \{\sigma\}_{\lambda} = \{0\}$, that is $\{\varphi\}_{\bar{\mu}} = [S]_{\bar{\mu}s} \{\varphi\}_s$. This is the case when the order of $[h]_{\mu\lambda}$ is $S < \mu$, the two vectors which come from the external load $\{\varphi\}_{\mu}$, that is $\{\varphi\}_{\bar{\mu}}$ and $\{\varphi\}_s$ must first satisfy the equilibrium condition. This is in conflict with Assumption 3b as well as with the ability of the internal and external constraining forces on a fixed-force-type structure to support or handle a given external load; this conflict confirms the fact that the order of $[h]_{\mu\lambda}$ must be μ .

Yet another action or functioning of Assumption 3b is this. If the external loading of a fixed-force-type of structure is $\{\varphi\}_{\mu} \neq \{0\}$ then $\{\sigma\}_{\lambda} \neq \{0\}$; it is best to assume that $[f]_{\lambda\lambda} = [e]_{\lambda\lambda}^{-1}$ is a positive value diagonal square matrix from which it follows that the energy of stress is

$$U = \frac{1}{2} \{\sigma\}_{\lambda} [f]_{\lambda\lambda} \{\sigma\}_{\lambda} \text{ always } > 0.$$

Section 4. Direct rigidity or stiffness methods appropriate for use with fixed-form and fixed-force structures

Sec. 4.1 Formulas for direct rigidity or stiffness methods

The important points concerning the direct rigidity method are as follows. If one takes the vector $\{\psi\}_\mu$ for the effective level nodal point displacement in a structure to be the main physical quantity of concern, then there is described a black enclosure such as the one in Figure 1. If we use this to represent strain and stress vectors, then this method can directly be used on fixed-form-fixed-force structures. The supplementary or additional assumption involved here is as follows: The structures being dealt with are both fixed-form and fixed-force structures; moreover, $[h]=[a]'$. For the proof of this see the proof of equation (2.20). On the basis of this, we then have the geometrical relationship, the physical relationship and the equilibrium relationship which follow:

$$\{\varphi\}_\mu = [k]_{\mu\lambda} \{\sigma\}_\lambda, \quad \{\sigma\}_\lambda = [e]_{\lambda\lambda} \{\epsilon\}_\lambda, \quad \{\epsilon\}_\lambda = [a]_{\lambda\mu} \{\psi\}_\mu$$

It follows from this that we can obtain the rigidity or stiffness equation

$$\{\varphi\}_\mu = [k]_{\mu\mu} \{\psi\}_\mu$$

Moreover, the rigidity or stiffness square matrix $[k]_{\mu\mu}$ is

$$[k]_{\mu\mu} = [h]_{\mu\lambda} [e]_{\lambda\lambda} [a]_{\lambda\mu} = [a]_{\lambda\mu}' [e]_{\lambda\lambda} [a]_{\lambda\mu}$$

$\mu = \lambda \quad \lambda = \lambda \quad \lambda = \mu$

Due to the fact that the order of $[a]_{\lambda\mu}$ is μ , it follows that we know that $\lambda \geq \mu$, because of the fact that $[e]_{\lambda\lambda}$ is a symmetrical positive fixed square matrix, it follows that we know that $[k]_{\mu\mu}$ is a symmetrical non-negative fixed square matrix.

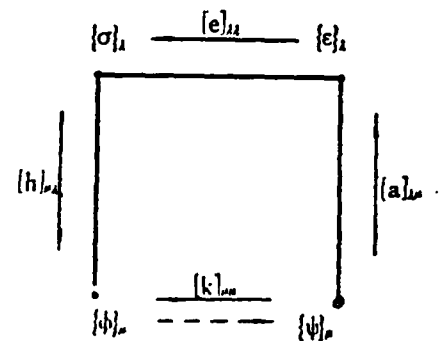


Figure 1

If we wish to carry the proof of $[k]_{\mu\mu}$ a step further, then we will find that it can be reversed; if we make use of the relationship $2W=2U$, then we obtain

$$[\psi][k]\{\psi\} = [\epsilon][e]\{\epsilon\},$$

If we assume that $\{\psi\}_n \neq \{0\}$, then from 1° in Section 3.3, we can obtain the relationship $\{e\}_n \neq \{0\}$; it follows from this that $U > 0$, that is to say, that from this we can obtain the knowledge that $[k]_{nn}$ can be reversed. End of proof. $\{\psi\}[k]\{\psi\} > 0$,

Sec. 4.2 Typical example (Figure 2)

$$\{e\}_n = \begin{Bmatrix} e_1 \\ e_2 \\ e_3 \\ e_4 \\ e_5 \end{Bmatrix}, \quad \{\sigma\}_n = \begin{Bmatrix} \sigma_1 \\ \sigma_2 \\ \sigma_3 \\ \sigma_4 \\ \sigma_5 \end{Bmatrix}, \quad [e]_{nn} = \begin{Bmatrix} e_1 & & & & \\ & e_2 & & & \\ & & e_3 & & \\ & & & e_4 & \\ & & & & e_5 \end{Bmatrix}$$

e_1 is the rod or bar extension;
 σ_1 is the rod or bar axial force,
 that is, $e_1 = \frac{1}{L_1} \frac{\sigma_1 A_1}{E_1}$, then $[e]_{nn} = e_i [f]_{ii}$.

The combined displacement level number is $\Sigma^\mu = 8$; the roller seat or base number is $N = 5$, and the effective level is $\mu = \Sigma^\mu - N = 3$.

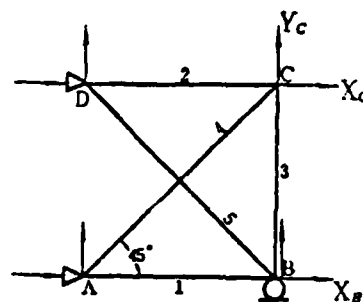


Figure 2

$$\{\psi\}_n = \begin{Bmatrix} u_B \\ u_C \\ v_C \end{Bmatrix}, \quad \{\varphi\}_n = \begin{Bmatrix} X_B \\ X_C \\ Y_C \end{Bmatrix} = \begin{Bmatrix} 6 \\ 6 \\ 6 \end{Bmatrix} \quad (\text{data already given})$$

$$[a]_{nn} = \begin{Bmatrix} 1 & 0 & 0 \\ 0 & 1 & 0 \\ 0 & 0 & 1 \\ 0 & \frac{1}{\sqrt{2}} & \frac{1}{\sqrt{2}} \\ \frac{1}{\sqrt{2}} & 0 & 0 \end{Bmatrix} = [k]'$$

$$[k]_{nn} = [a]'[e][a] = \frac{e_0}{2} \begin{Bmatrix} 3 & 1 \\ 1 & 3 \end{Bmatrix}$$

From this we can then figure out that

$$\{\psi\}_\mu = \frac{1}{e_0} \begin{Bmatrix} 4 \\ 3 \\ 3 \end{Bmatrix}, \quad \{\epsilon\}_\lambda = \frac{1}{e_0} \begin{Bmatrix} 4 \\ 3 \\ 3 \\ 3\sqrt{2} \\ 3\sqrt{2} \end{Bmatrix}, \quad \{\sigma\}_\lambda = \begin{Bmatrix} 4 \\ 3 \\ 3 \\ 3\sqrt{2} \\ 3\sqrt{2} \end{Bmatrix}$$

If we look at these results, then we can make the extension $2W=2U=\frac{60}{e_0}$ without doing any violence to anything.

The strong points of the direct rigidity or stiffness method are: 1° It is possible, member by member, to solve for $[k']$; after this is done, then one can raise the expression under consideration to the Σ^μ level or the μ level and do an addition; by this means it is possible to obtain $[k]_{\Sigma^\mu \Sigma^\mu}$ or $[k]_{\mu\mu}$. 2° The advantages of this type of method also extend even to the point where one can, in the modeling analysis stage, solve for $[k']$. 3° $[k]_{\mu\mu}$ is a form well suited to the task of solving for the inverse. 4° The generalized strain method and the generalized stress method can both be converted to the direct rigidity or stiffness method (see what follows).

Section 5. A generalized strain method suitable for use with fixed-form structures

Sec. 5.1 The process of deducing the formulas for the generalized strain method

Besides the three common assumptions we have already worked with, if we are to use this new method we must add an additional assumption, that is, that the structure we are dealing with is of the fixed-form type. The physical relationship for such a structure is

$$\{\sigma\}_\lambda = [e]_{\lambda\lambda} \{\epsilon\}_\lambda. \quad (5.1)$$

The geometrical relationship for a fixed-form structure is

$$\{\epsilon\}_\lambda = [u]_{\lambda\mu} \{\psi\}_\mu. \quad (5.2)$$

On the basis of assumption 2a and assumption 3a, we can obtain the information that the following is correct, that is, the order of $[a]_{\lambda\mu}$ is μ . (5.3) It is best to assume that $\lambda > \mu$; moreover, the reversible or invertible matrix $[a]_{\mu\mu}$ is found as the top section of $[a]_{\lambda\mu}$, that is

$$[a]_{\lambda\mu} = \begin{bmatrix} [a]_{\mu\mu} \\ [a]_{\nu\mu} \end{bmatrix}, \quad \nu = \lambda - \mu. \quad (5.4)$$

If we take $\{\varepsilon\}_\lambda$ and divide it up into two corresponding component vectors, then we get

$$\{\varepsilon\}_\lambda = \begin{Bmatrix} \{\varepsilon^q\}_\mu \\ \{\varepsilon\}_\nu \end{Bmatrix} \quad (5.5)$$

The significance of q in this expression will emerge later. On the basis of equation (5.2), we can divide this into two equations, that is

$$\{\varepsilon^q\}_\mu = [a]_{\mu\mu} \{\psi\}_\mu, \quad (5.6)$$

$$\{\varepsilon\}_\nu = [a]_{\nu\mu} \{\psi\}_\mu. \quad (5.7)$$

By solving equation (5.6), we can obtain

$$\{\psi\}_\mu = [a]_{\mu\mu}^{-1} \{\varepsilon^q\}_\mu, \quad (5.8)$$

If we substitute into equation (5.7), then we can obtain

$$\{\varepsilon\}_\nu = [G]_{\nu\mu} \{\varepsilon^q\}_\mu, \quad (5.9)$$

In this case,

$$[G]_{\nu\mu} = [a]_{\nu\mu} [a]_{\mu\mu}^{-1}, \quad (5.10)$$

According to equation (5.5), these results may be put together to obtain

$$\{\varepsilon\}_\lambda = \begin{bmatrix} [I]_{\mu\mu} \\ [G]_{\nu\mu} \end{bmatrix} \{\varepsilon^q\}_\mu, \quad (5.11)$$

Obviously, there is

$$[-[G]_{\nu\mu}, [I]_{\mu\mu}] \{\varepsilon\}_\lambda = \{0\}. \quad (5.12)$$

It follows from this that we can know that $\{\varepsilon\}_\lambda$ is not an independent vector. The relationship equation (5.9) explains the fact that the value of $\{\varepsilon^q\}_\nu$ changes with changes in the value of $\{\varepsilon^q\}_\mu$. It follows from this that we can call $\{\varepsilon^q\}_\mu$ an independent variable component vector and we can add the q as it functioned in the case

above to represent this fact; it also follows from the previous discussion that we can call $\{e\}_\mu$ a dependent variable component vector. $[G]_{\mu\nu}$ is called a lower level independent variable-dependent variable transformation matrix; moreover, $\begin{bmatrix} [I] \\ [G] \end{bmatrix}$ is called a full level transformation matrix. μ is called an independent variable level number and ν is called a dependent variable level number. From now on, then, we will change to the use of $\{\epsilon^q\}_\mu$ to individually represent strain situations.

In situations in which we are using the generalized strain method, we employ the independent variable component vector $\{\epsilon^q\}_\mu$ as the principal physical vector, and we use $\{\epsilon^q\}_\mu$ (sic) to represent other physical quantities or vectors.

The diagram for the principal relationships in the generalized strain method is as shown in Figure 3. The places in which it differs with what is shown in Figure 1 are as follows: $[h]_{\mu\lambda}$ does not exist and the way in which $\{\sigma\}_\lambda$ stands for $\{\phi\}_\mu$ is not the same. It should be noted that, under normal circumstances, $\{\phi\}_\mu$ is the only quantity which will already be known. In Figure 3 the double arrows which are drawn represent a method of separation, that is, according to equation (5.5), we can take $\{\epsilon\}_\lambda$ and separate it so that we obtain $\{\epsilon^q\}_\mu$ (the principal physical quantity or vector, represented as the drawing of the round enclosure) and $\{\epsilon\}_\nu$ (which is not shown in the figure). Up to now, the value of $\{\epsilon^q\}_\mu$ has still not been figured out; however, once it has been figured, then it is possible to use equation (5.8) to figure out $\{\psi\}_\mu$, it is possible to use equation (5.9) to figure out $\{e\}_\nu$, and it is possible to use equation (5.11) to figure out $\{e\}_\lambda$.

As far as twice the internal energy of the structure goes, it can be represented basically by using $\{\epsilon\}_\lambda$, that is

$$\begin{aligned} 2U &= \{e\}_\lambda [e]_{\lambda\mu} \{\epsilon\}_\mu \\ &= \{e\}_\lambda \cdot \begin{bmatrix} [I] \\ [G]' \end{bmatrix} \cdot [e]_{\lambda\mu} \cdot \begin{bmatrix} [I] \\ [G] \end{bmatrix} \cdot \{\epsilon^q\}_\mu, \end{aligned}$$

In this situation, it is already possible to use $\{\epsilon^q\}_\mu$ to represent $2U$, that is

$$2U = \{\epsilon^q\}_\mu \cdot [e^q]_{\mu\mu} \cdot \{\epsilon^q\}_\mu \quad (5.13)$$

Because of the fact that $\{\epsilon^q\}_\mu$ is an independent vector, it follows that we can obtain the square matrix for the corresponding independent variable levels and moduli of elasticity $[e^q]_{\mu\mu}$, that is

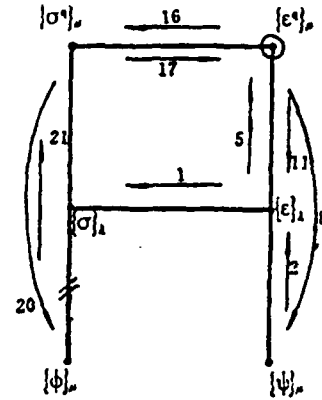


Figure 3

$$[e^q]_{\mu\mu} = [[I]_{\mu\mu}, [G]'] \cdot [e]_{\lambda\lambda} \cdot \begin{bmatrix} [I]_{\mu\mu} \\ [G]_{\mu\mu} \end{bmatrix} \quad (5.14)$$

If $[e]_{\lambda\lambda}$ can be divided up into two component matrices which form a diagonal structure as follows, that is

$$[e]_{\lambda\lambda} = \begin{bmatrix} [e]_{\mu\mu} \\ [e]_{\eta\eta} \end{bmatrix} \quad (5.15)$$

then it is possible to obtain the relatively simple formula

$$[e^q]_{\mu\mu} = [e]_{\mu\mu} + [G]'[e]_{\eta\eta}[G]_{\mu\mu}. \quad (5.15')$$

The independent variable level elasticity moduli square matrix $[e^q]_{\mu\mu}$ which we discussed above is symmetrical positive fixed and reversible or inversible; it can be called the main square matrix of the generalized strain method.

The corresponding independent variable level stress vector $\{\sigma^q\}_\mu$ satisfies the independent variable level physical relationship

$$\{\sigma^q\}_\mu = [e^q]_{\mu\mu} \{\epsilon^q\}_\mu, \quad (5.16)$$

By solving for the inverse, it is possible to obtain from $\{\sigma^q\}_\mu$ a formula for solving $\{\epsilon^q\}_\mu$, that is

$$\{\epsilon^q\}_\mu = [e^q]_{\mu\mu}^{-1} \{\sigma^q\}_\mu, \quad (5.17)$$

With great ease, it is possible to obtain equations (5.18) and (5.19) for the relationships which exist mutually between $\{\sigma^q\}_\mu$ and $\{\sigma\}_\lambda$, $\{\sigma\}_\mu$ and $\{\sigma\}_\nu$; this is done in order to prepare for their use in a comparison with the generalized stress method in Section 6. If we take the quantity $[e^q]_{\mu\mu}$ from equation (5.14) and substitute it into equation (5.16), then it is possible to obtain

$$\{\sigma^q\}_\mu = [[I]_{\mu\mu}, [G]']\{\sigma\}_\lambda. \quad (5.18)$$

$$\therefore \{\sigma\}_\lambda = \begin{Bmatrix} \{\sigma\}_\mu \\ \{\sigma\}_\nu \end{Bmatrix},$$

It follows from this that we can obtain

$$\begin{aligned} \{\sigma^q\}_\mu &= \{\sigma\}_\mu + [G]'\{\sigma\}_\nu, \\ \therefore \{\sigma\}_\lambda &= \begin{Bmatrix} \{\sigma^q\}_\mu - [G]'\{\sigma\}_\nu \\ \{\sigma\}_\nu \end{Bmatrix} = \begin{Bmatrix} \{\sigma^q\}_\mu \\ \{\sigma\}_\nu \end{Bmatrix} + \begin{bmatrix} -[G]' \\ [I]_{\nu\nu} \end{bmatrix} \{\sigma\}_\nu. \end{aligned} \quad (5.19)$$

It should be noted that $\{\sigma^q\}_\mu$ and $\{\sigma\}_\mu$ are different vectors; the former satisfies the independent variable level physical relationship (5.16) while the latter is simply obtained from a subdivision of $\{\sigma\}_\lambda$.

In order to take the only vector quantity which we already know $\{\phi\}_\mu$ and bring it into the calculation, we must make use of the principle of virtual work $W_* = U_*$; if we assume that we are given a certain virtual displacement $\{\psi^*\}_\mu$, then we can obtain the following:

$$\begin{aligned} \text{virtual strain} \quad \{e^q\}_\mu &= [a]_{\mu\mu} \{\psi^*\}_\mu, \\ \text{virtual potential energy} \quad U_* &= [\sigma^q]_\mu [a]_{\mu\mu} \{\psi^*\}_\mu, \\ \text{virtual work} \quad W_* &= \{\phi\}_\mu \{\psi^*\}_\mu \end{aligned}$$

It follows from this that we can obtain

$$\{\phi\}_\mu = [a]_{\mu\mu}' \{\sigma^q\}_\mu, \quad (5.20)$$

Solving this, we can obtain

$$\{\sigma^q\}_\mu = ([a]_{\mu\mu}')^{-1} \{\phi\}_\mu. \quad (5.21)$$

By using the diagram of the principal relationships involved, we can figure out $\{\sigma^q\}_\mu$ from the vector which we already know, that is, $\{\phi\}_\mu$ by the use of equation (5.21); after this, we can again

figure out the principal physical quantity $\{\epsilon^q\}_\mu$ by the use of equation (5.17). The two steps above can be included in one formula

$$\{\epsilon^q\}_\mu = [e^q]_{\mu\mu}^{-1} ([a]_{\mu\mu}')^{-1} \{\phi\}_\mu. \quad (5.22)$$

Once we have arrived at this point, the measures necessary for calculations used in the generalized strain method are relatively clear.

(i) After we get a clear understanding of the generalized strain vector $\{\epsilon\}_\lambda$ of the structure being considered, we can make use of the reversible or inversible component square matrix $[a]_{\mu\mu}$ of the geometric matrix $[a]_{\lambda\mu}$, and use it to get a clear understanding of the fact that $\{\epsilon^q\}_\mu$ is composed of those strains;

(ii) use equation (5.10) to figure out $[G]_{\nu\mu}$, and use equation (5.14) to figure out $[e^q]_{\mu\mu}$;

(iii) use equation (5.21) to figure out $\{\sigma^q\}_\mu$, and use equation (5.17) to figure out $\{\epsilon^q\}_\mu$;

(iv) then, carry on by solving for the other physical quantities.

(Typical example) The same as has been shown above; see Figure 2. We will not make use of the property of fixed forces; however, we will make use of the principal of virtual work which allows us to obtain equation (5.21).

(i) take $[a]_{\lambda\mu}$ and analyze it into components as follows:

$$[a]_{\lambda\mu} = \begin{bmatrix} 1 & & \\ & 1 & \\ & & 1 \\ 0 & \frac{1}{\sqrt{2}} & \frac{1}{\sqrt{2}} \\ \frac{1}{\sqrt{2}} & 0 & 0 \end{bmatrix} = \begin{bmatrix} [a]_{\mu\mu} \\ [a]_{\nu\mu} \end{bmatrix}, \quad \text{then we take } \{\epsilon^q\}_\mu = \begin{Bmatrix} \epsilon_1 \\ \epsilon_2 \\ \epsilon_3 \end{Bmatrix}.$$

(ii) if we use equation (5.10), then we obtain

$$[G]_{\nu\mu} = \begin{bmatrix} 0 & \frac{1}{\sqrt{2}} & \frac{1}{\sqrt{2}} \\ \frac{1}{\sqrt{2}} & 0 & 0 \end{bmatrix},$$

If we use equation (5.15'), we can then obtain

$$[e']_{\mu\mu} = \begin{bmatrix} e_0 & & \\ & e_0 & \\ & & e_0 \end{bmatrix} + [G]' \begin{bmatrix} e_0 & & \\ & e_0 & \\ & & e_0 \end{bmatrix} [G]_{\mu\mu} = \frac{e_0}{2} \begin{bmatrix} 3 & & \\ & 3 & 1 \\ & 1 & 3 \end{bmatrix}$$

(iii) if we use equation (5.21), then we obtain

$$\{\sigma''\}_\mu = ([a]_{\mu\mu}')^{-1} \{\phi\}_\mu = \begin{Bmatrix} 6 \\ 6 \\ 6 \end{Bmatrix}$$

And if we make use of equation (5.17), again, then we can get

$$\{e''\}_\mu = \frac{1}{e_0} \begin{Bmatrix} 4 \\ 3 \\ 3 \end{Bmatrix}$$

(iv) by using equation (5.8), we can obtain

$$\{\psi\}_\mu = [a]_{\mu\mu}^{-1} \{e''\}_\mu = \frac{1}{e_0} \begin{Bmatrix} 4 \\ 3 \\ 3 \end{Bmatrix}, \quad \dots \text{all other structures can be treated as we have just done}$$

Section 5.2 Continuing on from the generalized strain method over to the direct rigidity or stiffness method

The four μ level connected vectors $\{\psi\}_\mu$, $\{e''\}_\mu$, $\{\sigma''\}_\mu$, $\{\phi\}_\mu$ have relationships between them as set out in equations (5.20), (5.16) and (5.6), that is

$$\begin{aligned} \{\phi\}_\mu &= [a]_{\mu\mu}' \{\sigma''\}_\mu, \quad \{\sigma''\}_\mu = [e'']_{\mu\mu} \{e''\}_\mu, \\ \{e''\}_\mu &= [a]_{\mu\mu} \{\psi\}_\mu. \end{aligned}$$

These relationships are as shown in Figure 4. It follows from this that we can obtain the rigidity or stiffness equation

$$\{\phi\}_\mu = [k]_{\mu\mu} \{\psi\}_\mu, \quad (5.23)$$

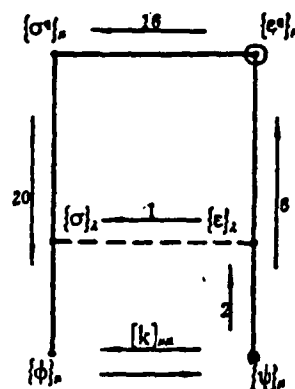


Figure 4

In this case, the effective level square rigidity or stiffness matrix is

$$[k]_{\mu\mu} = [a]_{\mu\mu}' [e^q]_{\mu\mu} [a]_{\mu\mu} \quad (5.24)$$

If we use this, then it is first possible to figure out the displacement vector

$$\{\psi\}_{\mu} = [k]_{\mu\mu}^{-1} \{\phi\}_{\mu}$$

This is nothing else than the method of calculation which is necessary to cross over from the calculations that we have been doing to the direct rigidity or stiffness method.

(Typical example) Employ the method for crossing over from one method to the other. First, precisely determine $\{\epsilon^q\}_{\mu}$, then figure out the calculations for $[e^q]_{\mu\mu}$ in the same way we have done it so far. On the basis of equation (5.24), then figure out

$$[k]_{\mu\mu} = \begin{bmatrix} 1 & & \\ & 1 & \\ & & 1 \end{bmatrix}' \frac{e_0}{2} \begin{bmatrix} 3 & & \\ & 3 & 1 \\ & 1 & 3 \end{bmatrix} \begin{bmatrix} 1 & & \\ & 1 & \\ & & 1 \end{bmatrix} = \frac{e_0}{2} \begin{bmatrix} 3 & & \\ & 3 & 1 \\ & 1 & 3 \end{bmatrix}$$

Having solved this, we can then obtain $\{\psi\}_{\mu} = \frac{1}{e_0} \begin{Bmatrix} 4 \\ 3 \\ 3 \end{Bmatrix}$; all of this is still according to the methods which we have already used before.

Section 5.3 A comparison of the two types of calculation methods for the generalized strain method and a comparison of the generalized strain method and the direct rigidity or stiffness method

If we are considering the case of fixed-form structures, then the amount of work required for the two types of calculation methods available (see Figure 3 and Figure 4) are pretty much equal. If we work through the typical example, we can see that both methods require one to precisely determine $\{\epsilon^q\}_{\mu}$ and figure out $[e^q]_{\mu\mu}$ (it is necessary to solve for the inverse $[a]_{\mu\mu}^{-1}$ one time). Equation (5.17) for the method shown in Figure 3 does not require solving for the inverse $[e^q]_{\mu\mu}^{-1}$; the cross-over method in Figure 4 also does not

require solving for the inverse $[k]_{\mu\mu}^{-1}$; because of these facts, we say that the amounts of work involved in the two methods is pretty much equal.

Let us consider the case of several elastic bodies which, after they undergo the process of modeling analysis, continue to conform to the assumption of fixed-form but cease to conform to the assumption of fixed force; in this sort of case, the structure involved has been transformed into a fixed-form-non-fixed-force structure; due to the fact that $[h]_{\mu\lambda}$ does not exist, the best thing we can do is to look for help to the principle of virtual work; by the means of this approach, we can obtain equation (5.20) or equation (5.21) in order to make up for what we lack. In this case, it is only possible to employ the generalized strain method. In the references for this article some authors still call this, after the old fashion, a direct rigidity method or direct stiffness method; in actuality, it is still nothing more than a type of cross-over method of calculation.

The selection of the method to be used and the points of emphasis in a problem are related. In vibration problems, it is naturally necessary to calculate the form of the vibration (displacement); in this sort of case, it is a good idea to make use of a cross-over method. In questions of minimum weight, if one is designing the parameters concentrated in e_1 , then it is much easier to adjust the value of $[e^q]_{\mu\mu}$ than it is to adjust the value of $[k]_{\mu\mu}$; this means that it is much more advantageous to make use of the generalized strain method and actual practical execution of this procedure verifies this proposition [4]; however, due to the fact that it is beyond the scope of this article, we must treat it only lightly.

As far as the case of fixed-form-non-fixed-force structures are concerned, the use of the direct rigidity or stiffness method to solve for the inverse is relatively advantageous. It is only in the case in which one has a chain form structure that it is possible to reduce the difficulties which come from solving the inverse square

matrix $[a]_{\mu\mu}$ of the two sets or belts of equations. In solving problems of minimum weight, there is a particular difficulty in solving for the inverse; basically, the method one needs to choose in a particular problem requires detailed consideration, and it is not necessary to be a slavish imitator of the methods which have been used in the past on particular types of problems.

Section 6. A generalized stress method appropriate for use with fixed-force structures

Section 6.1 The process of deducing the formulas for the generalized stress method

In addition to the three common assumptions which we have already dealt with, we must also add another assumption which is that the structures with which we are dealing are of the fixed-force type.

The equation for the physical relationship of the structure under discussion is

$$\{e\}_\lambda = [f]_{\lambda\lambda} \{\sigma\}_\lambda, \quad (6.1)$$

The equation for the equilibrium relationship of the fixed-force type structure is

$$\{\phi\}_\lambda = [h]_{\lambda\mu} \{\sigma\}_\mu, \quad (6.2)$$

On the basis of assumption (2b) and assumption (3b), we can obtain the knowledge that the order of $[h]_{\mu\lambda}$ is μ , ($\mu \leq \lambda$) (6.3). Take $[h]_{\mu\lambda}$ and divide it up; moreover, let us assume that there is a μ level reversible component matrix $[h]_{\mu\mu}$ situated on the left, that is,

$$[h]_{\lambda\lambda} = [[h]_{\mu\mu}, [h]_{\mu\nu}], \quad \nu = \lambda - \mu \geq 0, \quad (6.4)$$

It is best if we assume that $\nu > 0$. Once again, let us take $\{\sigma\}_\lambda$ and make a corresponding division of it into

$$\{\sigma\}_\lambda = \left\{ \begin{matrix} \{\sigma\}_\mu \\ \{\sigma\}_\nu \end{matrix} \right\}. \quad (6.5)$$

On the basis of this equation (6.2) is changed to be

$$\{\phi\}_\mu = [h]_{\mu\mu} \{\sigma\}_\mu + [h]_{\mu\nu} \{\sigma\}_\nu. \quad (6.71)^*$$

*The designation system for formulae in this section is as follows: Any formulae or equations which have a dual relationship with formula (51) are designated as being (61) equations; in cases besides this, beginning with (6.71), formulae and equations are designated in their proper order. ..

If we use $[h]_{\mu\mu}^{-1}$ to multiply equation (6.71), and we let

$$\{\sigma''\}_\mu = [h]_{\mu\mu}^{-1} \{\phi\}_\mu \quad (\text{this a quantity which is already known}) \quad (6.8)$$

then we can solve for $\{\sigma\}_\mu$ and obtain

$$\{\sigma\}_\mu = \{\sigma''\}_\mu + [B]_{\mu\nu} \{\sigma\}_\nu, \quad (6.72)$$

In this case,

$$[B]_{\mu\nu} = -[h]_{\mu\mu}^{-1} [h]_{\mu\nu}. \quad (6.10)$$

According to equation (5.6), if we put together $\{\sigma\}_\mu$ and $\{\sigma\}_\nu$, then we can arrive at

$$\{\sigma\}_\lambda = \begin{Bmatrix} \{\sigma''\} \\ \{0\}_\nu \end{Bmatrix} + \begin{bmatrix} [B]_{\mu\nu} \\ [I]_{\mu\nu} \end{bmatrix} \{\sigma\}. \quad (6.11)$$

In order to solve for all related quantities, we must do the following: (1) assume that there is a certain value given for $\{\sigma\}_\nu$ then on the basis of equation (11), figure out the value of $\{\sigma\}_\lambda$ and its balance with the external loading. The explanation for this is as follows: if one only employs the equilibrium relationship to solve the problem, then $\{\sigma\}_\lambda$ has many solutions. It follows from this that we know that the structure that we are dealing with is stationary but not fixed; the degree of this condition is $v = \lambda - \mu$. $\{\sigma\}_\mu$ is called the static level stress (or the basic system stress); $\{\sigma\}_\nu$ is called the redundant or excess level stress; μ is called the static level number (or basis level number); and v is called the redundant or excess level number.

(ii) if we take all of the elements which are related to the redundant or excess stress and cut them off or disconnect them so as to cause $\{\sigma\}_v = \{0\}$, then what we get is the static solution; this is nothing else than $\begin{Bmatrix} \{\sigma^p\}_\mu \\ \{0\}_v \end{Bmatrix}$, this static solution is also called the p as added into equation (6.8) and equation (6.11).

(iii) let us consider $\{\phi\}_\mu = \{0\}$; from equation (6.8) we obtain $\{\sigma^p\}_\mu = \{0\}$, and we can then solve the equilibrium relationship and obtain

$$\{\sigma\}_\lambda = \begin{bmatrix} [B]_{\lambda v} \\ [I]_{\lambda v} \end{bmatrix} \{\sigma\}_v,$$

It can be seen that each vertical row represents a set of self-balancing generalized stress vectors $\{\sigma\}_\lambda$; all together there are v sets of linear independent self-balancing vectors. $\begin{bmatrix} [B] \\ [I] \end{bmatrix}$ can be called a full level self-balancing matrix; moreover $[B]_{\mu v}$ is called a lowered level self-balancing matrix.

Due to this fact, the key to resolving a question of static strength lies in finding the value of $\{\sigma\}_v$.

The principal relationships in Figure 5 are explained by the relationships which follow, that is, the external load $\{\phi\}_\mu$ is a quantity which is already known; the generalized stress $\{\sigma\}_\lambda$ is the principal physical quantity which is not yet known. From $\{\sigma\}_\lambda$ we can use equation (6.1) to represent $\{\varepsilon\}_\lambda$, we can use equation (6.2) to represent $\{\phi\}_\mu$ and we can divide up equation (6.5) into $\{\sigma\}_\mu$ (which has not been noted on the diagram) and $\{\sigma\}_v$.

If we make use of equation (6.8), then it is possible to figure out the stress $\{\sigma^p\}_\mu$ of a condition p; if we make use of equation (6.78) which appears later, then it is possible to figure out $\{\sigma\}_v$; after this, on the basis of equation (6.11), it is then possible to figure out $\{\sigma\}_\lambda$.

The process for deducing the formula (6.78) relating to the solution for $\{\sigma\}_v$ is as follows: the principal of virtual excess energy points out the fact that any given set of virtual self-balancing stresses has a virtual excess energy equal to zero which it produces as actual strain. Now, if we make use of $\begin{bmatrix} [B]_{\mu\nu} \\ [I]_{\mu\nu} \end{bmatrix}$ to be a virtual set v of independent linear self-balancing stresses, then we have what follows, that is

$$[[B]', [I]] \cdot \{e\}_\lambda = \{0\} \quad (6.73)$$

$$[[B]', [I]] \cdot [f]_{\mu\nu} \cdot \left(\begin{Bmatrix} \{\sigma^p\}_\mu \\ \{0\}_\nu \end{Bmatrix} + \begin{bmatrix} [B] \\ [I] \end{bmatrix} \{e\}_\lambda \right) = 0 \quad (6.74)$$

let us remember that

$$[[B]', [I]] \cdot \begin{bmatrix} [f]_{\mu\nu} & [f]_{\mu\nu} \\ [f]_{\mu\nu} & [f]_{\mu\nu} \end{bmatrix} = [F]_{\mu\nu}, [F]_{\mu\nu}, \quad (6.75)$$

$$[[B]', [I]] \cdot [f]_{\mu\nu} \cdot \begin{bmatrix} [B] \\ [I] \end{bmatrix} = [d^{11}]_{\mu\nu}, \quad (6.76)$$

$$[[B]', [I]] \cdot [f]_{\mu\nu} \cdot \begin{Bmatrix} \{\sigma^p\}_\mu \\ \{0\}_\nu \end{Bmatrix} = [F]_{\mu\nu} \{\sigma^p\}_\mu, \quad (6.77)$$

then we can obtain

$$\{e\}_\lambda = -[d^{11}]^{-1} [F]_{\mu\nu} \{\sigma^p\}_\mu. \quad (6.78)$$

According to equation (6.11), we can arrive at $\{\sigma\}_\lambda$ the expression of which becomes

$$\{\sigma\}_\lambda = \begin{Bmatrix} \{\sigma^p\}_\mu \\ \{0\}_\nu \end{Bmatrix} - \begin{bmatrix} [B]_{\mu\nu} \\ [I]_{\mu\nu} \end{bmatrix} [d^{11}]^{-1} [F]_{\mu\nu} \{\sigma^p\}_\mu. \quad (6.79)$$

This is nothing else than the result of our calculations to solve the problem of static strength.

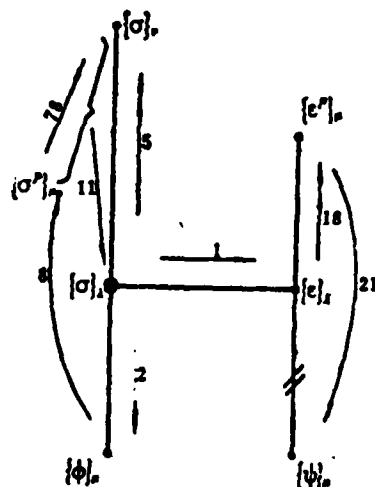


Figure 5

In order to solve for the displacement vector $\{\psi\}_\mu$ in a static rigidity question, we must first make use of equation (6.1) in order to figure out $\{\epsilon\}_\lambda$ as follows:

$$\{\epsilon\}_\lambda = [f]_{\lambda\mu} \begin{Bmatrix} \{\sigma^p\}_\mu \\ \{0\}_\nu \end{Bmatrix} - [f]_{\lambda\mu} \begin{bmatrix} [B]_{\mu\nu} \\ [I]_{\mu\nu} \end{bmatrix} [d^{11}]^{-1} [F]_{\nu\mu} \{\sigma^p\}_\mu \quad (6.80)$$

Because of the fact that there is no relationship which connects $\{\epsilon\}_\lambda$ and $\{\psi\}_\mu$, it is not easy to solve for $\{\psi\}_\mu$. It is better to take $\{\epsilon\}_\lambda$ and divide it into two component vectors, that is

$$\{\epsilon\}_\lambda = \begin{Bmatrix} \{\epsilon^p\}_\mu \\ \{\epsilon\}_\nu \end{Bmatrix}, \quad (6.81)$$

The index p which is added in the notations above has no purpose other than to formally designate the multiple functioning of the duality; $\{\epsilon^p\}_\mu$ and $\{\sigma^p\}_\mu$ certainly have no obvious direct relationship between them. After we carry out the kind of division or analysis we are talking about, then from equation (6.73), it is possible to obtain the relationship between the two component vectors, that is

$$\{\epsilon\}_\nu = -[B]_{\nu\mu}' \{\epsilon^p\}_\mu \quad (6.82)$$

It is best to call this an adjustment or coordination relationship. If we raise it to the λ level, then we have

$$\{\epsilon\}_\lambda = \begin{bmatrix} [I]_{\lambda\mu} \\ -[B]_{\lambda\nu}' \end{bmatrix} \{\epsilon^p\}_\mu \quad (6.19)$$

To be specific, if we separate out $\{\epsilon^p\}_\mu$ from equation (6.80), then we obtain

$$\{\epsilon^p\}_\mu = [\Delta f]_{\mu\mu} \{\sigma^p\}_\mu \quad (6.83)$$

In this case, the purged inverse square matrix of elasticity moduli is

$$[\Delta f]_{\mu\mu} = [f]_{\mu\mu} - ([F]_{\mu\nu})' [d^{11}]^{-1} [F]_{\nu\mu} \quad (6.84)$$

Once again, we can make use of yet another form of the principle of excess virtual energy, that is, the virtual external work

which is done in actual displacement by the virtual external load is equal to the virtual excess energy which is stored in actual strain by virtual stress in a p state, that is to say

$$\begin{aligned} \{\psi\}_n \{\phi_0\}_n &= [\{e^p\}_n, \{e\}_n]_n \begin{Bmatrix} \{\sigma_0^p\} \\ \{0\} \end{Bmatrix} \\ &= \{e^p\}_n \{\sigma_0^p\}_n = \{e^p\}_n [h]_{nn}^{-1} \{\phi_0\}_n \end{aligned}$$

It follows from this that we can obtain the formula for the displacement for the nodal points, that is

$$\{\psi\}_n = ([h]_{nn}^{-1})' \{e^p\}_n. \quad (6.21)$$

We can also obtain the geometrical relationship

$$\{e^p\}_n = [h]_{nn}' \{\psi\}_n. \quad (6.20)$$

If we write the rigidity or stiffness equation in the form of $\{\phi\}_n = [k]_{nn} \{\psi\}_n$, then we can obtain

$$[k]_{nn} = [h]_{nn} [Af]^{-1} ([h]_{nn})'. \quad (6.85)$$

Section 6.2 The generalized stress solution for a typical example (Figure 2)

This example does not make use of the fixed-form assumption; it only makes use of the fixed-force assumption, that is

the following exists: $[h]_{nn} = [h^1, h^2, h^3, h^4, h^5] = \begin{bmatrix} 1 & 0 & 0 & 0 & 1/\sqrt{2} \\ 0 & 1 & 0 & 1/\sqrt{2} & 0 \\ 0 & 0 & 1 & 1/\sqrt{2} & 0 \end{bmatrix}$,

let us choose $[h]_{nn} = [h^1, h^2, h^3] = [I]_{3 \times 3}$
 $[h]_{nn} = [h^4, h^5]$.

Let us get precise values for

$$\{\sigma\}_n = \begin{Bmatrix} \sigma_1 \\ \sigma_2 \\ \sigma_3 \\ \sigma_4 \\ \sigma_5 \end{Bmatrix}, \quad \{\sigma\}_n = \begin{Bmatrix} \sigma_1 \\ \sigma_2 \\ \sigma_3 \end{Bmatrix}, \quad \{\sigma\}_n = \begin{Bmatrix} \sigma_4 \\ \sigma_5 \end{Bmatrix},$$

On the basis of the relationship $\{\sigma\}_s = \begin{Bmatrix} X_u \\ X_c \\ X_r \end{Bmatrix} = \begin{Bmatrix} 6 \\ 6 \\ 6 \end{Bmatrix}$ and according to equations (6.8) and (6.10), let us figure out

$$\{\sigma^p\} = \begin{Bmatrix} 6 \\ 6 \\ 6 \end{Bmatrix}, \quad [B]_{su} = \begin{bmatrix} 0 & -1/\sqrt{2} \\ -1/\sqrt{2} & 0 \\ -1/\sqrt{2} & 0 \end{bmatrix}.$$

It is already given that

$$[f]_{\lambda\lambda} = \frac{1}{e_0} [I]_{ss},$$

On the basis of equations (6.75) and (6.77), we can figure out

$$[[F]_{su}, [F]_{su}] = \begin{bmatrix} 0 & -1/\sqrt{2} & -1/\sqrt{2} & : & 1 \\ -1/\sqrt{2} & 0 & 0 & : & 1 \end{bmatrix} \frac{1}{e_0}.$$

$$[d^{11}]_{\lambda\lambda} = \frac{1}{e_0} \begin{bmatrix} 2 & 0 \\ 0 & 1.5 \end{bmatrix}, \quad [d^{11}]_{\lambda\lambda}^{-1} = e_0 \begin{bmatrix} 1/2 & 0 \\ 0 & 2/3 \end{bmatrix}.$$

$$\{\sigma\}_s = -e_0 \begin{bmatrix} 1/2 \\ 2/3 \end{bmatrix} \cdot \frac{1}{e_0} \begin{bmatrix} 0 & -1/\sqrt{2} & -1/\sqrt{2} \\ -1/\sqrt{2} & 0 & 0 \end{bmatrix} \cdot \begin{Bmatrix} 6 \\ 6 \\ 6 \end{Bmatrix} = \begin{Bmatrix} 3\sqrt{2} \\ 2\sqrt{2} \end{Bmatrix}.$$

$$\{\sigma\}_s = \begin{Bmatrix} 6 \\ 6 \\ 6 \end{Bmatrix} + [B]_{su} \begin{Bmatrix} 3\sqrt{2} \\ 2\sqrt{2} \end{Bmatrix} = \begin{Bmatrix} 4 \\ 3 \\ 3 \end{Bmatrix}.$$

This example figures out to be

$$\{\sigma^p\}_s = \begin{Bmatrix} e_1 \\ e_2 \\ e_3 \end{Bmatrix} = \frac{1}{e_0} \begin{Bmatrix} 4 \\ 3 \\ 3 \end{Bmatrix}, \quad \{\psi\}_s = \begin{Bmatrix} u_B \\ u_O \\ u_C \end{Bmatrix} = \frac{1}{e_0} \begin{Bmatrix} 4 \\ 3 \\ 3 \end{Bmatrix}.$$

Section 7. The qualities of semi-duality, full duality and autoduality

Section 7.1 The semi-duality conditions in two structural dynamics problems and their nature

Let us assume that problem 1 has to do with a fixed-form structure, that it has a geometrical matrix $[a]_{\lambda\mu}$, and that we are

using the strain method to solve it. Problem 2 has to do with a fixed-force structure which has an equilibrium matrix $[h]_{\mu\lambda}$, and we will use the stress method to solve it. All the numerical quantities in problem 2 are marked with the asterisk sign * in order to designate them.

The semi-duality conditions: 1° The subscripts in the two problems λ, μ, ν are all equal.

2° $[a]_{\lambda\mu} = ([h^*])'$ (the order in all cases is μ). (7.1)

According to the way that (5.4) and (6.4) separate out, we can obtain the knowledge that

$$\begin{aligned} [a]_{\mu\mu} &= ([h^*]_{\mu\mu})', \quad [a]_{\nu\mu} = ([h^*]_{\mu\nu})' \\ [G]_{\mu\mu} &= -([B^*]_{\mu\mu})', \quad [[I], [G]] \cdot \begin{bmatrix} [B^*] \\ [I] \end{bmatrix} = [0] \end{aligned} \quad (7.2)$$

If we take the strain vector or the displacement vector from problem 1 and the stress or the external load from problem 2, then their product is called the mixed product; there are three mixed products all together, and they are as follows:

| | |
|---|--|
| twice the mixed full level internal energy | $2U^* = [e]_{\lambda} \{\sigma^*\}_{\lambda}$ |
| twice the mixed lowered level internal energy | $2U_{\mu}^* = [e^*]_{\mu} \{\sigma^{\mu*}\}_{\mu}$ |
| twice the mixed external work | $2W^* = [\psi]_{\mu} \{\phi^*\}_{\mu}$ |

If we take the stress vector or the external load vectors from problem 1 and the strain vector or displacement vector from problem 2, then their product is called the common constraint product; there are three common constraint products all together, and they are as follows:

| | |
|---|---|
| Twice the common constraint full level internal energy | $2U_{\bullet} = [e^*]_{\lambda} \{\sigma\}_{\lambda}$ |
| Twice the common constraint lowered level internal energy | $2U_{\bullet\bullet} = [e^{\mu*}]_{\mu} \{\sigma^{\mu}\}_{\mu}$ |

Twice the common constraint
external work

$$2W_* = \{\psi^*\}_\mu \{\phi\}_\mu.$$

When semi-duality conditions apply, there are two sets of equalities which are respectively in effect, that is

$$W^* = U^* = U_{\mu\mu}^*, \quad W_* = U_* = U_{\mu\mu}. \quad (7.3)$$

Proof:

strain method formula

stress method formula

$$(5.2) \quad \{e\}_\lambda = [a]_{\lambda\mu} \{\psi\}_\mu,$$

$$(6.2) \quad \{\phi^*\}_\mu = [h^*]_{\mu\lambda} \{\sigma^*\}_\lambda,$$

It is possible to obtain the following relationships

$$\begin{aligned} 2W^* &= \{\psi\} \{\phi^*\} = \{\psi\}_\mu [h^*]_{\mu\lambda} \{\sigma^*\}_\lambda = \{\psi\}_\mu ([a]') \{\sigma^*\}_\lambda = \{e\} \{\sigma^*\} = 2U^*. \\ (5.8) \quad \{\psi\}_\mu &= [a]_{\mu\lambda}^{-1} \{e^p\}_\lambda, \quad (6.8) \quad \{\sigma^{p*}\} = [h^*]_{\mu\lambda}^{-1} \{\phi^*\}_\mu, \end{aligned}$$

It is also possible to obtain the following relationships:

$$\begin{aligned} 2W^* &= \{\psi\} \{\phi^*\} = \{e^q\}_\mu ([a]_{\mu\lambda}^{-1})' \{\phi\}^* = \{e^q\}_\mu [h^*]_{\mu\lambda}^{-1} \{\phi\}^* = \{e^q\}_\mu \{\sigma^{p*}\}_\mu = 2U_\mu^*. \\ (5.11) \quad \{e\}_\lambda &= \begin{bmatrix} I \\ G \end{bmatrix} \{e^q\}_\mu, \quad (6.11) \quad \{\sigma^*\}_\lambda = \begin{Bmatrix} \{\sigma^{p*}\} \\ \{0\}_\nu \end{Bmatrix} + \begin{bmatrix} B \\ I \end{bmatrix} \{\sigma^*\}_\nu, \end{aligned}$$

It is further possible to obtain these relationships:

$$\begin{aligned} 2U^* &= \{e\}_\lambda \{\sigma^*\}_\lambda = \{e^q\}_\mu [I, G'] \left(\begin{Bmatrix} \sigma^{p*} \\ 0 \end{Bmatrix} + \begin{bmatrix} B \\ I \end{bmatrix} \{\sigma^*\}_\nu \right) \\ &= \{e^q\}_\mu \{\sigma^{p*}\}_\mu = 2U_\mu^*. \\ (5.19) \quad \{\sigma\}_\lambda &= \begin{Bmatrix} \{\sigma^p\}_\mu \\ \{0\}_\nu \end{Bmatrix} + \begin{bmatrix} -[G'] \\ I \end{bmatrix} \{\sigma\}_\nu, \quad (6.19) \quad \{e^q\}_\lambda = \begin{bmatrix} I \\ -[B^*]' \end{bmatrix} \{e^{p*}\}_\mu, \end{aligned}$$

$$U_* = U_{\mu\mu}.$$

$$(5.21) \quad \{\sigma^q\} = ([a]_{\mu\mu}')^{-1} \{\phi\}_\mu, \quad (6.21) \quad \{\psi^*\}_\lambda = [h^*]_{\mu\lambda}^{-1} \{e^{p*}\}_\mu,$$

It is possible to obtain the duality relationship $W_* = U_{\mu\mu}$.
End of proof.

Section 7.2 The full duality conditions for two structural dynamics problems and the properties of these conditions

As far as the two structures which we have been considering go, they not only satisfy the two semi-duality conditions 1° and 2°; they also satisfy the condition 3° which is $[e]_{\lambda\lambda} = [f^*]_{\lambda\lambda}^{-1}$; this is called the condition of full duality.

The properties or characteristics of full duality include the properties and conditions of semi-duality (7.3); besides this, on the basis of equations (5.1) and (6.1)

$$\{\sigma\}_\lambda = [e]_{\lambda\lambda} \{\varepsilon\}_\lambda, \quad \{\varepsilon^*\}_\lambda = [f^*]_{\lambda\lambda} \{\sigma^*\}_\lambda.$$

Beyond this we can also obtain

$$\begin{aligned} 2U_\bullet &= [\varepsilon^*]_{\lambda\lambda} \{\sigma\}_\lambda = [\sigma^*]_{\lambda\lambda} [f^*]_{\lambda\lambda} \{\sigma\}_\lambda = [\sigma^*]_{\lambda\lambda} [e]_{\lambda\lambda} \{\sigma\}_\lambda \\ &= [\sigma^*]_{\lambda\lambda} \{\varepsilon\}_\lambda = 2U^* \end{aligned}$$

In summary, then, the properties or conditions of full duality are expressed in the mutual equality of six quantities, that is

$$W^* = U^* = U_\bullet^* = W_\bullet = U_\bullet = U_{\bullet\bullet}.$$

This is an extension of the law of mutual equality.

But this is not all. Due to the existence of the conditions for semi-duality, equation (7.2) is in effect. If we compare equation (5.19) with equation (6.11), then we can see that, if we take $\{\varepsilon\}_\lambda$ and write it in the form $\{\varepsilon^*\}_\lambda$, and if we take $\{\varepsilon^q\}_\lambda$ and write it in the form $\{\varepsilon^p_*\}_\mu$, then the two equations are the same. If we compare equation (5.19) and equation (6.11) in the same way, and there are similar conditions in effect, then it can be seen that, under conditions of semi-duality, the formulae for the two types of methods can be divided into four types; these are

1° Those from which can be deduced equation (7.3) and which behave in accordance with conditions of semi-duality.

2° Those which behave in accordance with the two sets of duality relationships such as equation (5.2) and equation (6.2)...and so on and so on.

3° Those which behave as though the two sets are the same such as equation (5.11) and equation (6.19), ...and so on and so on.

4° Those which behave as though they were formulae required by a certain method itself by its very nature (for example, the stress method); these are exemplified by equations (6.71-6.85); when it is necessary, as far as the strain method is concerned, it is also possible to deduce formulae which are the same as the duality relationship equations for it.

What we have said above is also only in effect in a formal sense. Under conditions of full duality, the complete formulae for the strain method change into the full formulae for the stress method; this also works the other way around.

Under conditions of full duality, if we assume one step further that $\{\phi\}_n = \{\phi^*\}_n$, then from the relationship $W^* = W$, it is possible to obtain $\{\psi\}_n = \{\psi^*\}_n$; moreover, it is also possible to deduce $\{\epsilon\}_n = \{\epsilon^*\}_n$ and $\{\sigma\}_n = \{\sigma^*\}_n$. This means nothing else than that, as far as fixed-form structures are concerned, it is possible to employ the formula for the stress method in order to solve the problems we have been talking about; moreover, the results are the same as those gotten with other methods.

A fixed-form-fixed-force structure forms a full duality with itself; moreover, the value of the external load does not change. It follows from this that we can say that fixed-form-fixed-force structures have the quality of autoduality.

Below, we will present examples to explain the situations in which we find the occurrence of semi-duality, full duality and autoduality; in problem 1, the external load and $[e]_{\lambda\lambda}$ are not the same;

in problem 2, they are both common, and they are both chosen in a typical fashion for the sake of the problem. Moreover, we will figure out the mixed product and the common constraint product.

In problem 1, we have $[a]_{\lambda\lambda} = \begin{bmatrix} [a]_{\mu\mu} \\ [a]_{\nu\nu} \end{bmatrix}$, $[a]_{\mu\mu} = [I]_{3 \times 3}$, $[a]_{\nu\nu} = \frac{1}{\sqrt{2}} \begin{bmatrix} 0 & 1 & 1 \\ 1 & 0 & 0 \end{bmatrix}$.

In problem 2, we have $[h^*]_{\lambda\lambda} = [[h^*]_{\mu\mu}, [h^*]_{\nu\nu}]$, $[h^*]_{\mu\mu} = [I]_{3 \times 3}$, $[h^*]_{\nu\nu} = \frac{1}{\sqrt{2}} \begin{bmatrix} 0 & 1 \\ 1 & 0 \\ 1 & 0 \end{bmatrix}$.

All this at least satisfies the conditions for semi-duality.

| Problem 1 semi-duality example | Problem 1 full duality example | Problem 1 autoduality example | Problem 2 (carries * mark) (typical example) |
|--|---|-------------------------------------|--|
| data $\{\phi\}_\mu$ $\begin{Bmatrix} 12 \\ 6 \\ 6 \end{Bmatrix}$ | $\begin{Bmatrix} 12 \\ 6 \\ 6 \end{Bmatrix}$ | same as right | $\begin{Bmatrix} 6 \\ 6 \\ 6 \end{Bmatrix} = \{\phi^*\}_\lambda$ |
| data $\{e\}_{\lambda\lambda}$ $e_0 \begin{bmatrix} [I]_{3 \times 3} \\ 2[I]_{2 \times 2} \end{bmatrix}$ | $e_0 [I]_{5 \times 5}$ | same as right | $e_0 [I]_{5 \times 5} = [e^*]_{\lambda\lambda}$ (that $\frac{1}{e_0} [I]_{5 \times 5} = [f^*]_{\lambda\lambda}$) |
| result $\{e\}_\lambda$ $\frac{1}{e_0} \begin{Bmatrix} 6 \\ 2 \\ 2 \\ 2\sqrt{2} \\ 3\sqrt{2} \end{Bmatrix}$ | $\frac{1}{e_0} \begin{Bmatrix} 8 \\ 3 \\ 3 \\ 3\sqrt{2} \\ 4\sqrt{2} \end{Bmatrix}$ | same as right | $\frac{1}{e_0} \begin{Bmatrix} 4 \\ 3 \\ 3 \\ 3\sqrt{2} \\ 2\sqrt{2} \end{Bmatrix} = \{e^*\}_\lambda$ |
| result $\{\sigma\}_\lambda$ $\begin{Bmatrix} 6 \\ 2 \\ 2 \\ 4\sqrt{2} \\ 6\sqrt{2} \end{Bmatrix}$ | $\begin{Bmatrix} 8 \\ 3 \\ 3 \\ 3\sqrt{2} \\ 4\sqrt{2} \end{Bmatrix}$ | same as right | $\begin{Bmatrix} 4 \\ 3 \\ 3 \\ 3\sqrt{2} \\ 2\sqrt{2} \end{Bmatrix} = \{\sigma^*\}_\lambda$ |
| result $\{\psi\}_\mu$ $\frac{1}{e_0} \begin{Bmatrix} 6 \\ 2 \\ 2 \end{Bmatrix}$ | $\frac{1}{e_0} \begin{Bmatrix} 8 \\ 3 \\ 3 \end{Bmatrix}$ | same as right | $\frac{1}{e_0} \begin{Bmatrix} 4 \\ 3 \\ 3 \end{Bmatrix} = \{\psi^*\}_\mu$ |

| | | | | |
|-------------------------|------------------|------------------|------------------|------------------|
| $2U^* = 2U_s^* = 2W^*$ | $\frac{60}{e_s}$ | $\frac{84}{e_s}$ | same as right | $\frac{60}{e_s}$ |
| $2U_s = 2U_{1s} = 2W_s$ | $\frac{84}{e_s}$ | $\frac{84}{e_s}$ | same as right | $\frac{60}{e_s}$ |

When we are deducing the characteristics or qualities of duality, it should be made a rule that problem 1 uses the strain method in its solution and problem 2 uses the stress method in its solution. If we meet with the case in which we are considering a fixed-form-fixed-force structure, then it is possible to employ any method of solution; in such a case, none of the methods has any influence on the results discussed above or on the properties of duality.

Section 7.3 The utilization of the direct rigidity or stiffness method, the generalized strain method and the generalized stress method

All elastic bodies can be divided into four types; these are A, B, C and D (see the preface). If we work from the basis of the deduction processes for the three methods, then we can draw conclusions as follows:

In the case of A-type structures, one should employ the direct rigidity or stiffness method and figure out the displacement vector first.

In the case of B-type structures, one should make use of the generalized strain method and figure out the strain vector first.

In the case of C-type structures, one should make use of the generalized stress method and figure out the stress vector first. (This method is arrived at by a refinement of the traditional force method).

However, these methods are capable of transforming themselves into each other and overlapping. Because of this fact, the three methods are all capable of being used on the three types of structures discussed above; the computational results will be the same, and the amount of work required is more or less the same for each of them. Because of this, the factors which enter into the process of selecting a method of solution all depend on the objectives for which the problem is being solved. For example, a vibration problem requires a solution for the displacement involved; therefore, in such a case, one should use the direct rigidity or stiffness method; if one were solving a minimum weight problem, then one should make use of the strain method because this method makes it possible to be much more effective [4]. To summarize the whole thing, each of the methods has advantages and disadvantages.

Figure 6 shows a line or stick diagram structure which contains all together eight squares and 22 line segments or sticks. The squares are subject to shear forces on all four sides (fixed-force members); the sticks or bars are two-force rods (fixed-form-fixed force members) or they are uniformly stressed axial force rods (fixed-force-non-fixed form members. Except for the addition of internal nodal points, the $[a^{(i)}]$ of uniformly stressed axial force rods does not exist). To summarize all this, the stick or rod square structure is a fixed-force structure which has altogether six roller seats or bases. Let us assume that the external load stored at the nodal points is $\begin{Bmatrix} X_i \\ Y_i \end{Bmatrix} = \begin{Bmatrix} 0 \\ -2P \end{Bmatrix}$, that the rod length is 1 and that f square = f , f rod = $6f$.

If we are concerned with how to figure out the $[f^*]_{\lambda\lambda}$ and $[h^*]$ of a structure, then it is possible to figure it out completely with the use of the stress method. It is also possible to hypothetically simulate its duality structure (it is a fixed-form structure) and have

$$[a]_{\lambda\lambda} = ([h^*])', \quad [e]_{\lambda\lambda} = [f^*]_{\lambda\lambda}^{-1}$$

It is possible to alter this and solve it by the use of a strain method. It is also possible to go over to the direct rigidity or stiffness method once again; these differing methods all obtain the same results.

However, on the basis of different assumptions, that is to say, (i) that all rods or bars or sticks are two-force rods and (ii) that all rods are uniformly stressed axial force rods, we obtain quite different results. In the case of the first of these two assumptions, we obtain $2W = 10128 fP^2/l^2$, and in the case of the second of these assumptions, we obtain $2W = 10560 fP^2/l^2$; this disparity in results is the result of the use of different models (if we compare the two-force bars to the uniformly stressed axial force rod model, it seems that the second of the two has more strength or rigidity to it).

REFERENCES

- [1] Chen Pei-ping. The equivalent loading method and the equivalent beam method. Quarterly of Applied Math. Vol. VII. No. 2 July, 1949.
- [2] Chen Pei-ping. Matrix analysis of pin-connected structures, A.S.C.E. Vol. 114, 1949.
- [3] Zhen Baibing. Self balancing Characteristics in elastic structural mechanics. Design structural mechanics academic exchange committee research paper collection, 1978.
- [4] Zhen Baibing. Internal regularities which are most easily understood with regard to elastic structures. Design structural mechanics academic exchange committee research paper collection, 1978, Dairen.

The Dual Properties of Elastic Structures

Chen Baiping (Chen Pei-ping)

Any one-dimensional, two-dimensional, or three-dimensional statical problem of elastic bodies usually involves four function-vectors, namely, the displacement, strain, stress and distributed-load function-vectors:

$$\{\psi(x, y, z)\}, \{e(x, y, z)\}, \{\sigma(x, y, z)\}, \{\bar{p}(x, y, z)\}.$$

Within the linear theory, the linear partial differential equations obtained are self-adjoint ones. Hence an elastic body is naturally a self-adjoint system (§1). This system is built upon the following two assumptions:

(Assumption I) There exists the geometrical operator-matrix $[\alpha]$ which satisfies the geometrical relation

$$\left\{ \begin{matrix} e(x, y, z) \\ l \times 1 \end{matrix} \right\} = [\alpha] \left\{ \begin{matrix} \psi(x, y, z) \\ m \times 1 \end{matrix} \right\},$$

i.e., the displacement function-vector determines the strain function-vector.

(Assumption II) There also exists the equilibrium matrix $[h]$ which satisfies the equilibrium relation

$$\left\{ \begin{matrix} \bar{p}(x, y, z) \\ m \times 1 \end{matrix} \right\} = [h] \left\{ \begin{matrix} \sigma(x, y, z) \\ l \times 1 \end{matrix} \right\},$$

i.e., the distributed load function-vector is determined by the stress function-vector.

In §1, a three-dimensional elastic body is analyzed. A self-adjoint system can always be obtained, but to find its solution is rather difficult. A finite element technique is usually adopted for obtaining an approximate solution. This technique may be further divided into two stages, each involving three steps.

First Stage—the modelling stage.

(Step i) Divide the elastic body into finite elements. Take a finite number (say J) of points, called the joints, within the elastic body. Connect these joints to divide the elastic body into a finite number (say I) of elastic elements. Four function-vectors are associated with each elastic element.

For an one-dimensional beam element, these function-vectors are:

$$\left\{ \psi(x)^i \right\}_{m_i \times 1}, \left\{ e(x)^i \right\}_{l_i \times 1}, \left\{ \sigma(x)^i \right\}_{l_i \times 1}, \left\{ \phi(x)^i \right\}_{m_i \times 1}.$$

Model analysis of such element is made mainly for the purpose of making the strain state or stress state approximate the real state. It is best to start with the estimation of the derivative of internal energy. If

$$\frac{dU^i}{dx} = \frac{1}{2} (e_1(x)e_1(x)^2 + \dots + e_{l_i}(x)e_{l_i}(x)^2),$$

then the strain function-vector, the elastic moduli function square matrix, and the stress function vector may be taken as

$$\left\{ e(x)^i \right\}_{l_i \times 1} = \left\{ \begin{matrix} e_1(x) \\ \vdots \\ e_{l_i}(x) \end{matrix} \right\},$$

$$\left[e(x)^i \right]_{l_i \times l_i} = \begin{bmatrix} e_1(x) & \dots & e_{l_i}(x) \end{bmatrix},$$

$$\left\{ \sigma(x)^i \right\}_{l_i \times 1} = \left\{ \begin{matrix} e_1(x)e_1(x) \\ \vdots \\ e_{l_i}(x)e_{l_i}(x) \end{matrix} \right\} = \left\{ \begin{matrix} \sigma_1(x) \\ \vdots \\ \sigma_{l_i}(x) \end{matrix} \right\},$$

or if

$$\frac{dU^i}{dx} = \frac{1}{2} (f_1(x)\sigma_1(x)^2 + \dots + f_{l_i}(x)\sigma_{l_i}(x)^2),$$

then take

$$\left\{ \sigma(x)^i \right\}_{l_i \times 1} = \left\{ \begin{matrix} \sigma_1(x) \\ \vdots \\ \sigma_{l_i}(x) \end{matrix} \right\},$$

$$\left[f(x)^i \right]_{l_i \times l_i} = \begin{bmatrix} f_1(x) & \dots & f_{l_i}(x) \end{bmatrix},$$

$$\left\{ e(x)^i \right\}_{l_i \times 1} = \left\{ \begin{matrix} f_1(x)\sigma_1(x) \\ \vdots \\ f_{l_i}(x)\sigma_{l_i}(x) \end{matrix} \right\} = \left\{ \begin{matrix} e_1(x) \\ \vdots \\ e_{l_i}(x) \end{matrix} \right\}.$$

In short, the l_i components in $\{e(x)^i\}$ or $\{\sigma(x)^i\}$ should be made linearly independent, and they are also required to satisfy

$$\frac{dU^i}{dx} = \frac{1}{2} \{ \sigma(x)^i \}^T \{ e(x)^i \},$$

further, they should be physically related as follows:

$$\left\{ \sigma(x)^i \right\}_{l_i \times 1} = \left[e(x)^i \right]_{l_i \times l_i} \left\{ e(x)^i \right\}_{l_i \times 1} \text{ or } \left\{ e(x)^i \right\}_{l_i \times 1} = \left[f(x)^i \right]_{l_i \times l_i} \left\{ \sigma(x)^i \right\}_{l_i \times 1},$$

(step ii) Ascertain if $[\alpha]$ and $[h]$ exist. Whether the above-mentioned two assumptions, upon which self-adjoint system is built, continue to be valid or not affects decisively the computation work that follows. The validity of the assumptions depends on the existence of the two operator matrices $[\alpha']$ and $[h']$ which satisfy the following geometrical and equilibrium relations respectively:

$$\left\{ \varepsilon(x)' \right\}_{l_i \times 1} = \left[\alpha' \right]_{l_i \times m_i} \left\{ \psi(x)' \right\}_{m_i \times 1}, \quad \left\{ \phi(x)' \right\}_{m_i \times 1} = \left[h' \right]_{m_i \times l_i} \left\{ \sigma(x)' \right\}_{l_i \times 1}.$$

At the end of step ii, substitute for the distributed load on the i th element its structurally (or statically) equivalent load system⁽¹⁾ acting at the joints. Therefore, henceforth, $\{\bar{\phi}(x')\} = \{0\}$.

(step iii) Convert i th element into a structural member, i.e., convert four function-vectors into four definite-value vectors

$$\left\{ \psi' \right\}_{\mu' \times 1}, \left\{ \varepsilon' \right\}_{\lambda' \times 1}, \left\{ \sigma' \right\}_{\lambda' \times 1}, \left\{ \bar{\phi}' \right\}_{\mu' \times 1},$$

where $\{\bar{\phi}'\}$ is the external-force vector at the two ends of the member. These four vectors are likewise subject to the following limitations:

$$U' = \frac{1}{2} [\varepsilon'] \left\{ \sigma' \right\}, \quad W' = \frac{1}{2} [\bar{\phi}'] \left\{ \psi' \right\}.$$

Also, for the convenience of derivation of formulas and computation work, it is stipulated that corresponding function-vector and definite-value vector may mutually represent each other. For example, from $\{\varepsilon(x)'\}$ one may obtain

$\{\varepsilon'\}$ by using operator-matrix, from $\{\varepsilon'\}$ one may obtain $\{\varepsilon(x)'\}$ by using

auxiliary functions, etc.

This paper also fully explains the following for beams only:

1° If $[\alpha']$ exists, then the geometric matrix $[\alpha']$, which satisfies the geometrical relation $\{\varepsilon'\} = [\alpha'] \{\psi'\}$, also exists.

2° If $[h']$ exists, then the equilibrium matrix $[h']$, which satisfies the equilibrium relation $\{\bar{\phi}'\} = [h'] \{\sigma'\}$, also exists.

3° If $[\alpha']$ and $[h']$ both exist, then $[h'] = [\alpha']'$.

Second stage—the structural computation stage

(step iv) Form the assembly structure by assembling all free structural members. Its four assembly vectors are

$$\left\{ \psi \right\}_{\Sigma \mu \times 1}, \left\{ \varepsilon \right\}_{\Sigma \lambda \times 1}, \left\{ \sigma \right\}_{\Sigma \lambda \times 1}, \left\{ \bar{\phi} \right\}_{\Sigma \mu \times 1}.$$

(step v) Assume the structure to have N rigid roller joints. Cancel all zero displacements at rigid roller joints. Cancel the unknown restraining forces at the rigid joints. Finally, one arrives at four generalized vectors

$$\left\{ \begin{matrix} \psi \\ \mu \times 1 \end{matrix} \right\}, \left\{ \begin{matrix} e \\ \lambda \times 1 \end{matrix} \right\}, \left\{ \begin{matrix} \sigma \\ \lambda \times 1 \end{matrix} \right\}, \left\{ \begin{matrix} \phi \\ \mu \times 1 \end{matrix} \right\},$$

where $\{\phi\}$ is the known load vector of the elastic structural problem.

(step vi) solve the elastic structural problem.

It can be easily seen that both one dimensional beams and plane trusses are self-adjoint systems and can be easily solved. By studying these cases, one might know more about the properties of self-adjoint systems.

This paper points out: through the analysis of one-dimensional beams, one may reach the following conclusion. In the modelling analysis of elements of elastic bodies, observation on whether the two assumptions remain valid or not affects the computation that follows. The conclusion is stated specifically as follows:

1° If assumption I remains valid (i.e., $[a']$ exists), then all the geometrical matrices $[a']$, $[a]$, and $[a]$, which occur in the later steps, exist.

2° If assumption I remains valid (i.e., $[h']$ exists), then all the equilibrium matrices $[h']$, $[h]$, and $[h]$, which occur in the later steps, exist.

On the basis of the above conclusion, elastic structures may be classified into four types as follows:

Type A: Both $[a]$ and $[h]$ exist.

Type B: $[a]$ exists, but $[h]$ does not.

Type C: $[h]$ exists, but $[a]$ does not.

Type D*: Both $[a]$ and $[h]$ are not clear.

This paper also points out with emphasis that, for each of the three types of structures, there is a suitable method of solution:

The direct stiffness method⁽²⁾ for type A;

The generalized strain method⁽³⁾ for type B;

* It is beyond the scope of this paper to discuss type D structures.

The generalized stress method⁽¹⁾ for type C.

Starting with the assumptions (1), (2a), (2b), (3a), and (3b) as the general requirements for an elastic structure, one derives rigorously the formulas for these three methods. Detailed computations of a simple planar truss are also given to illustrate the computational processes involved in the three methods of solution.

It deserves to be noticed that a type-B structure and a type-C structure under certain dual conditions possess the astonishing feature that from the generalized strain method all formulas of the generalized stress method can be derived and vice versa. In other words, these three methods are very conveniently interchangeable and the amounts of computational work are approximately equal.

Then, which is the best method? In the author's opinion, it depends solely on what physical quantities are to be computed in a specific problem. The following two extreme cases may be taken as examples:

1° For finding the mode (or displacement) in a vibration problem, the direct stiffness method is best.

2° For finding the unknown design parameters in a minimum weight problem,⁽⁴⁾ the generalized strain method is superior, because it is much easier to adjust the value of $[\epsilon^*]_{nn}$ than the value of $[k]_{nn}$.

Unfortunately, most of the authors on finite element technique study it only from the viewpoint of theory of elasticity and almost completely ignore the significant features of the elastic structure itself. They usually standardize the form of presentation of the final results and give only direct stiffness matrix equations, even when such equations are sometimes transformed from equations derived by other methods. By so doing, they miss the opportunity of clearly bringing forth the generalized strain and generalized stress methods, thus disadvantageously making it very difficult to select the most suitable method for a specific problem.

MATRIX ANALYSIS OF WINGS

Xu Yuzan, Zhu Runxiang, Jiang Jinqiang, and Cai Yiuliu

ABSTRACT

The calculation of static strength of wings is an indispensable area in the design of flight vehicles. In general, different analysis methods are used for wings of different types of constructions. Even for wings of the same type of construction, due to the variation in shape and dimensions, the tedious calculation processes must be repeated. In this paper, the plate-beam wing constructions are simplified either as plane stress or plate bending models. It introduces the triangular element matrix of a laminated plate and the element stiffness matrix of the beam of axially-variable rectangular cross-section. Correspondingly, two general computer calculation programs are compiled. As examples, calculations are shown for wings consisting of plates and beams, honeycomb core and solid wings. Compared to the experimental results, the errors in the nodal deflections are generally less than 5%. Therefore, it is clear that the method adopted by this paper has finite accuracy and generality. It can be used as a reference in the future design of wings of all types of construction.

I. SIMPLIFIED CALCULATION MODEL

A direct calculation of static strength cannot be carried out directly, because of the complicated structure of

TABLE 1-1. COMPARISON OF TWO MODELS

| | PLANE STRESS MODEL | PLATE BENDING MODEL |
|------------------|--|---|
| ASSUMPTION | Upper and lower plates assumed to consist of many planar triangular plate elements. | (1) Satisfied straight normal assumption. (2) Wing assumed to consist of many triangular elements. (Only linear increase of plate thickness discussed.) |
| FORMING ELEMENTS | Upper plate, lower plate and beam. | Plates and beams. |
| STRESS CONDITION | (1) Upper and lower plates and beams form force-exerting structure. Beams take up bending, twisting and shearing forces. Bending stress transformed into plane stress stiffness by upper and lower plates. (2) Stress uniformly distributed along thickness of plate. | (1) Plate and beam can take bending, twisting and shearing. (2) Stress distributed linearly along thickness. |
| ELEMENT | Plane triangular stress element and beam element. | Triangular element and beam element. |
| NODAL POINT | On plane between upper and lower plates. | On center plane of wing. |
| NODAL DEFLECTION | x, y, z direction deflections. | z-axis deflection; x, y axes rotation. |
| NODAL FORCE | Force in x, y, z directions. | Force in z direction; torque, x, y axes. |

the actual wings. Therefore, simplifications must be made. Wings consisting of plates and beams generally can be simplified as plane stress or plate bending models. In the plane stress model, it is assumed that the upper and lower plates are under plane stress conditions with respect to torque. This model has been discussed in the literature [1], and it was used in the box-beam example in this paper. Because of symmetric structure and identical stiffness between the upper and lower plates, it is only necessary to analyze either plate to obtain the calculated stress strength of the entire wing under asymmetric load reactions. For solid plates or various types of laminated plate wing structures, the plate bending method is used to make wing calculation problems become plate bending problems. In this paper, a three-layer plate bending problem is discussed in detail. It is applicable to the solid plate as well as a variety of laminated wing structure problems.

For convenience, the comparison of the two models is tabulated (see Table 1-1).

II. BASIC EQUATIONS

1. Selection of Coordinate Systems

The coordinate system of the structure is shown in Figure 2-1. It is a right-hand coordinate system. The plate middle plane is in the xoy plane.

2. Nodal Deflections and Nodal Force

1) Plane stress model:

The nodal deflection of the triangular element is:

$$\{\delta\}_{3 \times 1} = \begin{Bmatrix} \{\delta_i\}_{3 \times 1} \\ \{\delta_j\}_{3 \times 1} \\ \{\delta_m\}_{3 \times 1} \end{Bmatrix}, \text{ 而 } \{\delta_r\}_{3 \times 1} = \begin{Bmatrix} u_r \\ v_r \\ w_r \end{Bmatrix}, \quad r = i, j, m \quad (2-1)$$

where i, j and m are the symbols of the three corners of the triangle.

The corresponding nodal forces are:

$$\{P\}_{3 \times 1} = \begin{Bmatrix} \{P_i\}_{3 \times 1} \\ \{P_j\}_{3 \times 1} \\ \{P_m\}_{3 \times 1} \end{Bmatrix}, \text{ 而 } \{P_r\}_{3 \times 1} = \begin{Bmatrix} U_r \\ V_r \\ W_r \end{Bmatrix}, \quad r = i, j, m \quad (2-2)$$

The above nodal deflections and forces are positive in the positive direction of the same coordinate system. Nodal deflection and nodal forces for beam elements are similar to the above equations. They will not be repeated here.

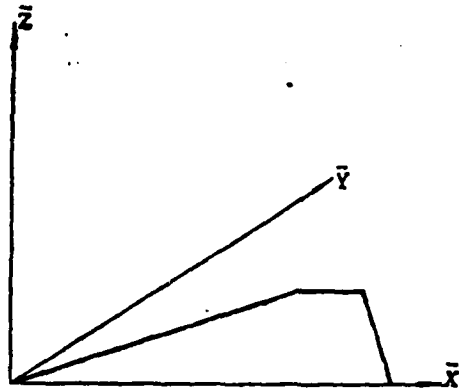


Figure 2-1.

2) Plate bending model:

The nodal deflection of the triangular elements is:

$$\{\delta\}_{6 \times 1} = \begin{Bmatrix} \{\delta_i\}_{3 \times 1} \\ \{\delta_j\}_{3 \times 1} \\ \{\delta_m\}_{3 \times 1} \end{Bmatrix}, \text{ 而 } \{\delta_r\}_{3 \times 1} = \begin{Bmatrix} w_r \\ \theta_{xr} \\ \theta_{yr} \end{Bmatrix}, \quad r = i, j, m \quad (2-3)$$

The corresponding nodal force is:

$$\{P\}_{3 \times 1} = \begin{Bmatrix} \{P_i\}_{3 \times 1} \\ \{P_j\}_{3 \times 1} \\ \{P_m\}_{3 \times 1} \end{Bmatrix}, \text{ 而 } \{P_r\}_{3 \times 1} = \begin{Bmatrix} W_r \\ M_{xr} \\ M_{yr} \end{Bmatrix}, r = i, j, m \quad (2-4)$$

Angular displacement and the vector quantity of the torque are determined using the right hand rule. Nodal deflection and nodal forces are positive in the positive direction of the axes of the coordinate system, as shown in Figure 2-2. The nodal deflection and nodal force of the beam element are similarly defined, and they will not be repeated.

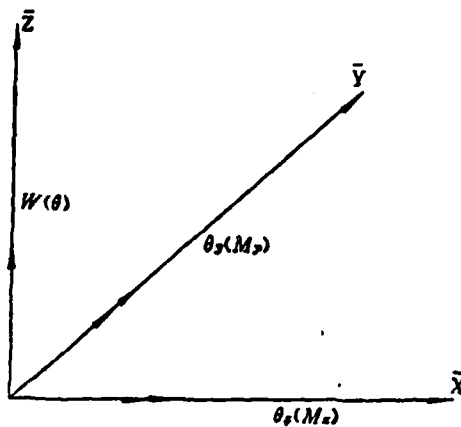


Figure 2-2.

3. Basic Equations

1) Plane stress model:

1) The stiffness matrix of plane stress triangular elements is taken directly from equation (5.141) in reference [2], i.e.:

$$[K] = [K_n] + [K_s] \quad (2-5)$$

where $[K_n]$ is the stiffness resisting stress in the normal direction and $[K_s]$ is the stiffness resisting shearing stress.

They are expressed as:

$$[K_1] = \frac{Et}{4\Delta(1-\mu^2)} \begin{bmatrix} y_{12}^2 & -\mu y_{12}x_{12} & x_{12}^2 & 0 & 0 & 0 \\ -y_{12}y_{31} & \mu x_{12}y_{31} & y_{31}^2 & 0 & 0 & 0 \\ \mu y_{12}x_{31} & -x_{12}x_{31} & -\mu y_{31}x_{31} & x_{31}^2 & 0 & 0 \\ y_{12}y_{31} & -\mu x_{12}y_{21} & -y_{31}y_{21} & \mu x_{31}y_{21} & y_{21}^2 & 0 \\ -\mu y_{12}x_{21} & x_{12}x_{21} & \mu y_{31}x_{21} & -x_{31}x_{21} & -\mu y_{21}x_{21} & x_{21}^2 \\ x_{12}^2 & -x_{12}y_{12} & y_{12}^2 & 0 & 0 & 0 \\ -x_{12}x_{31} & y_{12}x_{31} & x_{31}^2 & 0 & 0 & 0 \\ x_{12}y_{31} & -y_{12}y_{31} & -x_{31}y_{31} & y_{31}^2 & 0 & 0 \\ x_{12}x_{21} & -y_{12}x_{21} & -x_{31}x_{21} & y_{31}x_{21} & x_{21}^2 & 0 \\ -x_{12}y_{21} & y_{12}y_{21} & x_{31}y_{21} & -y_{31}y_{21} & -x_{21}y_{21} & y_{21}^2 \end{bmatrix}$$

where Δ represents the area of triangle 123 in Figure 2-3, E is the elastic modulus of the material, μ is the Poisson ratio, $x_{ij} = x_i - x_j$, $y_{ij} = y_i - y_j$ i, j are symbols for triangular nodes. The corresponding nodal deflection and nodal force for equation (2-5) are equations (21-1) and (2-2), respectively.

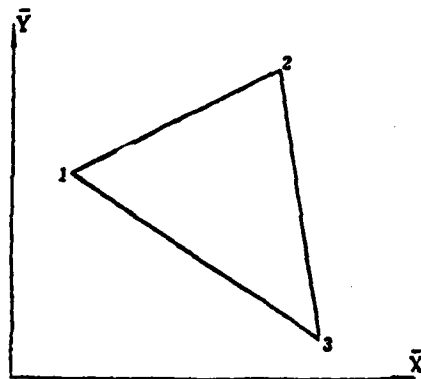


Figure 2-3

We are going to use the same partial coordinate system for the triangular element as the one shown in Figure 5-13 in reference [2]. Let the oy axis be in the direction of side $\overline{12}$ and include the axis in the same plane as the triangle. Then

the oz axis can be determined according to the right hand coordinate system. Therefore, the transformation matrix $[\lambda]$ is the same as the one described by equation (5.157) in reference [2] and will not be further repeated.

ii) Stiffness matrix of beam elements:

It is included in the Appendix. The derivation of the stiffness matrix of beam elements with rectangular cross-section (see Figure A-1 in the Appendix) and the results are:

$$[K] = \begin{bmatrix} ac_{11} & 0 & -ac_{12} & -ac_{11} & 0 & a(c_{12} - lc_{11}) \\ \beta & 0 & 0 & -\beta & 0 & 0 \\ a(c_{12} + c_0) & ac_{12} & 0 & a(lc_{12} - c_{11} - c_0) & & \\ & ac_{11} & 0 & a(lc_{11} - c_{12}) & & \\ & \beta & 0 & & & \\ & & a(l^2c_{11} - 2lc_{12} + c_{22} + c_0) & & & \end{bmatrix} \quad (2-6)$$

where the coefficients are shown in Table 2-1.

TABLE 2-1. COEFFICIENTS OF RECTANGULAR CROSS-SECTION BEAM WITH VARIOUS PARAMETERS

| BEAM CROSS-SECTION COEFFICIENT | c_0 | c_{11} | c_{12} | c_{22} |
|--|--|---------------------------|---|---|
| $B = \text{const.}$ $h(x) \sim x$ | $\frac{KEI_1}{GF_1} \frac{\ln a}{a-1} l$ | $\frac{(1+a)}{2a^2} l$ | $\frac{1}{2a} l^2$ | $(- \ln a - \frac{a^2}{2} + 2a - \frac{3}{2}) \frac{1}{(1-a^2)^3} l^3$ |
| $B = \text{const.}$ $h(x) \sim x^{1/2}$ | $\frac{KEI_1}{GF_1} \frac{2}{(1+a)} l$ | $\frac{2}{a(1+a)} l$ | $\frac{2}{(1+a)^2} l^2$ | $(\frac{3}{2} - 4a^2 + \frac{16}{3}a^3 - 2a^4) \frac{1}{(1-a^2)^3} l^3$ |
| $B = \text{const.}$ $h(x) \sim x^{1/3}$ | $\frac{KEI_1}{GF_1} \frac{3(1-a^2)}{2(1-a^3)} l$ | $\frac{\ln a^3}{a^2-1} l$ | $\frac{(1-a^3+a^3 \ln a^3)}{(1-a^3)^2} l^2$ | $(\frac{1}{2} - 2a^3 + \frac{3}{2}a^6 - a^6 \ln a^3) \frac{1}{(1-a^2)^3} l^3$ |
| $B(x) \sim x$, $h = \text{const.}$ | $\frac{KEI_1}{GF_1} \frac{\ln a}{(a-1)} l$ | $\frac{\ln a}{a-1} l$ | $\frac{1-a+a \ln a}{(1-a)^2} l^2$ | $(\frac{1}{2} - 2a + \frac{3}{2}a^2 - a^2 \ln a) \frac{1}{(1-a)^3} l^3$ |
| $B, h = \text{const.}$ | $\frac{KEI_1}{GF_1} l$ | l | $\frac{1}{2} l^2$ | $\frac{1}{3} l^3$ |

Tabulated K values are shear stress distribution coefficients. For a rectangular cross-section, $K = 1.2$. B is the width of the beam; h is the beam height. E is the elastic modulus. G is the shearing modulus. I is the moment of inertia; l is the length of the beam. F is the cross-section area. The subscripts i and j are symbols for the end points of the beam, $a = h_i h_j$, $a' = J_i J_j$, $C_{33} = I_n a' / (a' - 1)$, $a = EI_j / D$, $\beta = GJ_i / C_{33}$, $D = C_{11}(C_{22} + C_o) - C_{12}^2$.

The corresponding nodal deflection and nodal force for equation (2-6) are equations (2-3) and (2-4), respectively. In order to obtain consistent results to those of the plane stress triangular elements, equation (2-6) must be modified.

From Figure 2-4, it can be found that the relations between the two types of nodal deflections and nodal forces are:

$$\begin{aligned}\theta_{yr} &= u_r / (h_r / 2), & w_r &= w_r \\ M_{yr} &= h_r \cdot U_r, & Q_{xr} &= 2W_r\end{aligned}$$

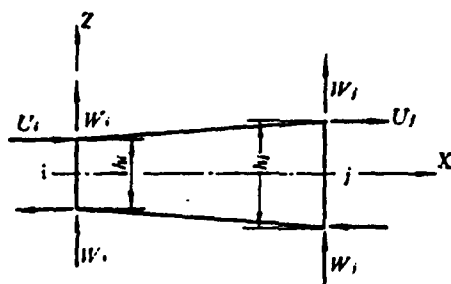


Figure 2-4.

Similarly $\theta_{xr} = -v_r / (h_r / 2)$, $M_{xr} = h_r V_r$

Substituting these into the stiffness equation, after simplification the nodal deflection and nodal force can be expressed in the same forms as equations (2-1) and (2-2). The stiffness matrix becomes

$$[K] = \begin{bmatrix} \frac{2}{h_i^3} K_{11} & 0 & \frac{1}{h_j} K_{11} & \frac{2}{h_i h_j} K_{11} & 0 & \frac{1}{h_i} K_{11} \\ & \frac{2}{h_i^3} K_{11} & 0 & 0 & \frac{2}{h_i h_j} K_{11} & 0 \\ & & \frac{1}{2} K_{11} & \frac{1}{h_j} K_{11} & 0 & \frac{1}{2} K_{11} \\ & & & \frac{2}{h_j^3} K_{11} & 0 & \frac{1}{h_j} K_{11} \\ & \text{symmetric} & & & \frac{2}{h_j^3} K_{11} & 0 \\ & & & & & \frac{1}{2} K_{11} \end{bmatrix} \quad (2-7)$$

where K_{ij} is the element at the i th row and j th column in equation (2-6).

Based on Figure 2-5, which shows the relation between the partial coordinate of the beam and the standard coordinate system of the wing, the transformation matrix can be obtained:

$$[\lambda] = \begin{bmatrix} \lambda_{ox} & 0 \\ \lambda_{oy} & 0 \\ \lambda_{oz} & 0 \\ 0 & \lambda_{ox} \\ 0 & \lambda_{oy} \\ 0 & \lambda_{oz} \end{bmatrix} \quad (2-8)$$

where $\lambda_{ox} = [l_{ox}, m_{ox}, n_{ox}]$, $\lambda_{oy} = [l_{oy}, m_{oy}, n_{oy}]$, $\lambda_{oz} = [l_{oz}, m_{oz}, n_{oz}]$. The elements are defined by the coordinates of the node points i and j at both ends:

$$\left. \begin{aligned} l_{ox} &= (x_i - x_j)/d_{ij} = x_{ji}/d_{ij}, & m_{ox} &= y_{ij}/d_{ij}, & n_{ox} &= 0 \\ l_{oy} &= -y_{ji}/d_{ij}, & m_{oy} &= x_{ji}/d_{ij}, & n_{oy} &= 0 \\ l_{oz} &= 0, & m_{oz} &= 0, & n_{oz} &= 1 \end{aligned} \right\} \quad (2-9)$$

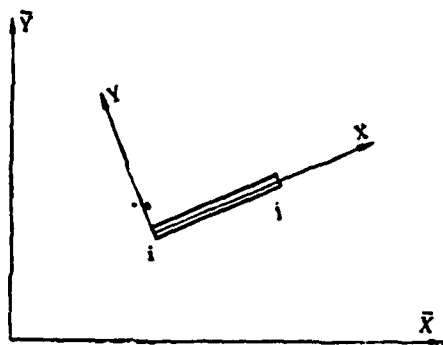


Figure 2-5.

ii) $d_{ij} = \sqrt{x_{ij}^2 + y_{ij}^2}$.

iii) Load matrix:

If the load action F is concentrated in the triangle 123, based on simple static mechanics, it is distributed onto the node points with nodal load F_1 , F_2 and F_3 :

$$\begin{cases} F = F_1 + F_2 + F_3, \\ Fx_0 = F_1x_1 + F_2x_2 + F_3x_3, \\ Fy_0 = F_1y_1 + F_2y_2 + F_3y_3. \end{cases}$$

and

$$\begin{Bmatrix} F_1 \\ F_2 \\ F_3 \end{Bmatrix} = \begin{bmatrix} 1 & 1 & 1 \\ x_1 & x_2 & x_3 \\ y_1 & y_2 & y_3 \end{bmatrix} \begin{Bmatrix} 1 \\ x_0 \\ y_0 \end{Bmatrix} F$$

Introducing area coordinate symbols, we get:

$$\begin{Bmatrix} L_1 \\ L_2 \\ L_3 \end{Bmatrix} = \begin{bmatrix} 1 & 1 & 1 \\ x_1 & x_2 & x_3 \\ y_1 & y_2 & y_3 \end{bmatrix} \begin{Bmatrix} 1 \\ x_0 \\ y_0 \end{Bmatrix}$$

and

$$\begin{Bmatrix} F_1 \\ F_2 \\ F_3 \end{Bmatrix} = \begin{Bmatrix} L_1 \\ L_2 \\ L_3 \end{Bmatrix} F$$

Therefore, the nodal load matrix is:

$$\{F\} = [0 \ L_1 \ 0 \ 0 \ L_2 \ 0 \ 0 \ L_3 \ 0]^T F \quad (2-10)$$

iv) Stress matrix:

Due to the linear distribution of deflection inside the triangular elements, the stress is the same at all points. The equation is as follows, which is equation (5.140) in reference [2].

$$\begin{Bmatrix} \sigma_x \\ \sigma_y \\ \tau_{xy} \end{Bmatrix} = \frac{E}{2A(1-\mu^2)} \cdot$$

$$\begin{bmatrix} y_{32} & -\mu x_{32} & -y_{31} & \mu x_{31} & y_{21} & -\mu x_{21} \\ \mu y_{32} & -x_{32} & -\mu y_{31} & x_{31} & \mu y_{21} & -x_{21} \\ -\frac{(1-\mu)}{2}x_{32} & \frac{(1-\mu)}{2}y_{32} & \frac{(1-\mu)}{2}x_{31} & -\frac{(1-\mu)}{2}y_{31} & -\frac{(1-\mu)}{2}x_{21} & \frac{(1-\mu)}{2}y_{21} \end{bmatrix} \begin{Bmatrix} u_1 \\ v_1 \\ u_2 \\ v_2 \\ u_3 \\ v_3 \end{Bmatrix} \quad (2-11)$$

2) Triple-layer plate bending model.

1) Triple-layer triangular plate element bending stiffness matrix:

Reference [3] introduced a stiffness matrix for triangular plate bending elements. Therefore, it is possible to separate the variable portion for consideration under non-linear increase in thickness and triple layer laminated plate conditions. The stiffness matrix is:

$$[K] = [F]^T ([\bar{\mathcal{F}}] + [\bar{\mathcal{F}}]) [F]$$

$$[\bar{\mathcal{F}}] = \frac{\bar{E}}{12(1-\bar{\mu}^2)} \begin{bmatrix} [R] & \bar{\mu}[R] & [0] \\ \bar{\mu}[R] & [R] & [0] \\ [0] & [0] & \frac{1-\bar{\mu}}{2}[R] \end{bmatrix} \quad (2-12)$$

where \bar{E} and $\bar{\mu}$ are the elastic modulus of the outside layer material and Poisson's ratio, respectively. For linearly increasing thickness plate:

$$[R] = \frac{\Omega}{840} \cdot \left. \begin{array}{l} 20t_i^3 + 4t_i^2 + (2t_j + t_m)(3t_i^2 + t_m^2) + 4t_i^2 + (2t_m + t_j)(3t_i^2 + t_j^2) + \\ + 2(t_i + t_m)(6t_i^2 + t_j^2 + t_m^2) + 2t_i(3t_j^2 + 2t_j t_m + t_m^2) + 2t_i(3t_m^2 + 2t_m t_j + t_j^2) + \\ + 6t_i(t_j^2 + t_m^2 + t_j t_m) + t_j^2(4t_i + 3t_m) + t_m^2(4t_m + 3t_j) \\ 20t_j^3 + 4t_j^2 + (2t_m + t_i)(3t_j^2 + t_i^2) + 4t_j^2 + (2t_i + t_m)(3t_j^2 + t_m^2) + \\ + 2(t_m + t_i)(6t_j^2 + t_m^2 + t_i^2) + 2t_j(3t_m^2 + 2t_m t_i + t_i^2) + \\ + 6t_j(t_m^2 + t_i^2 + t_m t_i) + t_m^2(4t_m + 3t_i) \\ \text{symmetric} \\ 20t_m^3 + 4t_m^2 + (2t_i + t_j)(6t_m^2 + 2t_j^2 + t_j^2) + \\ + 6t_m(t_i^2 + t_j^2 + t_i t_j) \end{array} \right\}$$

Ω is twice the area of the triangular element; i , j and m are symbols of nodes of the triangles in a counter-clockwise order; and t_i , t_j and t_m are heights of the three nodes with respect to the surface of the outside layer.

$$[\bar{\mathcal{F}}] = \frac{\bar{E}}{12(1-\bar{\mu}^2)} \begin{bmatrix} [\bar{R}] & \bar{\mu}[\bar{R}] & [0] \\ \bar{\mu}[\bar{R}] & [\bar{R}] & [0] \\ [0] & [0] & \frac{1-\bar{\mu}}{2}[\bar{R}] \end{bmatrix} -$$

$$- \frac{\bar{E}}{12(1-\bar{\mu}^2)} \begin{bmatrix} [\bar{R}] & \bar{\mu}[\bar{R}] & [0] \\ \bar{\mu}[\bar{R}] & [\bar{R}] & [0] \\ [0] & [0] & \frac{1-\bar{\mu}}{2}[\bar{R}] \end{bmatrix} \quad (2-13)$$

\bar{E} and $\bar{\mu}$ are the elastic moduli and the Poisson's ratio of the inner layer material, respectively. $[\bar{R}]$ is of the same form as $[R]$ with \bar{t}_i , \bar{t}_j and \bar{t}_{mo} as the thickness of the inner layer material.

Column 1

Column 2

Col.3 Cols.4-6 Cols.7-9

$$[F] = \frac{1}{\Omega} \cdot$$

| | | |
|--|--|--|
| $\begin{bmatrix} 2(2b_i^2 + b_j^2 + b_m^2) \\ 2b_i(2b_j - b_i) \\ 2b_i(2b_m - b_i) \\ \vdots \\ 4(2b_i c_i + b_j c_j + b_m c_m) \\ -4(b_i c_i - b_j c_j - b_m c_m) \\ -4(b_i c_i - b_j c_m - b_m c_j) \end{bmatrix}$ | $\begin{bmatrix} b_i b_m (b_m - b_j) \\ b_m b_i (b_m + 2b_i - b_j) \\ b_i b_j (b_m - 2b_i - b_j) \\ 4c_i (b_m c_j - b_j c_m) + c_j c_m (b_m - b_j) \\ c_i c_m (b_m - b_j) + 2b_m c_i^2 \\ c_i c_j (b_m - b_j) - 2b_j c_i^2 \\ 4b_i (b_m c_j - b_j c_m) + (b_m - b_j) (b_j c_m + b_m c_j) \\ 4b_m b_i c_i + (b_m - b_j) (b_m c_i + b_i c_m) \\ -4b_j b_i c_i + (b_m - b_j) (b_i c_j + b_j c_i) \end{bmatrix}$ | |
|--|--|--|

where

$$\begin{aligned} b_i &= y_j - y_m, & b_j &= y_m - y_i, & b_m &= y_i - y_j, \\ c_i &= x_m - x_j, & c_j &= x_i - x_m, & c_m &= x_j - x_i, \end{aligned}$$

The symbol \leftrightarrow means that b and c are interchanged with row number and subscript unchanged.

In $\bigcirc \rightarrow$, \bigcirc means that the subscripts i, j and m change in a cycle ; and \rightarrow means that the

row order changes according to

\rightarrow represents a one-way relationship.

11) Stiffness matrix of beam elements:

The derivation of stiffness matrixes with rectangular cross-section is included in the Appendix using various parameters. The results are shown in Equation (2-6) and also tabulated in Table 2-1. Since the corresponding nodal deflection and nodal force are identical to those for plate elements, they can

be directly applied.

The transformation matrix of beam elements (same coordinate system as shown in Figure 2-5) should be:

$$[A] = \begin{bmatrix} n_{xx} & l_{ox} & m_{ox} & 0 & 0 & 0 \\ n_{ox} & l_{ox} & m_{ox} & 0 & 0 & 0 \\ n_{oy} & l_{oy} & m_{oy} & 0 & 0 & 0 \\ 0 & 0 & 0 & n_{xx} & l_{ox} & m_{ox} \\ 0 & 0 & 0 & n_{ox} & l_{ox} & m_{ox} \\ 0 & 0 & 0 & n_{oy} & l_{oy} & m_{oy} \end{bmatrix} \quad (2-14)$$

where the elements have been obtained in Equation (2-9).

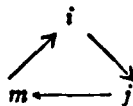
iii) Load matrix:

If the load is concentrated in the triangle, the load matrix becomes:

$$\{F\}_{6 \times 1} = \begin{bmatrix} \{F_i\}_{3 \times 1} \\ \oplus \\ \{F_j\}_{3 \times 1} \\ \oplus \\ \{F_m\}_{3 \times 1} \end{bmatrix} \quad (2-15)$$

The symbol \oplus means the same as described before. The row order remains unchanged, while the subscripts interchange

according to:



where:

$$\{F_i\}_{3 \times 1} = \begin{bmatrix} L_i + L_i L_j (L_i - L_j) + L_i L_m (L_i - L_m) \\ -b_m (L_i^2 L_j + \frac{1}{2} L_i L_j L_m) + b_j (L_i^2 L_m + \frac{1}{2} L_i L_j L_m) \\ -c_m (L_i^2 L_j + \frac{1}{2} L_i L_j L_m) + c_j (L_i^2 L_m + \frac{1}{2} L_i L_j L_m) \end{bmatrix} F(x_i, y_i)$$

$F(x_0, y_0)$ is the concentrated load value at (x_0, y_0) .

iv) Stress matrix:

Because the selected position function is third order, the stress in the triangular element is not a constant. In order to quantitatively specify stress, the stress at the center of each element is used to represent it. The equation is:

$$\begin{Bmatrix} \sigma_x \\ \sigma_y \\ \tau_{xy} \end{Bmatrix} = \pm \left(\frac{\bar{E}(t_i + t_j + t_m)}{18(1-\bar{\mu}^2)} + \frac{(\bar{E} - \bar{E})\bar{t}^3}{6(1-\bar{\mu}^2)\bar{t}^3} \right) \begin{bmatrix} 1 & 1 & 1 & \bar{\mu} & \bar{\mu} & \bar{\mu} & 0 & 0 & 0 \\ \bar{\mu} & \bar{\mu} & \bar{\mu} & 1 & 1 & 1 & 0 & 0 & 0 \\ 0 & 0 & 0 & 0 & 0 & 0 & \frac{1-\bar{\mu}}{2} & \frac{1-\bar{\mu}}{2} & \frac{1-\bar{\mu}}{2} \end{bmatrix} [F] \{\delta\} \quad (2-16)$$

where \bar{t} is the thickness of the inner layer, \bar{t} is the thickness at the center of an element, i.e. $(1/3) \cdot (5_i + t_j + t_m)$.

III. COMPUTATION PROGRAMMING

1. Original data information:

1) Constants:

AA - Number of free nodes; BB - number of fixed nodes;
D - number of triangular elements, EE - number of beam elements;
FF - number of concentrated loads; GG - number of triple-layer elements; QQ - parameter used in determination of the beam element model which is selected as 1, 2, 3, 4 and 5 according to the sequence listed in Table 2-1; HH - parameter used in the selection of height equation. If the height is obtained using a special equation (as presented in Example 1), then $HH = 1$. Otherwise, it can be any other integer ($HH \neq 1$), if the input of higher level information HE is required; EF - elastic modulus

of the outer layer of the triple-layer plate; EC - elastic modulus of the inner layer of the triple-layer plate; U - Poisson ratio of the material.

2) Numbering group:

- | | |
|---------------------|--|
| ME [1:DD, 1:3] | - Numbering system of the nodes of a triangular element (on the xoy plane, the nodes are numbered in counter-clockwise direction). |
| NE [1:EE, 1:2] | - Numbering of nodes of beam elements (the origin is selected at node i, and node j is along the \overline{ox} axis). |
| XE [1:AA + BB, 1:2] | - Coordinates of nodes (x, y). |
| HE [1:AA + BB] | - Coordinate of nodes (z). |
| MET [1:DD] | - Thickness of outer layer of triple-layer plate. |
| NET [1:EE, 1:2] | - Thickness of beam element at nodal point. |
| PA [1:FF, 1:3] | - Concentrated load signal (X,Y,F). |

2. Sequence of input data:

AD-A115 866

FOREIGN TECHNOLOGY DIV WRIGHT-PATTERSON AFB OH
RECENT SELECTED PAPERS OF NORTHWESTERN POLYTECHNICAL UNIVERSITY--ETC(U)
AUG 81

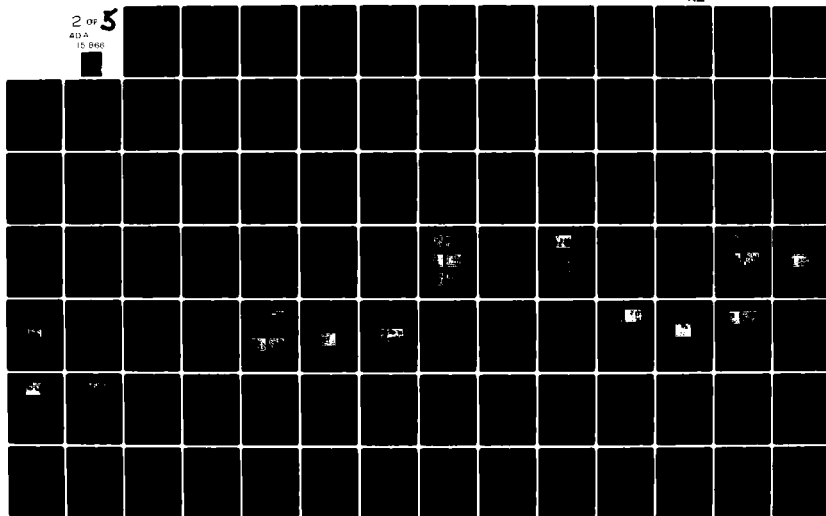
F/G 20/4

UNCLASSIFIED

FTD-ID(RS)T-0260-81-PT-2

NL

2 OF 5
413-4
15 068



- (1) AA, BB, DD, EE, FF, GG, QQ, HH;
- (2) EF, EC, U;
- (3) XE, PA;
- (4) ME;
- (5) NET; (no input if beam element is not there)
- (6) NE; (no input without beam element)
- (7) MET; (no input without triple-layer plate element)
- (8) HE; (no input if the height is determined using existing process in the program.)

3. Sequence of input results:

- (1) If a height determination program is used, type HE [1:AA + BB].
- (2) Type PE for a load at free node; PO for a load at fixed node.
- (3) Type DKM for row width of the general stiffness matrix; KK for the number of one-dimensional element symbol of the general stiffness matrix; DYZ for the column number of the first non-zero element in the reaction force matrix, the column number of the last non-zero element and the one-dimensional sequence number of the first non-zero element in the same matrix; YY for the number of one-dimensional

numbering elements in the reaction force matrix.

- (4) Type number of plate element and the elements of the stiffness matrix of the last plate element.
- (5) Type number of beam element and the elements of the stiffness matrix of the last beam element.
- (6) Type of results of deflection. There are AA sections and each contains three deflection components.
- (7) Type of results of reaction forces and total reaction force.
- (8) Type of stress of plate elements and total stress.
- (9) Type of stress of beam elements.

4. Storage and solution of linear equations.

The elements of the stiffness matrix are stored according to the one-dimensional numbering order of the variable band width. The linear equations are solved using the Choleski method. The programs are edited from those introduced in reference [4].

The above description applies to both plane stress and plate bending models.

IV. EXAMPLES

Example 1.

A wing is constructed with two solid plates (upper and

lower) with radial reinforcement of beams. Rivets are used to fasten the two plates at the middle of each beam. The thickness of the plate varies from thick to thin outward. The plane projection shape is a trapezoid. The cross-section shapes are like a symmetric wing formed by the two second-order curves describing the upper and lower plates. In the middle of the base of the wing, there are five comb-shaped joints. Two more auxiliary joints are located at the front and back of the wing as shown in Figure 4-1.

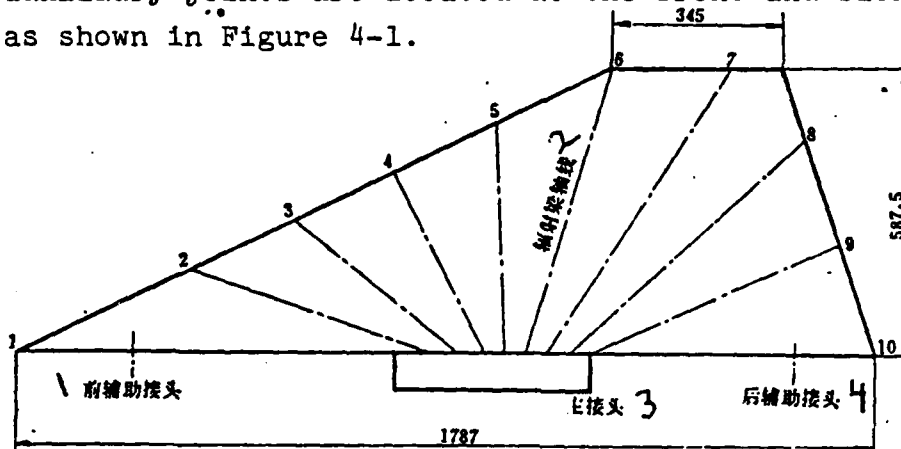


Figure 4-1: 1) front auxiliary joint; 2) radial beam axis; 3) main joint; 4) back auxiliary joint.

This wing can be solved using both plane stress as well as plate bending models. When the latter is used, it is considered that the wing is formed by the upper and lower plates and empty space in between. As long as the straight normal line assumption is satisfied, the triple-layer plate bending theory can be used to obtain solutions. Now that there are ten reinforcing radial beams in the empty middle layer and the upper and lower plates are connected into a solid body using rivets along the center of the beams, under such conditions it can be approximated that the wing stress satisfies the straight normal line assumption. In dividing into elements, the vertex of every triangular element and its opposite side should be located on the center line of

two neighboring radial beams. Certain relations exist among a finite number of elements. Every triangle forms a unit with its upper and lower triangular plates, which receive the stress together with a beam element. Experimental results and theoretical calculation both showed that it is feasible.

If solutions are sought using the triple-layer plate bending model, because the middle layer is empty, we can let $\bar{E} = 0$ in Equation (2-13). Then (2-12) becomes:

$$[\bar{\mathcal{F}}] + [\bar{\mathcal{F}}'] = \frac{\bar{E}}{12(1-\bar{\mu}^2)} \begin{bmatrix} [R] - [\bar{R}] & \bar{\mu}([R] - [\bar{R}]) & [0] \\ \bar{\mu}([R] - [\bar{R}]) & [R] - [\bar{R}] & [0] \\ [0] & [0] & \frac{1-\bar{\mu}}{2}([R] - [\bar{R}]) \end{bmatrix}$$

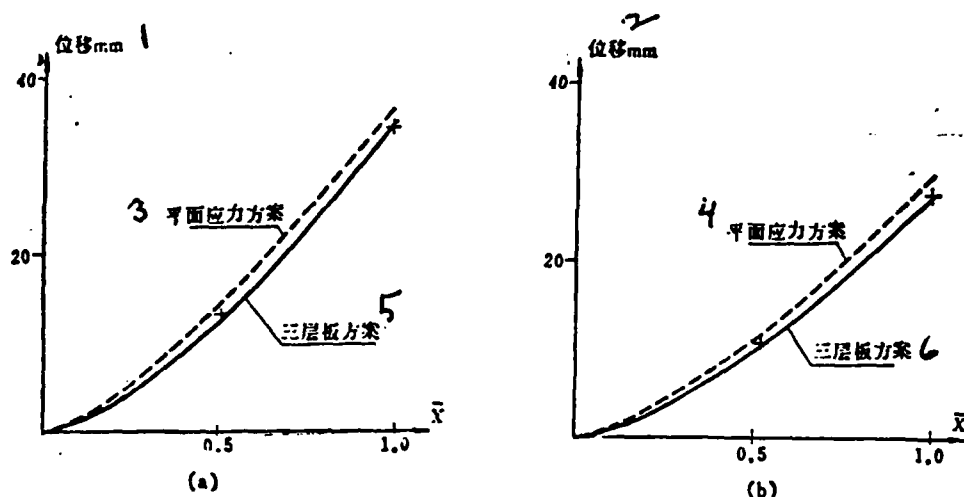


Figure 4-2.

Key: 1), 2) : deflection; 3), 4) : plane stress case; 5), 6) : triple-layer plate case.

Based on the requirement in the general program, the symbols for the fixed nodes come last. This is to facilitate the use of boundary conditions to eliminate the oddness of the general stiffness matrix.

Some of the results are shown in Figure 4-2, which shows the calculated (from both models) and experimental nodal deflec-

tions for the 6th (Figure 4-2a) and 7th (Figure 4-2b) beams.

The errors are rather insignificant* and generally less than 5%. It was found that the results obtained using the plate bending model were closer to the experimental values. The above also applies to the calculations of other nodal deflections, and they will not be repeated in detail.

Example 2.

A wing has a double-beam honeycomb laminated structure. Its shape is a right angle trapezoid. The front edge is slanted backward and its cross-section is a flat plate. The rear and middle beams are located at the rear edge of the wing. At the base of the beam, there are two fixed support joints A and B. An auxiliary joint C is situated at the front of the wing. It is shown schematically in Figure 4-3.

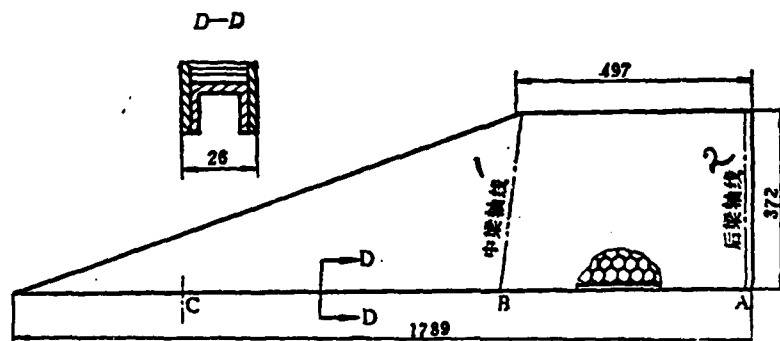


Figure 4-3: 1) middle beam axis; 2) rear beam axis.

Let us simplify this wing and use a triple-layer plate bending model to obtain a solution. Since the inside of the wing

* For easier comparison, the calculated values include the nodal deflections due to the displacement of the base and rotation during experiments.

is a honeycomb structure, the stiffness matrix (2-12) can be applied directly. Part of the calculated results are shown in the figure below.

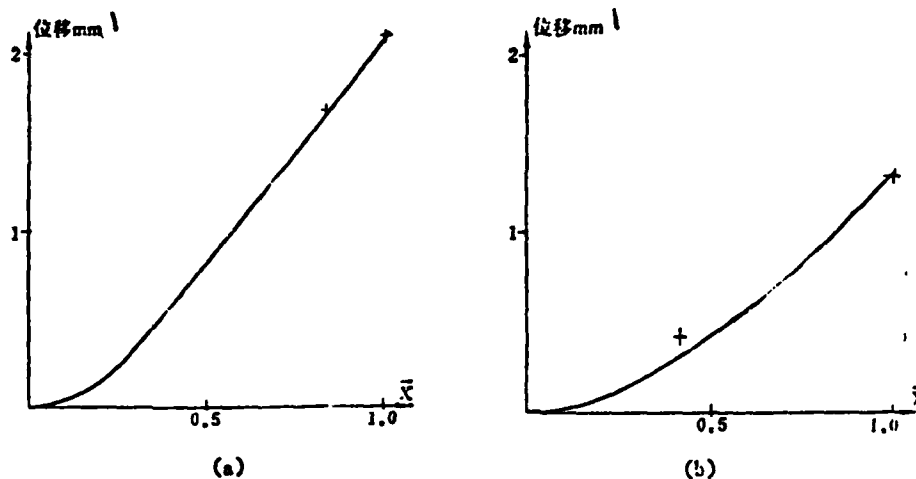


Figure 4-4.
1) deflection, mm

The calculated and experimental values of nodal deflections along the middle beam (Figure 4-4a) and rear beam (Figure 4-4b) are shown. The errors are within 5%. The remaining calculations are very similar and will not be presented.

Example 3.

A wing is made of solid structure. The horizontal projection is rectangular with one corner cut off from the rear tip of the wing. The cross-section is hyperbolic. The base is fastened at point ϕ 19 in Figure 19. The wing is schematically shown in Figure 4-5.

This wing can be solved using the plate bending model.

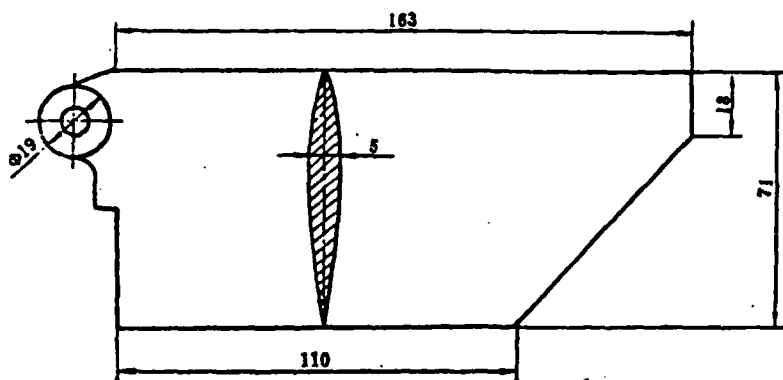


Figure 4-5.

Since it is solid, the elastic modulus of the middle layer is identical to that of the outer layers; Equation (2-12) can be used to obtain the solution. Part of the calculated results are shown in Figure 4-6. It shows the calculated and experimental nodal deflection values along the front (Figure 4-6a) and rear (Figure 4-6b) edges. The error is again about 5%. The other results are the same and will not be presented.

In addition, we used both models to solve the box-beam example in reference [1]. Results indicated that the calculated values are very close to those listed in that paper. The plane stress model seems to render better results.

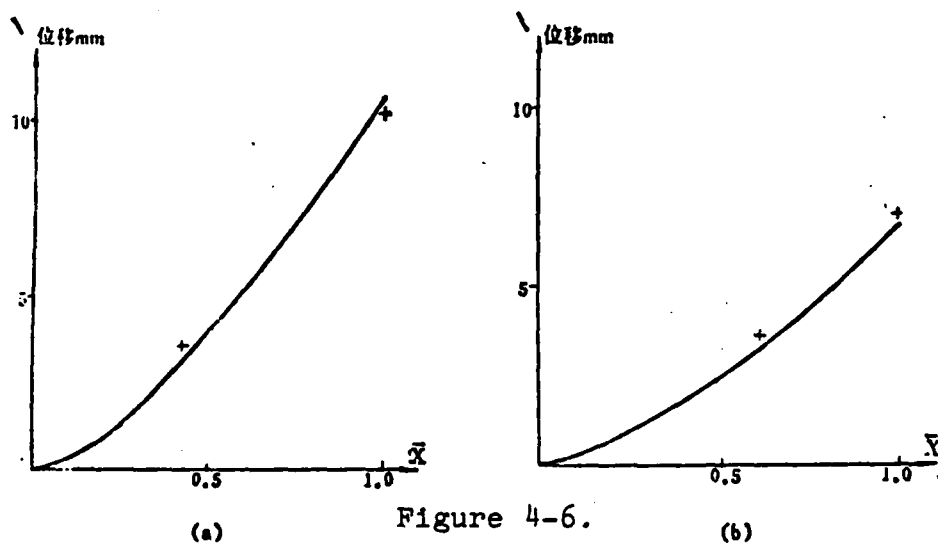


Figure 4-6.
1) deflection, mm

V. CONCLUSIONS

1. This paper introduced the equations and programs applicable to the estimation of static strength of wings, including solid plates and various laminated structures. Calculated and experimental nodal deflections differ by less than 5%. The values of nodal deflections obtained using both models are smooth across the wing which is close to experimental findings. Therefore, it may be concluded that both models reflect the physical properties of the problem.

2. For wings which can be simplified using either model, it was found from calculations that the plate bending model provides better results for wings with high strength, while the plane stress model is better for softer wings.

APPENDIX

STIFFNESS MATRIX OF A RECTANGULAR CROSS-SECTION

As shown in Figure A-1, for a rectangular cross-section beam element with nodal points i and j, it is possible to derive the stiffness matrix using the unit load method. The corresponding nodal forces to w , θ_x and θ_y are Q , M_x and M_y , respectively.

I. The displacement at i end and its relationships with external force.

When the nodal force is exerted on the end point of the beam i:

$$\begin{aligned}
w_1 &= \int_0^l \frac{M_{10} M_Q}{EI(x)} dx + \int_0^l \frac{M_{10} M_{M_1}}{EI(x)} dx + \int_0^l \frac{K Q_{10} Q_Q}{GF(x)} dx \\
&= \frac{Q_1}{E} \int_0^l \frac{x^2 dx}{I(x)} + \frac{M_{Y_1}}{E} \int_0^l \frac{x dx}{I(x)} + \frac{K Q_1}{G} \int_0^l \frac{dx}{F(x)}
\end{aligned}$$

where $K = 1.5$, $I(x)$ and $F(x)$ are parameters of the cross-section which vary with x . If

$$\begin{aligned}
c'_0 &= F_1 \int_0^l \frac{dx}{F(x)}, & c_0 &= \frac{KEI_1}{GF_1} c'_0, \\
c_{11} &= I_1 \int_0^l \frac{x^2 dx}{I(x)}, & c_{12} &= I_1 \int_0^l \frac{x dx}{I(x)},
\end{aligned}$$

The equation can be rewritten as:

$$w_1 = \frac{Q_1}{EI_1} (c_{11} + c_0) + \frac{M_{Y_1}}{EI_1} c_{12} \quad (A-1)$$

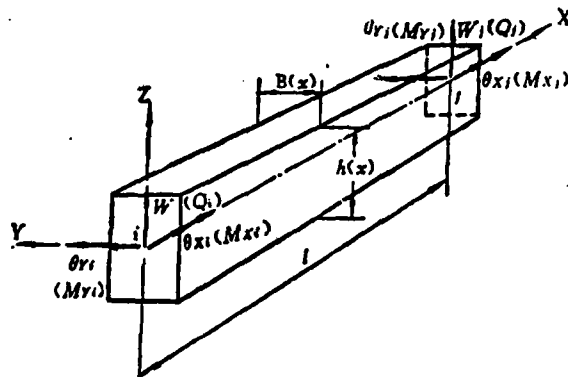


Figure A-1.

The angular change of the 1 end due to the nodal force is:

$$\begin{aligned}\theta_{11} &= \int_0^l \frac{M_{11x} M_Q}{EI(x)} dx + \int_0^l \frac{M_{11x} M_{11x}}{EI(x)} dx \\ &= \frac{Q_1}{E} \int_0^l \frac{x dx}{I(x)} + \frac{M_{11}}{E} \int_0^l \frac{dx}{I(x)} = \frac{Q_1}{EI_1} c_{12} + \frac{M_{11}}{EI_1} c_{11}\end{aligned}\quad (A-2)$$

where

$$c_{11} = I_1 \int_0^l \frac{dx}{I(x)}.$$

The expressions of M_{1Q} , M_Q derived from the above equation are shown in Figure A-2:

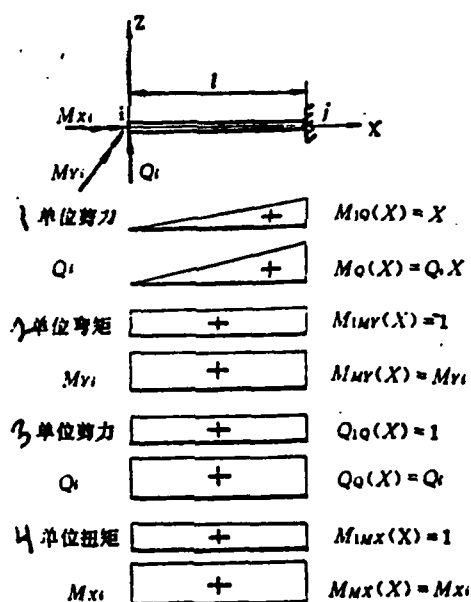


Figure A-2: 1) unit shear force; 2) unit torque; 3) unit shear force; 4) unit torque.

The angular displacement of the 1 end of the beam is:

$$\theta_{11} = \int_0^l \frac{M_{11x} M_{11x}}{GJ(x)} dx = \frac{M_{11}}{G} \int_0^l \frac{dx}{J(x)} = \frac{M_{11}}{GJ_1} c_{11}\quad (A-3)$$

(A-3) can also be written as:

$$M_{s1} = \frac{GJ_s}{c_{33}} \theta_{s1} \quad (A-4)$$

From (A-1) and (A-2) we get:

$$\begin{Bmatrix} w_1 \\ \theta_{y1} \end{Bmatrix} = \frac{1}{EI_1} \begin{bmatrix} c_{11} + c_0 & c_{12} \\ c_{12} & c_{11} \end{bmatrix} \begin{Bmatrix} Q_1 \\ M_{y1} \end{Bmatrix}$$

The inverse is:

$$\begin{Bmatrix} Q_1 \\ M_{y1} \end{Bmatrix} = \frac{EI_1}{D} \begin{bmatrix} c_{11} & -c_{12} \\ -c_{12} & c_{11} + c_0 \end{bmatrix} \begin{Bmatrix} w_1 \\ \theta_{y1} \end{Bmatrix} \quad (A-5)$$

where

$$D = \begin{vmatrix} c_{11} + c_0 & c_{12} \\ c_{12} & c_{11} \end{vmatrix}$$

Based on equilibrium conditions:

$$\begin{aligned} Q_2 &= -Q_1, \\ M_{y2} &= -M_{y1} - Q_1 l, \\ M_{s2} &= -M_{s1}. \end{aligned}$$

From the above and (A-5) we obtain:

$$Q_2 = -\frac{EI_1}{D} (c_{12} Q_{y1} - c_{11} w_1) \quad (A-6)$$

$$M_{y2} = -\frac{EI_1}{D} [(c_{11} - l c_{12}) w_1 + (l c_{12} - c_{22} - c_0) \theta_{y1}] \quad (A-7)$$

From the equilibrium conditions and (A-4), we get:

$$M_{s2} = -\frac{GJ_s}{c_{33}} \theta_{s2} \quad (A-8)$$

From (A-4) through (A-8), we get:

$$\begin{Bmatrix} Q_i \\ M_{xi} \\ M_{yi} \\ Q_j \\ M_{xj} \\ M_{yj} \end{Bmatrix} = \begin{bmatrix} \alpha c_{11} & 0 & -\alpha c_{12} \\ 0 & \beta & 0 \\ -\alpha c_{12} & 0 & \alpha(c_{22} + c_0) \\ -\alpha c_{11} & 0 & \alpha c_{12} \\ 0 & -\beta & 0 \\ \alpha(c_{12} - lc_{12}) & 0 & \alpha(lc_{12} - c_{22} - c_0) \end{bmatrix} \begin{Bmatrix} w_i \\ \theta_{xi} \\ \theta_{yi} \end{Bmatrix} \quad (\text{A-9})$$

where

$$\alpha = \frac{EI_i}{D}, \quad \beta = \frac{GJ_i}{c_{22}}.$$

II. The displacement at j end and its relationship with external forces.

When the nodal force is exerted onto the j end:

$$\begin{aligned} w_j &= \int_0^l \frac{M_{10}M_0}{EI(x)} dx + \int_0^l \frac{M_{10}M_{y1}}{EI(x)} dx + \int_0^l \frac{KQ_{10}Q_0}{GF(x)} dx \\ &= \frac{Q_j}{E} \int_0^l \frac{(l^2 - 2lx + x^2)}{I(x)} dx + \frac{M_{y1}}{E} \int_0^l \frac{(x-l)}{I(x)} dx + \frac{KQ_l}{G} \int_0^l \frac{dx}{F(x)} \end{aligned}$$

Using the symbols described above, this equation can be written as:

$$w_j = \frac{Q_j}{EI_i} (l^2 c_{11} - 2lc_{12} + c_{22} + c_0) + \frac{M_{y1}}{EI_i} (c_{12} - lc_{11}) \quad (\text{A-10})$$

The angular displacements:

$$\begin{aligned}\theta_{x1} &= \int_0^l \frac{M_{1xy} M_{x0}}{EI(x)} dx + \int_0^l \frac{M_{1xy} M_{xy}}{EI(x)} dx = \frac{Q_1}{E} \int_0^l \frac{(x-l)}{I(x)} dx + \frac{M_{x1}}{E} \int_0^l \frac{dx}{I(x)} \\ &= -\frac{Q_1}{EI_1} (c_{12} - l c_{11}) + \frac{M_{x1}}{EI_1} c_{11}\end{aligned}\quad (A-11)$$

and

$$\theta_{x1} = \int_0^l \frac{M_{1xy} M_{xy}}{GJ(x)} dx = \frac{M_{x1}}{G} \int_0^l \frac{dx}{J(x)} = \frac{M_{x1}}{GJ_1} c_{33} \quad (A-12)$$

$$M_{x1} = \frac{GJ_1}{c_{33}} \theta_{x1} \quad (A-13)$$

The expressions for M_{1Q} , M_Q as described in the above equation are shown in Figure A-3.

Let us repeat what we did before, and then we get:

$$\begin{Bmatrix} Q_1 \\ M_{x1} \\ M_{y1} \\ Q_1 \\ M_{x1} \\ M_{y1} \end{Bmatrix} = \begin{bmatrix} -\alpha c_{11} & 0 & \alpha(c_{12} - l c_{11}) \\ 0 & -\beta & 0 \\ \alpha c_{12} & 0 & \alpha(l c_{12} - c_{22} - c_0) \\ \alpha c_{11} & 0 & \alpha(l c_{11} - c_{12}) \\ 0 & \beta & 0 \\ \alpha(c_{11} - c_{12}) & 0 & \alpha(l^2 c_{11} - 2l c_{12} + c_{22} + c_0) \end{bmatrix} \begin{Bmatrix} w_1 \\ \theta_{x1} \\ \theta_{y1} \end{Bmatrix} \quad (A-14)$$

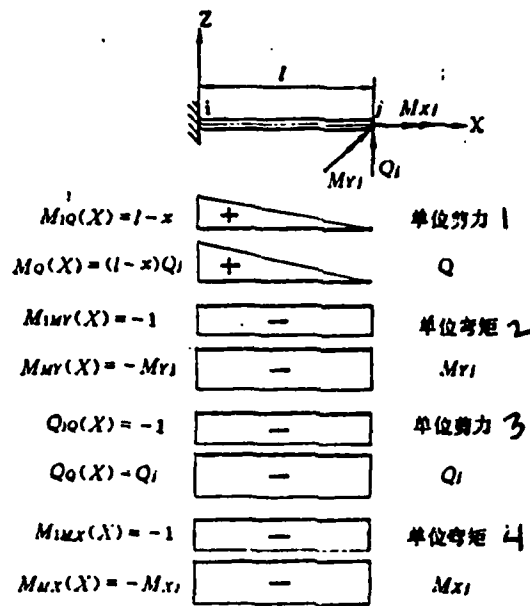


Figure A-3: 1), 3) unit shear force; 2), 4) unit torque.

III. STIFFNESS MATRIX OF THE BEAM ELEMENT

From (A-1) through (A-14), it is possible to obtain the equation for the stiffness of the beam element as:

$$\begin{Bmatrix} Q_1 \\ M_{r1} \\ M_{r1} \\ Q_2 \\ M_{r2} \\ M_{r2} \end{Bmatrix} = \begin{bmatrix} \alpha c_{11} & 0 & -\alpha c_{12} & -\alpha c_{11} & 0 & \alpha(c_{12} - lc_{11}) \\ \beta & 0 & 0 & -\beta & 0 & 0 \\ & \alpha(c_{22} + c_0) & \alpha c_{12} & 0 & \alpha(lc_{12} - c_{22} - c_0) & \\ \text{对} & & -\alpha c_{11} & 0 & \alpha(lc_{11} - c_{12}) & \\ & \text{称} & & \beta & 0 & \\ & & & & \alpha(l^2c_{11} - 2lc_{12} + c_{22} + c_0) & \end{bmatrix} \begin{Bmatrix} w_1 \\ \theta_{r1} \\ \theta_{r1} \\ w_2 \\ \theta_{r2} \\ \theta_{r2} \end{Bmatrix} \quad (A-15)$$

IV. THE BEAM COEFFICIENTS OF VARIOUS PARAMETERS

1. Beam with constant width B and linearly varying height $h(x)$:

$$\text{Beam height } h(x) = h_1 + \frac{x}{l} (h_j - h_1)$$

$$\text{Let } a = h_1/h_j, \text{ then } h(x) = h_j (a + bx) \text{ where } b = \frac{1-a}{l}.$$

$$\text{Moment of inertia } I(x) = \frac{Bh^3(x)}{12} = \frac{Bh_j^3}{12} (a + bx)^3 = I_j (a + bx)^3$$

$$\text{Cross-section area } F(x) = B \cdot h(x) = Bh_j(a + bx) = F_j(a + bx)$$

$$c_{11} = I_j \int_0^1 \frac{dx}{I(x)} = \int_0^1 \frac{dx}{(a + bx)^3} = \frac{l(1+a)}{2a^3},$$

$$c_{12} = I_j \int_0^1 \frac{x dx}{I(x)} = \int_0^1 \frac{x dx}{(a + bx)^3} = \frac{l^2}{2a^2},$$

$$c_{13} = I_j \int_0^1 \frac{x^2 dx}{I(x)} = \int_0^1 \frac{x^2 dx}{(a + bx)^3} = \frac{l^3}{(1-a)^3} \left(\ln \frac{1}{a} - \frac{a^2}{2} + 2a - \frac{3}{2} \right),$$

$$c_0' = F_j \int_0^1 \frac{dx}{F(x)} = \int_0^1 \frac{dx}{a + bx} = \frac{l \ln a}{a-1},$$

$$c_0 = \frac{KEI_j}{GF_j} c_0' = \frac{KEI_j}{GF_j} \frac{l \ln a}{a-1}.$$

2. Beam with constant width B and height varying with the square root.

$$\text{Beam height } h^2(x) = h_1^2 + \frac{x}{l} (h_j^2 - h_1^2)$$

$$\text{or } h(x) = h_j \left\{ \left(\frac{h_1}{h_j} \right)^2 + \frac{x}{l} \left[1 - \left(\frac{h_1}{h_j} \right)^2 \right] \right\}^{\frac{1}{2}} = h_j (r + bx)^{\frac{1}{2}}$$

$$r = \left(\frac{h_1}{h_j} \right)^2, \quad b = \frac{1-r}{l}.$$

$$\text{Moment of inertia } I(x) = \frac{Bh^3(x)}{12} = \frac{Bh_j^3}{12} (r + bx)^{\frac{3}{2}} = I_j (r + bx)^{\frac{3}{2}},$$

$$\text{Cross-section area } F(x) = Bh(x) = Bh_j (r + bx)^{\frac{1}{2}} = F_j (r + bx)^{\frac{1}{2}}$$

Therefore
$$c_{11} = I_1 \int_0^1 \frac{dx}{I(x)} = \int_0^1 \frac{dx}{(r+bx)^{1/2}} = \sqrt{\frac{2l}{r(1+\sqrt{r})}}$$

Let $a = h_i/h_j$, 则 $c_{11} = \frac{2a}{a(1+a)}$

$$c_{12} = I_1 \int_0^1 \frac{x dx}{I(x)} = \int_0^1 \frac{x dx}{(r+bx)^{3/2}} = \frac{2l^2}{(1+\sqrt{r})^2} = \frac{2l^2}{(1+a)^2},$$

$$c_{22} = I_1 \int_0^1 \frac{x^2 dx}{I(x)} = \int_0^1 \frac{x^2 dx}{(r+bx)^{3/2}} = \frac{l^3}{(1-a^2)^2} \left(\frac{2}{3} - 4a^2 + \frac{16}{3}a^3 - 2a^4 \right),$$

$$c_0' = F_1 \int_0^1 \frac{dx}{F(x)} = \int_0^1 \frac{dx}{(r+bx)^{1/2}} = \frac{2l}{1+a},$$

$$c_0 = \frac{KEI_1}{GF_1}, c_0' = \frac{KEI_1}{GF_1} \frac{2l}{1+a}.$$

3. Beam with constant width B and height varying with the cube root (linearly changing moment of inertia).

Beam height $h^3(x) = h_1^3 + \frac{x}{l} (h_j^3 - h_1^3)$ or

$$h(x) = h_j (r + bx)^{1/3}$$

where $r = (h_i/h_j)^3, b = (1-r)/l$

Moment of inertia
$$I(x) = \frac{Bh^3(x)}{12} = I_1(r+bx),$$

Cross-section area
$$F(x) = Bh(x) = F_1(r+bx)^{1/3}$$

Therefore
$$c_{11} = I_1 \int_0^1 \frac{dx}{I(x)} = \int_0^1 \frac{dx}{r+bx} = \frac{\ln r}{r-1} l = \frac{\ln a^3}{a^3-1} l,$$

$$c_{12} = I_1 \int_0^1 \frac{x dx}{I(x)} = \int_0^1 \frac{x dx}{r+bx} = \frac{l^2}{(1-r)^2} (1-r+r \ln r)$$

$$\begin{aligned}
&= \frac{l^3}{(1-a^2)^2} (1 - a^2 + a^2 \ln a^2) \\
c_{11} &= I_1 \int_0^1 \frac{x^2 dx}{I(x)} = \int_0^1 \frac{x^2 dx}{r+bx} = \frac{l^3}{(1-r)^2} \left(\frac{1}{2} - 2r + \frac{3}{2} r^2 - r^2 \ln r \right), \\
&= \frac{l^3}{(1-a^2)^2} \left(\frac{1}{2} - 2a^2 + \frac{3}{2} a^2 - a^2 \ln a^2 \right), \\
c_0' &= F_1 \int_0^1 \frac{dx}{F(x)} = \int_0^1 \frac{dx}{(r+bx)^{1/2}} = \frac{3l}{2(1-r)} (1-r^{1/2}) = \frac{3l}{2(1-a^2)} (1-a^2), \\
c_0 &= \frac{KEI_1}{GF_1} c_0' = \frac{KEI_1}{GF_1} \frac{3l(1-a^2)}{2(1-a^2)^2}
\end{aligned}$$

4. Beam with linearly changing width $B(x)$ and constant height h (linearly changing moment of inertia)

$$\text{Beam width } B(x) = B_1 + \frac{x}{l} (B_j - B_1)$$

$$\text{Let } a_1 = B_1/B_j$$

$$\text{Then } B(x) = B_j (a_1 + b_x) \text{ where } b = \frac{1-a_1}{l}$$

$$\text{Moment of inertia } I(x) = \frac{B(x)h^3}{12} = \frac{h^3 B_j}{12} (a_1 + bx) = I_1 (a_1 + bx),$$

$$\text{Cross-section area } F(x) = hB(x) = hB_j(a_1 + bx) = F_1(a_1 + bx)$$

Therefore

$$\begin{aligned}
c_{11} &= I_1 \int_0^1 \frac{dx}{I(x)} = \int_0^1 \frac{dx}{a_1 + bx} = \frac{\ln a_1}{a_1 - 1} l, \\
c_{12} &= I_1 \int_0^1 \frac{x dx}{I(x)} = \int_0^1 \frac{x dx}{a_1 + bx} = \frac{l^2}{(1-a_1)^2} (1 - a_1 + a_1 \ln a_1), \\
c_{22} &= I_1 \int_0^1 \frac{x^2 dx}{I(x)} = \int_0^1 \frac{x^2 dx}{a_1 + bx} = \frac{l^3}{(1-a_1)^2} \left(\frac{1}{2} - 2a_1 + \frac{3}{2} a_1^2 - a_1^2 \ln a_1 \right), \\
c_0' &= F_1 \int_0^1 \frac{dx}{F(x)} = \int_0^1 \frac{dx}{a_1 + bx} = \frac{\ln a_1}{a_1 - 1} l, \\
c_0 &= \frac{KEI_1}{GF_1} c_0' = \frac{KEI_1}{GF_1} \frac{\ln a_1}{a_1 - 1} l.
\end{aligned}$$

5. Equal cross-section beam.

Let's choose a or a' to be 1, we get:

$$\begin{aligned} c_{11} &= 1, \\ c_{12} &= l^2/2, \\ c_{22} &= l^2/3, \\ c_3 &= \frac{KEI_1}{GF_1} l. \end{aligned}$$

For all the above cases, $J(x) = J_j (a_2 + bx)$, $a_2 = J_1/J_j$,

$$b = \frac{1-a^2}{l}$$

$$c_{33} = J_j \int_0^l \frac{dx}{J(x)} = \int_0^l \frac{dx}{a_2 + bx} = \frac{\ln a_2}{a_2 - 1} l$$

if $a_2 = 1$ then $c_{33} = 1$.

REFERENCES

[1] Turner, M. G., Clough, R. W., Martin, H. C., and Topp, I. J., «Stiffness and Deflection Analysis of Complex Structures», J. A. S., 1956, Vol. 23, No. 9, pp. 805-823.

[2] Przemienicki, J. S., «Theory of Matrix Structural Analysis», McGraw Hill Book Company, 1968.

[3] Slyphes, H. A., «Development of Explicit Stiffness and Mass Matrices for a Triangular plate Element», Inter. J. of Solids and Structures, 1969, Vol. 5, No. 3, pp. 241-249.

[4] Cao Zhihao, Fudan Journal (Journal of Physical Sciences), 1974, No. 1.

Summary

THE MATRIX ANALYSIS OF WINGS

Xu Yuzan, Zhu Runxiang, Jiang Jinqing and Cai Yinlin

In the design of flight vehicles, the calculation of static strength of wings is indispensable. In general, the methods of analysis for wings of different constructions differ from each other. Even for wings of the same type of construction, the tedious calculation processes have to be repeated, because their shapes and dimensions are different.

In this paper, the plate-beam wing constructions are simplified either as plane stress or as plate bending models. For plane stress model, it is assumed that during bending and torsion the cover plates are in plane stress and the beams carry the shear forces, with the bending and torsional rigidities of the beams accounted for by equivalent additional cover plates. As the wings are usually symmetric with respect to its middle plane and the external load is usually antisymmetric, it suffices to analyze half of the wing. For plate bending model, it is assumed that both plates and beams can resist bending, torsion and shear.

In addition to applying the well-known element stiffness matrix of plane stress, this paper introduces triangular element matrix of laminated plate and the element stiffness matrix of the beam of axially-variable rectangular cross-section. This paper also gives two general programs for calculations by computers. As numerical examples, this paper calculates the deflections and stresses of the wing consisting of plates and beams, the wing with honeycomb core and the solid wing. The computation results are in good agreement with results of experiments specially conducted for the purpose of verifying the

proposed methods of analysis. The errors in the nodal deflections are generally not more than 5%. The formulas and programs introduced by this paper are fairly satisfactory in accuracy and generality. For the wing consisting of plates and beams as well as the box beam of reference [1], both of the above-mentioned models are used to make computations. It appears that, for stiffer wings, the selection of plate bending model gives better results, while in the case of flexible wings, the other model is preferable.

To proceed with calculations, only the original data need be prepared, all the rest will be quickly completed by the computer. Thus the design period can be considerably shortened. This paper is of some value in designing different types of wing constructions.

On a Method for the Determination of Plane Stress Fracture
Toughness K_{Ic} of 30 CrMnSiNi2A Steel and Some Related Problems

Cui Zhenyuan, Zheng Changqing, Shi Jize and 15 Students

During the past two decades, there has been significant /63
progress in the development of fracture mechanics. Especially
in the treatment of problems in linear fracture mechanical
plane, very mature techniques have been developed. However,
the determination of plane stress fracture toughness K_{Ic} (which
is of particular concern in aerospace technology) has not
been properly resolved over a long period of time. Inter-
nationally, it was not until 1976 that the American Society for
Testing and Materials (ASTM) officially issued a recommended
trial experimental procedure [1]. Compared with the existing
experimental method for the determination of plane strain
fracture toughness K_{Ic} , it is not mature enough. Nevertheless,
a preliminary method is finally available. There are many
institutions in our country working on the determination of K_{Ic} .
Much effort has been devoted to this area; however, more research
is still needed on this topic. We have to invest efforts and
time in order to derive a better experimental method to deter-
mine K_{Ic} to be used in our country.

We began our work in 1975 due to a request from the user.
Experiments have been carried out to determine K_{Ic} for various
materials, and we obtained some data and results. Owing to
the space limitations, this paper presents some experimental
results with 30CrMnSiNi2A steel using reference [1] as a guide
to further analyse the problem. It also includes a discussion
of some of the key problems in the determination of K_{Ic} using
CCT samples as the test vehicle.

I. The Analysis of Results on the Determination of K_c for 30CrMnSiNi2A Steel

The theory, procedures and symbols commonly used in the determination of K_c are described in detail in existing literatures [1] [3]. The original data and records related to the determination of K_c for 30CrMnSiNi2A steel need not be described in detail here. Based on need as the discussion progresses, some of the major results are presented in corresponding sections of this paper.

The sample used was a Center-Cracked Tension (CCT) specimen made of 30CrMnSiNi2A steel (see Figure 1), with width $W = 100\text{mm}$, total length $l = 324\text{ mm}$, in the L-T direction. The two ends of the specimen were drilled with five holes each (in two rows) to be fastened onto clamps. The nominal yield point

$\sigma_s = 124\text{ kg/mm}^2$, strength point $\sigma_s = 169\text{ kg/mm}^2$, true fracture strain $\sigma_f = 249\text{ kg/mm}^2$, and elastic modulus

$E = 20700\text{ kg/mm}^2$. The thickness was chosen based on the requirement of a user unit at 3, 5, 8, and 10 mm. COD method was used to determine the effective crack length at any instance corresponding to a load. Based on the COD-P* original recorded curve, R curve (i.e. the resistance of the material against the propagation of cracks), when the crack propagates slowly in a steady-state then its value is equal to the crack propagating force G , and the K_r curve (which is another expression for resistance of materials against crack propagation). During slow steady-state crack propagation, its value, equal to the stress intensity factor K in the region near the tip of the crack, can be obtained.

* COD represents the tension at the installation point of the displacement meter along sides of the crack. The installation point is located at the longitudinal symmetry line, and it is also symmetrical with respect to the crack.

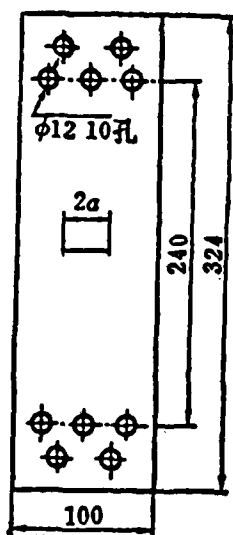


Figure 1

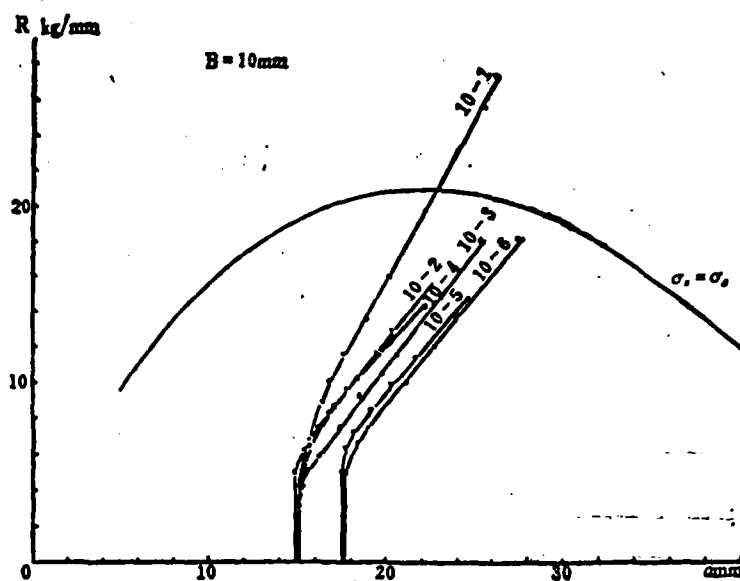


Figure 2(a)

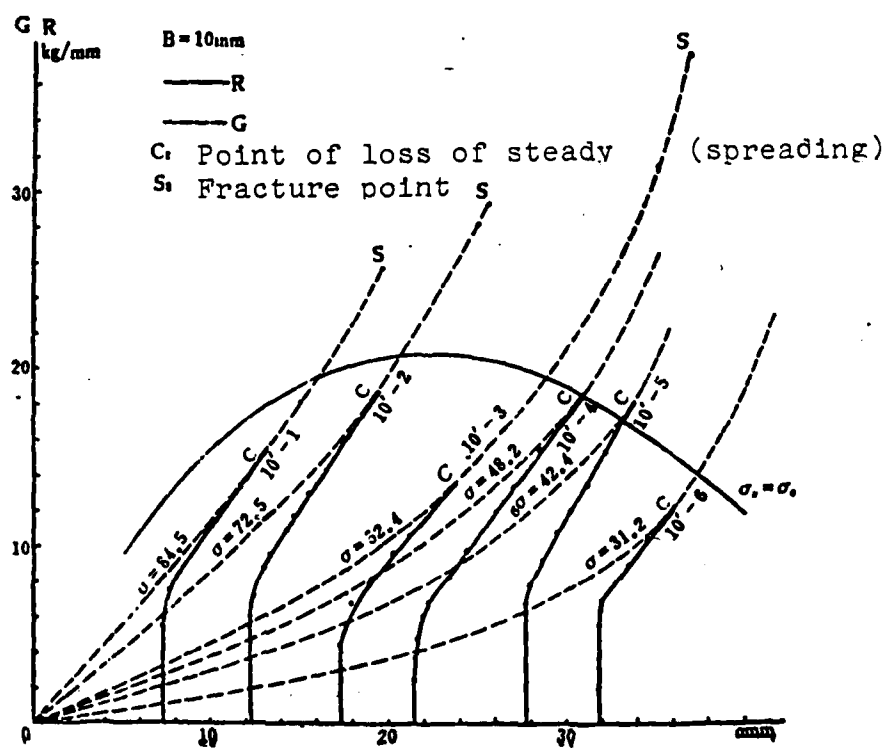


Figure 2(b)

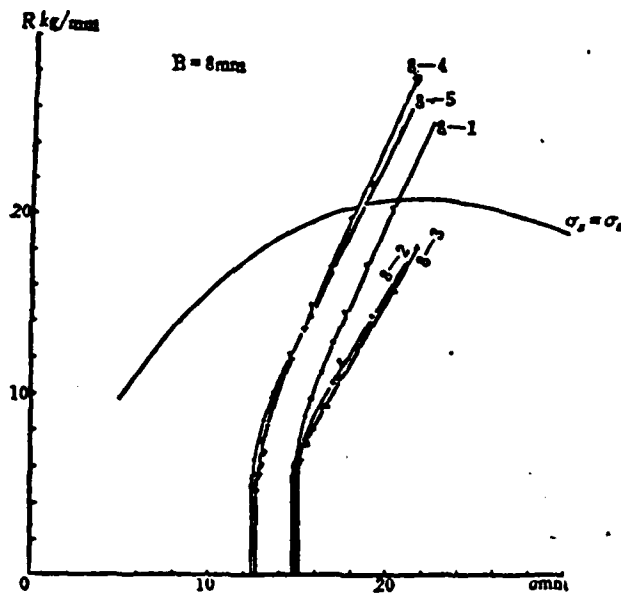


Figure 2(c)

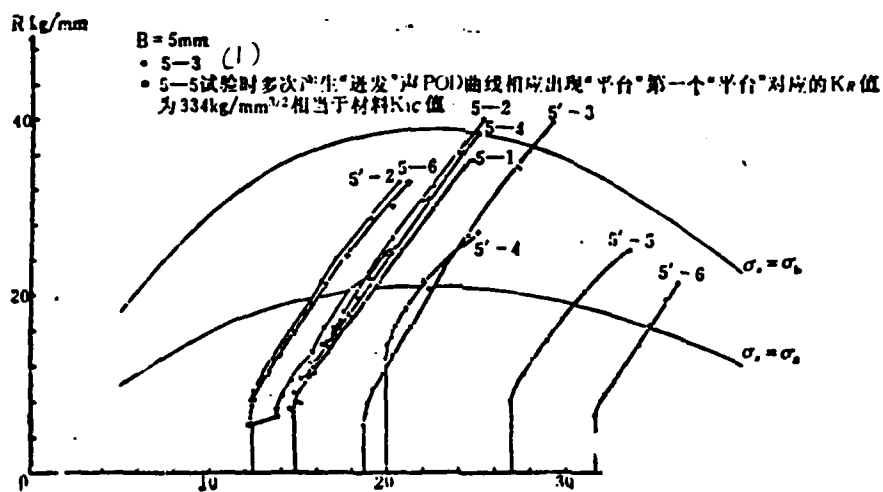


Figure 2(d)

Key: (1) 5-5 experiment often resulted in the production of "popping" sound, POD curve showed a "plateau". The first plateau has a corresponding K_R value equal to $334 \text{ kg/mm}^{3/2}$ which is equivalent to the K_{IC} value of the material.

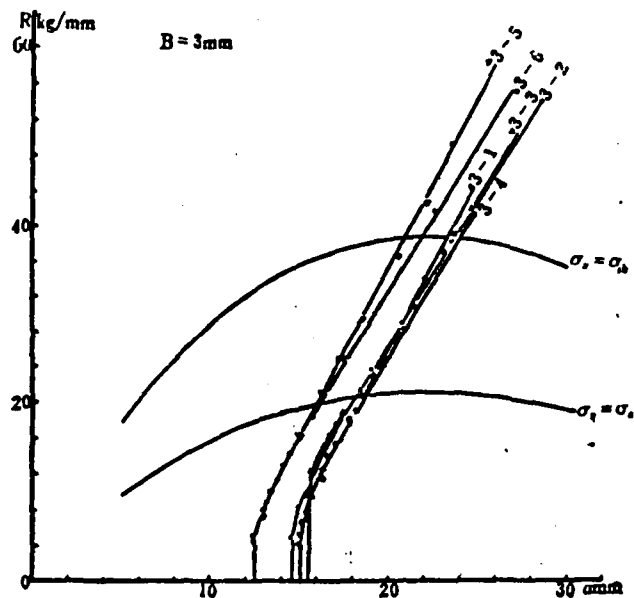


Figure 2(e) curve

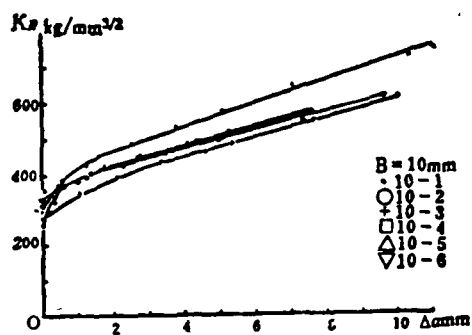


Figure 3(a)

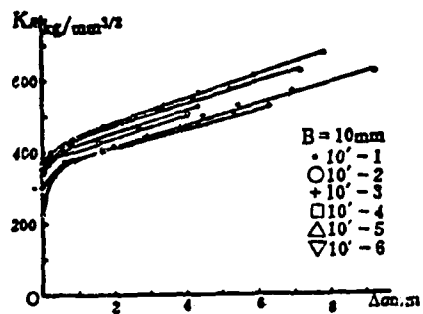


Figure 3(b)

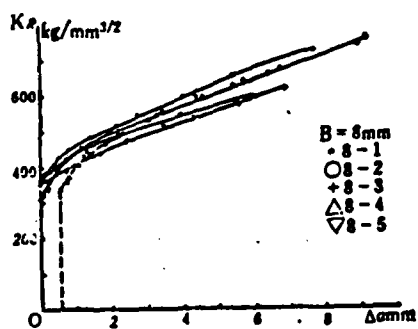


Figure 3(c)

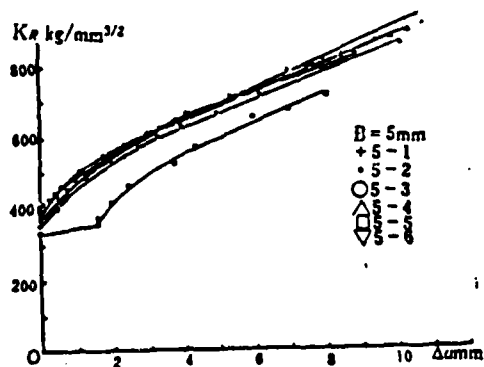


Figure 3 (d)

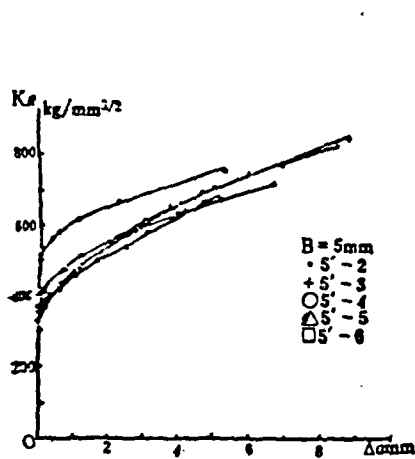


Figure 3(e)

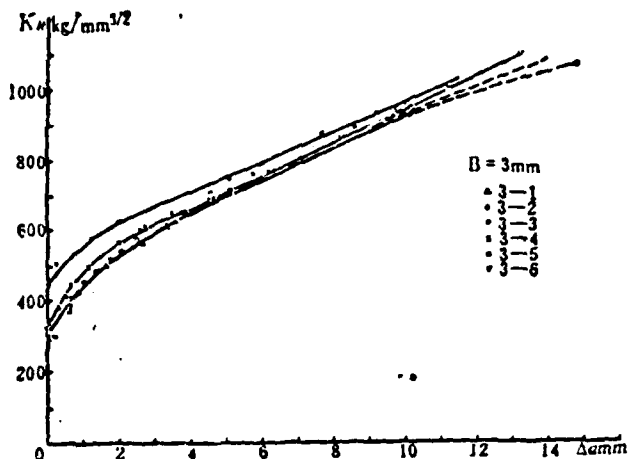


Figure 3(f) K_R Curve

The R (or K_R) curve totally demonstrated the development of resistance of materials against crack propagation (or toughness) under continuously increasing crack propagation force G (or stress intensity factor K) for cracked specimens. The intersection of the critical crack propagation force curve and the R curve is the unsteady propagating point of the crack. The K_R value corresponding to that point is the plane stress fracture toughness K_c . Point C in Figures 2 and 3 is the crack unsteady propagation point (for clarity, the G curve is only shown in Figure 2 (b)). In other figures, the end of the R curve is the point C. This corresponds to the point C^1 on the curve P-COD (see Figure 4) at which the curve becomes horizontal). The values of K_c are listed in Table 1. It must be pointed out that the crack length used to obtain K_c was the effective crack length (i.e., initial crack length $2a$ + actual crack propagation $2\Delta^a$ + effective propagation in plastic region $2r_y$). A correction was also made between the crack length obtained using the initial slope of the P-COD curve and the initial crack length of the sample [1].

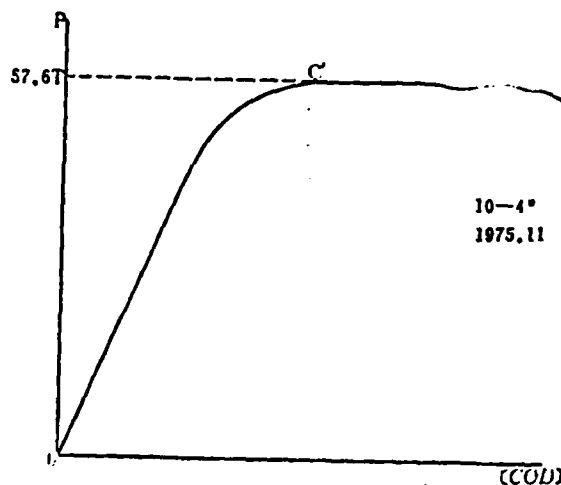


Figure 4

How can one judge the validity of the K_c value obtained? There are many explanations. We believe that the key is that the stress on the net cross-section (after subtracting the size of effective cracks) is $\sigma_N < \sigma_s$. Based on this assumption, it is possible to draw an equi-stress line $\sigma_N = \sigma_s$ in Figure 2. The $\sigma_N = \sigma_s$ curves are shown in Figures 2(a) - (e). In order to concentrate all the results, we indicated all the K_c values on the plane formed by the two coordinates σ_c (gross stress) and $2a_c$ (see Figure 5). The two straight lines in Figure 5 represent the net cross-section lines $\sigma_N = \sigma_s$ and $\sigma_N = \sigma_b$, respectively. From Figures 2 and 5, the data on K_c for the 3 and 5 mm samples are invalid, because their corresponding σ_N exceeded σ_s . The 3 mm specimens all have σ_N greater than σ_b . For the 8 mm thick samples, two are valid, while the other 3 are invalid. It appears that the width of the plane is not sufficient. As for the 10 mm thick samples they all are supposed to agree with the $\sigma_N < \sigma_s$ condition. Therefore, all ten of them should be valid. However, two of them were found to be invalid due to $\sigma_N > \sigma_s$. Why? Taking samples 10-1, 10-2, 10-3, and 10-4 and measuring the hardness, the HRC values are 45, 48, 48.5 and 48.5 with corresponding σ_b

TABLE 1

| Sample Number | Bmm | Wmm | $2a_0/W$ | $2a_c/W$ | $\sigma_c \text{ kg/mm}^2$ | $K_c \text{ kg/mm}^{3/2}$ |
|---------------|-------|------|----------|----------|----------------------------|---------------------------|
| 3-1 | 2.95 | 99.7 | 0.291 | 0.494 | 91.8 | 961 |
| 3-2 | 3.16 | 99.7 | 0.292 | 0.571 | 90.7 | 1085 |
| 3-3 | 2.96 | 99.7 | 0.309 | 0.541 | 90.2 | 1025 |
| 3-4 | 3.07 | 99.7 | 0.302 | 0.496 | 88.5 | 928 |
| 3-5 | 3.00 | 99.7 | 0.248 | 0.513 | 101.6 | 1098 |
| 3-6 | 3.14 | 99.7 | 0.248 | 0.545 | 97.0 | 1088 |
| 5-1 | 5.06 | 99.6 | 0.295 | 0.500 | 80.8 | 855 |
| 5-2 | 4.88 | 99.4 | 0.295 | 0.513 | 84.9 | 910 |
| 5-3 | 5.08 | 99.6 | 0.293 | 0.483 | 83.8 | 863 |
| 5-4 | 4.85 | 99.5 | 0.297 | 0.505 | 83.4 | 892 |
| 5-5 | 5.03 | 99.6 | 0.244 | 0.405 | 81.8 | 718 |
| 5-6 | 5.06 | 99.6 | 0.249 | 0.428 | 89.3 | 823 |
| 5'-2 | 5.07 | 99.6 | 0.246 | 0.415 | 91.8 | 825 |
| 5'-3 | 5.07 | 99.5 | 0.374 | 0.591 | 73.5 | 908 |
| 5'-4 | 5.07 | 99.5 | 0.400 | 0.507 | 70.1 | 749 |
| 5'-5 | 4.90 | 99.4 | 0.543 | 0.678 | 50.5 | 721 |
| 5'-6 | 4.84 | 99.5 | 0.637 | 0.742 | 42.8 | 676 |
| 8-1 | 8.14 | 99.4 | 0.299 | 0.455 | 72.9 | 721 |
| 8-2 | 8.15 | 99.3 | 0.305 | 0.424 | 65.5 | 596 |
| 8-3 | 8.15 | 99.3 | 0.298 | 0.438 | 65.4 | 616 |
| 8-4 | 8.12 | 99.4 | 0.252 | 0.432 | 80.4 | 758 |
| 8-5 | 8.16 | 99.3 | 0.249 | 0.429 | 78.4 | 732 |
| 10-1 | 9.95 | 100. | 0.303 | 0.523 | 67.8 | 751 |
| 10-2 | 10.10 | 99.2 | 0.305 | 0.460 | 58.5 | 566 |
| 10-3 | 10.15 | 99.6 | 0.305 | 0.508 | 57.6 | 611 |
| 10-4 | 10.13 | 99.5 | 0.298 | 0.446 | 57.0 | 545 |
| 10-5 | 10.09 | 99.8 | 0.352 | 0.492 | 53.6 | 555 |
| 10-6 | 10.10 | 99.7 | 0.355 | 0.550 | 53.2 | 612 |
| 10'-1 | 10.11 | 99.5 | 0.146 | 0.234 | 84 | 525 |
| 10'-2 | 10.09 | 99.5 | 0.245 | 0.390 | 72.2 | 622 |
| 10'-3 | 10.02 | 99.7 | 0.346 | 0.474 | 52.4 | 527 |
| 10'-4 | 10.19 | 99.6 | 0.431 | 0.616 | 47.5 | 616 |
| 10'-5 | 9.95 | 100. | 0.554 | 0.703 | 42.6 | 656 |
| 10'-6 | 10.12 | 99.5 | 0.638 | 0.722 | 31.0 | 502 |

as 148, 163.5, 166 and 166 kg/mm², respectively. The heat treatment for individual specimen was not controlled rigorously which led to a low σ_b for specimen 10-1. It did not reach the required value, and therefore produced high K_c values which should be deleted.

From ten 10mm thick samples with $\sigma_s < \sigma_b$, the average value of K_c is 568 kg/mm^{3/2}.

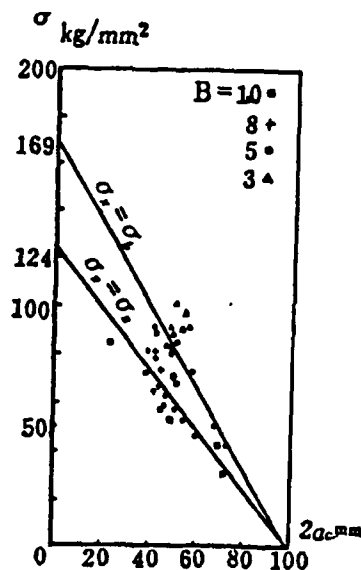


Figure 5

II. Concerning the Calibration Curve

In the determination of K_c using the COD method, the first key problem encountered is the precise measurement of the calibration curve which is the $\frac{E[COD]}{\sigma W} \sim \frac{2a}{W}$ curve (σ is the gross stress). It is related to the ratio of the dimensions of the plane L/W and the ratio of the distance between the two installa-

tion points of the displacement meter (2Y) and with Y/W. The curve shown in Figure 6 was obtained using 5 and 10 mm samples with 2Y = 3 mm.

The determination of this curve requires much time and effort. First a series of samples with various $\frac{2a}{W}$ will have to be prepared which adds significantly to the work load. During the past years, researchers have been seeking an analytical expression applicable to the situation. It appears that the following equation derived by H. Liebowitz and recommended by ASTM committee E24 is most accurate:

$$\frac{E[COD][\#1]}{\sigma W} = 2 \left[\frac{\pi a/W}{\sin(\pi a/W)} \right]^{1/2} \left\{ \frac{2W}{\pi Y} \cosh^{-1} \left[\frac{\cosh(\pi Y/W)}{\cos(\pi a/W)} \right] - \frac{1+\mu}{\left[1 + \left(\frac{\sin(\pi a/W)}{\sinh(\pi Y/W)} \right)^2 \right]^{1/2} + \mu} \right\} \frac{Y[\#2]}{W} \quad (1)$$

(validity range $0.2 \leq \frac{2a}{W} \leq 0.8$; $\frac{Y}{W} \leq 0.5$)

Footnotes for Equations.

[1] [COD] is a commonly used symbol. It no longer represents the displacement at the tip of the crack. Instead, it is the displacement between the two displacement monitors. It actually should be expressed as [2v] to make it more accurate.

[2] The original paper mistook $\frac{Y}{W}$ as the exponent. For the $\left[\frac{\sin(\pi a/W)}{\sinh(\pi Y/W)} \right]^{\mu}$ term, it does not affect the outcome whether "2" or "1" is chosen.

where μ is the Poisson ratio.

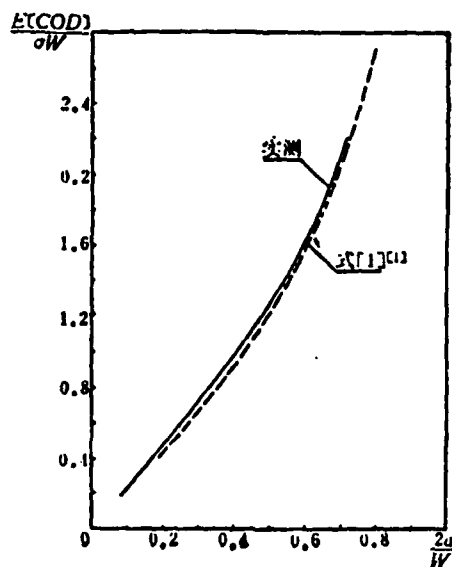


Figure 6

The results obtained using equation (1) are shown in Figure 6 as the dotted line. It is very close to the experimental results (shown as the solid curve). Therefore, this equation is reliable to a certain degree. Until more advanced treatment is attained, this equation can be used to express the calibration curve. It is worthwhile noticing that the theoretical curve lies to the right of the actual measured curve. It tends to overestimate the dimensions of the crack, and makes the experimental results less safe. For improved precision, convenience, and safety, it is possible to precisely determine the calibration curve experimentally using a number of standard samples or it is also possible to improve the theoretical analysis of the $\frac{E[COD]}{\sigma W}$ equation.

/70

III. The Selection of Geometrical Correction Factor F and Sample Length to Width Ratio L/W

1. Infinite Long Plane:

The stress intensity factor K can be expressed in general as:

$$K = \sigma \sqrt{\pi a} F\left(\frac{a}{W}, \frac{L}{W}, \dots\right) \quad (2)$$

For center-cracked tension specimens, when the plate becomes infinite, the geometric correction factor $F\left(\frac{a}{W}, \frac{L}{W}\right)$ is simplified to $F\left(\frac{2a}{W}\right)$. Under this condition, there are still many expressions for F. The relatively early solution by Irwin - Westergaard is:

$$F\left(\frac{2a}{W}\right) = \sqrt{\frac{W}{\pi a} \tan \frac{\pi a}{W}}, \quad (3)$$

It is still being used at this moment. It is not very accurate; even when $\frac{2a}{W} \leq 0.5$, the error reaches 5%.

It is commonly recognized that the most accurate value for $F\left(\frac{2a}{W}\right)$ is the Isida solution obtained numerically using 36 terms in the series expansion of $\left(\frac{2a}{W}\right)^2$ [4, 5, 6]. The values are listed in Table 2. The approximate expression for these values is [15, 16]:

$$F\left(\frac{2a}{W}\right) = \left[1 - 0.025\left(\frac{2a}{W}\right)^2 + 0.06\left(\frac{2a}{W}\right)^4\right] \sqrt{\sec \frac{\pi a}{W}}$$

This equation is different from the Isida results by only 0.1% when $\frac{2a}{W} \leq 0.9$.

Table 2

| $\frac{2a}{W}$ | $F(2a/W)$ | | | |
|----------------|--------------|-------|--------|------|
| | <i>Isida</i> | (3) | (4) | (5) |
| 0.0 | 1.0000 | 1.000 | 1.0000 | 1.00 |
| 0.1 | 1.0060 | 1.001 | 1.0062 | 1.00 |
| 0.2 | 1.0246 | 1.017 | 1.0254 | 1.02 |
| 0.3 | 1.0577 | 1.040 | 1.0594 | 1.06 |
| 0.4 | 1.1094 | 1.076 | 1.1118 | 1.12 |
| 0.5 | 1.1867 | 1.130 | 1.1892 | 1.20 |
| 0.6 | 1.3033 | 1.208 | 1.3049 | 1.30 |
| 0.7 | 1.4982 | 1.336 | 1.4841 | 1.42 |
| 0.8 | 1.8160 | 1.565 | 1.7989 | 1.56 |
| 0.9 | 2.5776 | 2.116 | 2.5283 | 1.72 |

Two more simple and accurate expressions are [7]:

$$F\left(\frac{2a}{W}\right) = \sqrt{\sec \frac{\pi a}{W}} \quad (4)$$

$$F\left(\frac{2a}{W}\right) = \left[1 - 0.1\left(\frac{2a}{W}\right) + \left(\frac{2a}{W}\right)^2\right] \quad (5)$$

The corresponding values are also listed in Table 2. The error of equation (4) is less than 1% when $2a/W \leq 0.8$ (only 0.3% when $2a/W \leq 0.7$). Equation (5) has a maximum error of 1% at $2a/W \leq 0.6$.

2. The Selection of Sample Length to Width Ratio L/W .

In relation an "infinitely long" specimen does not exist. However, when the length to width ratio L/W exceeds a certain number, the sample can be treated as an "infinitely long" specimen without losing the accuracy required. Infinitely long specimens not only can use the simple correction factor

$F\left(\frac{2a}{W}\right)$ instead of $F\left(\frac{2a}{W}, \frac{L}{W}\right)$, but also have more relaxed boundary conditions (uniform stress and uniform strain). The commonly used samples in the determination of K_c are very wide. Due to the limitations of space in experimental apparatus, it is more desirable to have a smaller L/W ratio. Therefore, more strict clamping conditions (for even stress on both ends) are required.

From the available literatures [5], [6], [8], [9] (using Isida's results), if the uniform stress boundary condition is assured, then the F value when $L/W = 1.5$ is considered to be the same as that at $L/W = \infty$ (The difference is less than 2% when $\frac{2a}{W} \leq 0.6$). Therefore, $L/W = 1.5$ can be considered as infinite.

It is pointed out in reference [1] that, when the width W is less than 300 mm using a single clamp, the sample length L should at least be $2W$. For $W \geq 300$ mm samples, using multiple clamps, L can be decreased to not less than $1.5 W$. These requirements seem to be marginal. If conditions allow, multiple clamps should be used for samples with $W \leq 300$ mm. All our specimens came multiple clamped with $L/W > 2$ which already exceeded the above requirement. /72

The existing practical problem is that due to the limited space inside the testing apparatus, in some cases with wider samples $L/W > 1.5$ cannot be met. Can samples with $L/W < 1.5$ be used? What are the effects on the determination of the R curve and K_c ? How much is the error? These are yet to be studied further.

IV. The Determination of Specimen Width W

1. Minimum Specimen Width and Suggested Specimen Width

Until this moment, throughout the world researchers have adopted the semi-empirical result obtained by Feddersen [10] which is that the minimum width of the specimen should be

$$W_{min} = 27r_y \div 4.29 \left(\frac{K_s}{\sigma_s} \right)^2 \quad (6)$$

crack dimension: $2a = \frac{1}{3} W_{min} \div 1.43 \left(\frac{K_s}{\sigma_s} \right)^{2.2} \quad (7)$

The required corresponding critical stress (gross stress)

$$\sigma_s \leq \frac{2}{3} \sigma_s \quad (8)$$

In reality it requires that the stress on the net cross-section $\sigma_s \leq \sigma_s$. Equation (6) is very simple and accurate. However, the original meaning [10] of "minimum" did not actually suggest that $27 r_y$ is the real "minimum width." The above equation was obtained using the infinitely large plane expression:

$$K = \sigma \sqrt{\pi a}$$

which means $F\left(\frac{2a}{W}\right) = 1$.

The above discussed "minimum plate width" problem can be solved as follows:

For a finite width (assuming the specimen is long enough to be considered as infinitely long) there exist:

$$K = \sigma \sqrt{\pi a} F\left(\frac{2a}{W}\right) \quad (9)$$

The gross stress σ in the above equation can be replaced by the net cross-section stress σ_N by the relation:

$$\sigma = \sigma_N \left(1 - \frac{2a}{W}\right) \quad (10)$$

Substituting (10) into (9), we get

$$\frac{K}{\sigma_N \sqrt{W}} = f\left(\frac{2a}{W}\right) = \left(1 - \frac{2a}{W}\right) \sqrt{\frac{\pi a}{W}} F\left(\frac{2a}{W}\right) \quad (11)$$

Since it is required that $\sigma_N \leq \sigma_s$, therefore

$$W \geq K^2 / \sigma_s^2 f^2 \quad (12)$$

The minimum width is
$$W_{\min} = \frac{1}{f_{\max}^2} \left(\frac{K_s}{\sigma_s}\right)^2 \quad (13)$$

Graphically solving f_{\max} with $\frac{2a}{W} \approx 0.44$, we get $f_{\max} \approx 0.53$. Substituting it into (13), we get /73

$$W_{\min} = 3.56 \left(\frac{K_s}{\sigma_s}\right)^2 \quad (14)$$

Comparing to Feddersen's result [10], it is 17% lower.

Table 3 lists several values of $f\left(\frac{2a}{W}\right) = \left(1 - \frac{2a}{W}\right) \sqrt{\frac{\pi a}{W}} F\left(\frac{2a}{W}\right)$ for reference and calibration. The correction factor $F\left(\frac{2a}{W}\right)$ was taken from Isida's results (Table 2). The individual data was calculated using a slide rule by the authors. They have sufficient accuracy with respect to the problems under discussion.

Table 3

| $2a/W$ | 0.1 | 0.2 | 0.3 | 0.4 | 0.44 | 0.45 | 0.5 | 0.6 | 0.7 | 0.8 | 0.9 |
|------------------------------|-------|-------|-------|-------|-------|-------|-------|-------|-------|-------|-------|
| $f\left(\frac{2a}{W}\right)$ | 0.358 | 0.459 | 0.507 | 0.527 | 0.530 | 0.529 | 0.525 | 0.506 | 0.468 | 0.417 | 0.307 |

From Table 3 and relevant figures (not shown in this paper), the value f is relatively "flat" near its maximum. In the region $\frac{2a}{W} \approx 0.38 \sim 0.5$, the change f is approximately 1%. This is very advantageous for the determination of K_c . From equation (12), as long as the width of the plate is 2% larger than W_{\min} (because $W \propto 1/f^2$), it is possible to determine the value of K_c in the region where $\frac{2a}{W} \approx 0.38 \sim 0.5$ (if $\sigma_N \approx \sigma_s$ is acceptable, when the required σ_N is lower, a similar argument can be derived).

If the σ_s and W of the tested material are known, the maximum value of K_c can be determined using equation (14). For 30CrMnSiNi2A steel samples, it is known that $\sigma_s = 124 \text{ kg/mm}^2$, and $W = 100 \text{ mm}$. It can be achieved that $K_{\max} = 656 \text{ kg/mm}^{3/2}$. Any higher values become invalid.

The minimum width defined by equation (14) corresponds to $\frac{2a}{W} \approx 0.44$. In practice it is not possible to control it that precisely. There is a tolerable range. The net cross-section stress σ_N is also too high if it reaches σ_s . Therefore, the practical plate width must be several times larger than W_{\min} . Considering all the factors and assuming $\sigma_N \leq 0.8\sigma_s$, then we get

$$W = 1.56 W_{\min} = 5.55 \left(\frac{K_c}{\sigma_s} \right)^2 \approx 35r, \quad (15)$$

In the design of the specimen, if the K_c/σ_s value is estimated, then the sample width can be calculated using equation (15). Table 4 lists several examples with our suggested values using the data available in reference [1].

| $K_c/\sigma_s \text{ mm}^{1/2}$ | 2.5 | 5.0 | 7.5 | 10 | 15 |
|---------------------------------|------|-----|-----|-----|------|
| 1 $W[(15)\text{式}] \text{ mm}$ | 34.8 | 139 | 312 | 558 | 1250 |
| 2 $W[\text{建议值}] \text{ mm}$ | 75 | 150 | 300 | 600 | 1300 |
| $W^{(1)*} \text{ mm}$ | 76 | 152 | 305 | 508 | 1219 |

Key: (1) W [Equation (15)] mm.

(2) W [suggested value] mm.

* Original paper in imperial units. Now they are converted to decimal units.

The recommended plate width in Reference [1] was derived using the thoughts presented in paper [10]. Basically it used $W_{\min} = 27r_y$, and then multiplied the result by a factor (e.g. 1.5) and further rounded off the result in inches (towards smaller values). The listed values were 1.2 - 1.3 times of those obtained by calculating $27r_y$ 1.2~1.3 ($K_c/\sigma_s = 2.5 \text{ mm}^{1/2}$ is the only exception). From Table 4, the recommended plate width in reference [1] is very consistent with that derived from equation (15). Reference [1] only provided a vague requirement that $\sigma_s < \sigma_s$, and it failed to recommend an equation to be used to calculate the plate width. As for $K_c/\sigma_s = 10$ and $15 \text{ mm}^{1/2}$, we suggest that the plate width be a little larger. It not only takes into account the rounding off of the calculation using (15), but also shows that the fabrication and testing of large size samples are not easy in order to further enhance the validity of the experiment. /74

2. The Selection of Relative Length of Incipient Crack $\frac{2a_0}{W}$

The effect of the relative length of an incipient crack $\frac{2a_0}{W}$ on the determination of K_c is not well defined. It appears that it is related to the properties of the material tested. Now let us show the experimental results of a 10 mm thick 30CrMnSiNi2A steel in Figure 7 with coordinates K_c and

$K_c - \frac{2a_0}{W}$. From Figure 7, if the scattered region of K_c is $\bar{K}_c \pm 10\%$ then only nine data points are within the limits. The value of K_c is $576 \pm 51 \text{ kg/mm}^{3/2}$. When $\frac{2a_0}{W}$ is in the region of $0.15 \sim 0.43$, it did not affect the determination of K_c at all. It is proper to confine $\frac{2a_0}{W}$ in the $0.15 \sim 0.43$ range? As a rule of thumb, the following factors are still to be considered: For optional use of the plate width, when the width is constant, then $\frac{W-2a}{2}$ and $2a$ should be made as large as possible (relative to the radius of the plastic region r_y) to obtain valid results in the determination of K_c . It is also more desirable to make the net cross-section stress σ_N upon fracturing to be smaller than σ_s (correspondingly to make $\frac{2a_0}{W}$ approach 0.44). Considering crack propagation along the boundary, it commonly adopts $\frac{2a_0}{W} \leq \frac{1}{3}$. In this paper $\frac{2a_0}{W} \approx 0.3$. Reference [1] requires $\frac{2a_0}{W} = 0.3 \sim 0.35$; it appears to be feasible at the present time. But rigorously speaking, this requirement still needs to be investigated further. Based on the favorable region of $\frac{2a_0}{W}$ discussed above, it should be attempted to maintain the value of $\frac{2a_0}{W}$ in the range $0.38 \sim 0.50$. For more fragile materials, $\frac{2a_0}{W}$ may be selected to be larger (e.g. $0.33 \sim 0.40$). For more tough materials, $\frac{2a_0}{W}$ should be small such as $0.25 \sim 0.30$. From the data on 10 mm samples in Table 1, when $\frac{2a_0}{W} = 0.25 \sim 0.55$ the corresponding boundary expansion $(\frac{2a_c}{W} - \frac{2a_0}{W}) \approx 0.12 \sim 0.22$ (average 0.16). Therefore the most favorable is $\frac{2a_0}{W} \approx 0.25 \sim 0.30$ (or $0.22 \sim 0.34$ if the average value is used).

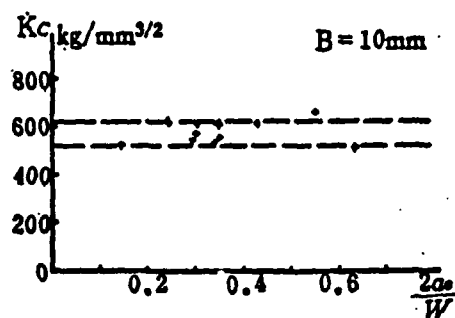


Figure 7

It is widely known that in the study of plane stress fracture toughness K_{Ic} [2] it is often emphasized that the sample crack length a , toughness band $(W-a)$ and thickness B must exceed $2.5(K_{Ic}/\sigma_s)^2$. Actually this requirement makes sure that the radius of the plastic region r_y is far less than crack length a , $(W-a)$, etc. Approximately $r_y/a \leq 1/15 \approx 1/50$, should ensure the validity of the elastic stress field around the crack determined by using K_I . Therefore, K_I can be the sole parameter to express the fracture process. How do we consider the above problem in the determination of K_{Ic} with plane stress? What should the dimensions of the specimen be to reflect this consideration? These are questions being avoided in the literature both domestically and abroad. Although we know this is a tough problem, yet we still bring it up for further discussion.

In the determination of K_{Ic} , except the fact that thickness B is not limited, other parameters need further consideration. If the requirement $r_y/a \leq 1/15$, still applies, under the thin plate condition r_y must be increased to 3 times that under the plane stress situation which means $a \geq 7.5(K_{Ic}/\sigma_s)^2$. For center-cracked tension specimens, the requirement becomes $2a \geq 15(K_{Ic}/\sigma_s)^2$. If the same requirement is imposed on the toughness band, then $W \approx 30 \sim 45(K_{Ic}/\sigma_s)^2$. Such dimensions are too large to be realized for most materials.

Now let us briefly review section IV or reference [1] and discuss the probable problems caused by $W \approx 35r_y$ and $r_y/a \approx 1/6$. Using Figures 51 and 52 in reference [1] and taking the plane $\theta = 0$ of the crack, we notice that the perpendicular direction crack stress σ_{yx} as determined by K_I is more than 10% off from the actual elastic stress σ_y . For a single-edge cracked tension specimen and excess loading

cracked specimen (when the plate width is the same as the center-cracked tension specimen, $r/a \approx 1/12$), the errors are 10% and 30%, respectively. Based on the above, the latter is inferior. These variations will affect the final determination of K_c and the effect will still have to be studied further.

The K_c values obtained to date still fluctuate significantly. Moreover, it usually increases with wider samples [11, 12]. Whether it is due to the fact that the plate width is not adequate is still to be determined.

VI. Conclusions

(1) This paper includes R curves obtained using 3, 5, 8 and 10 mm 30 CrMnSiNi2A steel samples under a variety of $\frac{2a_0}{W}$ conditions. They are of significant importance to the application of this material as well as to further research on techniques in the determination of R curves.

It is worthwhile pointing out from Figure 2 that the R curve for 30CrMnSiNi2A steel in all four thicknesses is composed of two sections apart from the initial vertical section, i.e., a transition curve section and a slanted straight line. Only the 5 mm thick sample behaved differently. When $\frac{2a_0}{W}$ varied from 0.146 to 0.638, the general shape of the R curve remained the same and did not change greatly as compared to the variation among all samples of the same thickness at $\frac{2a_0}{W} \approx 0.3$.

Figure 3 showed that the K_r values corresponding to the "incipient cracking" points are concentrated near $300 \text{ kg/mm}^{3/2}$. For Sample 5-5# $K_r = 334 \text{ kg/mm}^{3/2}$, a "popping" sound was heard. This corresponds to the K_{1c} value.

When plate thickness is 10 mm, the effective K_c value is $576 \pm 34 \text{ kg/mm}^{3/2}$ if $\sigma_s < \sigma_s$.

(2) The H. Liebowitz equation for the calibration curve as described in reference [1] is reasonably close to our experimental results. If an actual measured curve is not available, equation (1) can be used; however, it is on the unsafe side.

(3) When multiple loading clamp specimens are used, L/W can be reduced to 1.5. The geometrical correction factor F should follow equation (4) which is simple and accurate. When $L/W < 1.5$, F must be re-selected. The effect on the R curve and the determination of K_c is yet to be determined.

(4) The minimum specimen width as derived in this paper /76 is $W_{min} = 3.56 \left(\frac{K_c}{\sigma_s} \right)$ which is 17% less than Feddersen's previous result [10]. Based on this equation and under the conditions that the net cross-section stress $\sigma_s \leq 0.8 \sigma_s$, we are able to write the equation $W = 35r_s = 5.55 \left(\frac{K_c}{\sigma_s} \right)^2$. The calculated recommended values are listed in Table 4. The critical crack length should be controlled in the 0.38 ~ 0.50 range. The selected initial crack length $\frac{2a_s}{W}$ depends on the material. Until sufficient information is gathered, it is usually chosen to be 1/3.

(5) The fluctuation of the data on K_c is greater than that of K_{Ic} and usually increases with width. This problem is worth further investigation.

References

- [1] ASTM E561-76T Tentative Recommended Practice for R-Curve Determination, 1976 Annual Book of ASTM Standards, Part 10, pp. 539-557.
- [2] ASTM E399-74 Standard Test Method for Plane-Strain Fracture Toughness of Metallic Materials, 1976 Annual Book of ASTM Standards, Part 10, pp. 471-490.
- [3] Northwestern University of Technology, Mechanics Lab. Fracture toughness measurement principles and Methods, Nov. 1975, pp. 4-1 to 4-28.
- [4] Isida, M., Analysis of Stress Intensity Factors for the Tension of a Centrally Cracked Strip with Stiffened Edges, Eng. Fract. Mech., Vol. 5, No. 3, 1973, pp. 647-665.
- [5] Tada, H., Paris, P. and Irwin, G., The Stress Analysis of Cracks Handbook, 1973, pp. 2.1-2.2, p. 11.1.
- [6] Ishida Makoto, Analysis of elasticity of cracking and stress intensity factors, 1976, pp. 144-145, 150-153.
- [7] ASTM STP No. 410, 1966, pp. 77-79, p. 75.
- [8] Northwestern University of Technology, Mechanics Laboratory, cracking Mechanics Group, Introduction to Linear Elastic Cracking Mechanics, Apr. 1975, pp. 30.
- [9] Isida, M., Effect of Width and Length on Stress Intensity Factors of Internally Cracked Plates Under Various Boundary Conditions, Intern. J. Fract. Mech., Vol. 7, No. 3, 1971, pp. 301-316.
- [10] Feddersen, C. E., Evaluation and Prediction of the Residual Strength of Center Cracked Tension Panels, ASTM STP 486, 1971, pp. 50-78.
- [11] Feddersen, C. E., Hyler, W.S., Fracture & Fatigue-Crack Propagation Characteristics of 7075-T7351 Aluminum Alloy Sheet & Flat, AD-714019, Mar. 15, 1970.
- [12] Sullivan, A. M., Freed, C.N., A Review of the Plane-Stress Fracture Mechanics Parameter K_I Determined Using the Center-Cracked Tension Specimen, NRL Report 7460 or AD 757654.

On The Method for The Determination of Plane-Stress Fracture-Toughness K_{IC} of 30CrMnSiNi 2A Steel and some Related Problems

Cui Zhenyuan, Zheng Changqing, Shi Jize and 15 students

In this report, some experimental results on the R-curves of CCT sheet specimens made of 30CrMnSiNi 2A alloy steel are presented, and various aspects of the method for the determination of R-curves (including plane-stress fracture toughness K_{IC}) are discussed in some detail.

(1) In compliance with the stipulations of the user of the material, for the specimens with four different thicknesses of 3, 5, 8, and 10 mm., the values of $2a_0/W$ used are as follows: $2a_0/W \approx 0.15 \sim 0.64$ for thicknesses 5 and 10 mm, but $2a_0/W$ is only 0.25 or 0.30 for the other thicknesses. These results on R-curves are deemed to be of some reference value to users of the material and to further investigations in the method for the determination of R-curves.

Referring to figure 2, the authors believe it to be worth noticing that:

a) the R-curves of the 30CrMnSiNi 2A sheet specimens for all the thicknesses investigated generally consist of three different parts: namely, the initial vertical lines, the transition curves, and the final slanted straight lines, with only a few exceptions for the specimens of 5 mm. thickness.

b) When $2a_0/W$ (the ratio of initial crack length to width) varies from 0.15 to 0.64, all the R-curves are similar in shape, the differences between them being not greater than between those for specimens of the same thickness and of the same ratio $2a_0/W \approx 0.3$.

It can be seen from figure 3 that most of the K_{IC} values corresponding to the points of "incipient crack" (i.e., the points at which deviation from $\Delta a = 0$ begins) fall within $300 \sim 350 \text{ kg/mm}^{3/2}$. Among them specimen 5-5 "pops in" at $K_{IC} = 334 \text{ kg/mm}^{3/2}$ (the sound being audible), which corresponds to the K_{IC} value of the material.

Although many of the K_{IC} values obtained from this investigation are far from being valid (because the stress on the net section σ_A exceeds the yield point σ_s), these data are still of reference value to designers, because the dimen-

sions of the specimens are much the same as the dimensions of structural members actually used.

(2) A formula for minimum CCT specimen width is deduced for the determination of K_{IC} , i. e. $W_{min} \approx 3.56(K_{IC}/\sigma_A)^2$, which is about 17% less than that given by Feddersen^[10]. By requiring $\sigma_A \leq 0.8\sigma_{AS}$, then the formula for CCT specimen width should be $W \approx 35r_p = 5.55(K_{IC}/\sigma_A)^2$. It is advisable to control $2a_c/W$ (ratio of critical crack length to width) of specimens at about its optimum value 0.44 (not 1/3 as given by reference [10]), and a value within 0.38~0.50 can usually be employed. Thus, strictly speaking, different values of $2a_0/W$ (ratio of initial crack length to width) should be used for different specimen materials, as they have different toughness properties, and hence different amounts of subcritical crack growth. This question is only touched upon in this report. However, at the present stage of knowledge, the same value of $2a_0/W \approx 1/3$ may be temporarily used for all specimen materials for the sake of simplicity.

(3) The formula (1) proposed by H. Liebowitz et al. in reference [1] for COD calibration has been found to be in fair agreement with the experimental results presented in this report. When no experimental data is available, this formula can be used as a fairly satisfactory alternative, although a little on the unsafe side.

(4) After some analysis and comparison, the authors agree with reference [1] in regard to the following proposition: When the specimen is loaded with multiple pins, L/W down to 1.5 can be used and formula (4), which was first proposed by Feddersen^[7], is convenient and sufficiently accurate for the calculation of the geometrical modification factor F . But when specimens of $L/W < 1.5$ have to be used on account of some practical limitations, then other formulas must be sought for to replace formula (4). The effect of the decrease of specimen length to $L/W < 1.5$ on the determination of R curves and K_{IC} values remains to be studied.

Some references such as [12][13] have shown that the scatter of the experimental values of K_{IC} is usually larger than that of K_{I0} , and that the value of K_{IC} often increases with the increase of specimen width. The authors infer that this is possibly connected with the insufficient width of the specimens (on the basis of LEFM) and is probably worthy of further investigation.

The Island Structure of (M-A) in Hardened Low-Alloy High-Strength Steels

Kang Mokuang, Guan Dunhui, Guo Chengdao and Zhu Jinrong

1. Introduction

The quenching of low alloy high strength steel usually involved two methods: one is the isothermal quenching and the other is direct quenching (which is continuous cooling in a medium such as water, oil or air. Production results showed that neither quenching method can produce a uniform single structure. Island-formed structure constituents exist in various quenched steels.

Our experimental results demonstrated that these island-formed (or M-A) structures could significantly influence certain characteristics of the steel. For example, 18Mn2CrMoBA steel, under continuous slow cooling conditions the island structure volume increases and the dimensions grow significantly^[1]. In the meantime, although the tensile strength and yield strength of the steel decrease, the fatigue failure time is significantly improved.

Habraken et al^[2] reported the presence of granular bainite in studying the structure of low-carbon low-alloy steel and believed that this granular bainite was formed by island structures distributed in ferrite.

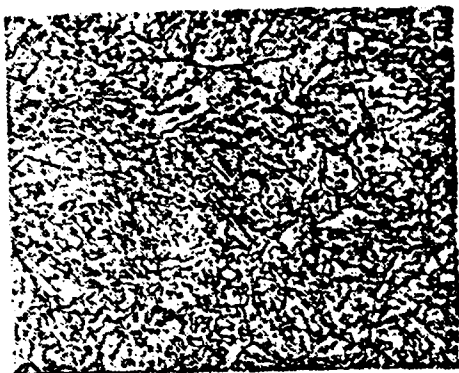
In summary, based on the combination of our experimental work and information in the literature, it is certain that island structures exist in low alloy high strength steels of various quenched structures regardless of whether they are martensite, bainite, granular bainite or a mixture of them.

However, even up to date, different opinions still exist regarding the formation of granular bainite island structures. In some papers, it is believed that island structure is the residual austenite in the transformation of bainite. In the subsequent cooling steps, the austenite may change into bainite, pearlite, or martensite^[2,3]. Other papers claimed that the island structure is a single phase austenite or a mixture of austenite and martensite; also known as (M-A)^[2,4-6]. In short, in various quenched structures, the characteristics of the island structures are still to be further studied. The purpose of this work was to investigate the characteristics, morphology, distribution, transformation process, and the effect of annealing for low-alloy high strength steels. The effect of island structure on the mechanical properties of steel and factors influencing the island structure are discussed in a separate paper.

II. Analysis of the Characteristics of the Island Structure

We have carried out an investigation on the quenched structures of alloys 18Mn2CrMoBA, 18Cr2Ni4WA, 20CrNi3A, 30CrMnSiA, 30CrMnSiNi2A, 40CrA, 40CrNiMoA and 40CrMnSiMoVA. Photographs 1-6 are some of the quenched structures of the steels mentioned above. From these photographs, it can be clearly seen that in various different base structures there exist island structures which look very much alike.

In order to clarify the nature of the island structure, we concentrated our effort on 18Mn2CrMoBA and 30CrMnSiA steels and performed metallographic as well as electron microprobe analysis, quantitative metallography, residual austenite determination, metal thin film electrons transmission observation and electron diffraction.



Photograph 1. Air-cooled structure of 18Mn2CrMoBA steel (ϕ 50mm) from 920°C. 1000X



Photograph 2. Air-cooled structure of 18Cr2Ni4WA steel from 950°C. 1000X



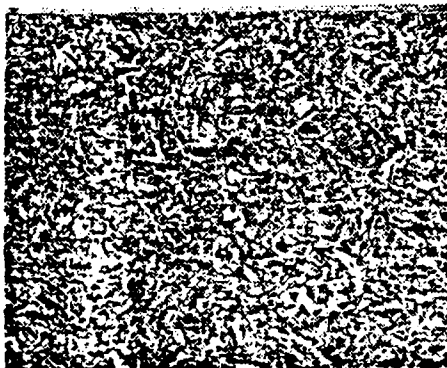
Photograph 3. Oil-cooled structure of 30CrMnSiA steel from 900°C.



Photograph 4. Structure of 30CrMnSiA steel after 3600 sec. at 390°C from 900°C.



Photograph 5. Structure of 30CrMnSiNi2A steel 3600 sec. at 260°C from 900°C. 800X



Photograph 6. Oil cooled structure of 40CrNiMoA steel from 850°C. 800X

1. The Electron Metallography of the Tempered Structures:

The second order complex electron metallographs of 30Cr-MnSiA steel quenched isothermally at 390°C from 900°C and then tempered at various temperatures are shown in photographs 7-9. From comparison of structures before and after tempering, it can be concluded that the island structure is basically uniform (see photograph 7); after tempering at 450-500°C, significant decomposition of the island structure occurs (see Photograph 8); tempering at 650-700°C, the decomposition of basic structure is complete and localized carbide formation is observed (see Photograph 9). For 18Mn2CrMoBA steel, the island structure in the quenched bainite or martensite matrix structure and its changes after tempering are basically the same as the experimental results discussed above.

Many electron micrographs showed that although the island structures of all types of quenched structure of low-alloy steels decompose during tempering, yet the decomposition situation is not the same for each island in the same sample. The corresponding temperature at which significant decomposition occurs is far higher than that of the matrix structure. This indicates that the island structure has a high resistance to tempering. Based on the decomposition of island structures during tempering, it is reasonable to believe that they should be over-saturated solid solutions. The only over-saturated solid solutions existing in quenched structures of steel are martensite, austenite, and over-saturated ferrite. Island structures must also belong to one of these structures.

2. Electron Probe Microanalysis

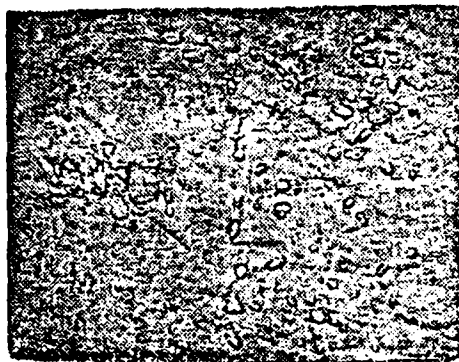
When heated to 920°C and slowly air cooled, the microstructure 18Mn2CrMoBA steel is a bainite matrix with a distri-



Photograph 7. Structure of 30CrMnSiA steel 3600 seconds tempering isothermally at 390°C from 900°C. Second order complex electron metallograph. 10000X



Photograph 8. Same as Photograph 7 and tempered at 500°C. Second order complex electron metallograph. 10000X



Photograph 9. Same as photograph 7 and tempered at 650°C. Second order complex electron metallograph. 10000X.

bution of island structures. Model M.S.46 electron probe was used to determine the alloy composition in various regions of the bainite structures and island structures of the above sample and the results are shown in Table 1.

Table 1. Elemental Intensities (number of times/10 sec) in various regions of a 18Mn2CrMoBA steel sample gradually air-cooled from 920°C.

| Alloy | Intensity of Bainite Matrix | Intensity of Island Structure |
|-------|--|---|
| C | 30, 11, 12, 4, 22, 15, 13, 30, 30, 30, 18, 21, 23 (Average 18.7) | 77, 78, 125, 88, 98, 94, 65, 65, 73, 215 (Average 97.6) |
| Mn | 97, 90, 101, 84, 86, (Average 91.6) | 93, 95, 90, 99, 105, 107, 98, (Average 96.6) |
| Cr | 153, 154, 156, 152, 158, (Average 54.2) | 159, 173, 191, 138, 144, 132, 171, (Average 158.3) |
| Mo | 12, 18, 13, 15, 21, (Average 15.4) | 14, 18, 12, 7, 15, 7, 9, (Average 11.9) |

From the table above, it is clearly shown that the average carbon content in the island structure is about 5 times the amount in the bainite matrix. For the island structures measured, their carbon contents are 3.5 ~ 12 times of that of the matrix. Therefore, all the island structures are rich in carbon. In addition, the carbon content in each island structure differs significantly. Based on these findings, it can be concluded that island structures are over-saturated solid alloy solutions with different carbon contents. For low-alloy steels, these solid solutions can only be martensite or austenite.

3. Quantitative Metallography and Determination of Residual Austenite

30CrMnSiA steel was heated to 900°C and then quenched

isothermally at 390°C for 15 minutes. Quantitative metallographic analysis was carried out using a Model 720-30 Metallographic Analyser. It was determined that the island structure in a sample is 30% by volume. For the same sample, using a 3000 oersted magnet, the residual austenite was measured to be 24%. Compare the above two percentages, though such a comparison is very rough, it can be seen that the island structure is not totally austenite. Similarly, the same measurements were made with 18Mn2CrMoBA steel and very similar results were obtained.

4. Electron Transmission Observation of Metal Thin Film and Electron Diffraction

18Mn2CrMoBA steel was heated to 920°C and then underwent air-cooling and gradual air-cooling processes separately^[1].

The light metallographs, second order complex electron metallographs and thin film transmission structures are shown in Photographs 10-16. It was shown that the structures obtained under these two cooling speeds were bainite and martensite and island structure and bainite and island structure, respectively. The island structures shown in Photographs 12, 13 and 15 were found to be long strips and polygons. Electron diffraction was performed on these island structures and some of the diffraction patterns are shown in Photographs 17 and 18. Figures 1 and 2 are the schematics of matrix structure corresponding to Photographs 17 and 18, respectively.



Photograph 10. Air-cooled structure of 18Mn2CrMoBA steel from 920°C. 1000X



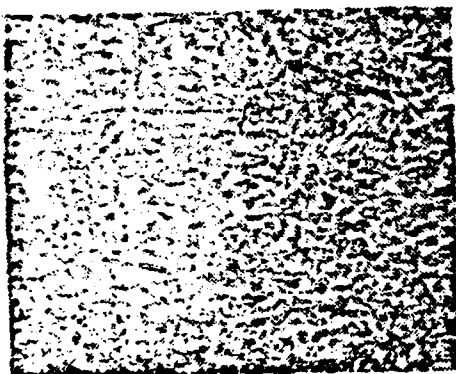
Photograph 11. Same as Photograph 10. Second Order Complex electron Metallograph. 20000X



Photograph 12. Same as Photograph 10. Thin Film Electron Transmission Structure. 16000X



Photograph 13. Same as Photograph 12. 20000X.



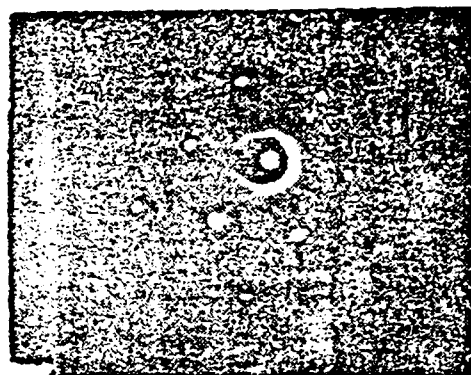
Photograph 14. Gradually Air-Cooled Structure of 18Mn2CrMoBA steel from 920°C.



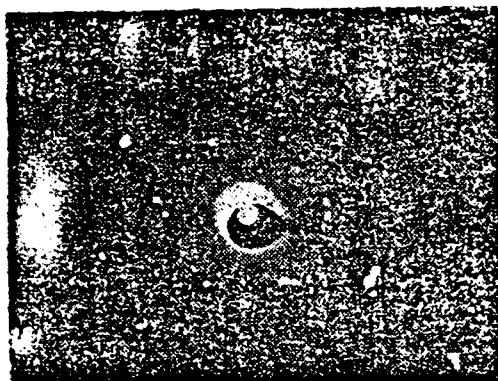
Photograph 15. Same as Photograph 14. Second Order Complex Electron Metallograph. 5000X.



Photograph 16. Same as Photograph 4. Thin Film Transmission Electron Structure. 20000X



Photograph 17. Electron Diffraction Pattern of Island Structure in Air-Cooled 18Mn2CrMoBA Steel quenched from 920°C.



Photograph 18. Same as Photograph 17.

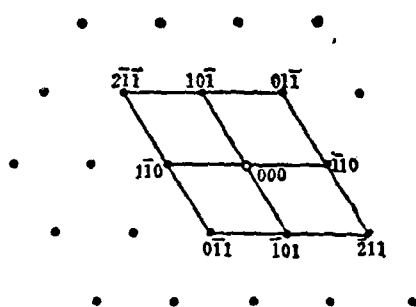


Figure 1. Schematic Diagram of Electron Diffraction Pattern Shown in Photograph 17.

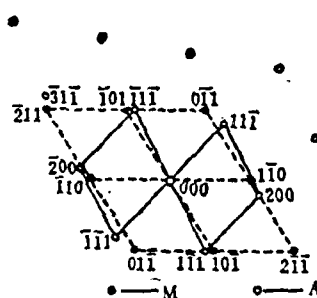
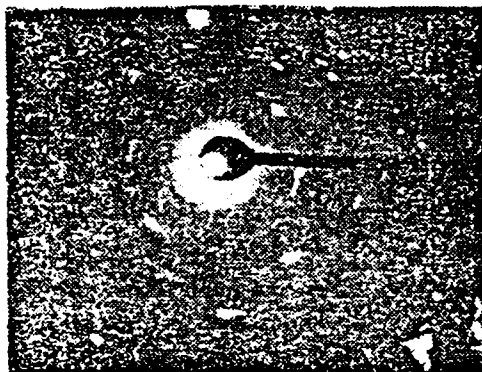


Figure 2. Schematic Diagram of Electron Diffraction Pattern Shown in Photograph 18.

From the above figures, it was found that the island structure crystal lattice sometimes is a body center cubic (martensite) matrix and sometimes is a mixture of body center cubic (martensite) and face center cubic (austenite) matrices.

In addition to the two diffraction patterns described above, for some island structures their electron diffraction patterns approximately but not completely form a diffraction ring (Photograph 19). From calculations performed, it was found that most of them are mixtures of martensite and austenite. Therefore, it can be concluded that the island structure in general is formed by a mixture of martensite and austenite.



Photograph 19. Electron Diffraction Pattern of Island Structure in Air-Cooled 18Mn2CrMoBA Steel quenched from 920°C.

Summarizing the above analyses of experimental results, it can be concluded that the island structures of low-alloy high strength steel are mixtures of carbon-rich austenite and martensite very different in carbon contents (i.e. M-A structure). In the (M-A) structure, single phase austenite or martensite exists in some area. The residual austenite mainly stayed in the (M-A) structure after quenching. This conclusion can also very indirectly be verified by calculating the transportation temperature of martensite. Using 18Mn2CrMoBA

steel as an example, when the alloy composition* is invariant and only carbon content is varying, a series of martensite transformation points Ms and Mz corresponding to various carbon contents can be obtained with the empirical equations in references [5,7]. The results are in Table 2.

Table 2. Calculated Values of Temperature of Ms and Mz of Super-Cooled Austenite with Various Carbon Contents.

| Carbon Content % | 0.2 | 0.5 | 0.6 | 0.7 | 0.8 | 0.9 | 1.0 | 1.1 | 1.2 |
|------------------|-----|-----|-----|-----|------|------|------|------|-----|
| Ms °C | 331 | 235 | 203 | 171 | 139 | 107 | 75 | 30 | -2 |
| Mz °C | 196 | 21 | -26 | -73 | -121 | -168 | -215 | -227 | - |

Although the carbon content of any island structure is far higher than the average carbon content of the matrix and it varies from island to island, yet they should all be carbon rich austenite at temperatures above 330°C. Based on the calculated values in Table 2, at room temperature the austenite island with relatively low carbon content should be martensite. The high carbon content islands should be austenite and the island structure with carbon content in between the two should be the simultaneous presence of austenite and martensite. This agrees with our conclusion based on the analysis of experimental results.

However, in the analysis of the electron diffraction pattern of 18Mn2CrMoBA steel, we did not find a face center cubic matrix (austenite). This effect may be caused by many sources. For example: the composition of material and heat treat condition, the process to fabricate the thin film and the localized limitation of electron diffraction can be influential factors. However, based on the distribution of

*The chemical composition of 18Mn2CrMoBA steel is: C-0.19%, Mn-1.68%, Cr-1.20%, Mo-0.50%, B-0.0011%, Ms point is 330°C.

carbon content in the (M-A) structure as shown in Table 2, (M-A) islands with extremely high carbon are least probable to appear in microanalysis. Although the formation of a stable austenite is not only determined by the carbon content, yet carbon content is indeed an important factor. Therefore, though pure austenite probably exists in the (M-A) structure of low alloy high strength steels, yet its quantity may be very small.

III. Morphology and Distribution of the (M-S) Structure

Under optical microscopes, it can be observed that there is a significant boundary between the (M-A) structure and the matrix. This boundary is irregularly shaped. Therefore, with respect to the matrix (M-A) structure are called island structures. However, this does not describe the complete actual morphology. Under electron microscopes, the shape of the boundary between the (M-A) structures and the matrix is still irregular. Some looks as irregular polygons, some looks like a circle, and some appears to be a long strip. For simplicity, it is possible to distinguish them into two types - the granular and the strip.

The distribution of (M-A) structure in the quenched structure varies with the type of matrix structure. In general, it can be distributed inside the original austenite and also at the grain boundary (Photographs 1 and 14). The (M-A) structures inside bainite, ferrite, lower bainite, mismatched martensite strips are usually granular as shown in Photographs 20-23. For some low carbon content structural steel, the (M-A) structures in the bainite ferrite matrix sometimes appears in strips. In upper bainite matrix, (M-A) structures usually appear as granular and strips and are always distributed in between the bainite strips. They usually are dis-

played in the same direction as the carbides in the upper bainite (see Photographs 24 and 25). Strip (slice) shaped morphology is usually also distributed in between stripes of martensite (Photograph 26). Using the thin film transmission technique, the morphology of the (M-A) structure can be more clearly and truly described (see Photographs 12, 13 and 16).

Experimental results indicate that factors such as the chemical composition of the steel and the heat treatment process used are directly affecting the (M-A) structure. Even for the same steel composition and under the same austenite temperature and soaking period, the value of the isothermal quenching temperature, the quenching time, and the speed of continuous cooling are seriously affecting the morphology, distribution, dimensions, and the volumic fraction with respect to the matrix of the (M-A) structure. Increase the isothermal temperature in the transformation zone of the bainite or decrease the cooling speed in direct quenching will significantly increase the dimensions of the (M-A) structures. Its volumic fraction in the quenched structure is also significantly increased. With increasing isothermal temperature and decreasing upper and lower bainite contents, most of the (M-A) structures are distributed in the bainitic ferrite matrix. As described before, this (M-A) structure distributed in the bainitic ferrite is generally called the granular bainite.

Experimental results also showed that the granular bainite structure can be obtained not only limited to the isothermal quenching in the bainite transformation zone. In the upper bainite transformation zone, isothermal quenching not only yields some upper bainite but also produces some austenite which later transforms into granular bainite. Photograph 27



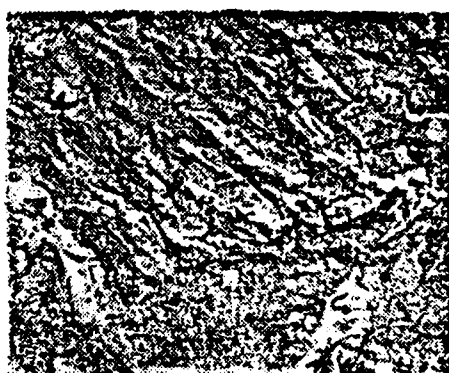
Photograph 20. Granular and strip shaped (M-A) structure in between carbonless bainite matrix of 18Mn2CrMoBA steel heated to 920°C and quenched isothermally at 500°C for 400 sec. 1000X.



Photograph 21. Second Order Complex Electron Metallograph of (M-A) structure in lower bainite stripes. 18Mn2CrMoBA steel heat to 920°C and furnace cooled. 5000X.



Photograph 22. Second Complex Electron Metallograph of (M-A) structure distributed between lower bainite strips. 18Cr2Ni4WA steel heated to 850°C and then isothermally quenched at 640°C for 1.44x10 sec and then air cooled. 10000X.



Photograph 23. - Granular (M-A) structure distributed in martensite strips. Second Order Complex Electron Metallograph of 18Mn2CrMoBA steel heated to 920°C and quenched isothermally at 250°C for 30 minutes. 10000X.



Photograph 24. Second Order Complex Electron Metallograph of 18Mn2CrMoBA steel heated to 920°C and air-cooled. 5000X.



Photograph 25. Second Order Complex Electron Metallograph of 30CrMnSiA steel heated to 900°C and quenched first at 360°C isothermally for 900 sec and then air-cooled. 10000X

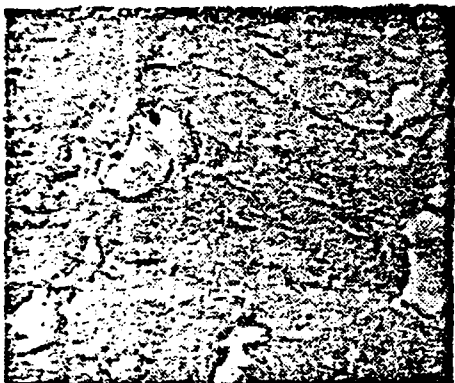


Photograph 26. Second Order Complex Electron Metallograph of strip-shaped (M-A) structure distributed between martensite strips of 30CrMnSiNi2A steel heated to 900°C quenched isothermally at 260°C for 3600 seconds. 8000X

shows the isothermally transformed structure of 18Mn2CrMoBA steel in the upper bainite zone. From the photograph, there is granular bainite structure besides upper bainite structure. Isothermal quenching in the lower bainite zone still produced

some amount of granular bainite similar to the upper bainite case as shown in Figure 28.

It should be pointed out that not all the (M-A) island structures are called granular bainite structures, only those distributed in the bainitic ferrite matrix should be called granular bainite. As for the (M-A) structures distributed in upper and lower bainite matrices, they should not be called granular bainite either.



Photograph 27. Second Order Complex Electron Metallograph of 18Mn2Cr-MoBA steel Heated to 920°C and Quenched Isothermally at 370°C for 1200 seconds. 10000X.



Photograph 28. Second Order Complex Electron Metallograph of 10Mn2CrMoBA Steel Heated to 920°C and Quenched Isothermally at 350°C for 1200 seconds. 10000X.

IV. Transformation Process of (M-A) Structures

From the experimental results presented so far, it is known that the (M-A) structures in low alloy high strength structural steel is a mixture of carbon rich alloy martensite and austenite with varying carbon content. Their carbon contents far exceed the average value in the matrix. Therefore,

the enrichment of carbon in austenite ought to be the necessary condition for the formation of (M-A) structures. In the study of the transformation of (M-A) structures, the major task is then the investigation of the carbon enrichment process in austenite.

It is well known that austenite can be transformed into carbonless bainite by quenching super-cooled austenite isothermally at temperatures slightly lower than the initiation temperature (B_s) of the bainite transformation region. However, this transformation cannot proceed all the way to the end (i.e., the completeness of bainite transformation^[8]). The reason is that at high isothermal quenching temperatures the driving force for phase transformation is small. Consequently, the transformation of bainite is more difficult and results to longer incubation period for bainite transformation. It is because that the isothermal temperature is high, the diffusion of carbon becomes easier. Regardless whether it is in the incubation period of bainite transformation or during the process of bainite transformation, carbon atoms will be enriched in certain microscopic areas of the austenite.^[9,10] Therefore, some carbon-rich austenite zones are formed. Simultaneously, it is causing some area to become carbon-poor austenite zones. At the end of the incubation period for bainite transformation, carbonless bainite nuclei formation and growth begin in carbon-poor austenite zones (see Figure 3, I-b). With increasing isothermal period, carbonless bainite grows along and on the sides of the axis. In the meantime, carbon atoms enter the neighboring austenite zone through the bainite/austenite (B/A) interphase. Since there are preferentially concentrated areas of carbon in the carbon-rich austenite, the propagation of the B/A boundary can not be at the same rate at all locations; the rate should be lower in carbon-rich austenite zones and higher in carbon-poor zones. There-

fore, the B/A boundary is not uniform as shown in Figure 3 Ic and d. Continuous lengthening of isothermal period, the transformation of carbonless bainite further increases and the carbon content in the surrounding carbon-rich austenite also increases to form the very stable carbon-rich austenitic islands (granular or in strips) as shown in Figure 3, I-e. The size and morphology are irregular. Undoubtedly, the carbon content in each island is different. For an island,

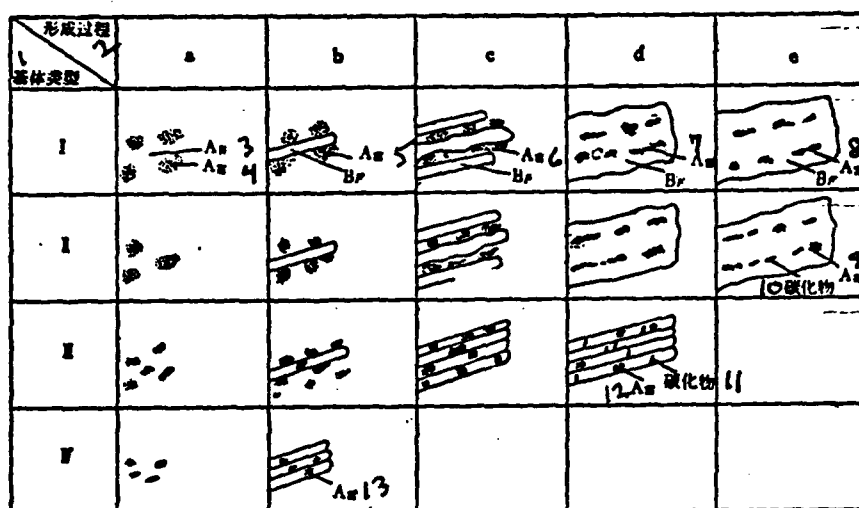


Figure 3. Schematic Diagrams of the Formation Processes of (M-A) Structures in Various Matrices.

Key: 1. matrix-type, 2. formation process, 3. A poor, 4,5,6, 7,8,9,12, 13. A rich, 10, 11. Carbide.

- I - temperature region of carbonless bainite transformation.
- II - temperature region of upper bainite transformation.
- III - temperature region of lower bainite transformation.
- IV - temperature region of martensite transformation.
- A rich - carbon-rich austensite zone.
- A poor - carbon-poor austensite zone
- BF - bainitic ferrite zone

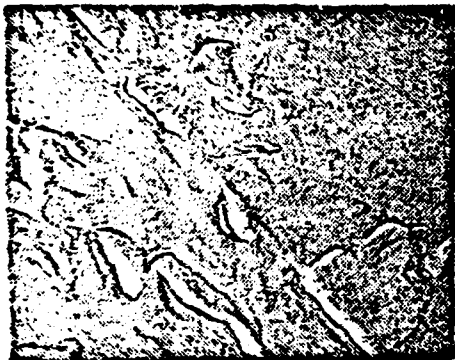
there is a concentration gradient across the center to the edge and it is schematically shown in Figure 4a. Because different martensite transformation points M_s and M_z exist for austensite of various carbon concentrations, in the sub-

sequent cooling process some of these carbon rich austenite islands transform into martensite, some with their centers transform into martensite and edges remain as austenite. For those islands with extremely high carbon content, it is possible that they remain to be austenite completely. Thus forms the (M-A) structure. Since this structure is formed through the diffusion of carbon, it is called diffusion model (M-A).

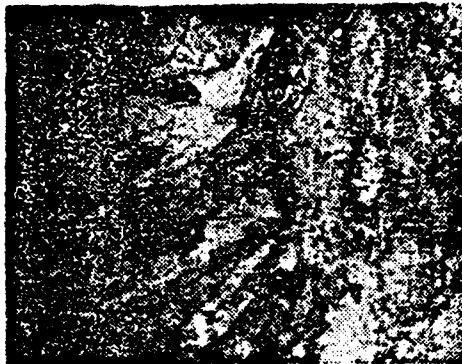
From the above mentioned (M-A) formation procedures, it is clear that the (M-A) structure is not necessarily simple single crystals or single phase polycrystalline. This must be cause for the mixed diffraction pattern of both face centered and body centered cubic matrices in the electron diffraction of some of these (M-A) structure. For other islands, the characteristics of polycrystalline diffraction patterns were shown approximately (Photograph 19).

(M-A) structures can be distributed in the original austenite. It can also be in the crystal boundary. The shape and size are very different. Sometimes layer pieces of (M-A) interlink and almost go through the entire austenite crystal very similar to another interphase (see Photograph 29). Sometimes large pieces of (M-A) exist in the crystal boundary of the original austenite (Photographs 1 and 14). This is probably due to the defects at the boundary which makes it more favorable for carbon atoms to dissolve into the area through diffusion at either high temperature or under gradual cooling.

Observations using metal thin film electron transmission technique showed that the structure of carbonless bainite matrix is still in strip shape (see Photograph 30). This agrees with the above analysis. However, we also discovered another situation. When the samples undergo long-term isothermal treatment or extremely slow continuous cooling, the



Photograph 29. Second Order Complex Electron Metallograph of 18Mn2CrMoBA steel heated to 920°C and gradually air cooled. 5400X



Photograph 30. Metal Thin Film Transmission Structure of 18Mn2CrMoBA steel heated to 920°C and gradually air cooled. 16000X

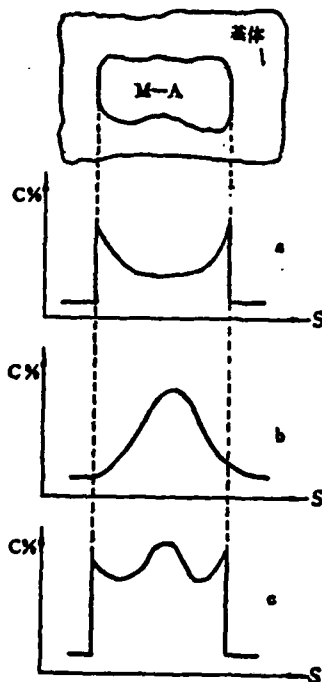
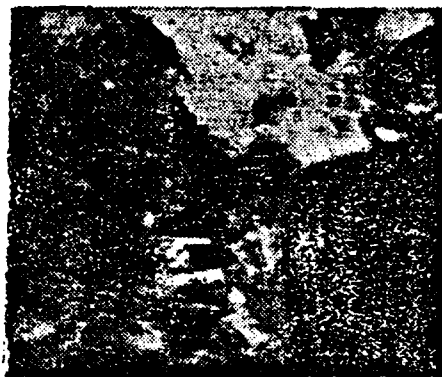


Figure 4. Schematic Diagrams of Carbon Distribution in (M-A) Structures.
Key: 1. Matrix.

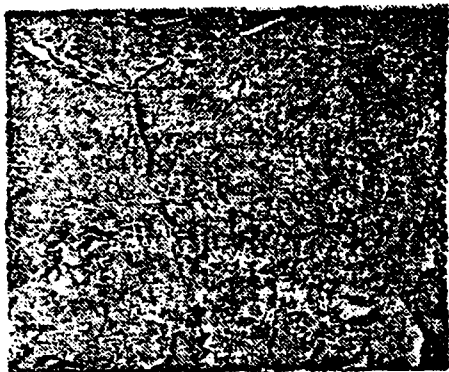
carbonless bainite matrix is no longer in strips as shown in Photograph 31 (in pieces). We believe that this is due to the consolidation of strips under the above conditions. Carbonless bainite, regardless whether in strips or in pieces, belongs to bainitic ferrite^[12]. Reference [11] stated that there is a finite amount of strip formed ferrite in a chunk for iron based alloys. Reference [12] believed that the chunk ferrite has the characteristics of the strip. These statements are basically consistent with our observations.



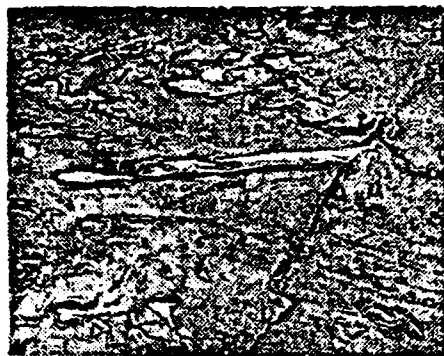
Photograph 31. Same as Photograph 30. 30000X

Although carbonless bainite (bainite finite) matrix has very low carbon content, yet there is considerable amount of over-saturated carbon around. Annealing at 250 ~ 300°C or high temperatures, these over-saturated carbon particles will precipitate out in the form of microscopic carbides (see Photograph 32). In addition, the carbon-rich austenite neighboring the carbonless bainite (bainitic ferrite) does not completely transform into the (M-A) structure. Isothermal or continuous quenching will transform it into other types of bainite. As shown in Photograph 33, next to a carbonless bainite the upper bainite structure appears which rarely occurs.

When austenite is isothermally quenched in the upper



Photograph 32. Second Order Complex Electron Metallograph of 30CrMnSiA steel heated to 900°C quenched isothermally at 390°C for 900 seconds, air-cooled and tempered at 450°C. Small carbide precipitates were found after tempering. 10000X.



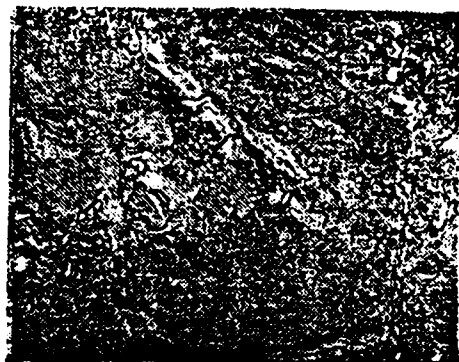
Photograph 33. Second Order Complex Electron Metallograph of 18Mn2CrMoBA steel heated to 920°C, gradually air-cooled. 3000X

bainite transformation zone, the formation of (M-A) structures follows basically the same process as the one described above for the formation of (M-A) structures in the carbonless bainite region. At the end of the incubation period, strips of bainitic ferrite are formed in the austenite. Along with the growth of these strips, carbon atoms continuously diffuse through the B/A boundary into the austenite zone between ferrite strips. This is schematically shown in Figures 3, II-b, II-c, and II-d. Due to the relatively low transformation temperature, the long range diffusion of carbon is rather limited in this case. When the carbon content in the carbon-rich austenite between strips reaches a concentration high enough for carbide formation, precipitates of carbides will be produced. For other carbon-rich austenite zones with high carbon contents, because it is not high enough for carbide formation, they remain as austenite (as shown schematically in Figure 3 II-e) and are later transformed into (M-A) structures during the subsequent cooling process. Therefore, the (M-A) structures in an upper bainite matrix are islands in granular or strip form locating in between bainite ferrite strips. They are

also aligned in the same direction as that of the carbide precipitates. This shows that the (M-A) structure in the upper bainite matrix is also the diffused type. Its existence once again demonstrates the incompleteness of bainite transformation.

The isothermal quenching over extended period of time in the upper bainite transformation region will lead to two other situations, in addition to the formation of upper bainite, due to the conditions that allow carbon atoms to diffuse sufficiently. The first one is the formation of high uniform carbon content austenite between the ferrite strips. In this case, the carbon concentration is not sufficiently high to form carbide precipitates. Secondly, carbon enrichment continues to occur in some originally carbon-rich austenite regions causing the simultaneous formation of carbon-poor austenite zones in the surroundings. These carbon-poor austenite regions continue to transform into upper bainite or even bainitic ferrite zones. During the cooling process after isothermal quenching, carbon-rich austenite zones in the two above cases are transformed into (M-A) structures. Part of the (M-A) structures combine with the bainite ferrite matrix to form granular bainite. The bainite ferrite formed under these conditions is in strip or chunk shape, the same as in carbonless bainite transformation zone. The size of these (M-A) structures should be much larger than those in the upper bainite matrix.

For quite a few low alloy high strength structural steels, under either long period of isothermal quenching in the upper bainite transformation zone or continuous cooling at very low rates, their structural transformation is very similar to whatever is described above. Photograph 34 is a second order

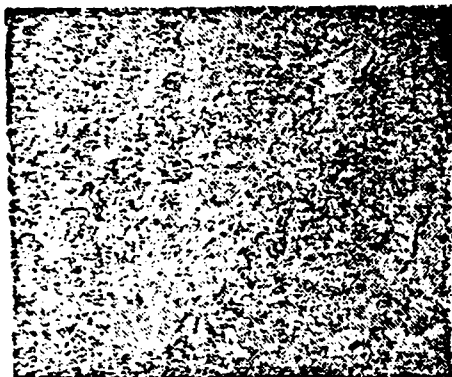


Photograph 34. Second Order Electron Metallograph of 18Mn2CrMoBA steel heated to 920°C and isothermally quenched at 420°C for 3600 seconds. 5000X

electron metallograph of 18Mn2CrMoBA steel isothermally quenched for a long period of time in the upper bainite transformation region. With the exception of very few upper bainite, the rest is granular bainite.

It is worthwhile to note that 18Cr2Ni4WA steel have been believed to be a martensitic type of steel. However, our experimental results revealed that only when the samples are small, that we can get the mixed structure of martensite and a small amount of bainite as shown in Photograph 35. For samples slightly larger in dimension, the granular bainite structure as shown in Photographs 2 and 36 is obtained under air-cooled conditions. The (M-A) structure in this case is approximately distributed as strings in the bainitic ferrite matrix. This structure is neither a martensite strip nor a typical feather shaped bainite.

In the isothermal treatment of austenite in lower bainite transformation zone, the formation process of the (M-A) structure is not exactly the same as the two above mechanisms. Although it is possible for carbon to redistribute inside austenite during the incubation period, yet carbon atoms can



Photograph 35. Second Order Electron Metallograph of 18CrNi4WA steel (small specimen) heated to 850°C and air-cooled. 10000X



Photograph 36. Second Order Complex Electron Metallograph of 18Cr2Ni4WA Steel (large size parts) heated to 850°C and 550°C air-cooled. 10000X

not always undergo long range diffusion due to the low transformation temperatures. Therefore, the concentration differential between the carbon-rich and carbon-poor austenite regions is relatively smaller. During the growth period after the nuclei formation of bainite ferrite strip, it may grow directly across the carbon-rich austenite region (see Figures 3 III-b and III-c) with the simultaneously short range diffusion of carbon. Finally, carbide precipitates are formed in parts of the carbon-rich austenite region of high carbon concentration. The other parts of the carbon-rich austenite region does not have carbide precipitation because of the relatively low carbon concentration. In the subsequent cooling process it transforms into the (M-A) structure (see Figure 3 IV-d). Therefore, the (M-A) structure in lower bainite is still diffusion type. It is usually distributed in the bainitic ferrite strips. Experimental results revealed that most of the (M-A) structures in lower bainite are like that (see Photographs 21 and 22). If quenched isothermally over extended periods of time in the lower bainite transformation zone, similar to the case in upper

bainite transformation region, in addition to the continual formation of a small amount of lower bainite., it is also possible to form considerable amounts of granular bainite. In reality, the lower bainite structures in low alloy high strength structural steel are mostly of the morphology type as shown in Photographs 7, 21, 22, and 28.

In summary, it is not possible to obtain a single phase structure in either upper or lower bainite transformation region. It is usually a mixed structure. In addition to the presence of (M-A) structures in the upper or lower bainite matrix, there is a certain amount of granular bainite in the system.

If bainite is obtained from transformation during cooling, then the formation process of the (M-A) structure is similar to the one proposed in isothermal transformation, i.e. due to the diffusive enrichment of carbon.

Continuous cooling at a rate greater than the critical cooling rate or the isothermal quenching at temperatures below M_s usually results in the formation of martensite strips. (M-A) structures still exist in this type of martensite matrix. It is not formed through carbon diffusion. This is due to the preferential gathering of carbon in significant amounts in microscopic zones in the carbon-rich austenite. During the transformation of martensite, martensite strips very rapidly run across these carbon-rich austenite zones which makes these areas remain at (M-A) structures (see Figure 3 IV-6). Because that no carbon diffusion occurs during martensite transformation, the (M-A) structure in the martensite matrix is of course the non-diffused type. Its carbon concentration distribution is schematically shown in Figure 4-6. For ordinary low alloy structural steel, under normal quenching and tempering condi-

tions, the preferential gathering of carbon in austenite is unavoidable. If carbide forming elements are present in the steel or under conditions that the temperature and time for the austenite formation are insufficient, this preferential gathering of carbon problem becomes more severe. The presence of non-diffused (M-A) structures in martensite, therefore, is totally possible.

In the transformation of bainite, it is also possible for microscopic zones of carbon-rich austenite which are formed not through diffusion of carbon to exist. With the diffusive enrichment of carbon atoms in these areas, the surrounding carbon content must be increased. Its carbon concentration distribution is schematically shown in Figure 4c. This (M-A) structure formed by carbon-rich austenite is a mixture of diffusive and non-diffusive types, or it is called the mixed type.

Diffusive, non-diffusive, and mixed type (M-A) structures are the same in characteristics. They only differ in their formation processes and carbon concentration distributions.

V. The Decomposition and Transformation of (M-A) Structures on Tempering

As discussed above, the residual austenite in the quenched structure of low alloy high strength structural steel mainly exist in the (M-A) structure. The electron metallograph of tempered (M-A) structures also showed that decomposition may happen upon tempering of the (M-A) structure. Apparently, this decomposition is a combination of decompositions of both martensite and austenite during the heating and soaking in the tempering process. If the austenite in the (M-A) structure is not completed decomposed during heating and soaking in

the tempering process, there must be transformation of residual austenite in the cooling process after tempering. Therefore, if the quenched structure of steel has significant amounts of (M-A) structures, then the property changes after tempering is not only related to its matrix structure. It can be sure that the decomposition and transformation of (M-A) structures have significant effects on the properties of the annealed steel. Therefore, the research on the regularity of the decomposition and transformation of tempered (M-A) structures is no longer a simple theoretical problem. It is also an important practical problem. We used thermal magnet and optical expansion meters to analyse quenched steel.

The martensite in the (M-A) structure is a carbon rich alloy martensite which has a higher tempering resistance than the matrix structure. This has been confirmed by structural analysis. With increasing tempering temperature, martensite is decomposed into tempered martensite, etc. It is not too different from the tempering of martensite in high carbon content alloy steel. The transformation of residual austenite in the tempering process involves very complicated mechanisms. We used thermal magnet to temper samples of quenched steel and obtained tempering heat and variations in austenite content during soaking and air-cooling. The decomposition and transformation of austenite in the (M-A) structure then became known. The samples used were made of 18Mn2CrMoBA steel, heated to 920°C and gradually air quenched^[1]. The structure was bainite + (M-A). The average residual austenite content measured was 11.5%. Figure 5 shows the heating and soaking curves of the sample during tempering relative to the isothermal transformation curve C of austenite. Table 3 summarizes the variations of austenite content in the sample on tempering. The data in Table 3 indicates that the austenite in the (M-A) structures may decompose during the heating step on tempering.

For 18Mn2CrMoBA steel tested, the decomposition began at temperatures in the range of $300 \sim 400^{\circ}\text{C}$. The temperature difference may be due to the variation in austenite carbon content in (M-A) variation in carbon content in the austenite. Based on the relative position of the heating and insulations standards in Figure 5 with respect to the C-curve heating and soaking with respect to C-curve, it is clear that residual austenite may be transformed into bainite. Although the C-curve of the residual austenite is not identical with that of the steel, yet the incubation period for residual austenite to be transformed to bainite is shorter than that for the original austenite to be transformed into bainite. Therefore, on tempering within a given temperature range it is entirely possible to transform part of the austenite in the (M-A) structure into bainite.

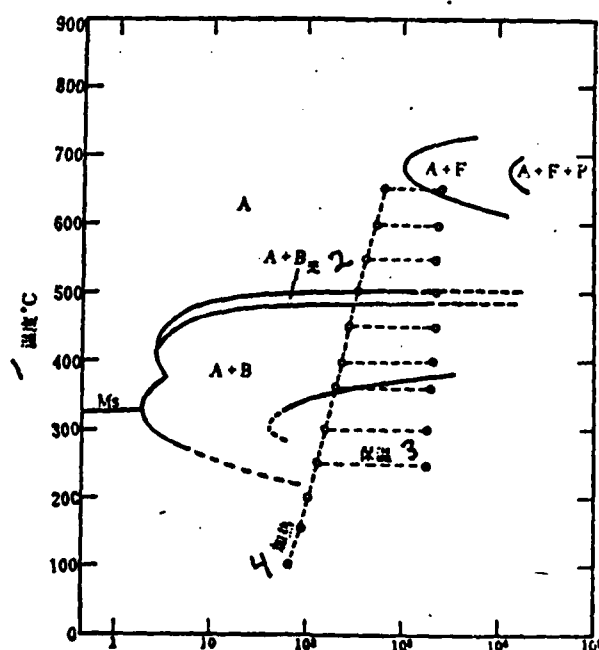


Figure 5. Relative positions of heating and soaking of 18Mn2CrMoBA steel on Tempering with respect to its C-curve. Key. 1. Temperature $^{\circ}\text{C}$, 2. $A+B_{no}$, 3. Soaking, 4. Heating

Table 3. Transformation of Austenite in 18Mn2CrMoBA Steel Slow Air-Cooled Quenched Sample on Tempering (Residual Austenite 11.5% Before Tempering).

| 回火温度 ℃ | 2 随炉加热 | | 3 保温(30分) | 4 空气中冷却 | | 5 回火后的残 留奥氏体量 % |
|-----------|----------------|-------------------------|---------------|----------------|------------|-----------------------|
| | 奥氏体分解 开始温度℃ | 到达回火温 度时的奥氏 体分解量% | 奥氏体分解 量% 8 | 奥氏体转变 开始温度℃ | 转变量% 10 | |
| 380 | 350 | 2.0 | 2.5 | 150 | 2.5 | 4.5 |
| 400 | 300 | 2.5 | 1.0 | 200 | 1.5 | 6.5 |
| 450 | 400 | 2.0 | 0 | 300 | 2.5 | 7.0 |
| 500 | 400 | 3.0 | 0 | 150 | 2.5 | 8.0 |
| 650 | 400 | 3.5 | 4.5 | 350 | 3.0 | 0.5 |

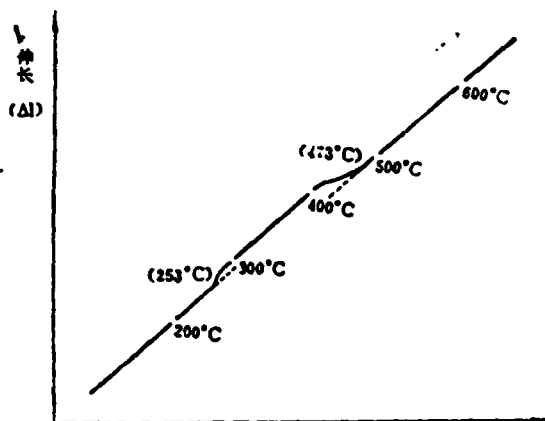
Key: 1. Tempering temperature, 2. Heating in furnace, 3. Soaking (30 minutes), 4. Cooling in air, 5. Residual austenite content after tempering %, 6. Starting temperature of austenite decomposition °C, 7. Decomposed austenite content when temperature reaches the tempering temperature, 8. Decomposed austenite content %, 9. Initiation temperature of austenite transformation °C, 10. Transformed amount %.

Experimental results indicate, during the tempering process, the tempering soaking temperature is directly relevant to the continuation of austenite decomposition. As presented in Table 3, the decomposition of austenite in the (M-A) structure practically stopped during the 30 minute soaking at the temperature range 450 - 500°C. It is probably due to the fact that the tempering temperature just so happened to be in the austenite stable zone of the C-curve for the residual austenite in the tested steel sample. As shown in Figure 5, tempering at a higher temperature (650°C), this temperature is already located in the pearlite transformation region. Therefore, austenite decomposition in the (M-A) structure may take place regardless whether it is in the heating or soaking process.

The residual austenite in quenched steel structures usually does not decompose completely after one heating and soaking tempering process. Therefore, the air-cooling of the steel in a certain temperature range serves as a second tempering step for the undecomposed residual austenite. Part of the remaining austenite may undergo martensite transformation. Since the carbon content in the (M-A) structure varies quite significantly, the anti-stabilization reaction of austenite on tempering at different temperatures is also different. Consequently, the temperature at which the residual austenite begins to transform into martensite also varies. Table 3 listed that this temperature ranged from 150 ~ 350°C.

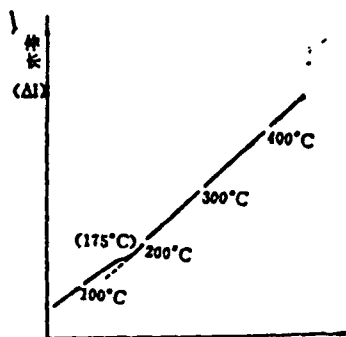
The decomposition and transformation of (M-A) structures on tempering can also be reflected by the volumetric variation during the tempering process. Optical expansion measurements were made during tempering of 30CrMnSiNi2A and 18Mn2CrMoBA steels quenched under different conditions and the results are shown in Figures 6 and 7. From Figure 6, it can be observed that the lower bainite + (M-A) structured 30CrMnSiNi2A steel specimen showed expansion deflection at around 250°C. This deflection indicated the decomposition of austenite in the (M-A) structure. A contraction deflection shown at about 470°C marked the decomposition of martensite in the (M-A) structure. Under this condition it is consistent with the observed apparent decomposition of the (M-A) structures at 400 ~ 500°C using structure analysis. The 18Mn2CrMoBA steel sample identical to the are used in the thermal magnetic experiment showed an expansion deflection (Figure 7) at about 175°C during air cooling after tempering at 500°C. For 18Mn2CrMoBA steel samples using series temperature tempering, the austenite was measured to start decomposing at 250-350°C upon heating. The transformation temperature from residual austenite to martensite is 150 ~ 303°C during cooling. These results are basically

the same as the ones obtained using thermal magnetic measurements.



l - tempering temperature

Figure 6. Heating Expansion Curve of 30CrMnSiNi2A steel heated to 900°C, quenched at 320°C for 3600 sec. upon tempering.



l - tempering temperature (°C)

Figure 7. Cooling Expansion Curve of 18Mn2CrMoBA steel upon tempering, heated to 920°C slowly air-cooled.

For many low alloy structural steel quenched and tempered at various temperatures, the decomposition and transformation of residual austenite do not increase linearly with the tempering temperature. Figures 8, 9, and 10 are the residual austenite content curves of 30CrMnSiA, 30CrMnSiNi2A and 18Mn2CrMoBA steels quenched under different conditions as a function tempering temperature after sequential tempering, respectively.

Although their alloy compositions and heat treatment conditions are different, yet the residual austenite content basically varies with tempering temperature in a similar way. We believe that this regularity is a combined effect of different degrees in decomposition and transformation of austenite in the (M-A) structure at various tempering temperatures. It also implies that for low alloy structural steel after quenching, at low temperatures tempering can not cause the decomposi-

tion and transformation of austenite in the (M-A) structure. At slightly higher tempering temperatures, austenite decomposition and transformation occur during heating, soaking and cooling steps to reduce the residual austenite content after tempering. When the tempering temperature reaches the stable zone of the C-curve for the residual austenite in the quenched structure of the steel, it is then very difficult or impossible for austenite to decompose during soaking. Under this condition, considerable amounts of residual austenite still remain after tempering. Increasing the temperature for tempering further, although it still remains in the stable region of the C-curve, under this condition austenite decomposition only takes place during heating. A very strong anti-stabilization reaction for austenite exists during soaking^[13]. Therefore, it is still possible to cause austenite transformation to martensite during cooling. Tempering at temperatures in the pearlite transformation region makes the decomposition and transformation of austenite complete. This causes the saddle shaped curve in the variation of residual austenite content versus sequential temperature tempering.

In addition, under different quenching conditions, owing to the different (M-A) structure content in the quenched structure, the residual austenite content is quite different even after tempering at the same temperature. The isothermal quenching of bainite at higher temperatures and the gradual continuous cooling under conditions to obtain bainite can result in general in a considerable amount of (M-A) structure formation. The corresponding residual austenite after tempering is also relatively higher. But the variation of residual austenite content with tempering temperature remains the same as under other quenching conditions.

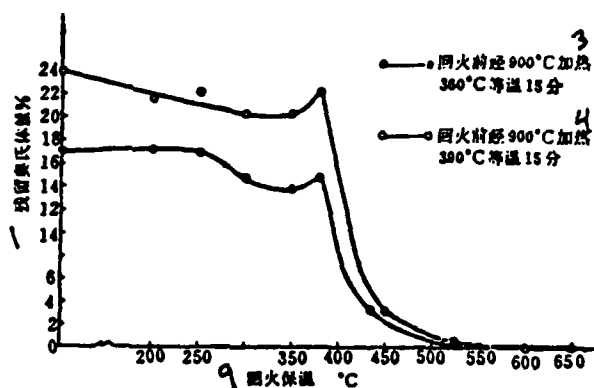


Figure 8. Relation between residual austenite content and tempering temperature for 30CrMnSiA steel.

Key: 1,2. residual austenite content %, 3. heated to 900°C, quenched at 360°C for 15 minutes, 4. heated to 900°C, quenched isothermally at 390°C for 15 minutes.

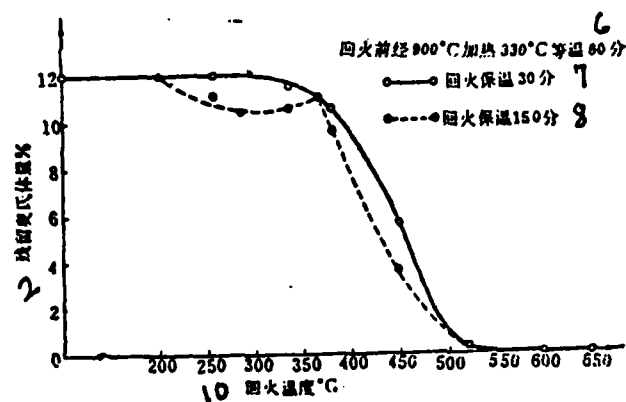


Figure 9. Relationship between residual austenite content and tempering temperature for 30CrNmSiNi2A steel.

Key: 6. heat to 900°C and quenched isothermally at 330°C for 60 minutes, 7. 30 minute soaking, 8. 150 minute soaking, 9, 10. tempering temperature °C.

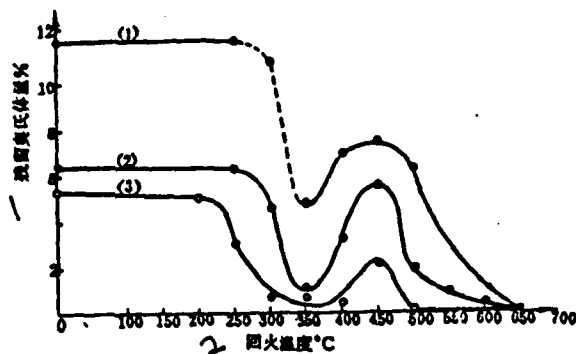


Figure 10. Relationship between residual austenite temperature with tempering temperature for 18Mn2CrMoBA steel. Sample cooling speed at quenched is expressed by the time from 920°C → 400°C: 1) 36000 seconds, 2) 1500 seconds, 3) 500 seconds.

Key: 1. residual austenite content %, 2. tempering temperature °C.

VI. Conclusions

Based on our structural analysis on a series of low alloy high strength structural steel and experimental results obtained from selected alloy steel samples, we reached the following preliminary conclusions:

(1) In the quenched structures of low alloy high strength structural steel, the (M-A) structure usually exists. Steel composition and heat treatment are affecting the size, distribution and volumetric fraction in the matrix of the (M-A) structure directly.

(2) The (M-A) structure is a carbon-rich alloy martensite or austenite or a mixture of martensite and austenite of varying carbon content. The residual austenite in the quenched structure of low alloy high strength structural steel basically exists in the (M-A) structure.

(3) The (M-A) structure is usually distributed in the quenched structure of steel as islands. The morphology is either granular or in strips. The (M-A) structures are usually granular in bainitic ferrite chunk, lower bainite, and martensite strips. It exists in strip form in bainitic ferrite strips, upper and lower bainite, and in between martensite strips. (M-A) structures also exist in the grains of original austenite and it may also be distributed at the grain boundary of the original austenite.

(4) In quenched structures, only the (M-A) structures distributed in the bainitic ferrite matrix are called granular bainite. When (M-A) structures are also distributed in other matrices, it is not proper to use the term "granular bainite." The structure of bainitic ferrite is either needle or chunk shaped.

(5) The formation process of the (M-A) structure can be considered as the diffusive enrichment of carbon in austenite to form stable carbon-rich austenitic zones. In the subsequent cooling process, it remains as either martensite or austenite or a mixture of both. The preferential gathering of carbon in the original austenite is another reason for (M-A) formation. The (M-A) structure is divided into diffusive, non-diffusive, and mixed types. However, their characteristics are the same.

(6) Decomposition of (M-A) structure occurs upon tempering. It has a higher resistance to tempering than the matrix structure. The decomposition of martensite in the (M-A) matrix begins at about $400 \sim 500^{\circ}\text{C}$. For tempering at temperatures in some regions above 250°C the austenite in the (M-A) structure can be decomposed into bainite in the heating and soaking processes. In the austenite stabilization zones of the C-

curve of residual austenite, very little or absolutely no austenite decomposition occurs in the (M-A) structure during soaking. The tempering in the pearlite transformation zone will cause most of the austenite in the (M-A) structure to decompose into pearlite. Part of the undecomposed austenite in (M-A) structure may be transformed to martensite during cooling after tempering.

(7) The residual austenite content in low alloy high strength structural steel does not decrease linearly with increasing tempering temperature. It usually follows a saddle shaped curve with increasing tempering temperature. This is directly related to the amount of austenite decomposed and transformed upon tempering.

REFERENCES

- [1] Northwestern University of Technology, Metallic Materials and Heat Treatment Laboratories, "Metal Heat Treatment" 6 (1977), pp. 1-8.
- [2] Habraken, L., «De Ferri Metallographia», Presses Académiques Européennes S. C. Bruxelles (1966), p.208-213.
- [3] Bush, M. E., «Acta Metallurgica», Vol.19, No.12, (1971), p.1363.
- [4] Mangono, P. L., «Met. Trans.», Vol.7A, No.9 (1976), p.1389.
- [5] Biss, V., «Met. Trans.», Vol.2, No.9 (1971), p.260.
- [6] Bojarski, Z., «Acta Metallurgica», Vol.22, No.10 (1974), p.1203
- [7] Shmel'kov "Soviet Heat Treatment Workers Handbook" Chinese Industrial Publishing House (1956), pp. 94.
- [8] Hehemann, R. F., «Phase Transformation», American Society for Metals, Metals Park, Ohio (1968), p.397.
- [9] R. I. Enshin "Transformation of Austenite in Steel" Chinese Industrial Publishing House (1965) pp. 137-157.
- [10] Houillier, A. L., «Met. Trans.», Vol.2, No.9 (1971), p.2645.
- [11] Massalski, T. B., «Phase Transformation», American Society for Metals, Metals Park, Ohio (1968), p.433.
- [12] Bee, J. V., «Met. Trans.», Vol.9A, No.4, (1975), p.578.
- [13] Блаутер, М. Е., «Фазовые Превращения при Термической Обработке Стали», Металлургиздат (1962), p. 123~124.

The authors suggest that the formation process of (M-A) in bainitic matrix might be as follows:

In the transformation of the bainite, carbon atoms from the bainite diffuse through the bainite/austenite (B/A) boundary into the austenite to make it rich in carbon content. The austenite regions may be gradually reduced to some small islands when the bainite laths continuously grow. These small regions of carbon-rich austenite do not decompose and then they reach finally a stable state with martensite points at different temperatures. Thus they turn into (M-A) of diffused type after cooling.

The authors suggest that the formation process of (M-A) in martensitic matrix might be as follows:

In the prior austenite, there are initially small regions of higher carbon content (carbon-segregation) with lower martensite points at different temperatures. During general transformation of austenite into martensite, these small regions of lower martensite points remain unchanged and the martensite laths can pass through them. Thus the (M-A) of undiffused type is formed during further cooling. Under usual steel quenching conditions, there must exist small regions of high carbon content in the prior austenite. These carbon-rich regions are further enriched when transformation of bainite takes place. Thus a (M-A) of mixture type is formed after cooling. There are differences in (M-A) in type, morphology, and distribution, but the nature of them is essentially the same.

On tempering, (M-A) undergoes transformation. Martensite in (M-A) begins to decompose at about 400—500°C. During the heating and soaking period of the tempering, part of the austenite in (M-A) transforms into bainite at some temperature above 250°C, but remains unchanged at other temperatures of temper-soaking. A portion of the unchanged austenite in (M-A) becomes unstable by tempering at higher temperature and transforms into martensite partially or completely during subsequent cooling. Therefore, the amount of retained austenite decreases with the increase of tempering temperature and reaches a minimum value at a certain temperature, which depends on the decomposition and transformation of (M-A) during tempering. (M-A) decomposes and transforms completely at about 520~650°C. The resistance of (M-A) to tempering is higher than that of matrix.

A Study on Insulated Risers

Zhou Yaohe, Zhang Yanwei, Qu Weitao, Lin Zaiue, Mao Zhiying,
Wang Youxu, Niu Jingxin, and Zhang Qixun

ABSTRACT

The plate-shaped casting method was used to determine the thermal physical parameters of three insulating materials - pearlite; formed plaster, and ceramic wool together with a wet sand mode. From the freezing characteristics of sand castings, a calculation method was described to describe the insulated riser. Using the measured physical thermal coefficients, this method was verified on a pure aluminum cubic casting. Experimental and calculated results were consistent. Pearlite and formed-plastic risers were seven times smaller than the conventional ones. A ceramic wool riser was found to be eight times smaller. Finally, a theoretical analysis of the effectiveness of the insulated risers was made. It demonstrated that the use of insulated risers for alloy castings which formed concentrated shrinkage cavities could significantly improve productivity and casting yield, saving the expenses involved in metal melting and riser cutting and minimizing waste.

I. Introduction

Risers of sand castings generally weigh from 40 - 100% of the weight of the castings. Therefore, the effective yield of the casting is low. Actually, the volume shrinkage during metal freezing is only a few percent. In a conventional riser (using the same material as the casting without taking

any measures to strengthen and compensate for shrinkage), the metallic equilibrium during the freezing process is shown in Figure 1-a. Upon completion of freezing, the metallic part (1-2) of the riser is used to compensate for the shrinkage of the casting. The liquid portion (2-3) is the reserve kept to maintain a certain head pressure and to prevent shrinkage cavity and impurities from going into the castings. The major portion (3-4) has been solidified before the castings are totally frozen. Insulated risers are used to ensure adequate compensation action as well as to minimize depletion of metals. Figure 1-b shows the metallic equilibrium of an ideal insulated riser (remaining in the liquid phase until castings are frozen). Although insulated risers have been used in recent years, the thermal coefficients and the principles of the design of insulated risers are not widely available in the open literature [1,2,3,4,5,6,7,8]. This paper first reports the determination of thermal coefficients of three insulation materials and then introduces a design process for insulated risers. Finally, the effectiveness of insulated risers is theoretically estimated.

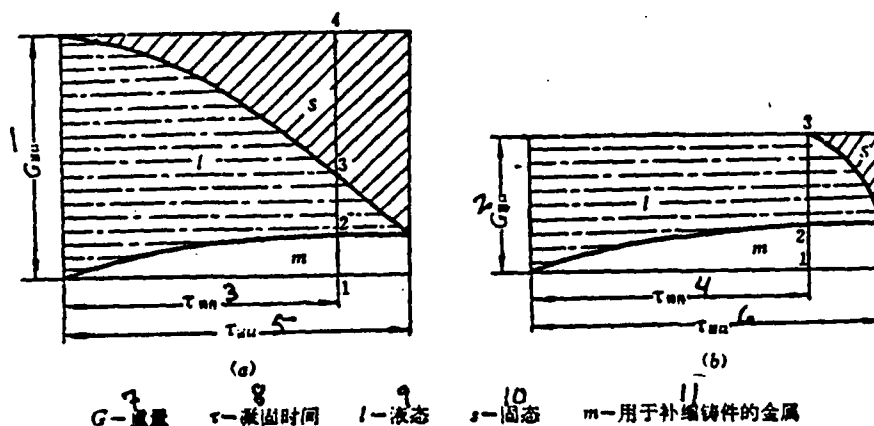


Figure 1. Metallic equilibria conventional (a) and ideal insulated (b) risers.

Key: 1,2. Griser, 3,4. τ casting, 5,6. τ riser, 7. G-weight, 8. τ freezing time, 9. l-liquid, 10. s-solid, 11. m-metal used to compensate for shrinkage.

II. The Determination of Thermal Coefficients for Insulated Materials

Thermal coefficients are the most important characteristics of insulated materials. Among the methods available to determine the thermal coefficients of the mode-making materials, the unsteady state method involving melting and casting is most applicable to this particular technical problem. In this method, the most important thing is to establish the necessary heat exchange condition.

If the temperature is initially t_0 on the surface of a semi-infinite solid and at time $\tau=0$ the temperature increases suddenly to t_b , then the temperature t at a point which is x away from the surface (perpendicularly) after time τ is

$$t - t_0 = (t_b - t_0) \left[1 - \operatorname{erf} \left(\frac{x}{\sqrt{4\alpha\tau}} \right) \right] \quad (1)$$

where α - thermal conductivity

$\operatorname{erf} \left(\frac{x}{\sqrt{4\alpha\tau}} \right)$ - error function

It is generally believed that for poured, zero super heat, pure metal, sand mode plate castings the above heat exchange condition is applicable. Under such conditions, the freezing temperature of the pure metal can be treated as the boundary temperature of the plate casting during the solidification process. The heat dissipated during freezing of the flat plate is

$$Q_1 = FX_1\gamma_1\rho_1$$

where F and X_1 represent the surface area and the thickness of the side of the casting respectively.

γ_1, ρ_1 are the metal weight and crystallization heat, respectively.

(from here on the subscript 1 represents metal; 2 - casting).

The amount of heat absorbed by one side of the casting upon completion of freezing of the casting is:

$$Q_2 = \frac{2}{\sqrt{\pi}} b_2 F (t_k - t_0) \sqrt{\tau_k} \quad (2)$$

where b_2 - heat storage coefficient of the casting
 t_k - metal freezing temperature
 τ_k - solidification time of the plate casting

$$\begin{aligned} \frac{2}{\sqrt{\pi}} b_2 F (t_k - t_0) \sqrt{\tau_k} &= \frac{1}{2} F X_1 \gamma_1 \rho_1 \\ b_2 &= \frac{\sqrt{\pi}}{4} \cdot \frac{X_1 \gamma_1 \rho_1}{(t_k - t_0) \sqrt{\tau_k}} \end{aligned} \quad (3)$$

The thermal coefficients of the insulator materials are usually calculated using equations (1) and (3).

Another method [9,10] involves the use of a nth degree parabola to approximate the mode temperature distribution:

$$t - t_0 = (t_k - t_0) \left(1 - \frac{x}{x_2}\right)^n \quad (4)$$

where X_2 - thermal penetration thickness of the mode. When $\tau = \tau_k$, $x_2 = X_2$.

The thermal storage coefficient and thermal conductivity of the mode are

$$b_2 = \frac{1}{2} \sqrt{\frac{n+1}{2n}} \cdot \frac{X_1 \gamma_1 \rho_1}{(t_k - t_0) \sqrt{\tau_k}} \quad (5)$$

and

$$a_2 = \frac{X_2^2}{2n(n+1)\tau_k} \quad (6)$$

respectively.

If a_2 and b_2 are known and γ_2 is approximately the weight of the mode at room temperature, then coefficients c_2 and λ_2 can be obtained using the following:

$$c_2 = \frac{b_2}{\gamma_2 \sqrt{a_2}} \quad (7)$$

$$\lambda_2 = \frac{b_2^2}{c_2 \gamma_2} \quad (8)$$

The results obtained using the above methods must be experimentally verified.

EXPERIMENTAL PROCEDURES

Pure aluminum was chosen as the test metal to determine the thermal coefficients of the three insulator materials - pearlite, foamed plaster, and ceramic wool (compositions shown in Table 1).

With the exception of the wet mode, the other experimental modes were constructed using plates formed with the insulating materials. Nine NiCr-NiAl thermocouples were installed at fixed locations on the plate. At the end of each experiment, upon peeling off the mode, the positions of the thermocouples were re-determined. The plate dimensions are 6 x 160 x 200 mm³ and 20 x 200 x 200 mm³. The length and width are much larger than the thickness, so that the heat transfer between the casting and the mode can be considered one-dimensional. Another NiCr-NiAl thermocouple wire protected by a double-hole 2 mm OD ceramic tube was inserted into the cavity from the bottom to measure the metal temperature. The distribution of thermocouples in the mode is shown in Figure 2.

Pure aluminum was melted using a conventional technique. It was slowly cooled to remove gas and poured at low superheat

TABLE 1 MODE COMPOSITION

| Mode Material | Major Constituents | Weight % |
|--|---------------------------|----------|
| Expansion perlite | expansion perlite | 48 |
| | water glass | 38 |
| | 10% NaOH aqueous solution | 14 |
| Foamed plaster | plaster | 79 |
| | cement | 20 |
| | synthesized washing apart | 0.25 |
| | potassium alumin | 0.5 |
| | water (additional) | 79 |
| Ceramic wool | wood fiber (added) | 0.3 |
| Wet Natural sand (Nanking red sand) | water content | ~6 |

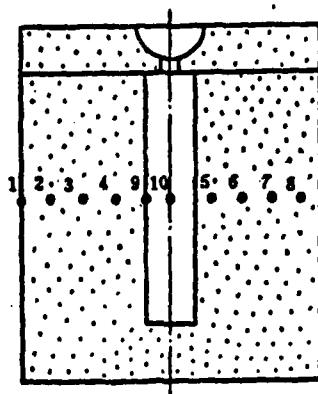
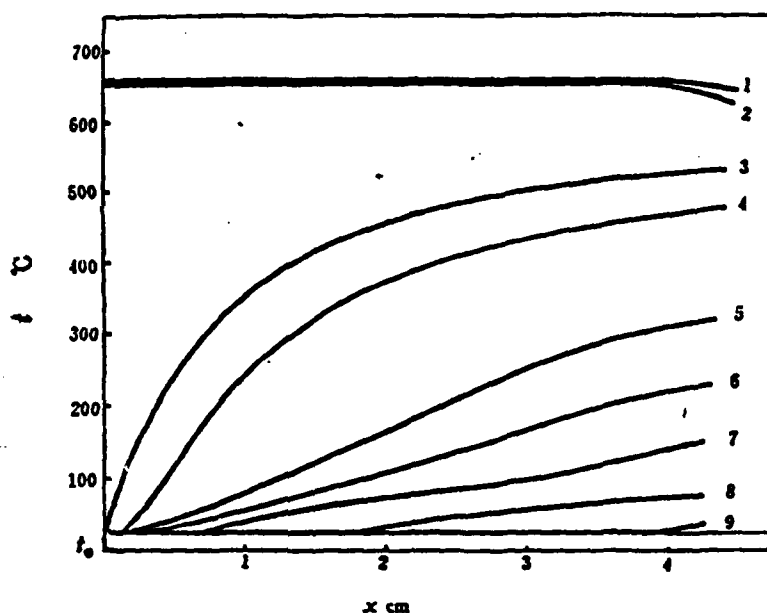


Figure 2. Distribution of thermocouples in the mode.

(3 ~ 5°C). The cooling curve of the casting was obtained using a two-channel high speed recorder. The heating curves of the mode were obtained using two 12-channel recorders. Figure 3 is the temperature - time curve of a 6 x 160 x 200 mm³ aluminum plate during the freezing process after poured into a perlite mode.



1. 铸件中心: 2. 界面: 以下热电偶均在型内;
 3. 距界面 4.5 毫米: 4. 距界面 7.5 毫米: 5. 距界面 13 毫米: 6. 距界面 19 毫米;
 7. 距界面 21.5 毫米: 8. 距界面 29.5 毫米: 9. 距界面 40 毫米: 铸件尺寸: 6×160×200 毫米

Figure 3. Cooling curves of the casting and heating curves of the mode for a pure aluminum plate casting.

Key: 1. center of the casting, 2. boundary, The following thermocouples are in the mode: 3. 4.5 mm from boundary, 4. 7.5 mm from boundary, 5. 13 mm from boundary, 6. 19 mm from boundary, 7. 21.5 mm from boundary, 8. 29.5 mm from boundary, 9. 40 mm from boundary. Dimensions of casting: 6 x 160 x 200 mm.

EXPERIMENTAL RESULTS AND DISCUSSION

Figure 3 shows that the surface temperature of the flat plate casting was very close to the freezing temperature during the entire solidification process. Since the surface temperature remained constant, there was no gap formation due to the shrinkage of the casting. Therefore, the assumption that there is ideal contact between the casting and the mode is reasonable. It can be approximated that the boundary temperature is the freezing temperature of pure aluminum during the solidification process.

The data points in Figure 4 are the actual temperatures measured in a pearlite mode when freezing was completed. When

equation (1) was used to approximate the actual temperature distribution, we get the following:

$$t = 26 + (659 - 26) \left(1 - \operatorname{erf} \frac{x}{\sqrt{5.37}} \right)$$

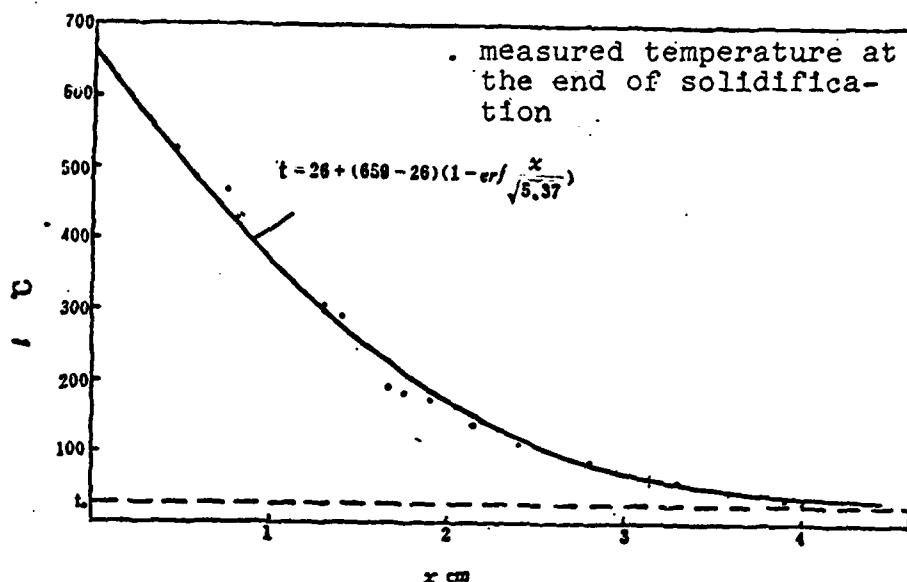


Figure 4. Comparison of actual temperature distribution and equation (1) in a pearlite mode.

The above demonstrates that the theoretical curve is very consistent with the measured points. The theoretical temperature is slightly higher close to thermal penetration thickness X_2 as shown in Figure 4.

When equation (4) is used to calculate the thermal coefficients, it is most important to determine the exponent n . Anisovich [10] recommended the use of an average value of n from a few arbitrary measured points. From our test analysis, this average n value is going to lead to larger errors in calculation, because these exponents are quite different from one another. If n is determined using a reverse analysis method, then results obtained using equation (4) are very close to those determined experimentally (see Figure 5).

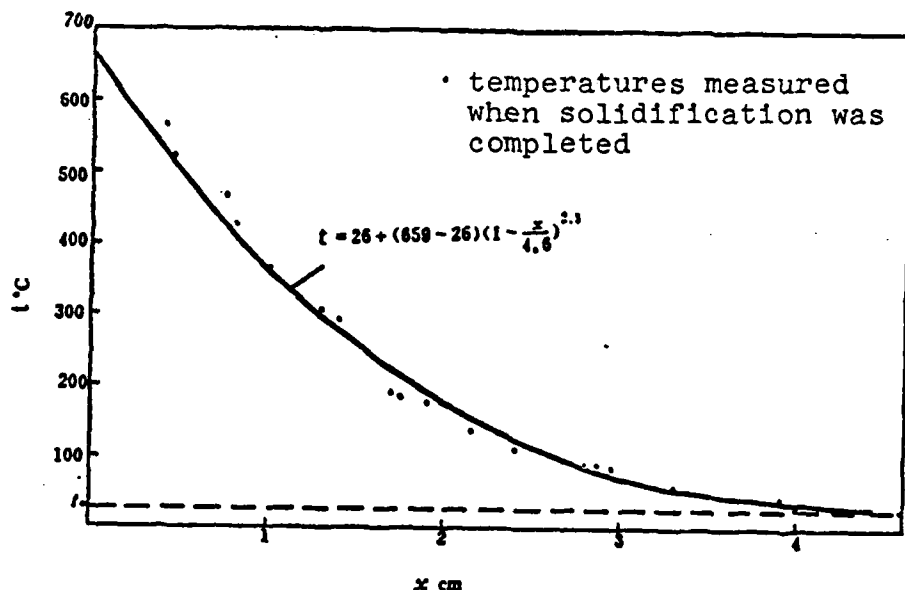


Figure 5. Comparison of temperature distributions obtained experimentally and using equation (4).

The thermal coefficients of the pearlite mode were calculated using equations (1), (3) and (4), (5) and are tabulated in Table 2. It can be seen that the two methods bring about very similar results.

Table 2. Calculated Thermal Coefficient of Pearlite Mode ($\gamma_2 = 240 \text{ kg/m}^3$).

| Method | α_2 m^2/hour | b_2 $\text{Kcal/m}^2 \cdot \text{hour}^{1/2} \cdot ^\circ\text{C}$ | c_2 $\text{Kcal/kg}^\circ\text{C}$ | λ_2 $\text{Kcal/m} \cdot \text{hour } ^\circ\text{C}$ |
|-------------------|--|---|---|--|
| Equation (1), (3) | 0.00202 | 4.00 | 0.373 | 0.179 |
| Equation (4), (5) | 0.00182 | 3.78 | 0.368 | 0.162 |

Table 3 lists the thermal coefficients of modes of the three insulating materials and wet sand. The data for wet mode and foamed plaster which undergo phase changes upon heating is obtained using the Veinik [11] method.

Table 3. Thermal Coefficients of Insulator and Wet Sand Modes

| Material | α_2 m ² /hour | b_2 Kcal/m ² . hr. 1/2°C | c_2 Kcal/kg. °C | λ_2 Kcal/m. hr. °C | γ_2 Kg/m ³ |
|-----------------------|------------------------------------|---|-------------------------|----------------------------------|---------------------------------|
| Expansion pearlite | 0.0018- 0.0021 | 3.8- 4.2 | 0.36- 0.38 | 0.16- 0.18 | 230-250 |
| Foamed Plaster | 0.0010- 0.0017 | 6.0 6.6- | 0.30 0.36 | 0.21 0.26 | 510-550 |
| Ceramic Wool | 0.0013- 0.0017 | 3.0- 3.5 | 0.37- 0.40 | 0.11 0.14 | 210-230 |
| Wet Sand | 0.0007- 0.0013 | 18- 22 | 0.36- 0.52 | 0.56 0.71 | 1580-1630 |

Among these materials, ceramic wool has the best insulating properties. Its thermal storage coefficient is 1/6 of that of wet sand. Pearlite and foamed plaster have 1/5 and 1/3 of the thermal storage coefficient of the wet sand, respectively. Since the specific heat is not too different among these materials (the specific heat of a wet sand mode is related to its water content). Thermal conductivity and weight are major factors in the determination of heat storage coefficient.

III. The Design of Conventional and Insulated Risers.

The objective of riser design is to ascertain the proper position and dimensions of the riser. For insulated risers, the rules used in determination of position basically are

identical to those for the conventional risers. As for the dimensions of insulated risers, the popular method [3,5,6,7] involves the calculation of a riser modulus through the use of some surface coefficients. For example, the riser modulus for a cylindrical insulated riser is

$$M = \frac{RH}{2Hx + Ry} \quad (9)$$

where M - modulus R - riser radius
H - riser height X - side coefficient y - top coefficient

This method appears to be simple, but it fails to establish any relationship between the surface coefficients and the thermal characteristics of the insulating materials. In addition, the volume of the riser may or may not be sufficient to compensate for metal shrinkage.

For pure metals and alloys with narrow crystallization temperature bands, the two following conditions must be considered in the derivation of design equations of risers:

1. The freezing time of the riser should be greater or at least equal to that of the casting.
2. The riser should contain sufficient amounts of metal to compensate for shrinkage of the casting.

The freezing time of the riser or the casting can be approximately expressed as

$$\tau = \left(\frac{M}{K}\right)^2 \mu_s \cdot \mu_h \cdot \mu_g \cdot \mu_{\Delta t}$$

where τ - freezing time μ_h - superheat coefficient
 μ_s - geometric coefficient μ_g - gap coefficient

μ_{sk} - crystallization temperature band coefficient

K - solidification coefficient, it can be derived from the following conditions: Crystallization temperature band is zero, no superheat, and ideal contact between plate-casting and mode.

The gas gap problem in sand modes can be neglected and μ_g is taken as 1. Since generally the riser and the casting are poured from the same melt, the first condition mentioned above can be written as

$$\left(\frac{M_r}{K_r}\right)^2 \mu_{sr} \cdot \mu_{hr} \geq \left(\frac{M_c}{K_c}\right)^2 \mu_{sc} \cdot \mu_{hc} \quad (10)$$

Because the metallic volume of the riser decreases during the solidification process, it is more reasonable to take the the volume after the solidification process is completed in the calculation of riser modulus. The riser volume thus calculated already includes some extra amount and equation (10) can be substituted by:

$$\left(\frac{V_{rf}/A_r}{K_r}\right)^2 \mu_{sr} \cdot \mu_{hr} = \left(\frac{V_c/A_c}{K_c}\right)^2 \mu_{sc} \cdot \mu_{hc} \quad (11)$$

$$\frac{V_{rf}}{A_r} = \frac{V_c}{A_c} \frac{K_r}{K_c} \cdot f_s \cdot f_h$$

where V - volume A - surface area available for heat dissipation

f - geometric factor = $\sqrt{\frac{\mu_{sc}}{\mu_{sr}}}$

V_{rf} - residual metal volume at the riser

f_h - superheat factor = $\sqrt{\frac{\mu_{hc}}{\mu_{hr}}}$

The solidification coefficient of sand castings can be expressed as

the dimensions are $\phi = 90 \times 120$. But the calculated riser dimensions will enable the castings to get sufficient shrinkage compensation.

Equation (14) was used to calculate pearlite insulated risers. Wet mode was used in casting. The top of the riser was covered by a layer of pearlite after pouring. Let $b_r = 4.2 \text{ Kcal/m}^2\text{hr}^{1/2}\text{°C}$, $b_c = 20 \text{ Kcal/m}^2\text{hr}^{1/2}\text{°C}$, and $H/D = 1$, the riser dimensions are $\phi 53 \times 53$ based on Equation (14). Considering that the insulated cover was thinner (15, 25, and 35 mm) than the heat penetration thickness during solidification we chose a $\phi 60 \times 60$ insulated riser. Experimental results show that they can all be used to replace the conventional sand mode riser. Insulated covers made of foamed plaster and ceramic wool can achieve the same satisfactory results. Their dimensions are $\phi 60 \times 60$ and $\phi 57 \times 57$, respectively. Figure 6 compares the conventional risers with the insulated risers.

VI. Theoretical Estimation of the Effectiveness of Insulated Risers

Has the extreme of insulated risers been reached in the experimental results for pure aluminum? How small can insulated risers be for other alloys? To answer these questions, it is necessary to theoretically estimate the effectiveness of the insulated risers. For that we introduce the concept of riser metal utilization rate. It is the ratio of the shrinkage cavity volume and the initial volume. There is not yet an accurate method to determine the volume of the shrinkage cavity. It can be approximately considered using the equation of a parabola:

$$V_s = \frac{1}{24} \pi D^2 H_s$$

where V_s and H_s are the volume and depth of the shrinkage cavity, respectively.

AD-A115 866

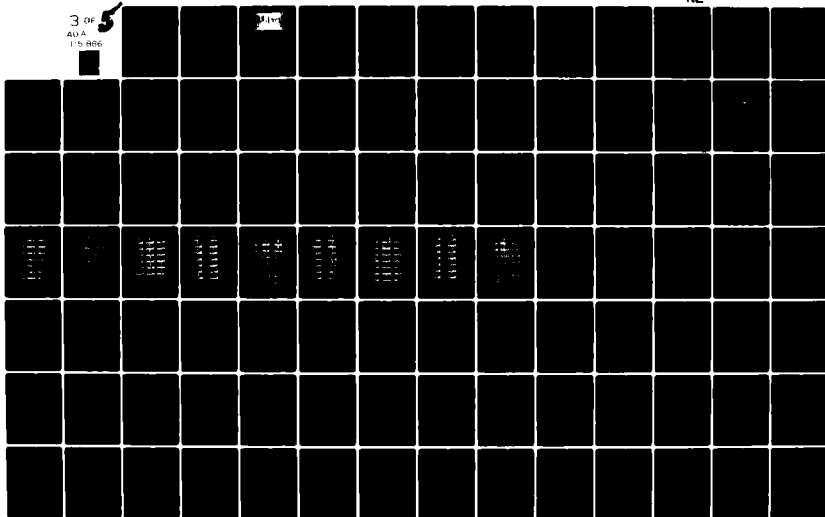
FOREIGN TECHNOLOGY DIV WRIGHT-PATTERSON AFB OH
RECENT SELECTED PAPERS OF NORTHWESTERN POLYTECHNICAL UNIVERSITY--ETC(U)
AUG 81

F/G 20/4

UNCLASSIFIED FTD-ID(RS)T-0260-81-PT-2

NL

3 OF 5
AD-A
1-5 866



$$(1 - \beta) \frac{V_r}{V_s} = \frac{A_{rs} \cdot b_{rs} + A_{rt} \cdot b_{rt}}{A_s \cdot b_s} f_s \cdot f_s + \beta \quad (16)$$

where A_{rs} - side area of the riser
 A_{rt} - top area of the riser
 b_{rs} - thermal storage coefficient of the side insulating material
 b_{rt} - thermal storage coefficient of the top insulating material

These riser design equations are experimentally verified using 100 x 100 x 100 mm cubic castings. Since the physical coefficients and thermal coefficients of pure aluminum are more precisely known, it was chosen as the test metal. We approximately selected the solidification shrinkage as β (6.6% for aluminum) and neglected liquid phase shrinkage and metal freezing during pouring, two counter-acting secondary factors. Geometric factors and superheat factors can be obtained in the literature [8,13]. In our calculations they were both assumed to be 1. The results obtained using equation (15) for the dimensions of a cylindrical sand mode riser are tabulated in Table 4.

Table 4. Calculated Dimensions of Riser for Cylindrical Sand Mode

| | | | |
|-------|-----|-----|------|
| D/H | 1.2 | 1 | 0.8 |
| D, mm | 108 | 114 | 1.24 |
| H, mm | 130 | 114 | 100 |

From the results obtained using pure aluminum poured at 760°C, conventional sand mode riser is not large enough when

the dimensions are $\phi = 90 \times 120$. But the calculated riser dimensions will enable the castings to get sufficient shrinkage compensation.

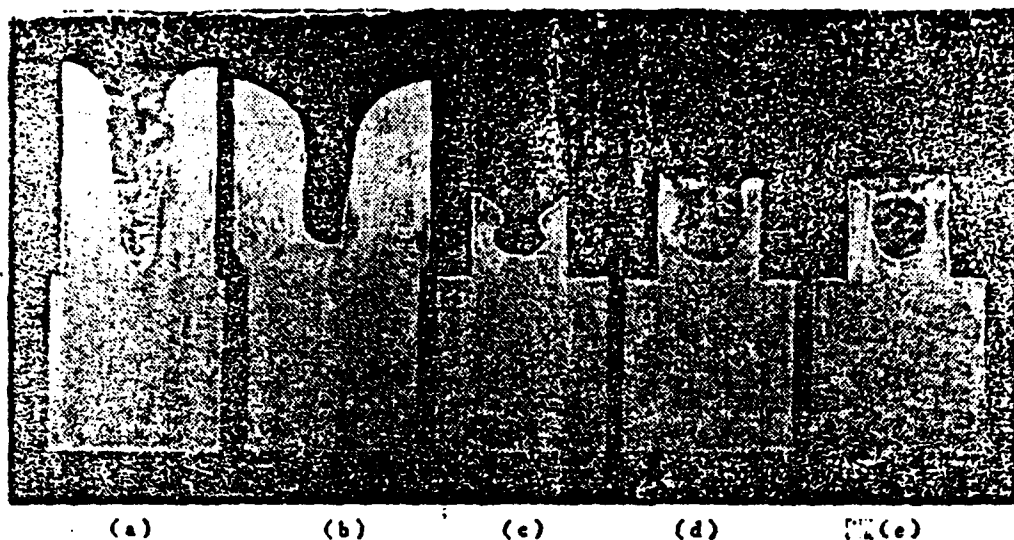
Equation (14) was used to calculate pearlite insulated risers. Wet mode was used in casting. The top of the riser was covered by a layer of pearlite after pouring. Let $b_r = 4.2 \text{ Kcal/m}^2\text{hr}^{1/2}\text{C}$, $b_c = 20 \text{ Kcal/m}^2\text{hr}^{1/2}\text{C}$, and $H/D = 1$, the riser dimensions are $\phi 53 \times 53$ based on Equation (14). Considering that the insulated cover was thinner (15, 25, and 35 mm) than the heat penetration thickness during solidification we chose a $\phi 60 \times 60$ insulated riser. Experimental results show that they can all be used to replace the conventional sand mode riser. Insulated covers made of foamed plaster and ceramic wool can achieve the same satisfactory results. Their dimensions are $\phi 60 \times 60$ and $\phi 57 \times 57$, respectively. Figure 6 compares the conventional risers with the insulated risers.

VI. Theoretical Estimation of the Effectiveness of Insulated Risers

Has the extreme of insulated risers been reached in the experimental results for pure aluminum? How small can insulated risers be for other alloys? To answer these questions, it is necessary to theoretically estimate the effectiveness of the insulated risers. For that we introduce the concept of riser metal utilization rate. It is the ratio of the shrinkage cavity volume and the initial volume. There is not yet an accurate method to determine the volume of the shrinkage cavity. It can be approximately considered using the equation of a parabola:

$$V_s = \frac{1}{24} \pi D^2 H_s$$

where V_s and H_s are the volume and depth of the shrinkage cavity, respectively.



(a), (b) - 普通冒口 $\phi 90 \times 120$, $\phi 114 \times 114$ 毫米。

(c) - 陶瓷棉保温冒口 $\phi 57 \times 57$ 毫米 (d) - 珍珠岩保温冒口 $\phi 60 \times 60$ 毫米

(e) - 发泡石膏保温冒口 $\phi 60 \times 60$ 毫米 铸件尺寸: $100 \times 100 \times 100$ 毫米

Figure 6. Comparison of Conventional and Insulated Risers. (a), (b) - conventional riser, $\phi 90 \times 120$, $\phi 114 \times 114$ mm, (c) - ceramic wool riser $\phi 57 \times 57$ mm, (d) pearlite riser $\phi 60 \times 60$ mm, (e) - foamed plaster riser 60×60 mm casting dimensions: $100 \times 100 \times 100$ mm.

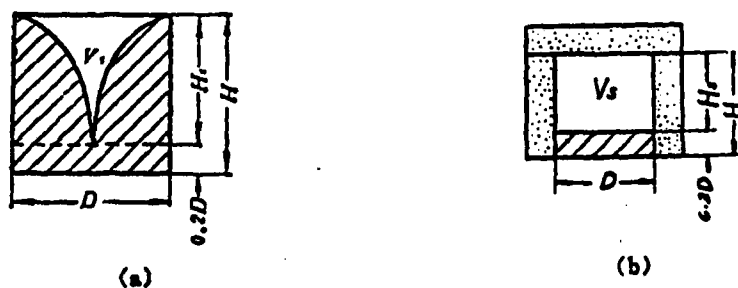


Figure 7. Shrinkage cavities of (a) conventional riser and (b) ideal insulated riser.

For a cylindrical conventional riser with height equal to its diameter and shrinkage cavity depth equal to $0.8D$ (see Figure 7-a), the metal utilization rate is:

$$\eta = \frac{V_s}{V_r} = \frac{\frac{1}{24} \pi D^2 \cdot 0.8D}{\frac{1}{4} \pi D^3} = 13.3\%$$

The shrinkage cavity of an ideal insulated riser can be considered as a hollow cylinder (see Figure 7-b). Under similar conditions ($H/D=1$ and riser base height equals to $0.2D$), the metal utilization rate is

$$\eta = \frac{\frac{1}{4} \pi D^2 \cdot 0.8D}{\frac{1}{4} \pi D^3} = 80.0\%$$

This is the maximum value for metal utilization rate under such conditions.

Metal utilization rate varies with the ratio of riser height and diameter. From Table 5, it can be concluded that short and thick risers tend to have low metal utilization rates. This is especially true for insulated risers.

Table 5 Riser Metal Utilization Rate

| H/D | 1.2 | 1.0 | 0.8 |
|------------------------------|------|------|------|
| Conventional sand mode riser | 13.9 | 13.3 | 12.5 |
| η Ideal Insulated Riser | 83.3 | 80.0 | 75.0 |

If the volume of the shrinkage cavity is expressed by

$\beta(V_r + V_c)$, then

$$\eta = \frac{\beta(V_r + V_c)}{V_r} \quad (17)$$

after rearrangement:

$$\frac{V_r}{V_c} = \frac{\beta}{\eta - \beta} \quad (18)$$

Based on the definition of actual casting yield (ratio of the weight of the casting and weight of the casting plus that of the riser):

$$\alpha = \frac{V_c}{(1-\eta)V_r + V_c} = \frac{1}{(1-\eta)\frac{V_r}{V_c} + 1}$$

where α is the casting yield.

Substituting Equation (18) into the above and simplifying it, we get

$$\alpha = \frac{\eta - \beta}{\eta(1 - \beta)} \quad (19)$$

Using Equations (18) and (19) and taking β approximately as the solidification shrinkage rate of the metal, the yields and volume ratios of conventional and ideal insulated risers can be estimated. For cylindrical risers ($H/D=1$, riser base height = $0.2D$) used in the casting of pure aluminum and steel, the calculated results are tabulated in Table 6.

Table 6. Yields and Volume Ratios of Conventional and Ideal Insulated Risers

| Metal | β | V_r/V_c | V_{r1}/V_c | $\alpha\%$ | $\alpha_1\%$ | V_{r1}/V_{c1} |
|----------|---------|-----------|--------------|------------|--------------|-----------------|
| Aluminum | 0.066 | 0.985 | 0.090 | 53.9 | 98.2 | 10.9 |
| Steel | 0.030 | 0.291 | 0.039 | 79.8 | 99.2 | 7.5 |

subscript 1 is designated for insulated risers..

Table 6 demonstrates that the use of an insulated riser can reduce the volume of the riser by about 11 times for aluminum and 7.5 times for steel. Simultaneously, the yields can be increased by 44.3% and 19.4%, respectively. Our experimental pure aluminum cubic casting used pearlite and foamed plaster risers approximately 7 times smaller than the conventional riser. The ceramic wool riser was 8 times smaller. Yields were increased by 33% and 35%.

The economic incentive for use of insulated risers is to increase productivity, to save the expenses in melting and cutting of metals, and to reduce waste of metals during cutting of risers. Aluminum and steel castings using insulated risers ($H/D=1$) can achieve the following optimal objectives (Table 7):

Table 7 Estimated Maximum Effectiveness of Insulated Risers

| Item | | Aluminum | Steel |
|---|---|----------|-------|
| Savings in Metal Melting | $= \frac{V_r - V_{r1}}{V_c + V_r} = \frac{V_r/V_c - V_{r1}/V_c}{1 + V_r/V_c}$ | % 45.1 | 19.5 |
| Savings in Riser Cutting | $= \frac{\pi R^2 - \pi R_1^2}{\pi R^2} = 1 - \left(\frac{V_{r1}}{V_r}\right)^{2/3}$ | % 79.7 | 73.8 |
| Reduction in Waste During Riser Cutting | $= 1 - \left(\frac{V_{r1}}{V_r}\right)^{2/3}$ | % 79.7 | 73.8 |

Tables 6 and 7 are compiled based on conventional and insulated risers with $H/D=1$ and riser base height = 0.2D. If insulated risers with $H/D=1.2$ is used to replace conventional risers with $H/D=1$, the results are more pronounced. For aluminum and steel, insulated risers can be smaller than conventional ones by 11.5 and 7.9 times, respectively.

Conclusions

1. Equations $t - t_0 = (t_s - t_0) \left(1 - \operatorname{erf} \frac{x}{\sqrt{4\alpha\tau}} \right)$ and $t - t_0 = (t_s - t_0) \left(1 - \frac{x}{x_s} \right)$ can both be used to calculate the thermal coefficients on insulating materials without phase change. The second equation requires the determination of exponent n using a reverse analysis method.
2. Based on the average thermal coefficients between room temperature and 659°C , ceramic wool has the best thermal retention property among the materials tested and pearlite and foamed plaster are next.
3. The pure aluminum cubic casting experiment demonstrated that the use of insulated material can reduce the riser volume by a factor of 7-8.
4. The general riser design equation $(1-\beta) \frac{V_r}{V_c} = \frac{A_r}{A_c} \frac{b_r}{b_c} f \cdot f_1 + \beta$ also applies to the sand castings which tend to form concentrated shrinkage cavities.
5. Introducing the concept of metal utilization coefficient, we can approximately estimate the maximum benefits attainable by using insulated risers. Due to the tremendous benefits in saving energy and labor, it is expected that further development in the use of insulated risers will continue.

References

- [1] Brown J. et al, Determination of the Thermal Efficiency of Some Insulating Materials for Feeding, *The British Foundryman*, Vol. 65, No. 7 (1972), pp. 254-264.
- [2] Prasad, M. Rama et al, Properties of Vermiculite—A Material for Insulating Feeder Heads, *Cast Metals Research Journal*, Vol. 10, No. 4 (1974), pp. 171-177.
- [3] Corbett, C. F., The Use of Insulating Materials for Feeder Heads in Steel Castings, *The British Foundryman*, Vol. 67, No. 4 (1974), pp. 106-115.
- [4] Rao, G.C.Kutumba et al, Effect of Insulating Sleeves on Feeding of Aluminum—12% Silicon Alloy Plate Castings, *AFS Transactions*, Vol. 83 (1975) pp. 525-530.
- [5] Ruddle, R.W., Riser Aids in Steel Foundry Practice, *AFS Transactions*, Vol. 83 (1975) pp. 577-584.
- [6] Atterton, D.V. et al, Methods and Materials Promoting the Feeding of Steel Castings, *Russian Casting Production*, No. 7 (1976), pp. 19-21.
- [7] Umble, A.E., Insulated Risers for Large Steel Castings, *AFS Transactions*, Vol. 84 (1976) pp. 49-54.
- [8] Poirier, D.R. and Gandhi, N.V., Optimization of Riser Designs with Insulating Sleeves to Achieve Minimum Cost, *AFS Transactions*, Vol. 84 (1976), pp. 577-584.
- [9] Veinik, A.I., *Approximate Calculation of Heat Conduction Processes*, Moscow (1959).
- [10] Anisovich, G.A. and Grinkevich, R.N., Method for Determination of the Thermal Properties of Mold Materials, *Problems of Heat Transfer in Foundry*, Minsk (1960), pp. 81-87.
- [11] Veinik, A.I., *Theory and Calculation for the Solidification of Casting in Sand Mold*, Technology of Casting Mold, Moscow (1954), pp. 20-33.
- [12] Adams, C.M. and Taylor, H. F., Fundamentals of Riser Behavior, *AFS Transactions*, Vol. 61 (1953), pp. 686-693.
- [13] Sciama, G. and Jeancolas, M., Solidification Times of Simple Shaped Castings, *Cast Metals Research Journal*, Vol. 9 No. 1 (1973), pp. 1-7.

Summary

A Study on Insulated Risers

Zhou Yaohe, Zhang Yanwei, Qu Weitao, Lin Zaixue,

Mao Zhiying, Wang Youxu, Niu Jingxin, and Zhang Qixun

Conventional large risers of sand castings have been responsible for low casting yield. More and more attention has been paid recently to insulated risers on account of their effectiveness in saving energy and labor.

By using the unsteady state method involving melting and casting, this investigation has determined the mean thermal coefficients for the range from room temperature to 659°C. of three insulating materials — pearlite, foamed plaster, and ceramic wool. Length and width of the plate-shaped test castings are designed to be much larger than their thicknesses, consequently the heat transfer may be considered as an one dimensional problem. When pure aluminum at very low superheat is poured to obtain a plate casting, its freezing point can be taken as the boundary temperature during the solidification stage. For materials which, upon heating, suffer no phase change, the equation $t - t_0 = (t_s - t_0) \left(1 - \operatorname{erf} \sqrt{\frac{x}{4\alpha\tau}} \right)$ is used to approximate

the true temperature distribution. Another method is to approximate the mold temperature distribution by a n th degree parabola. In this case, the rational determination of the exponent n is of paramount importance, and it is recommended that n be found by a regression technique.

The prevailing practice in the design of insulated risers is to make use of some surface coefficients when the riser modulus is to be calculated. Although the method is simple, the relationship between surface coefficients and thermal properties of insulating materials has not yet been established. Besides, the problem of ascertaining whether the riser is large enough to compensate for the shrinkage in volume of the casting remains unsolved. Chvorinov's rule modified by shape and superheat coefficients is adopted by the authors to evaluate the solidification time of the casting and the riser. For sand castings which tend to form concentrated shrinkage, the generalized equation for the design of risers is of the form

$$(1 - \beta) \frac{V_r}{V_s} = \frac{A_r}{A_s} \frac{b_r}{b_s} f_s \cdot f_h + \beta$$

where b_r, b_c are heat diffusivities of the mold materials for the riser and the casting respectively, f_s is the surface coefficient, and f_A is the superheat coefficient.

When both shape and superheat coefficients are assumed to be unity and both casting and riser are molded from the same material, the above equation will reduce to the expression derived by Adams and Taylor. Riser dimensions calculated from these equations agree closely with the experimental results on pure aluminum cube castings. The size of the risers insulated with pearlite or foamed plaster is about one seventh that of the conventional sand risers; that of the risers insulated with ceramic wool, only one eighth. Casting yields are increased by 33% and 35% respectively.

In order to predict the benefits to be gained through the use of insulated risers, the concept of metal utilization coefficient of the riser, which is defined as the ratio of its shrinkage cavity volume to the original riser volume, has been introduced. The shrinkage cavity volume of a conventional riser can be calculated approximately by using the equation of a parabola, while that of an ideal insulated riser may be taken as a hollow cylinder. Under these conditions, the metal utilization coefficients and the casting yields can be found, and it is then possible to predict the maximum benefits of the insulated risers. The effectiveness of the insulated risers depends to a great extent on the coefficient β — the fraction of feed metal needed. For example, the insulated riser of a pure aluminum casting may be one eleventh the volume of the conventional one due to its large solidification shrinkage, while in the case of steel the volume can only be reduced to 1/7.5. Through the use of insulated risers the savings in metal melting and riser removal costs can be predicted by using respectively the expressions

$$\frac{\frac{V_r}{V_c} - \frac{V_{r1}}{V_c}}{1 + \frac{V_r}{V_c}}$$

and

$$1 - \left(\frac{V_{r1}}{V_r} \right)^{1/3}.$$

THE STUDY ON TECHNOLOGICAL FUNDAMENTALS OF PULSED SPRAY
TRANSFER ARC WELDING (IV) -- OBSERVATIONS ON ARC PHENO-
MENA IN THE CASE OF STABLE WELDING CONDITION (REPORT I)

Duan Liyu, Cheng Gongshou, Feng Jijiang, Wang Xuxi and
Lu Xuezheng

ABSTRACT

This paper is one of the experimental research reports on the observations made on arc phenomena in the case of stable arc conditions of pulsed spray transfer arc welding. Based on a large quantity of high speed photographic pictures and synchronous oscillograms of the arc parameters, this paper qualitatively described the arc phenomena, such as arc forming, droplet transfer and sputter at representative test condition points. It attempted to analyze the droplet "transfer-back" problem in a pulsed arc. On the basis of experimental results obtained from nearly 50 test condition points, the authors made a preliminary evaluation of the principle that "the frequency of droplet transfer must be synchronous with that of the current pulse" stated in the foreign literature. It clearly pointed out that the combined condition to obtain both synchronous transfer and that for a synchronous transfer possess a corresponding application range of its own. Therefore, both of them can be a choice method. The authors believe that the concept of the so-called "pulse current controlled transfer (or controllable transfer)" should be extended. That is that droplet transfer and pulse current (not the frequency of the pulse current) are synchronous and a periodic reappearance property exists.

I. INTRODUCTION

Currently, the experimental research on spray transfer arc welding has been extended into the area of production of some important welded structures. Therefore, more stringent requirements are specified with regard to the performance and quality control using the pulse current during the welding process.

In foreign countries, it is in the literature [1] that the arcing process obtained by synchronizing droplet transfer with the frequency of pulse current (i.e., one pulse per droplet transfer or synchronous transfer for short) is the optimal pulse current control level. It seems that this is a principle which must be obeyed in the pulse current control technique applied to the melting electrode gas protection welding technology. Some papers in the literature even established the optimal combination condition and the relevant stable arc condition range based on such a principle.

On the basis of our actual experience on the experimental research and wide application in the pulsed spray transfer arc welding technology during the past several years, we feel that the synchronous control of pulse current with droplet transfer may not be the optimal method for every welding technology. Therefore, it is not a principle to be strictly followed. In some actual applications, the condition combination under which droplet transfer does not synchronize with the pulse frequency can obtain more satisfactory results.

The objective of this special topic experimental research work was to observe the relevant arc phenomena, such as arc forming, droplet transfer and sputter, etc. at those representative condition points in the specified stable arc condition zones documented in reference [2]. We wished that on the basis of this study we would be able to bring about the practical correction to the principle that synchronous transfer must be obtained in an arc process.

II. EXPERIMENTAL APPARATUS AND METHOD

The experimental apparatus adopted was a wave chopping type melting electrode pulsed argon arc welder developed by the Northwest Industrial University [3]. The experimental technological conditions were the same as stated in reference [2], i.e.,

Base material: 30 CrMnSiA steel, $\delta = 5$ mm;

Protective gas: Ar + 5.2% CO₂;

Distance between nozzle and the working surface: 14 mm;

Filament: H10Mn2SiCrMoVA, ϕ 1.6 mm;

Pulsing frequency: 50 cycle/sec;

Weld: flat plate pile weld.

Before the experiment, testing condition points were chosen in the stable arc condition region. The distribution of these points is shown in Figure 1. A total number of 50 condition points is used.

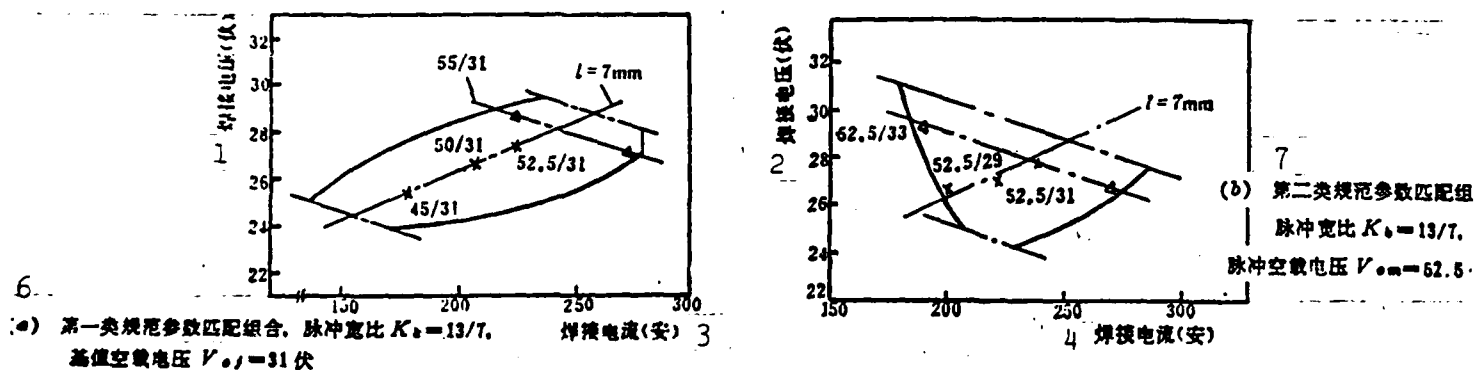


Figure 1. Example of distribution of testing condition points

1--welding voltage (volts); 2--welding voltage (volts); 3--welding current (amperes); 4--welding current (amperes); 6--(a) first type of condition parameter combination, pulse width ratio $K_p = 13/7$, no load base value vsltage $V_{oJ} = 31$ volts; 7-- (b) second type of condition parameter combination, pulse width ratio $K_p = 13/7$, no load pulse voltage $V_{om} = 62.5$ volts

In the selection of condition points, the following combination was included:

1. Under the condition of fixed no load base value voltage (31 volts) and pulse width ratio ($K_p=13/7$), various condition points were obtained through the adjustments of no load pulse voltage and filament feeding speed (see Figure ([a])). It also included several points with constant arc length (u mm);

2. under the condition of fixed no load pulse voltage (52.5 volts) and pulse width ratio ($K_p=13/7$), various condition points were obtained through the adjustments of no load base value voltage and filament feeding speed (see Figure ([b])). It also included several points with constant arc length (7 mm).

For each selected condition point*, welding was performed. High speed photography, synchronous oscilloscope as well as arc observation and photographic optical systems were used to record the kinetic status, the visual arcing process and the arc parameter oscillogram.

III. PULSED SPRAY TRANSFER AND ARC FORMING

The so-called arc forming refers to the shape of the arc and its geometrical dimensional parameters.

It has already been known that for a fixed filament composition and diameter arc forming depends on the cooling effect on the arc due to the welding current and the protective gas.

Based on the minimum voltage principle postulated by Steenbeks [4,5], under fixed boundary conditions (composition and pressure of the protective gas) and at a fixed welding current, the electrical potential gradient X of the arc should have a minimum with respect to the radius r of a stable cylindrical arc or to the arc temperature T . That is

* For different pulse width ratio, pulsing frequency and CO_2 ratio, the results will be reported as a continuation of this special topic paper.

$$\frac{\partial X}{\partial r} = 0 \text{ or } \frac{\partial X}{\partial T} = 0 \quad (1)$$

The electrical potential gradient of the arc column of a free arc is a function of the electrical conducting properties of the ions in the arc. Therefore, it is also a function of the arc column temperature. The arc column temperature is determined by the energy balance of the entire arc column. Under the free arc condition, the loss of heat from the arc column is mainly due to conduction (radiation and convection are negligible) and it is proportional to the radius of the arc column. Therefore, with increasing current, the temperature of the arc column rises and the radius of the arc column increases correspondingly. As for the actual value of possible increase in the arc column radius, it should be determined by the minimum voltage principle.

During pulsed welding, the welding current varies in a pulse form. Therefore, the three parameters r , T and X used to express the property of the arc as well as the arc forming are all situated in a dynamically changing process. The usually observed visual forming of pulsed arc is nothing but a spectacular display of the cumulative dynamic processes.

Based on the above consideration, for the more practical description of our experimental results, we are going to divide the arc forming of a pulsed spray transfer into visual and dynamic types. Based on the cumulative principle in film exposure, we believe that under pulse current conditions the visual arc forming obtained through visual observation or using an optical system photographically (exposure time greater than pulse period) should correspond to the cumulative exposure appearance of the arc. The dynamic arc forming, however, should correspond to the variation process of the pulse current and it is quite different from the visual forming of the arc.

1. Visual forming of the arc

Through the observation and analysis of the arcing process with respect to approximately 50 testing condition points, it showed that the visual arc forming is different for various condition points. However, its shape follows a certain statistical rule. Figure 2 is a sketch of an example of the visual arc forming based on the movie film. From Figure 2, it is known that the visual forming consists of three parts: the arc center, the arc and the arc flame. The arc center is located at the middle. The arc flame is situated at the outer layer of the arc and the arc is in between the arc center and the arc flame. Because of the existence of large amounts of gas vapor in the arc center, the ionization level is the highest, the electrical conductivity is the best, and the current density is the highest. Therefore, its luminosity is the strongest. Experimental results indicated that its shape did not vary significantly with the condition points and it is approximately in cylindrical shape. The arc flame is in contact with the unmelted base material. Due to its low ionization level, its luminosity is the lowest and it is usually difficult to show. Through the use of high speed black-and-white as well as color photography and single frame color photography, our combined observation in both the dynamic and static modes showed that there were quite a lot of microscopic cathode spots which are usually in a fluctuating state on the surface of the base metal neighboring the edge of the arc crater (see note in Figure 2). It has been demonstrated (see reference [3]) that the study of cathode spots and their migration state provided first-hand information on the further understanding of the behavior of the cathode spots and the stabilization of the welding technology.

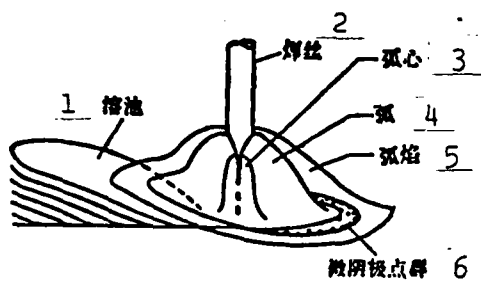
2. Dynamic forming of the arc

Because the arc has a fixed heat capacity (thermal inertia), the arc temperature is always lagging behind the variation in current. Under the condition that the thermal inertia of the arc is not considered, the variation process of the dynamic forming of a pulsed

arc in a cycle can be described by referring to photograph 1 as follows:

At the instance when the pulse current is impressed, current can only pass through a small area concentrating at the end of the filament, which means that the anode spot area is very small and the arc center appears to be cylindrical in shape. With increasing current, the area of the anode spot also increases, the diameter of the cylindrical arc center thickens and the luminosity increases. When the area of the anode spot expands to the entire tip of the filament and occupies the side surface of the filament, the filament melting process is accelerated. The liquid metal at the end of the filament under the electromagnetic force, which is proportional to the square of the instantaneous value of the pulse current, flows to the conical tip of the filament at high speed to form a droplet. At this time, the arc center covers the droplet and looks like a bell jar. With further increase in the pulse current, the cross section of the bell jar shaped arc center becomes thicker. The neck diameter becomes thinner and the size of the droplet is enlarging. As the first drop with its dimension comparable to the diameter of the filament falls near the peak value of the pulse current, the anode spot instantly moves up and occupies the position on the side of the liquid cone of the filament. The filament continues to melt and two smaller droplets are transferred. As the pulse current decreases, the area of the anode spot also decreases, the cross section of the arc center gradually shrinks into a cylindrical shape, and the brightness of the arc gradually darkens. After the pulse current is stopped, it transforms to the base value period. The process repeats itself in this manner alternately.

It should be noticed that, based on the additive principle of film exposure, there is a big difference in the display of the shape of the arc center between visual arc forming and dynamic arc forming. The shape of the arc center shown in Figure 2 is not the actual shape of a pulsed arc (refer to photograph 1). The real shape of the arc center is in a periodically varying dynamic process,



- 1--melt pool
- 2--filament
- 3--arc center
- 4--arc
- 5--arc flame
- 6--microscopic cathode spots

Figure 2. An example of the visual forming of the pulsed spray transfer arc.

Through the combined observation of the dynamic arc forming process at various condition points, the rules related to the variation of the shape of the arc center are obtained:

(1) During one pulsing cycle, there are two types of dynamic variation processes involved with the shape of the arc center.

First one is: cylindrical--bell jar shaped + cylindrical

Second one is: cylindrical--bell jar shaped-conical + cylindrical

(2) For all the testing condition points, if a drop with dimensions comparable to the diameter of the filament is formed and after the droplet has fallen, a thin long liquid cone cannot be formed at the end of the filament, the shape of the arc center appears to be like a bell jar in all cases. Bell jar shaped arc centers usually correspond to the condition points of the one pulse per droplet transfer or the one pulse multiple droplets transfer (see photographs 1 and 2).

(3) Whether the shape of the arc center is going to transform from a bell jar-like shape to a conical one depends on the magnitude of the energy coefficient of the pulses. When the pulse energy coefficient is large, after the first droplet has fallen, the liquid metal at the end of the filament appears to be in thin long conical shapes. The anode spot rapidly occupies the side surface of the liquid cone and a conical arc center formation is an apparent result. Usually, the conically shaped arc center corresponds to the pulsed

spray transfer condition points (as shown in photographs 7 and 9).

(4) Under the condition that the pulse energy is too low, before the neck-shrinking process of the droplet at the end of the filament occurs, the shape of the arc center is cylindrical. After several pulses, the droplet grows larger, the neck-shrinking process has occurred and the anode spot covers the droplet. The arc center at this time looks like a bell jar (as shown in Figure 3).

Cylindrical arc center usually corresponds to the multiple pulse single droplet transfer condition points.

(5) Therefore, based on the difference in the energy coefficient of the pulse, the arc center variation process does not necessarily follow the cylindrical-bell jar shaped → conical-cylindrical format.

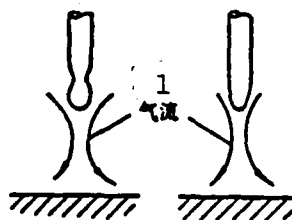
There is some difference in the shape of the arc center for free arc burning in the atmosphere. It is related to the fluid dynamics inside the arc. It is well known that in gas protective welding there is a gas flow in the arc. This flow (also known as the branch flow of the equi-ionic flow) enters the arc near the electrode and leaves the arc radially near the surface of the base material (as shown in Figure 3). This high speed equi-ionic gas flow has a cooling effect on the arc. It is also one of the reasons that the arc in gas protective welding has an ascending static characteristic. Since the ionic gas flow diffuses radially from the electrode towards the base material, the electrically conducting cross section of the arc also correspondingly becomes larger gradually from the electrode toward the base material. Usually, the observed bell jar or conically shaped electrically conducting arc center is a result of the fluid dynamic flow inside the arc [6].

Experimental results indicated that the expanding droplet at the end of the filament would interfere with the downward motion

of the equi-ionic gas flow which causes the irregular distortion and thickening of the arc. As an example, when the droplet at the end of the filament suddenly expands and the droplet just so happens to be located symmetrically at the center of the arc column, the arc center instantaneously thickens uniformly (see photograph 8). When the expanding droplet tilts to one side, the arc center also tilts to the droplet side. When the expanding droplet bursts, the arc center creates a sudden distortion and some irregular oscillation also exists [7]. Therefore, it can be concluded that the geometrical shape of the liquid metal at the end of the filament also has some effect on the forming of the arc center. When a droplet of the same dimension as the diameter of the filament is formed, the arc center becomes thicker in bell jar shape because the equi-ionic gas flow is blocked and scattered. On the contrary, when the liquid metal at the end of the filament is in conical shape, the equi-ionic gas flow is first concentrated in the electrode area and then diffused which makes the arc center appear in conical shape.

Figure 3. The fluid dynamic flow inside an arc of high strength.

1--gas flow



IV. CHARACTERISTICS OF DROPLET TRANSFER

The results obtained from the observation and analysis on the droplet transfer at various testing condition points showed that there existed several mutually related types:

(1) No matter whether droplet transfer synchronizes with the frequency of the pulse, it can be divided into synchronous and asynchronous transfers. The latter also includes two situations. The first is that one pulse transfers several droplets. The second is that two pulses transfer only one droplet.

(2) On the basis that whether the droplet transfer is on the same axis as the filament, it can be divided into axial transfer and non-axial transfer.

(3) On the basis of the diameter of the droplet transfer, it can be divided into pulsed spray transfer and pulsed jet transfer.

(4) On the basis of the length of the arc during stable spray transfer, it can be divided into long arc pulsed spray transfer and short arc pulsed spray transfer.

Based on statistics, out of nearly 50 condition points, there are very few condition points at which synchronous transfer can be obtained. One of the examples is shown in photograph 2. The condition points which lead to the transfer of one droplet by two pulses is also very limited. One example is shown in photograph 3. The majority of the condition points correspond to the two or more droplets per pulse situation (see photograph 1). The difference discussed above in the characteristic droplet transfer at various condition points is, of course, basically determined by the intrinsic factor which is the energy coefficient of the pulse current. Therefore, it is imperative to precisely understand the characteristics of the energy of pulse current and its practical behavior in the control of the droplet transfer process.

We believe that the major characteristics of the energy of pulse current are expressed in its thermal and mechanical effects. Observations made from the angle of filament melting and transfer alone showed that the thermal effect of the pulse current is to provide additional heat to melt the filament on top of the pre-melting basis rendered by the base value current. It is a preparation step in terms of quality and quantity for droplet transfer. The mechanic effect of the pulse current, however, is to provide the amount of energy [8] or momentum [8,9] equivalent to "escape energy" to the droplet at the end of the filament through the

electromagnetic force generated by its own magnetic field. Then the droplet falls and undergoes accelerated transfer through the arc space. (In order to distinguish them from the energy or momentum produced by ordinary mechanical force, we will call the energy or momentum generated by the electromagnetic force as electromagnetic energy or electromagnetic momentum). Since the "escape energy" is a constant under the condition of fixed filament and protective gas, the amount of energy or momentum provided by the pulse current should have a critical value. In addition, as we have pointed out in previous sections of this paper that because all the parameters such as r , T , X used to express the characteristics of the arc are going to change together with the fluid dynamic flow in the arc, the pulse current will also significantly influence the arc forming.

Regarding the parameters expressing the electromagnetic momentum of the pulse current: Since the mechanical effect of the pulse current on the droplet at the tip of the filament is instantaneous (reaction time is extremely short), it is usually examined using the momentum theory. For simplicity, let us assume that the only external forces exerting on the solid liquid interface of the droplet are surface tension and electromagnetic force. For a droplet to fall from the end of the filament at a certain velocity, the following equation can be obtained using the momentum theory:

$$M_{\text{droplet}} v_{\text{droplet}} = \int_{t_1}^{t_2} F_{\text{axis}}(t) dt - \int_{t_1}^{t_2} F_{\text{surface}}(t) dt \quad (2)$$

where M_{droplet} --mass of the droplet;
 v_{droplet} --instantaneous velocity of the droplet as it is falling from the end of the filament;
 F_{axis} --axial component of the electromagnetic force;
 F_{surface} --surface tension;
 $t = t_2, t_1$ --pulse current duration.

From Equation (2) we know that if the electromagnetic momentum

$\int_{t_1}^{t_2} F_{\text{axial}}(t)dt < \int_{t_1}^{t_2} F_{\text{surface}}(t)dt$ then $v_{\text{droplet}} < 0$, i.e.,
 the droplet cannot fall. If $\int_{t_1}^{t_2} F_{\text{axial}}(t)dt$
 $> \int_{t_1}^{t_2} F_{\text{surface}}(t)dt$ and its value is appropriate,
 then $v_{\text{droplet}} > 0$ and only one droplet falls. If $\int_{t_1}^{t_2} F_{\text{axial}}(t)dt$
 is too large, then it creates a multiple drop-
 let transfer by a single pulse [9].

Assuming that the pulse current is a square wave and consider-
 ing that F_{axial} is proportional to the square of the instantaneous
 value of the pulse current, it is not difficult to prove:

$$\int_{t_1}^{t_2} F_{\text{axial}}(t)dt = A I_{\text{peak}}^2 t \quad (3)$$

where: A --proportionality constant,
 I_{peak} --peak value of the pulse current,
 t --pulse current duration.

Equation (3) indicates that the electromagnetic momentum due to
 the interaction of the pulse current on the droplet at the tip of
 the filament (i.e., the cumulative effect of electromagnetic force
 with respect to reaction time) depends on the product of the square
 of the peak value of the current pulse and the duration of the pulse
 current. We believe that this is an important concept and founda-
 tion in the study of droplet transfer control with pulse current.

Regarding the electromagnetic force and the forming of arc:
 Actually, the axial component of the electromagnetic force is not only
 proportional to the square of the instantaneous value of the pulse
 current but also related to the dimension of the anode spot of the
 arc. Through a series of assumptions in reference [10], it was pro-
 posed that the equation for the axial component of the electromagnetic
 force calculated under continuous current condition is

$$F_{\text{axial}} = I^2 \left[\ln \frac{\sin \theta}{\sin \phi} - \left(\frac{1}{4} + \frac{1}{1 - \cos \theta} \right) + \frac{2}{(1 - \cos \theta)^2} \ln \frac{2}{1 + \cos \theta} \right] \quad (4)$$

If we let
$$R = \left[\ln \frac{\sin \theta}{\sin \psi} - \left(\frac{1}{4} + \frac{1}{1 - \cos \theta} \right) + \frac{2}{(1 - \cos \theta)^2} \ln \frac{2}{1 + \cos \theta} \right] \quad (5)$$

then

$$F_{\text{axial}} = RI^2 \quad (6)$$

where: I --current (electromagnetic unit);

θ, ψ --see note in Figure 4.

From equation (5) we know that with a fixed current value of $0 < 180^\circ - \psi$, then $R < 0$ which means F_{axial} is a negative number. It indicates that it is arcing upward to prevent droplet transfer. On the contrary, of $0 > 180^\circ - \psi$, then F_{axial} acts downward to promote droplet transfer.

In summary, it can be realized that the various droplet transfer characteristics in the stable arc zone are created by the various arc formings which are determined by the different energy coefficient of the pulse. Arc forming not only has strong influence on and control over the degree of intensity of the heat transfer from the anode spot to the metallic filament and the melting process of the filament, but also strongly affects and controls the direction and magnitude of the electromagnetic momentum of the droplet at the tip of the filament. In addition, under the combined reaction of both thermal and mechanical effects related to the forming of the arc, it also controls the geometrical shape, size and motion of the liquid metal at the tip of the filament. Therefore, viewing from the areas of filament metal melting and transfer, the control of arc forming is very important.

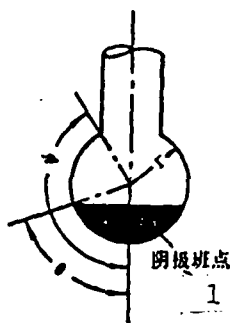
1. Synchronous and asynchronous droplet transfers

As shown in Figure 2, during synchronous transfer the anode spot is located at the upper surface of the droplet, the arc center just covers the droplet and the reduced neck is short and thick. The droplet falls towards the end of the pulse current. After the droplet falls, the residual liquid metal at the tip of the filament quickly withdraws and becomes dull due to surface tension. Under such condition, the remaining energy pulse is not sufficient to once

again separate a second droplet. This indicates that the electromagnetic momentum provided by the pulse current within its duration is comparable to the necessary "escape energy" for a droplet to fall.

Figure 4. Definition of central angles related to the electromagnetic force.

1--cathode spot



If the energy coefficient of the pulse becomes large (as shown in photograph 1), the peak pulse current value increases and the first droplet will fall at near the peak pulse current value. After the droplet has fallen, the remaining pulse energy will make the tip of the filament to continue to melt and to form another droplet. This smaller droplet will fall towards the rear part of the pulsed current. With the further increase in the energy coefficient of the pulse, the anode spot will rapidly occupy the side surface of the end of the filament which accelerates the melting process of the filament. The first droplet will fall in the front part of the pulse current. Afterwards, due to the residual energy of the pulse, the liquid metal cone at the end of the filament becomes thin and long and twisting and irregular movement also occur. Several small droplets are separated from the tip of the liquid cone. The axial transfer characteristic is poor and it may cause sputtering (see photograph 7).

As shown in photograph 3, when the energy coefficient of the pulse is too small, then the anode spot of the arc is located at the lower surface of the droplet. The arc center is in a cylindrical shape. Filament melting, neck shrinking and droplet formation processes are progressing very slowly. The axial component of the

electromagnetic force and its reaction time cannot provide enough momentum to promote droplet transfer. Therefore, it appears that it takes two or more pulses to complete one droplet transfer.

2. Axial and non-axial droplet transfer

The axiality and synchronism of droplet transfer are closely related. Usually, axial transfer and synchronous transfer are corresponding to each other. Non-axial transfer, however, corresponds to the transfer of multiple droplets per pulse. In the latter case, the droplets are the granular droplets falling from the tip of the thin long liquid cone located at the end of the filament. When the end of the filament is dull or the liquid cone is short and thick, the probability of getting a non-axial transfer decreases significantly. Therefore, the non-axial condition in droplet transfer is primarily determined by the energy coefficient of the pulse and its arc forming which is dependent upon the geometrical shape, size and movement of the liquid metal at the end of the filament.

3. Pulsed spray and pulsed jet

As shown in photograph 9(a), pulsed jet transfer frequently occurs at the condition point at which the no load pulse voltage and the welding current are relatively high and the arc length is relatively short. The unique property is that the anode spot ascends to the side surface of the end of the filament and the liquid metal at the end of the filament is in a thin long conical shape. Many small microscopic droplets are separated from the tip of the cone and they form a jet stream transferring to the melt pool. At this time, the length of the arc becomes shorter with the characteristic of a "penetrating arc". The "arc crater effect" is apparent. The deep melting capability is very strong. It should be noticed that in order to obtain non-shortening pulsed jet transfer, the key lies on the correct control of the arc length. When the arc length is slightly too short, the arc produces a gentle noise with an increase

in small sputter. The droplet transfer may change to the "pulsed jet with shorting" transfer [3].

IV. THE PHENOMENON OF "TRANSFER-BACK" OF DROPLET IN THE ARC

From the film taken during the arcing process using high speed phtography, we discovered a relatively new phenomenon which is the droplet "transfer-back" phenomenon. The so-called droplet "transfer-back" is to describe that a droplet falls from the end of the filament and enters a position in the arc and then changes its direction of motion and finally returns to the end of the filament.

Based on the observation from the film, there are two types of droplet "transfer-back" phenomenon: The first is small droplet "transfer-back" and the second is large droplet "transfer-back".

The general description of small droplet "transfer-back" (see photograph 5):

(1) Small droplet "transfer-back" always occurs when the droplet transfer and the pulse frequency are asynchronous and in the condition parameter combination for multiple droplet transfer with one pulse.

(2) The droplets participating in the "transfer-back" process are all small droplets finally separated from the tip of the metallic liquid cone at the end of the filament. The number of droplet in "transfer-back" is usually one and sometimes two,

(3) The time at which the droplet begins to "transfer-back" basically corresponds to the moment at which the pulse current stops and the residual liquid metal at the end of the filament begins to withdraw. When the residual liquid metal is in a conical shape and shrinks back at high rate, the rate of droplet "transfer-back" also increases significantly.

(4) All the small droplets participating in the "transfer-back" are usually located in the arc column directly or indirectly underneath the end of the filament. Some droplets, although they cannot "transfer-back", yet they can decelerate in the arc or even stay momentarily.

(5) Those droplets which gradually slowed down or temporarily stop in the arc will obtain tremendous acceleration to transfer to the droplet when the following pulse current is impressed. When the pulsing frequency increases (e.g., III cycle/sec), it can be frequently observed that the droplets which are in the "transfer back" process suddenly change their "transfer-back" direction towards the melt pool when the pulse current is again impressed. This indicates that there really is downward arc force which is synchronous with the pulse current in the arc.

(1) Large droplet "transfer-back" also occurs when the droplet transfer and the pulse current frequency are asynchronous. But it belongs to the condition parameter combination under which one droplet is transferred by multiple pulses (free falling).

(2) The "transfer-back" large droplets are droplets formed by multiple current pulses. The transferred droplets usually have a diameter approximately 1.5 times that of the diameter of the filament.

(3) Based on the indication obtained from high speed photographs, the moment that the droplet begins to "transfer-back" is in the duration of the pulse current.

Droplet "transfer-back" indicates that the vector quantity of the momentum of the droplet has changed instantaneously. Based on the basic equation in dynamics, i.e.,

$$\frac{d(mv)}{dt} = f$$

it is known that the rate of change in momentum with respect to time is the same in value as the external force exerted on the object and it is also in the same direction as the force.

Therefore, the observed droplet "transfer-back" phenomenon provides another actual evidence on the further understanding of the force field in the pulsed spray transfer welding arc.

Preliminary judgement suggests that the small droplet "transfer-back" may be related to the fluid dynamic effect in the arc at the pulse interruption instance.

Reference [5] pointed out that the electromagnetic force at any point in the arc column can be expressed by the following equation based on a simplified arc model as shown in Figure 5 and several other relevant assumptions:

$$P = \frac{2I^2}{\pi l^2(1 - \cos\theta)^2} \cdot \log \frac{\cos(\psi/2)}{\cos(\theta/2)} \quad (\text{dyne/cm}^2) \quad (6)$$

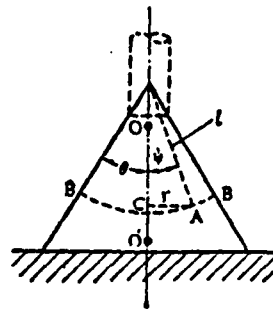


Figure 5. The conical shaped arc model

where: I --current (electromagnetic unit)

θ --1/2 of the vertex angle of the conical arc

ψ --the angle between point A and the symmetry axis

l --the distance between point A and the vertex (cm).

From Equation (6) it is known that the electromagnetic force at any point in the arc is proportional to the square of the current, inversely proportional to l^2 , and also related to θ and ψ . The gradient of electromagnetic pressure along the axis of the arc can be obtained by getting the derivative of Equation (6) with respect to l and assuming $\psi = 0$:

$$-\left. \frac{dp}{dl} \right|_{v=0} = -\frac{4I^2}{\pi l^2 (1 - \cos \theta)^2} \log \frac{1}{\cos(\theta/2)} \quad (7)$$

where the negative sign indicates that when $dt > 0$, $dp < 0$ which is to say that the electromagnetic force is gradually decreasing from the end of the filament to the base material.

During the pulse current period, because of the high current, the electromagnetic pressure gradient along the arc axis is very large. Therefore, the fluid static pressure at point O is far higher than that at point O'. Thus, an equi-conic flow going from point O to point O' is formed in the arc. This gas flow promotes the falling of the droplet from the end of the filament and also the accelerated transfer in the arc to the melt pool. As described earlier, the fine droplet which temporarily stayed at one position in the arc would undergo accelerated transfer towards the melt pool when the pulse current is again impressed. This indicates that there actually is a transfer acceleration force produced by the ionic gas flow which is synchronous with the pulse current.

But at the instant that the current is stopped, the above pressure gradient instantaneously decreases drastically. The source of the equi-ionic gas flow is interrupted instantly. The gas flow near point O' immediately decelerates. In addition, due to the work done by the original pressure field, it has a higher energy than O at point O. Thus, it creates the situation that the static pressure of point O' is instantly higher than that of point A. In order to stabilize the pressure along the arc column direction, a "back-pressure" is produced to the droplet with small mass which is in the process of transfer towards the melt pool. It makes the droplet decelerate, stop or even "transfer-back" to the tip of the filament.

VI. SPUTTERING PHENOMENON

Experimental results indicated that the sputtering problem is closely related to the mode of droplet transfer. Especially, it is

determined to a large extent by the geometrical shape, size and movement of the liquid metal at the end of the filament during the current pulse. The sputter frequently observed at stable arc condition points has the following types:

1. Sputter caused by non-axial droplet transfer (see photograph 7).

This type of sputter mainly happens when the energy coefficients of the pulse (such as no load pulse voltage and pulsed current duration) are large. After the current pulse is applied, the anode spot of the arc covers the entire tip of the filament. The filament melting and droplet forming processes progress very violently. After 1-2 relatively large droplets are transferred during the beginning of the pulse, the liquid metal at the end of the filament is in a thin long conical shape. The liquid cone is distorted, twisted and moved irregularly under the force of the arc. This causes the fine droplets separated from the tip of the liquid cone to have poor axial orientation. Thus, they may escape from the arc zone to cause the sputtering problem.

Since for different condition points the pulse energy, arc forming and type of droplet transfer are all different and the shape, size and motion of the liquid metal at the end of the filament are also different. Therefore, the probability, shape and size of the sputter created by non-axial droplet transfer are not the same. Photograph 7 merely shows some of the types of such a phenomenon.

If during the pulse current period the liquid metal at the end of the filament is dull or the liquid cone is short and thick, then due to the better axial orientation the probability of non-axial droplet transfer and the extent of sputtering can be significantly reduced.

2. Sputter caused by droplet bursting (see photograph 8).

The droplet, located at the end of the filament or during transfer through the space in the arc, would suddenly expand rapidly like a balloon before bursting. Sometimes the diameter of the sphere can be over four times the diameter of the filament. It can be predicated that gas is formed in the droplet. When the gas at high temperatures is causing droplet explosion due to volumetric expansion, a large amount of irregular small droplets will be formed. These fine droplets will escape the arc zone to create a fine particle sputter.

The expanded droplet interferes with the movement of the equi-ionic gas flow towards the melt pool in the arc which causes arc distortion. The situation that the cross-section of the arc column is thickened instantaneously can be observed.

This type of sputter often occurs under the welding condition of a long arc or a high CO_2 ratio. With increasing arc length, it not only increases the duration of stay of the droplet at the end of the filament and the distance in the temperature zone for the droplet to pass through, but also decreases the speed of droplet transfer. All these factors would increase the contact time between the melted metal and the gas. The oxidation of the metallic element at the metal-gas interface is vigorous and the gas content in the droplet will increase. When the CO_2 ratio is increased to 20%, almost with every pulse current the droplet expansion or expansion bursting phenomenon occurs. From this one can postulate that the gas generated on the droplet may be CO . In addition, the surface oxide layer or rust of the filament and the dissolved gas in the filament metal may also cause this type of sputter.

3. Sputter caused by the instantaneous arc gap short circuiting from the thin long liquid cone at the end of the filament (see photograph 9). As described in reference [2], in order to obtain a stronger arc deep melting capability, under the correct controlled condition of short circuit depth the "arc crater effect" is apparent.

It partially penetrates into the melt pool. The arc emits a "pee-pa" noise. The droplet transfer is in the pulsed jet with short circuiting form. High speed photographic film and synchronous parametric waveforms on the oscilloscope verified that arc gap short circuit is due to the instantaneous short circuiting of the arc gap by the thin long liquid cone at the end of the filament. It also causes sputtering but the sputtered droplets are extremely fine.

4. Sputter caused by the arc gap short circuiting due to droplet at the end of the filament (see photograph 10).

When the energy of the pulse is too low and the arc length is relatively short, the energy of one pulse is not sufficient to make a droplet fall. Under such conditions after several current pulses, the droplet accumulation at the end of the filament increases. Because the position of the spot fluctuates, the repulsive force will make the droplet swing violently. It may be possible to short circuit the arc gap to cause a large droplet sputter. The welding process is extremely unstable.

5. Sputter caused by the poor arc starting capability and the lack of current interruption capability of the pulse source (see photograph (2) in Reference [2]).

It was proved in practice that, under the condition that the pulse power source can be reliably shut off at the instance of arc starting, the ϕ 1.6 mm filament arc has good starting capability as long as it is matched with the current electrical feedback value and aided by the decelerated starting technological compensation procedure. However, because there are so many factors affecting the starting characteristics of the arc, when the peak short circuit current is too high the pulse current source thus shows a phenomenon that the current cannot be shut off completely. Its characteristic is that after the start-up of the arc, it transforms into an arc ignition arc breaking--short circuiting--arc reignition cycle which

is a periodic dynamically varying process [2]. The filament is melted and ejected in large sections. The sputtering is violent. The arc starting process is very difficult to stabilize. Therefore, we believe that the shutting off capability of the wave chopping type of pulse power supply is an important indicator in the judgment of the arc starting capability.

In the above types of sputter, the most frequently seen one is due to the non-axial droplet transfer under normal conditions. This type of sputter depends on the energy parameters of the pulse, i.e., the arc forming determined by the parameters. This is because that arc forming determines the geometrical shape, size and motion at the end of the filament. Therefore, with fixed alloy system of the added metal and constant protective gas composition, the correct control of the energy parameter of the pulse and the arc forming is necessary to minimize sputtering.

In addition, since at some condition points sputter caused by droplet bursting is still frequently seen, therefore, in order to control this type of sputter from occurring, not only the filament should have sufficient de-oxygenation capability but also the relevant metallurgical reaction kinetic parameters corresponding to the droplet transfer (i.e., $\frac{F}{V} \cdot \tau$ where F --surface area of the droplet; V --volume of the droplet; τ --the sum of time the droplet stayed at the end of the filament and time it took to pass through the space in the arc) should be controlled. Therefore, looking from this angle, as we have pointed out before, that when a long arc is used in welding it is more probable to have sputter caused by droplet explosion.

VII. REGARDING THE CONTROL OF PULSE CURRENT AND THE OPTICAL CONTROL LEVEL

In the early stage of application of pulse current to the melting electrode gas protective welding, the welding technicians both foreign and domestic primarily used the following two points to

identify the control behavior of the pulse current; they are:

(1) Synchronous control with respect to droplet transfer. Based on this point, some people called the pulsed spray transfer arc welding as "controllable transfer" welding or "pulsed controlled transfer welding". Relevant information [11] especially stressed the importance in the obtaining of a synchronous transfer control and also established an optimal selection of pulse energy parameters. It appears that the use of pulse current to control the synchronous droplet transfer is an important principle to be obeyed in practical applications.

(2) By lowering the thermal input of the arc, the melting and overheating of the base metal are reduced to a relatively low level. Along with the profound research in pulsed spray transfer arc, people more and more clearly realized that the control behavior of the pulse current is not only shown in the area of droplet transfer control. More importantly, it also appears in the technology of characteristics the arc and in the quality control of the welded joint. For example, the control of the primarily and secondary structures of the welded joint in order to satisfy the metallurgical requirement; the control of the melting depth and shape of the welded seam; the control of melting and freezing in the welding process to accommodate entire position welding, etc.

Of course, the relevance between the optimal control of droplet transfer and the optimal control of the arc technological characteristics and quality of the welded joint by using pulse current should be noticed. However, the two things are not completely identical. Up to date information in this area obtained from systematic and profound experimental studies is still lacking. The understanding is also not unified.

Using the condition parameter combinations selected by our laboratory, we investigated the droplet transfer at near 50 testing

condition points in the stable arc region. There were very few condition points at which rigorous synchronous transfer was obtained. The majority belonged to the asynchronous transfer condition points. However, the condition parameter combinations determined by these condition points could all obtain the stable arc process of the spectacular arc characteristics of the non-short-circuit, non-broken-arc spray transfer arc. Based on the principle, as long as it is correctly matched with different welding speed, the linear energy of the arc can be controlled to satisfy the requirements of various welding technologies. Of course, with the increasing number of condition points, especially through the correct matching of between the waveform of the pulse current and pulse frequency, the probability of getting a synchronous control is correspondingly higher.

On the basis of preliminary experimental results, we have the following comments on the principles involved in the synchronous droplet transfer with pulse current frequency:

(1) The condition parameter combination to obtain the optimal control of droplet transfer (i.e., synchronous transfer) may not be the same as the one needed for the optimal control of arc technological characteristics and welded point quality in actual application. For example: In the welding of medium thick plate of structural alloy steel with small diameter ring seam which requires 100% melting through at the root welding path and good controllability of the melt pool under the selected condition parameter combination which has a good technological characteristic, the droplet transfer is asynchronous. There are many actual cases in this area,

(2) In the pulsed spray transfer arc welding, the investigation on the control behavior of the pulse current can only be done in an over-all manner. As for its control level, as the bottom line, it can only be judged by the optimization of the quality of the joint. Therefore, from this angle, the requirement of synchronous droplet

control is not unique. In some applications, the combinations of condition parameters for asynchronous transfer can also be chosen.

(3) Based on the above viewpoint, we believe that the concept of the so-called "controllable transfer" and "pulsed controlled transfer" should be broadened to the realization that as long as the droplet transfer and pulse current (Note: not frequency of pulse current) are synchronous and appear periodically, then the droplet transfer is controllable.

(4) For some specified welding technologies, the condition parameter combinations for synchronous and asynchronous transfer and their effects on the difference in electrical process, thermal process, metallurgical process and mechanical properties are yet to be experimentally studied in order to obtain a more complete and profound comparison and identification.

VIII. CONCLUSION

1. There are one to one corresponding relations in pulse energy--arc forming--droplet transfer--sputter. The most important one is pulse energy and the arc forming determined by it.

2. The energy possessed by the pulse current. In the process of filament metal melting and transfer, the energy of the pulse current is shown through the thermal effect and mechanical effect of the pulse current. Under a fixed pulse waveform and pulse frequency, the characteristic parameters of the pulse energy are the peak pulse current and its duration.

3. The visual and dynamic formings of the pulsed arc both consist of three parts; arc center, arc and arc flame. Its dynamic forming varies periodically. The shape of the arc center is determined by the energy parameter of the pulse and the fluid dynamic flow in the arc. The arc forming strongly influences the

melting of the filament metal and the transfer process.

4. The droplet transfer characteristics are different at various condition points in the stable arc condition region. They are divided into synchronous and asynchronous, axial and non-axial, pulsed spray and pulsed jet, and long arc spray and short arc spray types. The majority of them belong to the asynchronous transfer type.

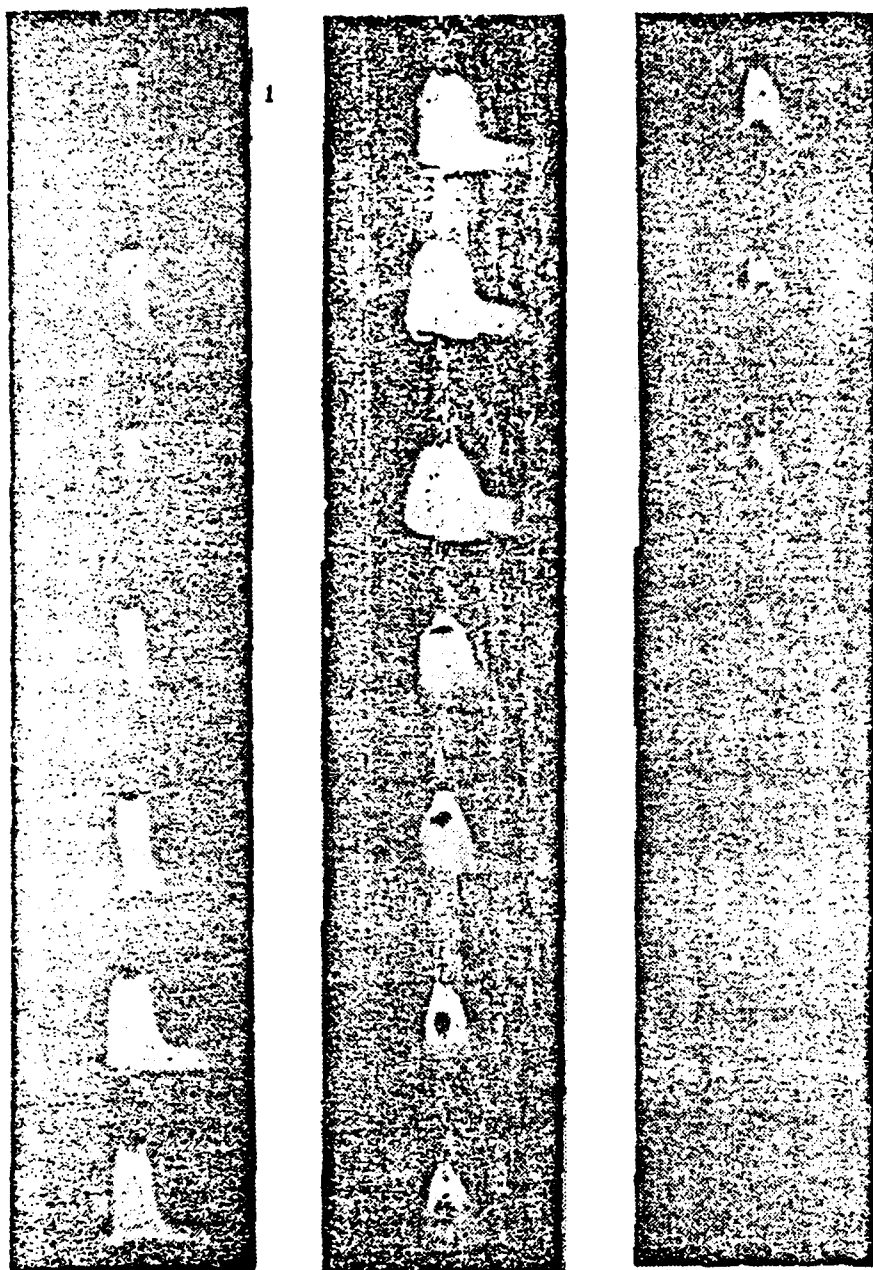
5. The primary formation format of sputter is from the non-axial transfer of droplets. This type of sputter is determined by the geometric shape, size and motion of the liquid metal at the end of the filament.

6. The droplet "transfer-back" phenomenon discovered in the experiment provided another actual proof in the further understanding and study of the force field in the arc. Based on preliminary judgment, the small droplet "transfer-back" phenomenon may be related to the fluid dynamic effect in the arc.

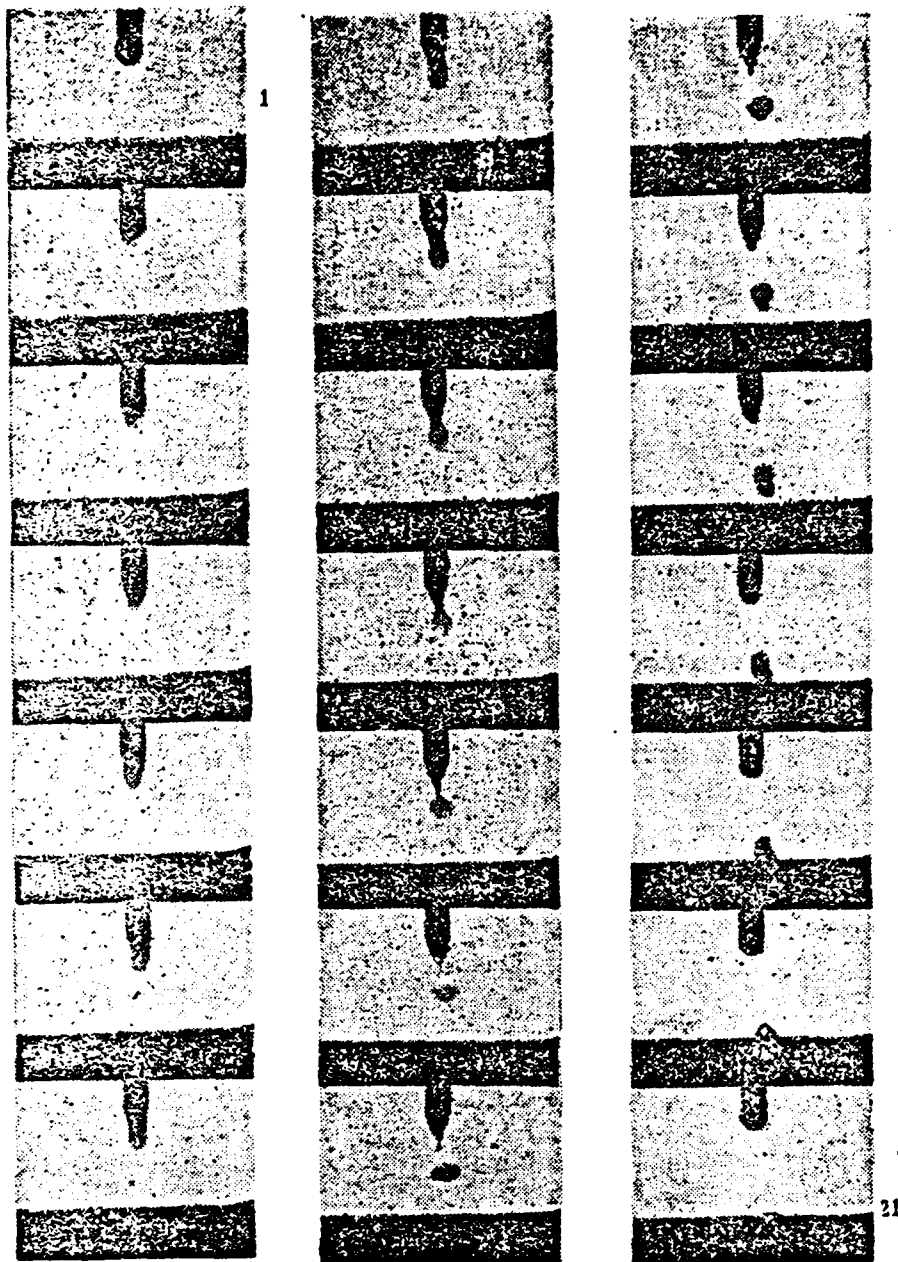
7. Based on the experimental results from nearly 50 testing condition points, the majority of those points showed asynchronous droplet transfer with the pulse frequency as well as on the actual experience in production application, evaluation and correction were made on the principle that "droplet transfer must synchronize with the frequency of the pulse current".

References

- [1] Translated and edited by Duan Liyu, Research on foreign melting electrode pulsed argon arc welding. Foreign Aviation Technology, Engineering, etc. No. 50 (1974) pp. 1-55.
- [2] Cheng Gongshan, Duan Liyu, Feng Jiqiang, Wang Xuxi, Lu Xuechen. Experimental research based on pulsed spray transfer electric arc welding process (Part 2) - Standard parameters matching composites and their electric arc processes, unpublished.
- [3] Northwestern University of Technology, Welding laboratory, chopped type pulsed argon arc welder test manufacturing technological testing, and welding, No. 3 (1977), pp. 2-8.
- [4] Gross, B., Gryez, B., and Miklo'ssy, K., Plasma Technology, Iliffe Books Ltd., London, 1968, pp. 237-256.
- [5] Ando Hirotoishi, Hasegawa Mitsuo. Welding arc phenomena Industrial Book Co., Ltd., 1962, pp. 65-67, 162-169
- [6] Schoeck, P., An Investigation of the Anode Energy Balance of High Intensity Arcs in Argon, Modern Developments in Heat Transfer, Warren Ibele, 1963, pp. 353-400.
- [7] Lucas, W. and Amin, M., Effect of Wire Composition in Spray Transfer Mild Steel Mig Welding, Metal Construction, Vol. 7, February 1975, pp. 77-83.
- [8] Потальевский, А. Г., Сварка в Защитных Газах Плавящимся Электродом. МАШИНОСТРОЕНИЕ. 1974, pp. 32-51.
- [9] Kitani Satomi, Wakino Yoshikao. Pulse arc welding of aluminum alloys and light metals welding, Vol. 6, No. 72, 1968, 12, pp. 554-563.
- [10] Greenc, W. J., An Analysis of Transfer in Gas-shielded Welding Arcs, Transactions of The American Institute of Electrical Engineers, Vol. 79, Part I, Applications And Industry, American Institute of Electrical Engineers, 1960, pp. 194-202.
- [11] Daggeet, E. H. and Zircher, W. E., New Developments in Pulsed Spray Welding, Welding Journal, Vol. 49, October 1970, pp. 780-787,

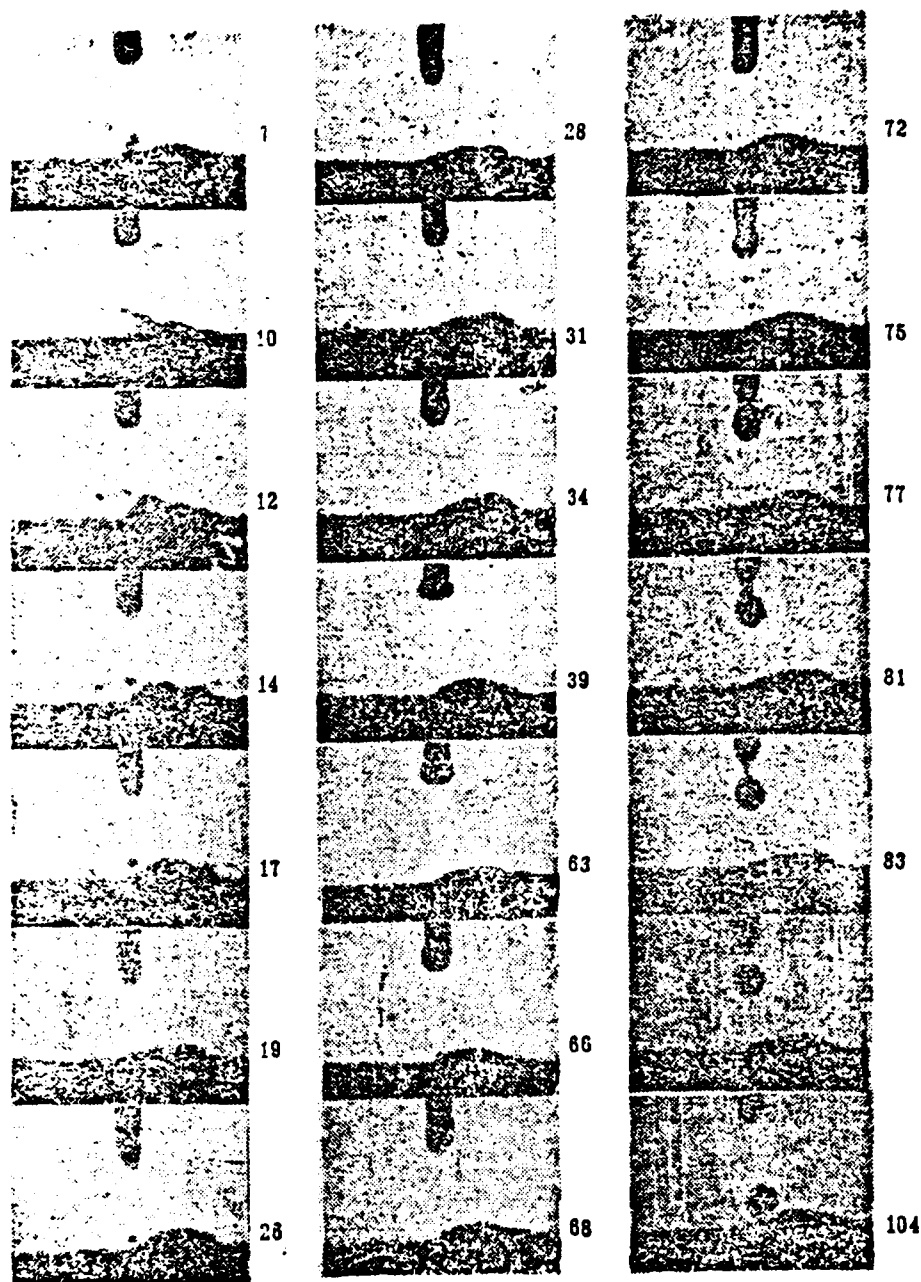


Photograph 1. The variation process of dynamic arc forming of a pulsed arc in a cycle,
 1--no load pulse voltage: 52.5 volts; 2--pulse width ratio: 13/7;
 4--welding voltage: 28 volts; 4--welding current: 210 ampere; 5--
 no load base voltage: 31 volts; 6--pulsing frequency: 60 cycle/sec;
 7--filament feeding speed: 204 m/hour; 8--photograph shooting
 speed: 1800 frames/sec.



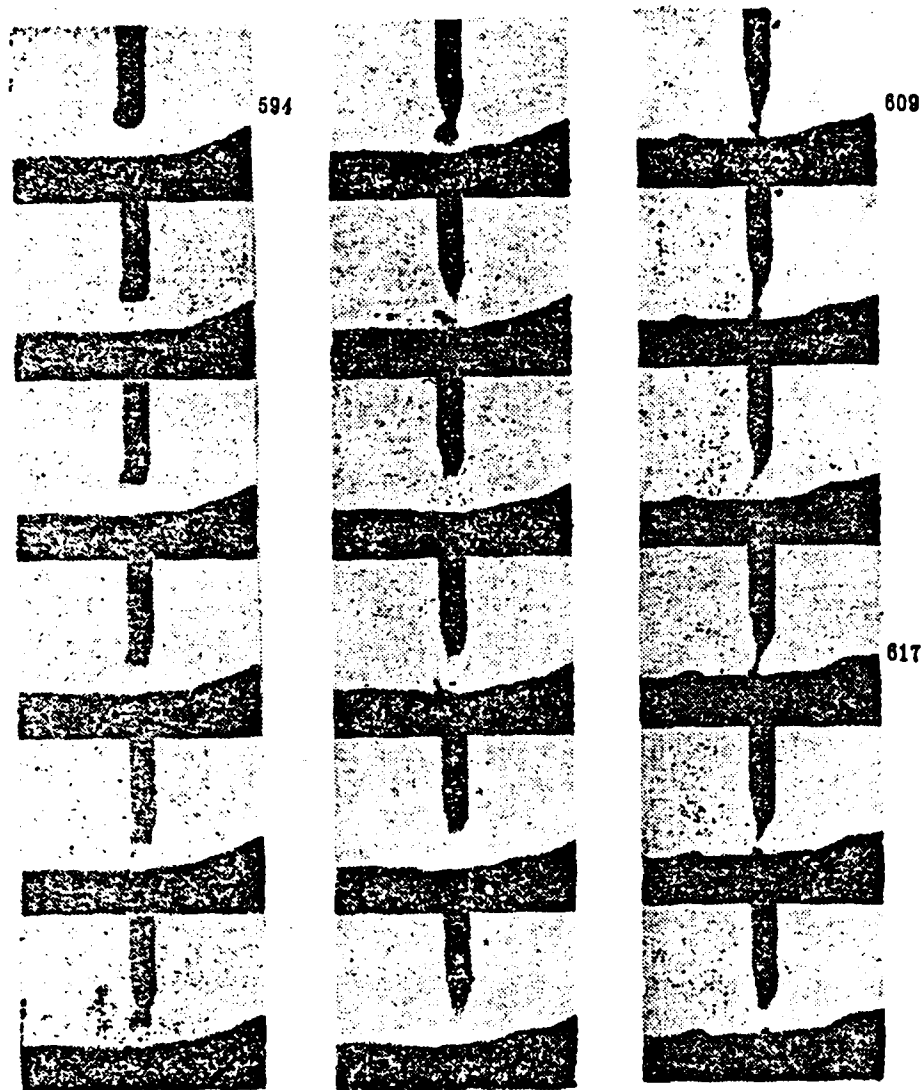
Photograph 2. Droplet transfer synchronizes with pulsed current frequency.

1--no load pulse voltage: 45 volts; 2--pulse width ratio: 13/7;
 3--welding voltage: 2315 volts; 4--welding current: 180 ampere;
 5--no load base voltage: 31 volts; 6--pulse frequency: 50 cycle/sec;
 7--filament feeding speed; 151 m/hour; 8--photograph shooting speed:
 2300 frames/sec.



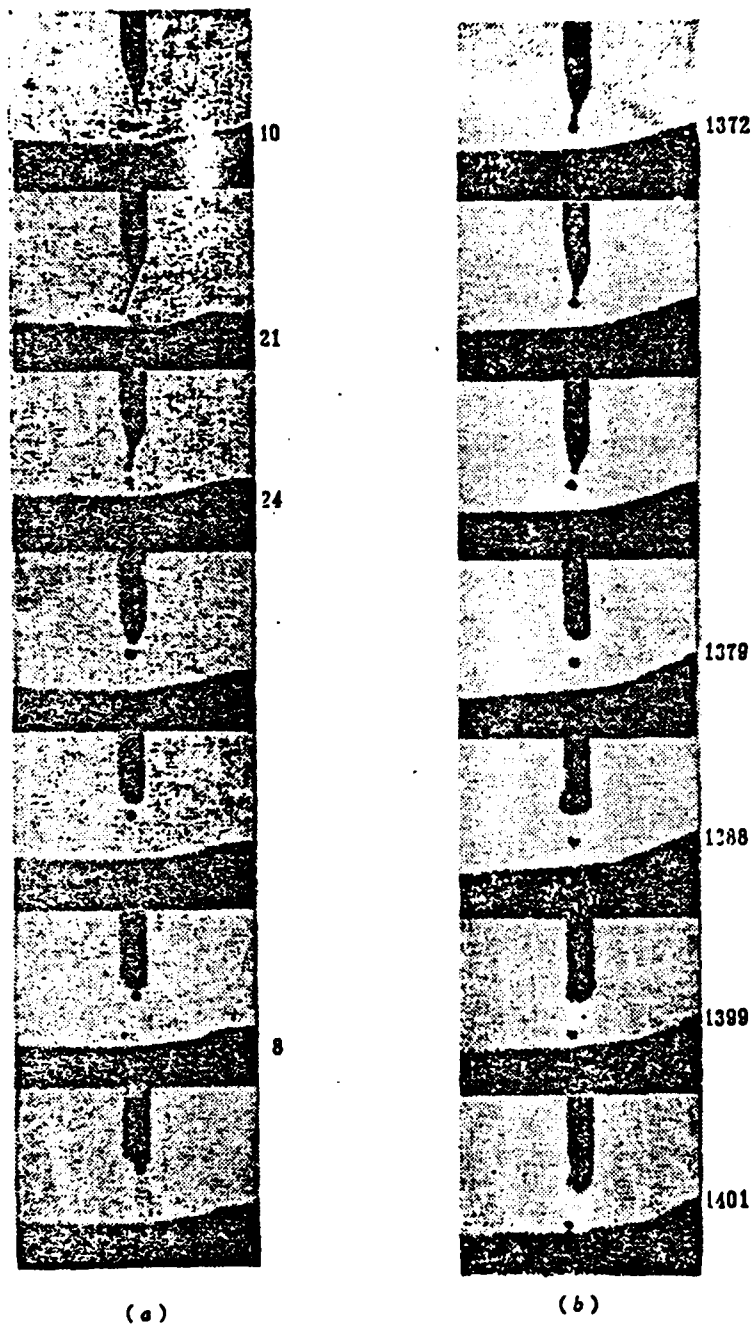
Photograph 3. Asynchronous droplet transfer with pulsed current frequency--one droplet transfer every two pulses.

1--no load pulse voltage: 40 volts; 2--pulse width ratio: 13/7; 3--welding voltage: 24.8 volts; 4--welding current: 140 ampere; 5--no load base voltage: 31 volts; 6--pulse frequency: 50 cycle/sec; 7--filament feeding speed: 100 m/hour; 8--photograph shooting speed: 2700 frames/sec

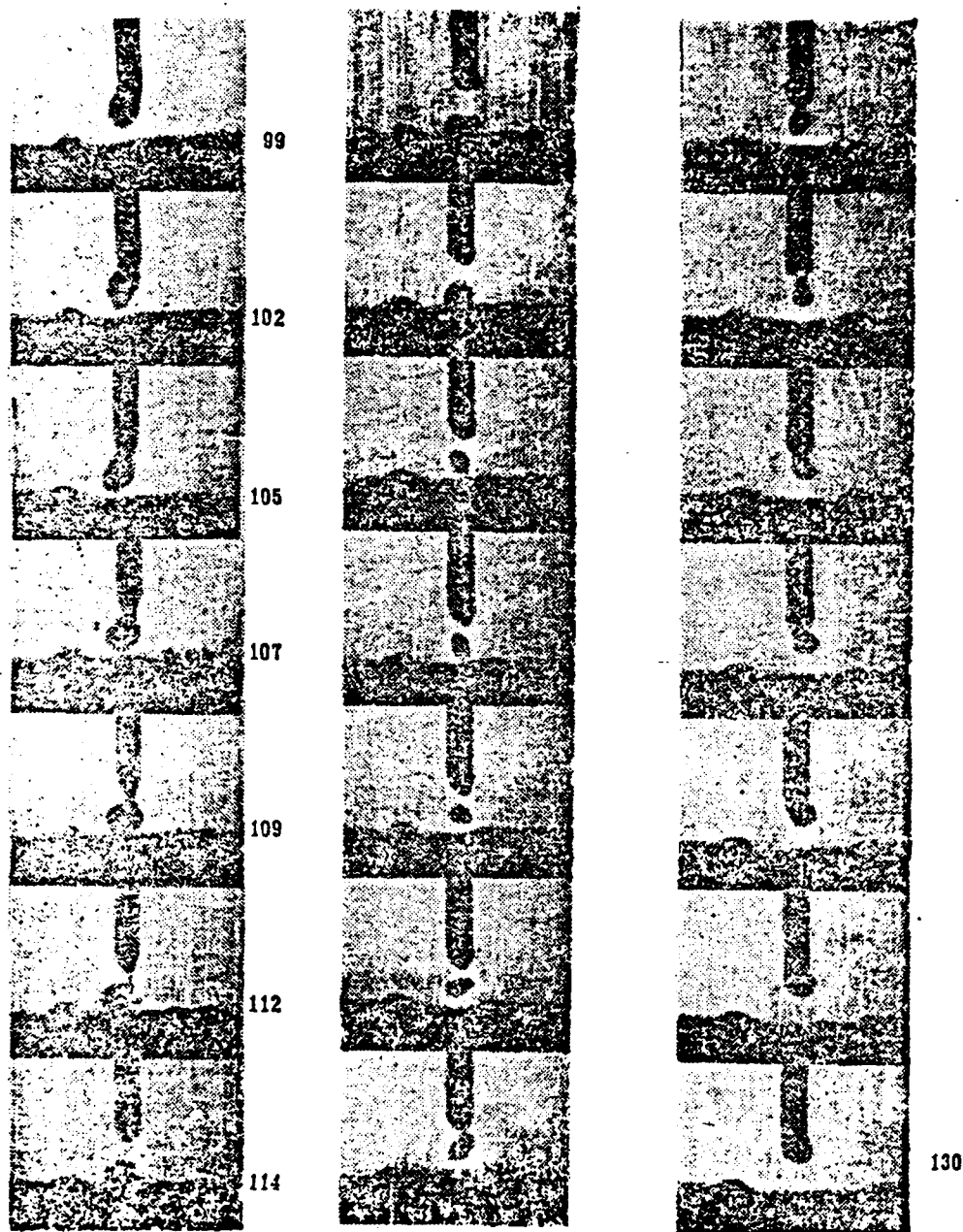


Photograph 4. Short arc pulsed spray transfer

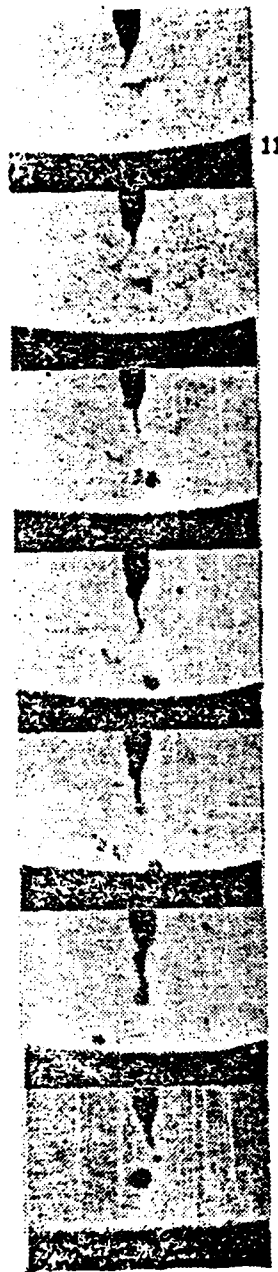
1--no load pulse voltage: 55 volts; 2--pulse width ratio: 13/7; 3--welding voltage: 27 volts; 4--welding current: 275 ampere; 5--no load base voltage: 31 volts; 6--pulse frequency: 50 cycles/sec; 7--filament feeding speed: 288 m/hour; 8--photograph shooting speed: 2300 frame/sec.



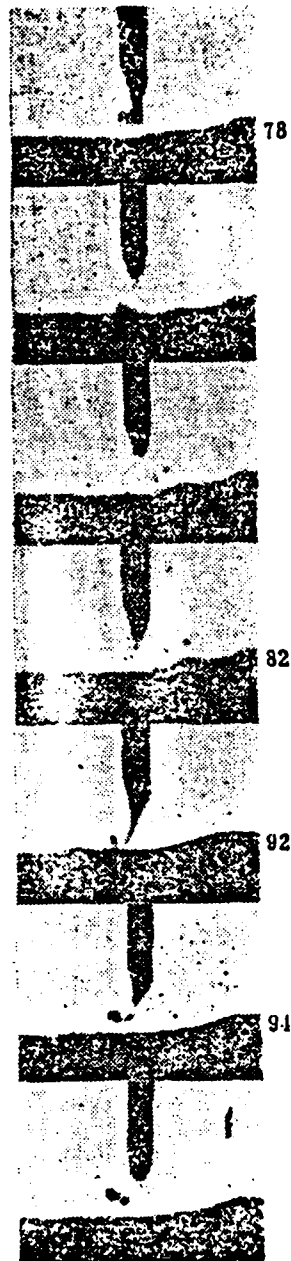
Photograph 5. Phenomenon of small droplet "transfer-back" in the space of the arc.
 2--(a) the small droplet "transfer-back" to the tip of the filament;
 3--(b) the small droplet decelerated and stopped for a short period of time in the arc space. Immediately after the pulse current was applied, the transfer was accelerated toward the melt pool



Photograph 6. The phenomenon of large drop "transfer-back" in the arc.



(a)

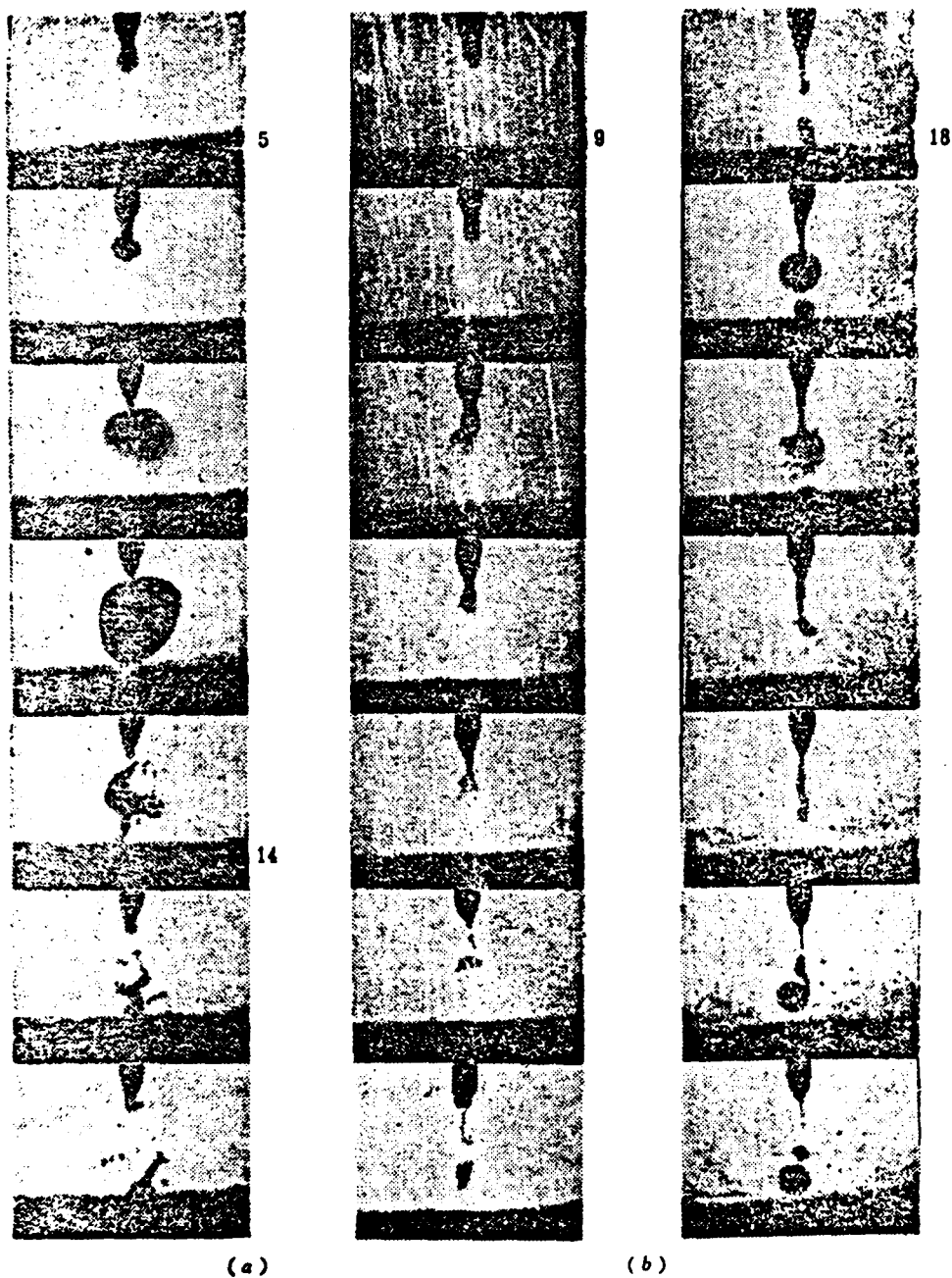


(b)

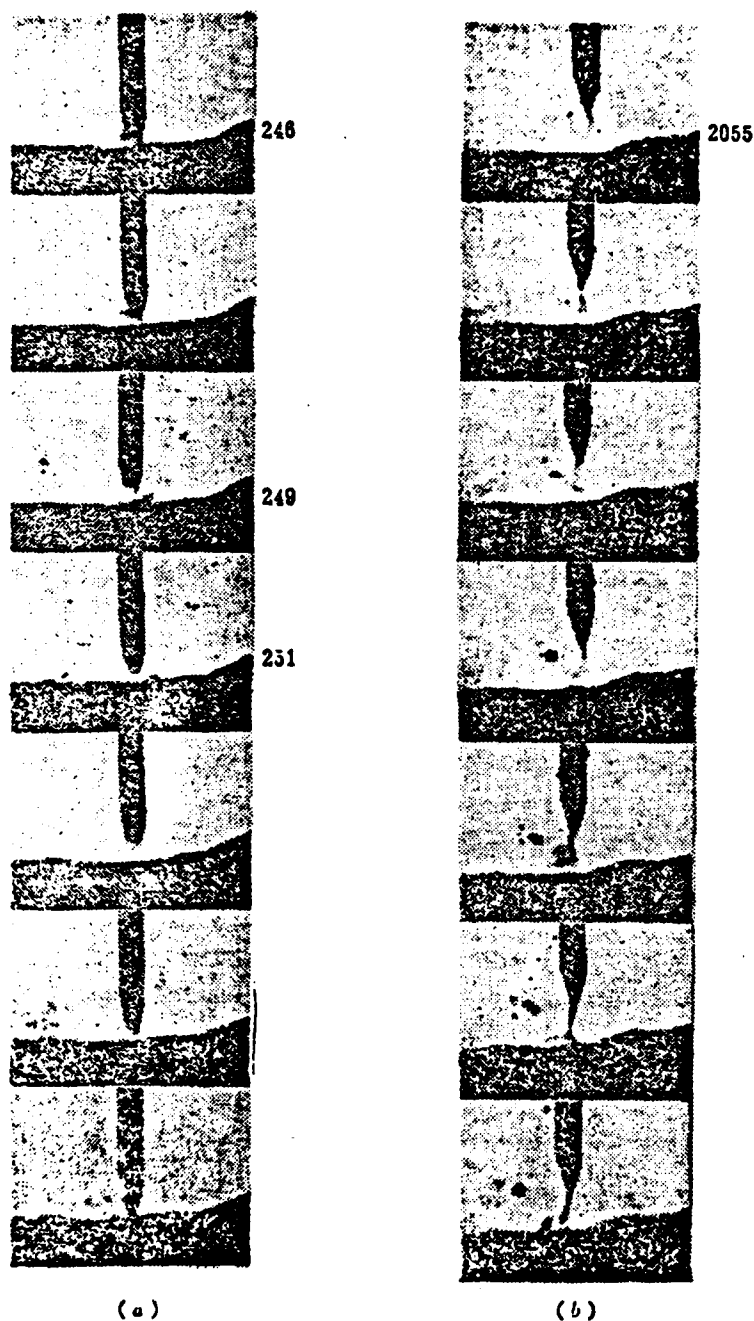
Photograph 7. Two examples of sputter due to non-axial transfer of droplet

2-- (a) no load pulse voltage: 55 volts; no load base voltage: 31 volts; pulse width ratio: 13/7; pulse frequency: 50 cycles/sec; welding voltage: 28.7 volts; filament feeding speed: 216 m/hour; welding current: 223 ampere

3-- (b) conditions same as those in Photograph 4



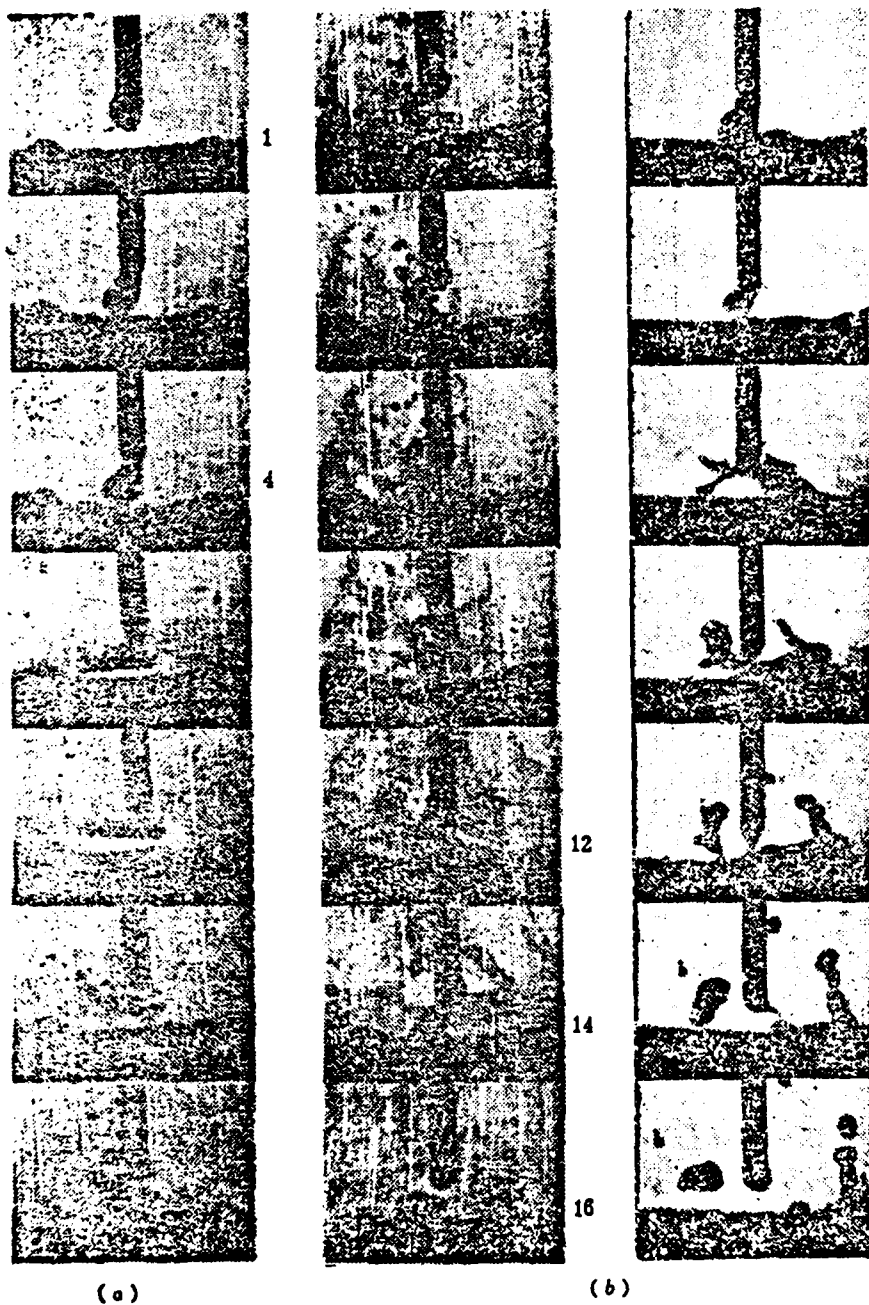
Photograph 8. Two examples of sputter due to droplet bursting
 2--(a) droplet bursting at the tip of the filament;
 3--(b) multiple expansion or bursting of the tip of the liquid cone



Photograph 9. Sputter created by (a) short circuit at the arc gap by the liquid cone or (b) the liquid cone is thrown.

2--no load pulse voltage: 57.5 volts; no load base voltage: 31 volts; pulse width ratio: 13/7; pulse frequency: 50 cycle/sec; welding voltage: 28 volts; filament feeding speed: 294 m/hour; welding current: 280 ampere

3--conditions same as those in Photograph 4.



Photograph 10. Sputter created by the arc gap due to droplet short
 circuiting at the end of the filament
 2--(a) droplet bursting; 3--(b) droplet splashing

The Study on Technological Fundamentals
of Pulsed Spray Transfer Arc Welding (II)
—Observations on Arc Phenomena in the
Case of Stable Welding Condition (Report 1)

*Duan Liyu, Cheng Gongshan, Feng Jijiang,
Wang Xuxi and Lu Xuezheng*

By employing high speed photographic technique, pictures of arc phenomena are taken and synchronous oscillograms of arc voltage and current are recorded.

Some arc phenomena at typical test condition points, such as arc forming, droplet transfer, and spatter are qualitatively described. Some phenomena concerning transfer-back of droplet in pulsed spray transfer arc are also revealed.

On the basis of the experimental results taken from nearly fifty welding condition points, the authors make a preliminary evaluation of the principle stated in foreign literature that the frequency of droplet transfer must synchronize with the frequency of pulse current (generally known as synchronous transfer). They wish to point out that not only the welding condition combination of synchronous transfer (one droplet per pulse current) but also the welding condition combination of asynchronous transfer (two or more droplets per pulse-current) possess each an application range of its own. Therefore the authors are of the opinion that the concept of controlled transfer by pulse-current (so-called controlled spray transfer) should be extended, that is, droplet transfer has to synchronize only with the pulse-current, but the number of transfer droplets per pulse-current may be one, two or more, provided that there exists the repeatability of such transfer.

A FAST FOURIER TRANSFORM HARDWARE PROCESSOR

Kang JI-CHANG AND Xu Naiping

ABSTRACT

The fifth branch of the National Ocean Bureau and the Tianjin Electronic Instrument Factory developed a real-time FFT processor to analyze acoustic frequency signals. The analysis time for the 1024 frequency spectrum points is approximately 40 ms. We proposed a new approach in the development of this processor to simplify the original design which reduced the size of CPU and memory by about one-half. This new method was adopted and developed successfully in early 1979. This article introduces the design concepts and main circuits in the new approach.

I. INTRODUCTION TO FFT

Fast Fourier transform is widely used in radar signal processing, sonar signal processing, language analysis, earthquake signal processing, vibrational signal processing and picture identification.

For the benefit of the reader to understand the working principles of the FFT processor, let us briefly introduce the FFT method.

The discrete Fourier transform equation is

$$X(k) = \sum_{i=0}^{N-1} x(i) W_N^{ik} \quad i=0,1,\dots,N-1, \quad k=0,1,\dots,N-1 \quad (1)$$

where $x(i)$ is the sampling sequence of the time varying quantity $x(t)$; $X(k)$ is the corresponding frequency spectrum sequence of the Fourier transform.

$$W_N^{ik} = e^{-j \frac{ik}{N} 2\pi} = \cos \frac{ik}{N} 2\pi - j \sin \frac{ik}{N} 2\pi \quad (2)$$

Therefore, it is obvious that the main work load in calculation is the multiplication of complex numbers. In order to calculate each spectral value $X(k)$, it is necessary to perform N complex multiplications. To calculate the entire N spectral values then, one must carry out N^2 complex number multiplications.

The use of the FFT method can simplify the calculation process in order to improve the calculation speed. The verification of the FFT method is available in the literature in many sources; it will not be repeated here. Let us explain this method by choosing the condition that $N = 4$.

Using the conventional method from the expansion of Equation (1), we obtain

$$\left. \begin{aligned} X(0) &= W_4^0 x(0) + W_4^0 x(1) + W_4^0 x(2) + W_4^0 x(3) \\ X(1) &= W_4^0 x(0) + W_4^1 x(1) + W_4^2 x(2) + W_4^3 x(3) \\ X(2) &= W_4^0 x(0) + W_4^2 x(1) + W_4^4 x(2) + W_4^0 x(3) \\ X(3) &= W_4^0 x(0) + W_4^3 x(1) + W_4^0 x(2) + W_4^0 x(3) \end{aligned} \right\} \quad (3)$$

Using the periodical property of W_N^{1k} , the above equation can be simplified.

$$\begin{aligned} W_4^0 &= 1 & W_4^2 &= W_4^4 = W_4^0 = 1 \\ W_4^1 &= e^{-j\frac{\pi}{2}} = -j = W_4^3 & W_4^3 &= W_4^5 = W_4^1 = -j = W_4^1 \\ W_4^2 &= e^{-j\pi} = -1 & W_4^4 &= W_4^8 = W_4^2 = -1 \\ W_4^3 &= e^{-j\frac{3\pi}{2}} = j = -W_4^1 & W_4^1 &= W_4^9 = W_4^3 = j = -W_4^1 \end{aligned}$$

Substituting into Equation (3), we get

$$\left. \begin{aligned} X(0) &= x(0) + x(1) + x(2) + x(3) \\ X(1) &= x(0) + W^1 x(1) - x(2) - W^1 x(3) \\ X(2) &= x(0) - x(1) + x(2) - x(3) \\ X(3) &= x(0) - W^1 x(1) - x(2) + W^1 x(3) \end{aligned} \right\} \quad (4)$$

The above equation can be expressed in a second order progressive deduction form. The first time a two term algebraic

is obtained. The second time a four term algebraic sum results.

$$\begin{aligned}
 X_1(0) &= x(0) + W^0 x(2), & X_1(1) &= x(1) + W^0 x(3), \\
 X_1(2) &= x(0) - W^0 x(2), & X_1(3) &= x(1) - W^0 x(3), \\
 X_2(0) &= X_1(0) + W^0 X_1(1) = x(0) + x(1) + x(2) + x(3) = X(0) \\
 X_2(1) &= X_1(0) - W^0 X_1(1) = x(0) - x(1) + x(2) - x(3) = X(2) \\
 X_2(2) &= X_1(2) + W^1 X_1(3) = x(0) + W^1 x(1) - x(2) - W^1 x(3) = X(1) \\
 X_2(3) &= X_1(2) - W^1 X_1(3) = x(0) - W^1 x(1) - x(2) + W^1 x(3) = X(3)
 \end{aligned}$$

This is the FFT method. The results are the same as the ones shown in Equation (4), with only the sequence of $X(1)$ and $X(2)$ reversed. Therefore, it is apparent that the FFT method uses the periodicity of the trigonometric functions and transforms the calculation process into a progressive deductive form to simplify the process.

The above discussed calculation process can be represented by Figure 1. It is also called the flow chart. From this figure, it is easy to see that all the data are calculated in pairs. A very similar method is used for all the pairs which can be expressed as shown in Figure 2. This is called the butterfly operation. A and B are the operating numbers, and \hat{A} and \hat{B} are the operating results.

$$\begin{aligned}
 \hat{A} &= A + W^N B \\
 \hat{B} &= A - W^N B
 \end{aligned} \quad (6)$$

It can be seen that only one multiplication of complex numbers is required for each butterfly operation. Therefore, 16 complex number multiplications can be simplified to four multiplications.

Figure 3 is the flow chart when $N = 8$. After three iterations, the

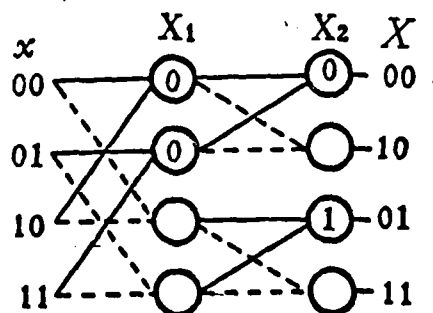


Figure 1

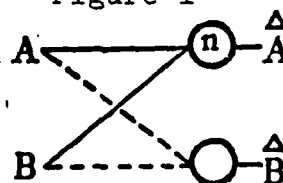


Figure 2

results can be obtained. They are all the algebraic sum of eight terms. The calculated results are not listed sequentially. However, a certain order is still obeyed. When a binary system is used to label the sequence, the sequence for the results happens to be in reverse order compared to the original sequence. It is also called inverse positioning.

The above method can be extended to N points. When $N = 2^p$ and p is the iteration number, every iteration requires $\frac{N}{2} \cdot p = \frac{N}{2} \log_2 N$ complex number multiplications are needed for p iterations. Assuming $N = 2^{10} = 1024$ points, the conventional method must carry out $N^2 \approx 10^6$ times of complex number multiplications, while the FFT method only requires $\frac{1024}{2} \times 10 \approx 5 \times 10^3$ times. It is approximately 200 times faster than the conventional method.

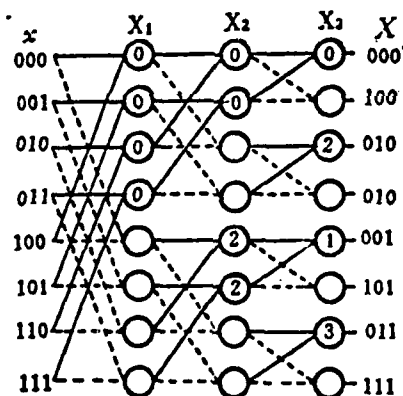


Figure 3

II. THE BUTTERFLY OPERATION

From the above, it is apparent that the major objective in the FFT processor is to accelerate the speed of the butterfly operation. For the butterfly operation, the major problem is complex number multiplication.

Under normal conditions, the data participating in the butterfly operation are complex numbers, i.e.,

$$A = a + ja', B = b + jb', W^n = \cos \frac{n}{N} 2\pi - j \sin \frac{n}{N} 2\pi$$

$$W^n B = (b \cos \frac{n}{N} 2\pi + b' \sin \frac{n}{N} 2\pi) + j(-b \sin \frac{n}{N} 2\pi + b' \cos \frac{n}{N} 2\pi) = c + jc' \quad (7)$$

$$c = (b \cos \frac{n}{N} 2\pi + b' \sin \frac{n}{N} 2\pi) \quad (8)$$

$$c' = (-b \sin \frac{n}{N} 2\pi + b' \cos \frac{n}{N} 2\pi) \quad (9)$$

$$\begin{aligned} \hat{A} &= (a + c) + j(a' + c') \\ \hat{B} &= (a - c) + j(a' - c') \end{aligned} \quad (10)$$

Equations (7), (8), (9) and (10) are the major calculations carried out in the processor.

III. THE DUPLEX MULTIPLIER

One requires four multiplications and six additions and/or subtraction in a butterfly operation. The conventional multiplier is too slow in performing four multiplications, which will not satisfy the requirements of real-time analysis. Two multipliers can be used: One for the real part, and the other for the imaginary part. However, the cost for equipment will be too high to be practical. Therefore, a special duplex multiplier particularly designed for butterfly operations is developed which is capable of obtaining the algebraic sum of two products c and c' .

Figure 4 is the circuit of the duplex accumulator in the duplex multiplier. It mainly consists of two arrays of accumulators. L is the partial product (final product at the end). M and M' are the two multiplicands which are controlled by the multiplier $\cos \frac{n}{N} 2\pi$, and $\sin \frac{n}{N} 2\pi$. Figure 5 shows the block diagram of the duplex multiplier. We adopted a two digit compensation multiplication with 10 digits for the trigonometric function. Thus, a duplex multiplication can be completed in five bits. J_g and J_g'

are the storage devices for the trigonometric functions (i.e., multipliers). During the multiplication, every bit shifts by two digits to the right and mutually exchanges position in order to prepare for the next duplex multiplication. After the first multiplication, L is obtained and the duplex multiplication can continue to determine L' . The partial product is controlled by a MX main multiple switch to shift to the right by 2 or 1 digit. J_{ox} is the internal rewriting memory. In order to prevent overflowing, it can control the multiplier by taking it out and shifting one digit and sending into M or M' . The duplex multiplier can also be used for addition and subtraction to save equipment.

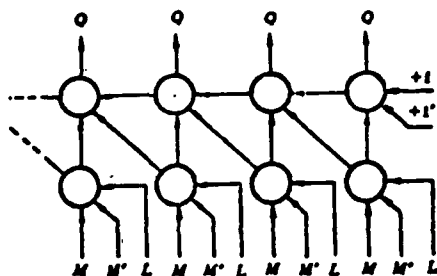


Figure 4

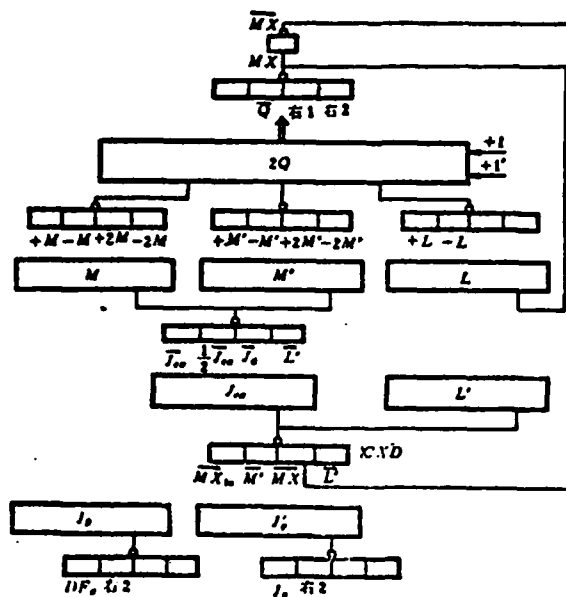


Figure 5

1--right 1 right 2; 2--right

IV. RAM FOR DATA

The data memory (i.e., internal memory) generally uses conventional magnetic core memory devices with the data stored sequentially. From the above method, it is possible to take a pair of numbers from the memory to carry out the butterfly operation

and still store them back to the original pair unit. The principle of magnetic core memory requires two bits to store or to have access to a number. During access, it reads first and then writes. In storage, a reading current to clear the magnetic core must be applied and then the number is written into the memory. Based on the characteristics of the FFT method, we adopted the working format which does not require rewriting during access and reading before storage. Because data must only be read once in the butterfly operation, there is no need to rewrite. The magnetic core remains zero; it is then no longer required to clear the memory before entering. Originally, due to the lack of speed in core memory, two memory units were required, one for the real part and the other for the imaginary part. Now that the access time in the memory core is practically doubled, one memory unit is sufficient. The main frequency of this equipment is 1 μ s per bit. Storage and access requires one bit each. The duplex multiplier has 1 μ s per bit. Sufficient time is available. Therefore, the main frequency and the processing speed of the entire device still have a potential to be further improved.

V. ROM FOR TRIGONOMETRIC FUNCTIONS

Usually the input time functions are real numbers and only the calculated results are complex numbers. In order to save time, N point of real numbers can be transformed into $\frac{N}{2}$ point of complex numbers in operation. 1024 real number points can be transformed into 512 complex number points. Every iteration involves 250 butterfly operations. The maximum number of the corresponding 0-180° trigonometric function values is 256. The trigonometric function values in the second quadrant can be derived from those in the first quadrant. Therefore, only 128 corresponding sine function values between 0-90° are needed. We adopted a transform coil type of ROM. The capacity is 128 location with 10 bits word length. Once the address of the ROM is ascertained, the needed trigonometric function value can be taken out.

The address can be eight digits,

$$x = x_0 x_1 \dots x_7 = \boxed{x_0} \boxed{x^*}$$

The first digit x_0 represents the quadrant. When $x_0 = 0$, it represents the first quadrant. x^* is the address of the sine function which is the ROM address.

$$J_{\sin} = x^*$$

Cosine and sine functions are related by the complimentary relation, therefore, the cosine ROM address is

$$J_{\cos} = 128 - x^* = \bar{x}^* + 1$$

In other words, if we use the complement of x^* as the address, then it reads $\cos \frac{x}{128} 90^\circ$.

When $x_0 = 1$, it indicates that the angle is $\geq 90^\circ$. The sine function address then becomes

$$J_{\sin} = 256 - (x_0 + x^*) = 128 - x^* = \bar{x}^* + 1$$

or, using the complement of x^* as the address, we can read $\sin \frac{x}{128} 90^\circ$. Using x^* as the address, we can read $\cos \frac{w}{128} 90^\circ$. However, we must take its negative value because the cosine function in the second quadrant is negative.

VI. THE INDEXING UNIT

The data participating in the butterfly operation should be obtained and stored based on the need as indicated by the flow chart. From Figure 3, it can be listed that the sequence of data address is as follows:

It can be summarized that address a and address b seem to obey the following regularity:

| 1 第一遍 | | 2 第二遍 | | 3 第三遍 | |
|--------|--------|--------|--------|--------|--------|
| a 地址 4 | b 地址 5 | a 地址 6 | b 地址 7 | a 地址 8 | b 地址 9 |
| 0 0 0 | 1 0 0 | 0 0 0 | 0 1 0 | 0 0 0 | 0 0 1 |
| 0 0 1 | 1 0 1 | 0 0 1 | 0 1 1 | 0 1 0 | 0 1 1 |
| 0 1 0 | 1 1 0 | 1 0 0 | 1 1 0 | 1 0 0 | 1 0 1 |
| 0 1 1 | 1 1 1 | 1 0 1 | 1 1 1 | 1 1 0 | 1 1 1 |

1--the first time; 2--the second time; 3--the third time;
4--5--6--7--8--9--address

The first time: the first digit of address a is 0
the first digit of address b is 1

The second time: the second digit of address a is 0
the second digit of address b is 1

The third time: the third digit of address a is 0
the third digit of address a is 1

For this a shift register of iteration J_{dd} is installed. Initially, the first digit is 1 and the remaining are 0. After each iteration, it is shifted to the right by one digit. Let us set up an address register J_a for address a. By sending J_a to the internal address register J_a , we get the number a. When J_a and J_{dd} are simultaneously sent to J_a , it is then address b and the number b can be taken out immediately (refer to Figure 6).

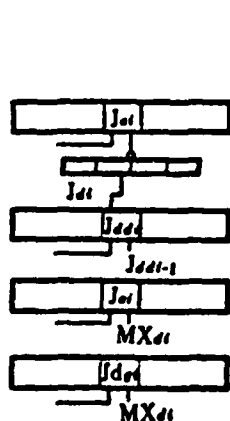


Figure 6

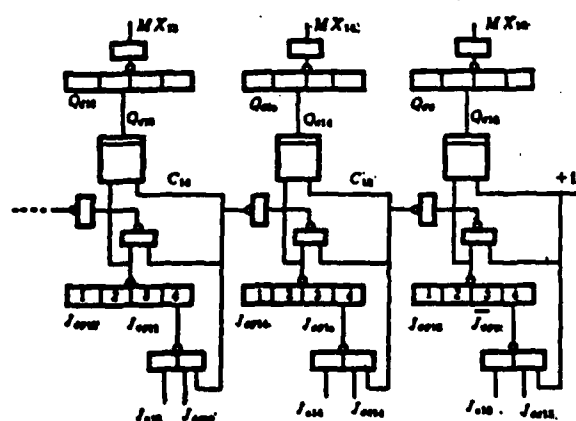


Figure 7

J_a is usually counted sequentially. However, if it meets J_{dd} with its digit equals to 1, then it must skip it and move on. For this purpose, a special counting logic circuit as shown in Figure 7 was designed. A conventional counting logic diagram is formed by an array of discriminating gates and another array of conventional indexing logic. J_a passes through the multiple switching number 4 gate to arrive at the entrance of the counter. The +1 signal is then added to it. The output goes through the multiple switch MX_d to arrive at the D end of the trigger D of the memory J_a . It is then entered into the memory J_a by DRJ_a pulsing. Usually, J_a is counting sequentially. When it is shifted to a digit with J_{dd} equal to 1, or when the "no" gate makes the addition of 1 to that digit, then skipping occurs. When the highest digit is filled and must be shifted, then it means the end of one iteration. It emits a pulse which causes J_{dd} to shift 1 digit. Trigonometric functions must also be read from the ROM according to the flow chart. From the flow chart Figure 3, the sequence is listed as follows:

| ¹ 第一遍 | | ² 第二遍 | | ³ 第三遍 | |
|------------------|-----|------------------|-----|------------------|-----|
| W^0 | 0 0 | W^0 | 0 0 | W^0 | 0 0 |
| W^0 | 0 0 | W^0 | 0 0 | W^1 | 1 0 |
| W^0 | 0 0 | W^1 | 1 0 | W^1 | 0 1 |
| W^0 | 0 0 | W^1 | 1 0 | W^1 | 1 1 |

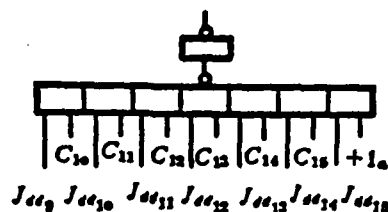
1--the first time; 2--the second time; 3--the third time

Although the sequence is not the same for each time, a certain order still exists. First, we noted that the address is in inverse order which is that the first digit is used as the last one in indexing, and it shifts to the right. Secondly, not every butterfly operation requires counting. It only requires counting when skipping occurs. There is no counting the first time. The second time counting occurred once and it happened three times the third time. In the ROM (real only memory) and core memory share the same indexing unit. It is also included in Figure 7. The ROM address register J_{dg} inversely goes through the multiple

switch at gate no. 3 to enter the indexing unit. After adding 1 to it, it goes through the multiple switch MX_d at gate no. 1 in the reverse direction to the memory J_{dg} . This completes the inverse indexing.

The logic circuit to control skipping is shown in Figure 8.

Figure 8.



It has been introduced above, when the value sine or cosine function is taken out of the ROM, sometimes it is necessary to use the complement of the address of the ROM depending on the quadrant. This is to send J_{dg} and $+1_d$ which can be realized by the multiple switch gate no. 1.

VII. MICRO-PROGRAMMING CONTROL UNIT

The entire machine adopted the micro-programming control technology. Its working principle is well known to everyone and will not be repeated here. Here we are only going to briefly introduce the control flow chart of a butterfly operation.

Every iteration requires many repeated butterfly operations. Therefore, the flow chart was designed in a looping cycle form. In order to make the core memory and the operating unit re-select their functions, there is an initiating cycle before the looping cycle, and there is also an end cycle after the looping cycle. The first time begins with the initiating cycle. It reads b , b' , \sin and \cos and then carries out the duplex multiplication to determine c . The last bit in the multiplication brings the b' in M' to be temporarily stored in L' . The space is used to place the

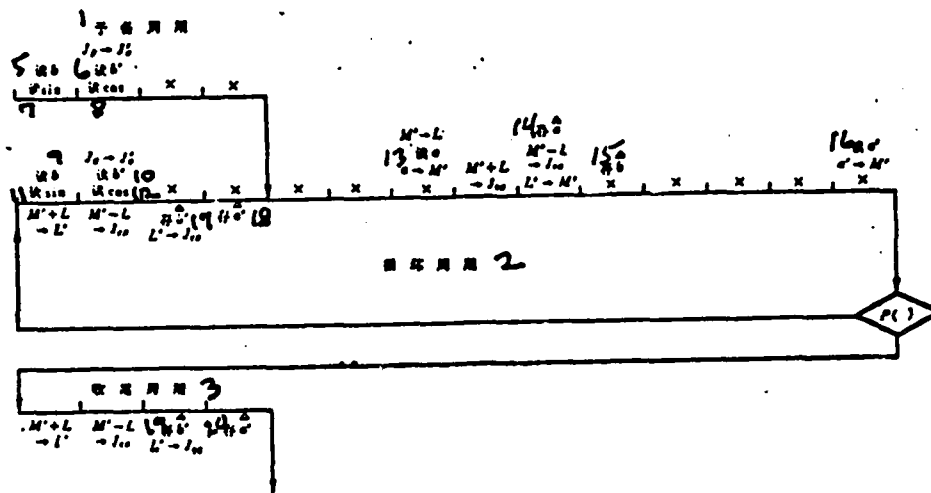


Figure 9

1--initiating cycle; 2--looping cycle; 3--end cycle; 5--read b
6--read b'; 7--read sin; 8--read cos; 9--read b; 10--read b' .
11--read sin; 12--read cos; 13--read a; 14--store a; 15--store b;
16--read a'; 17--store b'; 18--store a'; 19--store b'; 20--store
a'

a just being read. After the multiplication it performs $a + c$ and $a - c$ to determine the calculated results \hat{a} and \hat{b} , and stores them in the original units. It then sends the b' from L' back to M' to carry out the duplex multiplication for the second time to obtain c' . Similarly, a' is read in the last bit of the multiplication. The following operation and the next iteration proceeds in an iterative manner. On one hand, it must read the b , b' , \sin and \cos needed for the next butterfly operation which is the same 4 bit job as in the initiating cycle. On the other hand, it must continue finishing $a' + c'$ and $a' - c'$ to obtain the calculated results \hat{a}' and \hat{b}' and store then to the original units. During the last butterfly operation in an iteration, it cannot go into the looping cycle again. It should switch to the end cycle. This is realized by the transform made by the control of micro-address using $P()$.

```

graph TD
    1[1. 初始化] --> 2[2. 循环]
    2 --> 3{3. 判断}
    3 -- 是 --> 4[4. 输出结果]
    3 -- 否 --> 2

```

1. 初始化

2. 循环

3. 判断

4. 输出结果

1--initiating cycle; 2--judgmental skip; 3--looping cycle;
4--end cycle

Finally, it must be explained that this method has been fully discussed at the 5th Branch of the National Ocean Bureau and the FFT Section of the Tianjin Electronic Instrument Factory which led to the further improvement and completeness of this plan. It experienced the collective experience and wisdom of all the people.

Summary

A Fast Fourier Transform Hardware Processor

Kang Jichang and Xu Naiping

The National Ocean Bureau and the Tianjin Electronic Instrument Factory were developing a real-time FFT processor for acoustic signals, with the computing time of Fourier Transform of 1024 data points being about 40 ms. We proposed a new project for the purpose of reducing by 50% the size of CPU and memory. The new project was accepted and successfully carried out in early 1979. The idea and the essential logic of the new project are presented in this paper.

DUPLEX MULTIPLIER A duplex multiplier is adopted to satisfy the requirements of the butterfly operation. It requires 4 multiplications and 6 additions for every butterfly operation. In the original project, two separate multipliers are required, one for real part and the other for imaginary part. It is evidently too expensive. In the new project, a duplex multiplier is adopted, as shown in fig. 4, and the algebraic sum of the two products can be obtained at once. Because time is saved, both the real and the imaginary parts can share the very same duplex multiplier, and the logic circuits are saved as well. Fig. 5 shows the block diagram of the whole arithmetic unit. M, M' are data registers, i. e., two multiplicands. J_c, J_s are cosine and sine functions respectively, i. e., two multipliers. L, L' are accumulators, i. e., real and imaginary parts of products respectively. J_{out} is buffer register of memory.

RAM FOR DATA Data are stored in core memory. In the original project, two separate memories are required, one for real part and the other for imaginary part, due to limitation of access time. In fact, each butterfly operation takes a pair of data from memories, and the results are returned to the original locations. Hence, the "load" and "store" operations can be combined into only one access cycle instead of two separate ones. The time is saved again, and the two data can be accessed serially from one memory. Therefore only one memory is required by the new project.

ROM FOR TRIGONOMETRIC FUNCTIONS Sine table for 0-90 degrees is stored uniformly in a ROM, with 128 locations and 10 bits word length. Sine functions for other quadrants and cosine functions for all quadrants can also be obtained from the very same ROM by appropriate transformation.

IDNEXING UNIT For butterfly operation, the addresses of data are counted with skipping, while the addresses of trigonometric functions are counted in inverse order. Both indexing rules can be carried out by the combined indexing logic unit, as shown in fig. 6 and fig. 7.

J_a — Address register of RAM

$J_{a\theta}$ — Address register of ROM

J_a — Address register of data a

J_{aa} — Shift register of iteration

MICRO-PROGRAMMING CONTROL UNIT The control unit is micro-programmed. Fig. 9 shows the flow diagram of the arithmetic unit and memory and Fig. 10, that of the indexing unit. It usually takes a loop for every butterfly operation with the following two exceptions. The first butterfly operation takes an initiating cycle, and the last one, an additional end cycle. The micro-operations in each step are indicated on these two flow diagrams.

Color Discrimination by a Color-Picture Reader

Chen Chenghang

Textile pattern design is one area where computer aided design method can be applied. The direct control of the weaving loom on the automatic punching of the Jacquard card requires the reading of an artist's sketch or a point paper manuscript which can either be in black and white or in color. Different color indicates that a different technological processing method is used. Since this area is still in its infancy in our country, most of our readers installed adopted a photo-sensitive unit which transforms the reflected light intensity from sampling points into electricity. The contrast of the pattern is then transformed into a variation in voltage. The artist's sketch or point paper manuscript is adhered to a cylinder which rotates in a circular manner. For each evolution, the reader's head moves by one column along the axis. This is repeated until every point in the whole sketch has passed under the reader's head and received by the sampling process. Because the pattern is drawn by the artists, the inconsistency of the coloring materials used and the non-uniformity in the coloring are affecting the consistency of the brightness of the pattern. Furthermore, because the focus of an optical system is closely related to several physical dimensions, the concentricity of the roller, conicity, and the fitness of the pattern to the cylinder during the display are relevant. Therefore, the voltage level read for the same color may vary significantly. For the reliable recognition of patterns, at this moment, it can only identify the two colors black and white. In 1975 an electronic pattern weaving collective effort unit was formed in Siam. During the first phase in the testing of a 272 pin single loom Jacquard, the above method was adopted. Back then the objective was to weave a single layer patterned textile with 2 - 3 different structures. After over a year of

experimentation, it was demonstrated that this method could distinguish 3 - 4 colors with careful adjustment and delicate preparation of the sketches. Basically, it was stable and reliable in performance. The second phase began in 1978 and it was centered around the automatic punching of Jacquard cards in order to satisfy the 6 - 12 technological requirements for products such as satin comforter covers. Therefore, the original method could not meet those requirements. In order to reach the capability of discriminating twelve colors, we used the three-color basic principle for color televisions. The pattern color (reflected light) is decomposed into red, green, and blue, the three basic colors, and then the three basic color signals are analysed and given a corresponding color code. Although this was the first attempt at using this method in the silk textile industry without any matured successful precedent, yet it has already become a matured technique in printing and color television. Therefore, we considered that this method was practical. Of course, our requirements and those for the printing and color television industries have their differences. They require the reappearance of color of the patterns in printed materials or on television screens which demands the absolute magnitudes of the three basic colors do not vary during transmission. Then they reappear at the receiving end in proportion and thus the objective of no distortion is reached. However, in silk textile because the color of the pattern represents different composition technologies, it does not require the absolute magnitude of the transmitted signal to be unchanged. On the contrary, because of the nonuniformity of coloring in manmade drawings, the non-ideal mechanical dimension of the roller, and other reasons, the three basic color voltage values of a certain color may vary quite significantly in a pattern. This requires the equipment to have the maximum tolerance in input signals without causing any misjudgment. The equipment not only must have the ability to distinguish color but also should be able to categorize color. In other words, the equipment should work

like human eyes. It not only is capable of differentiating the color between one point and another but also should be able to judge that they belong to the same color even when the data show some difference and assigns the same color code. There is conflict. Up to date the various color discriminating apparatus cannot offer an ideal solution to this problem. The reason is that there is no reasonable processing method available to handle the three basic color data.

Usually the rigorous description of color must include the three parameters: brightness, hue and saturation level, where the combination of hue and saturation level is called colority. In order to discuss the possible variation of data on a color in a pattern, we must obtain the signals of the brightness, hue and saturation level of the three basic color and then carry out an analysis on their mutual relationship.

For a three basic color colorimetric system, when the standard light source is shining on a piece of reference white paper the received reflected light signals in the Red (R), Green (G), and Blue (B) channels are considered as the maximum value 100. With reference to the reference white color, $R = G = B = 100$. In that case R, G, and B can be made into three coordinate axes which are perpendicular to each other and the reflected light intensity from any color can be quantitatively expressed as a point in the RGB space. The RGB value varies for different color ranging from 0 to 100 which forms various points at different positions in the RGB space. The combination of these points forms a color cube as shown in Figure 1.

The color zone picture reader's design concept is that a color occupies an irregularly shaped zone in the color cube as the color zone shown in Figure 1. Its shape and size are difficult to predict. Therefore, in order to distinguish color the machine is equipped with many transformation methods such

as the calibration channel, the elimination channel, and the operation channel, etc. which can be selected by the user in combination arbitrarily. Of course, this is a very flexible method. However, it is too vague to be operated easily. Although the manual listed many tables summarizing which transformation is suitable for the discrimination of a particular color by prior experience, yet the user still has to acquire a long term operating experience so that the machine can be handled at will. Especially when multiple colors are chosen simultaneously, the equipment becomes very complicated. It is not only very expensive but also too troublesome to use.

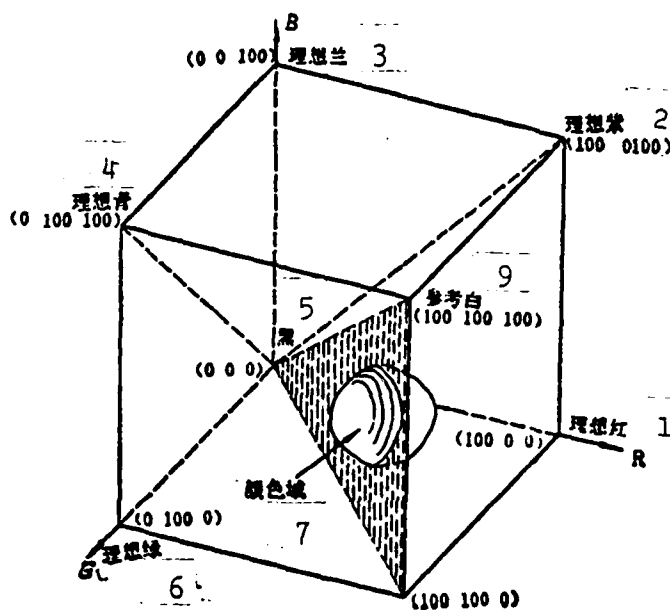


Figure 1. Color Cube. Key: 1. ideal red, 2. ideal violet, 3. ideal blue, 4. ideal indigo, 5. black, 6. ideal green, 7. color zone, 9. reference white.

Does the distribution of color zone in the color cube really follow no rules? No. The distribution of color does obey certain rules. The study of this problem belongs to the category of a not too new science - colorimetry. Over a hundred years ago Grassman had already established a systematic colorimetry. Famous scientists such as Maxwell and Schrodinger have done a lot of research in this area. With the development of color printing and color television technologies, colorimetry has been fully developed.

II. THE COLOR ANALYSING TOOL - COLORIMETRY

In 1931 CIE officially approved that the three basic color system should use RGB and XYZ units which not only provided a rigorous mathematic basis for colorimetry but also established an internationally unified system. The meeting also decided that the standard wavelengths for the monochromatic light of the three basic colors should be:

| | |
|--------------------------------|--------------------|
| Red (R) - 700 mμ (millimicron) | } mercury spectrum |
| Green (G) - 546.1 mμ | |
| Blue (B) - 435.8 mμ | |

With respect to the standard white light (equi-energetic white), the intensity relationship of the three follows:

$$L_R : L_B : L_G = 1:4,5907:0.00601 \text{ (unit light watt)}$$

In the three color system in colorimetry, the flux of all given monochromatic or polychromatic light can be expressed by the three color coefficients r' , g' , and b' of the three basic colors.

The light flux (brightness) of a given color light

$$F'_\lambda = r'L_\lambda + g'L_\lambda + b'L_\lambda$$

When only the colority must be given for a color light and the brightness is not considered, then the relative three color coefficients

$$r = \frac{r'}{r' + g' + b'}, \quad g = \frac{g'}{r' + g' + b'}, \quad b = \frac{b'}{r' + g' + b'}$$

can be used as the substitutes. It is apparent that $r + g + b = 1$. Therefore, it is very easy to use two out of the three coefficients r, g, b as parameters in a right angle coordinate system to find the solution graphically. It is customary to choose r and g as the abscissa and ordinate, respectively. It is also called a colority diagram as shown in Figure 2.

The CIE also provided the three color coefficients of monochromatic light with wavelength ranging from 380 mμ to 780 mμ at an interval of 5 mμ which is shown as the horse shoe shaped curve AMR in Figure 2. It is also called the spectral trajectory. Their purity is defined as 100%. The point at which $r = g = b = 1/3$ in the figure is called reference white C whose purity is 0. Any color K can be considered as a combination of the white light C and a monochromatic light M. Its hue is determined by the monochromatic light M mixed into it. Therefore, the wavelength of the monochromatic light M is its main wavelength. Its purity is determined by the ratio of its distance to point C and the distance from points M to C.

$$p = \frac{CK}{CM}$$

The point K' inside the triangle formed by point A at 380 mμ, point R at 780 mμ, and point C appears to be violet in color. However, it cannot be formed by the combination of a monochromatic light and white light. It can be considered as if it is obtained by removing a monochromatic light M' from the

white light. Therefore, its main wavelength is expressed by the wavelength of M' but with a minus sign. This means that K' is the complementary color to M'.

$$P = \frac{CK}{CM}$$

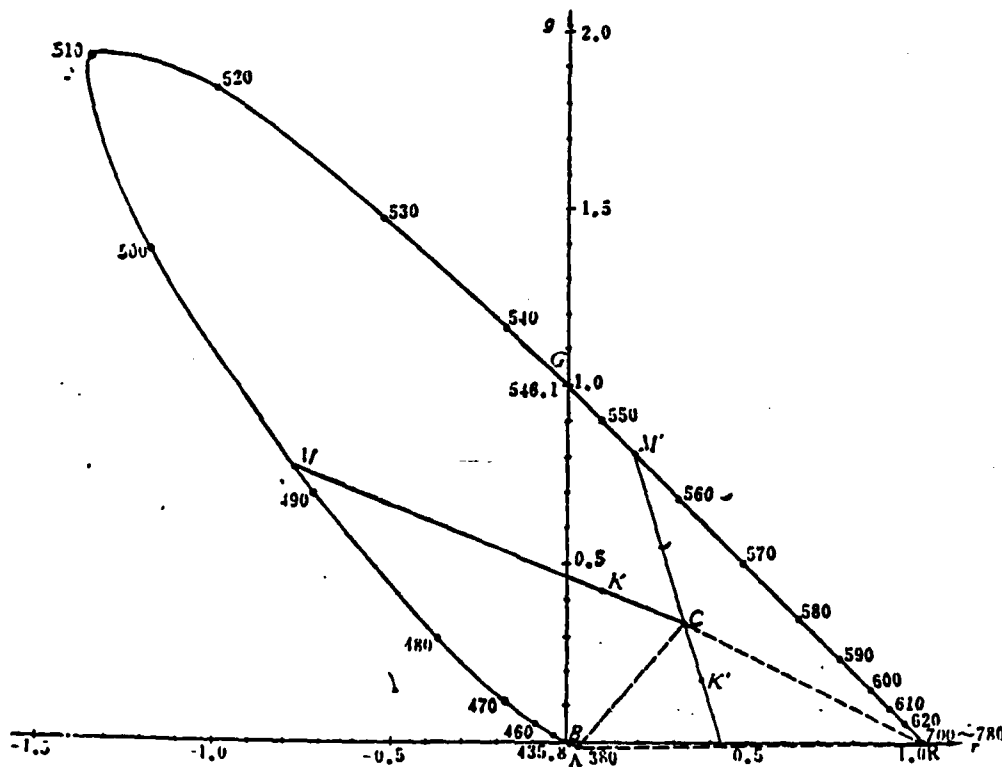


Figure 2. Right Angle Coordinate Colority Diagram.

Henceforth we can also use the main wavelength and purity of a color to represent its colority. The main wavelength determines its hue while its purity determines its saturation level. Its colority value rgb has already been determined by CIE. Therefore, it can be divided into approximate areas in the colority diagram based on the main wavelength as red, orange, yellow, green, blue, purple, and violet, etc. They radiate away

from point C as shown in Figure 3. The dotted lines in the figure provide equi-purity lines. They are centered around point C and similar in shape as the horse-shoe curve.

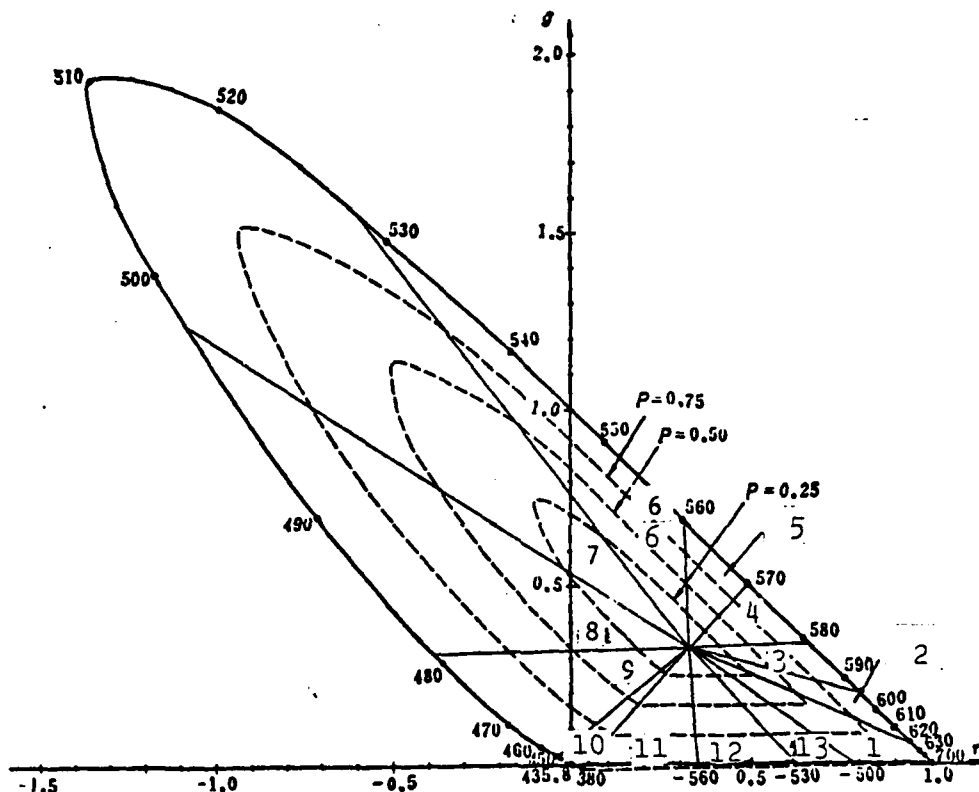


Figure 3. Color Zone Distribution in the Colority Diagram.
Key: 1. red, 2. orange red, 3. orange, 4. yellow, 5. yellowish green, 6. viridescent, 7. green, 8. bluish green, 9. indigo, 10. blue, 11. bluish violet, 12. violet 13. purplish red.

III. CURRENT COLORIMETRIC METHODS

In the color television technology, due to special consideration made on the characteristics of human vision and fluorescent materials, the standard three basic colors established by

CIE were not adopted. The R and B are shifted slightly. The colorimeter we adopted is the same as the one used in the color television industry. Therefore, the actual RGB values are the same as those in the color television system. They are:

$$R_e = 620m\mu, \quad G_e = 546.1m\mu, \quad B_e = 450m\mu.$$

For our actual system, R_e , G_e , and B_e cannot show negative values. Therefore, all the colors which can be analysed must be inside the $R_e G_e B_e$ triangle. Actually, this is already capable of including the majority of the colors of currently available coloring and color film.

Let us change R_e , G_e , and B_e into coefficient of a right angle coordinate system (actually not too different from the original RGB triangle). Since it is meaningless outside the triangle for an actual system, we then can define the color along the three sides as the ideal color. At least one of the three color coefficients r , g , and b is zero. As for the other two, once only one is determined, it is possible to define its position in the colority diagram and main wavelength. Let us further define the purity of the ideal color $p_e = 100\%$; then for any color K its purity is changed to $p_e = \frac{CK}{CN}$; N is the position of the ideal color which has the same main wavelength as the color K as shown in Figure 4. Since there are only twelve colors to be distinguished in the system, we can roughly divide the color zone into red, yellow, green, indigo, blue and violet six zones. We can further assume that when purity $p_e = 25\%$ and below the color has approximately faded. The only feeling it gives is the difference in brightness in black, grey, and white. The division of color zones in color vision of human eyes is approximately shown as the dotted lines in Figure 4. In actual system it is further simplified for the convenient

realization in electric circuitry. The color distinguishing zones of the simplified circuit are shown as solid lines in Figure 4. It can be seen that the distribution of each zone is approximately the same as in human vision. On the basis of these seven colors, we further distinguish several colors which show great differences in brightness. For example loud red and rose, light yellow and light green, deep purple and light purple, and white, gray, and black are further distinguished by brightness. Thus it realizes the differentiation of twelve colors. For the twelve colors we have already selected their corresponding colorings. The actually measured ranges of brightness, main wavelength, and purity of those colorings are approximately the same as those shown in the Table. Experimental data verified that the variation of the brightness of the reflected light is very high. The changes in purity rank second. The variation in main wavelength is extremely small. Therefore, we are concentrating on the determination of main wavelengths and dividing the colors into six zones. It is further distinguished roughly by brightness into black, grey, and white, loud red and rose, light green and light yellow, and deep purple and light purple together with primary green, secondary indigo, and prussian blue to form a total of twelve colors. Based on the above data, it is believed that the equipment is capable of handling the requirement. The actual electrical circuit and error analysis is available in the article entitled "The Analysis of the Theory in Color Discrimination of the Photo-electric Scanning Electronic Order Discrimination" written by the Sian electronic pattern weaving research and development group [4].

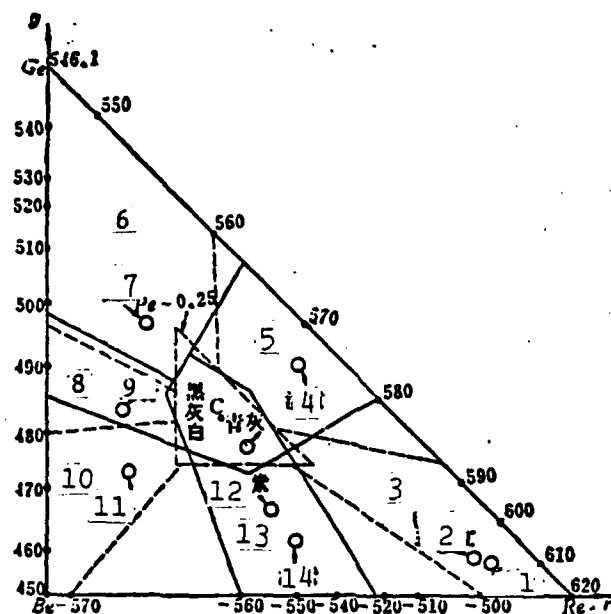


Figure 4. The Color Zone Distribution in Real Systems.
 Key: 1. loud red, 2. rose, 3. red, 4. light yellow, 5. yellow, 6. green, 7. primary green, 8. indigo, 9. secondary indigo, 10. blue, 11. prussian blue, 12. light purple, 13. violet, 14. deep purple.

| 1 染料名称 | | 12 测得值 | | | 13 坐标值 | | 14 亮度 | 15 主波长 | 16 纯度 | 17 偏差 | | |
|--------|-------|--------|----|----|--------|-------|-------|-------------|-------|--------------|--------------------|--------------|
| | | R | G | B | r | g | L_e | λ_e | P_e | ΔL_e | $\Delta \lambda_e$ | ΔP_e |
| 2 淡黄 | 18 最大 | 100 | 75 | 7 | 0.550 | 0.412 | 80.9 | 573m μ | 0.880 | 8.7% | 0.17% | 1.38% |
| | 19 最小 | 90 | 67 | 7 | 0.548 | 0.408 | 74.2 | 574m μ | 0.868 | | | |
| 3 大红 | 20 最大 | 92 | 11 | 11 | 0.807 | 0.096 | 35.4 | 620m μ | 0.712 | 18.5% | 0 | 1.20% |
| | 21 最小 | 79 | 9 | 9 | 0.873 | 0.093 | 30.0 | 620m μ | 0.721 | | | |
| 4 玫瑰红 | 22 最大 | 87 | 7 | 10 | 0.798 | 0.083 | 25.4 | 640m μ | 0.751 | 26.3% | 0.32% | 4.6% |
| | 23 最小 | 50 | 8 | 8 | 0.780 | 0.094 | 19.4 | 638m μ | 0.718 | | | |
| 5 紫罗兰 | 24 最大 | 53 | 11 | 44 | 0.490 | 0.102 | 27.3 | -528m μ | 0.694 | 26% | 0.38% | 2.83% |
| | 25 最小 | 40 | 9 | 34 | 0.482 | 0.108 | 21.0 | -530m μ | 0.676 | | | |
| 6 浅紫 | 26 最大 | 98 | 34 | 90 | 0.440 | 0.160 | 59.5 | -530m μ | 0.520 | 16.8% | 0.51% | 16.9% |
| | 27 最小 | 91 | 25 | 78 | 0.468 | 0.128 | 50.8 | -533m μ | 0.618 | | | |
| 7 酞菁蓝 | 28 最大 | 8 | 10 | 31 | 0.128 | 0.212 | 11.1 | 470m μ | 0.616 | 14.4% | 0.43% | 15.8% |
| | 29 最小 | 6 | 9 | 23 | 0.158 | 0.296 | 9.8 | 472m μ | 0.528 | | | |
| 8 二青 | 30 最大 | 10 | 41 | 61 | 0.164 | 0.338 | 36.9 | 485m μ | 0.508 | 18.1% | 0.21% | 0.6% |
| | 31 最小 | 17 | 35 | 51 | 0.165 | 0.340 | 31.4 | 486m μ | 0.505 | | | |
| 9 头绿 | 32 最大 | 20 | 52 | 34 | 0.189 | 0.480 | 40.4 | 521m μ | 0.433 | 15.1% | 0.58% | 4.25% |
| | 33 最小 | 18 | 44 | 30 | 0.195 | 0.478 | 34.7 | 519m μ | 0.415 | | | |
| 10 浅绿 | 34 最大 | 87 | 85 | 17 | 0.396 | 0.502 | 72.0 | 566m μ | 0.695 | 22.7% | 0.35% | 9.9% |
| | 35 最小 | 50 | 70 | 10 | 0.384 | 0.538 | 57.3 | 564m μ | 0.768 | | | |

11 某些颜料的亮度和色度测量数据

Key: 1. name of coloring, 2. light yellow, 3. loud red, 4. rose, 5. violet, 6. light purple, 7. prussian blue, 8. secondary indigo, 9. primary green, 10. light green, 11. measured data on the brightness and colority of some colorings, 12. measured values, 13. coordinate values. 14. brightness, 15. main wavelength, 16. purity, 17. deviation, 18, 20, 22, 24, 26, 28, 30, 32, 34. maximum, 19, 21, 23, 25, 27, 31, 33, 35. minimum.

IV. ADVANCED DISCUSSION ON THE COLORIMETRIC METHOD

Color picture readers using similar principles to distinguish colors are also available in foreign countries as research and development products. For example, the Japanese's

"Hitachi" electronic automatic sketch readers is the one which adopted the brightness and colority separation method to solve the problem of measuring error due to the unevenness of coloring in the sketches. However, it uses a digital electronic computer to process the separation of brightness and colority. Therefore, it must first transform the R,G,B singles of all the sampling points using an A/D converter and then send them to the computer for processing. The A/D converter requires a longer transformation time. It labels the three quantities R,G, and B sequentially which leads to the occurrence of time difference. In order to solve this problem, before each transformation a sampling maintenance apparatus must be plugged in to assure that the R,G,B. values converted belong to the same sampling point. This arrangement also drastically reduces the sampling speed. Also in order to ensure the precision of the data acquired, it requires that the sampling maintenance apparatus and the A/D converter have sufficiently high accuracy. If special applications such as color discrimination for a map are considered, then a digital computer must be assigned to handle color data exclusively. It may even be necessary to read one color at a time. This is a very expensive method.

Actually the separation of brightness and colority can be realized using a simple operation. For the discrimination of color, the accuracy required for this operation is not very high (approximately 1% for example). Therefore, the use of a simulated solution apparatus cannot only increase the sampling rate but also simplify the equipment circuitry. It is certainly worth considering.

In order to distinguish colors it is required to calculate the brightness L , purity p , and main wavelength λ . Let us assume that the three channel input signals of the basic color are R, G, and B and they correspond to the three color

coefficients r' , g' , and b' . The brightness L then is:

$$L = L_R R + L_G G + L_B B,$$

where L_R , L_G , and L_B are the relative brightness coefficients of the three channels. They vary with the defined wavelengths for R, G, and B. In the color television system it is usually the values that $L_R = 0.30$, $L_G = 0.59$ and $L_B = 0.11$.

For the determination of purity, let us examine the following three cases (see Figure 5):

1. Point K is located inside ΔCBG , which is point K_1 .
By definition purity $p_s = \frac{CK_1}{CM_1}$.

Since $\Delta CK_1 K'_1 \sim \Delta CM_1 M'_1$
then $\frac{CK_1}{CM_1} = \frac{CK'_1}{CM'_1}$

and $CM'_1 = \frac{1}{3}$, $CK'_1 = \frac{1}{3} - r_1$

therefore $p_s = 1 - 3r_1$

From $r_1 = \frac{R}{R+G+B}$ we get:

$$p_s = \frac{B+G-2R}{R+G+B}.$$

Which is the case where R is the smallest among the three quantities, R, G, and B.

2. Point K is located inside ΔCBR which is point K_2 .
This is the case where G is the smallest:

$$p_s = \frac{CK_2}{CM_2} = \frac{CK'_2}{CM'_2} = \frac{\frac{1}{3} - g_2}{\frac{1}{3}} = 1 - 3g_2$$

From $g_1 = \frac{G}{R+G+B}$, we get $p_c = \frac{R+B-2G}{R+G+B}$

3. Point K is located inside ΔCRG which is point K_3 . This is the case where B is the smallest:

$$p_c = \frac{CK_3}{CM_3} = \frac{CK'_3}{CK''_3}$$

From $CM'_3 = \frac{1}{3}$, $CK'_3 = CN + NK'_3 = CN + NK_3$, $CN = r_3 - \frac{1}{3}$, $NK_3 = g_3 - \frac{1}{3}$

we get $CN + NK_3 = r_3 - \frac{1}{3} + g_3 - \frac{1}{3} = r_3 + g_3 - \frac{2}{3} = 1 - b_3 - \frac{2}{3} = \frac{1}{3} - b_3$

then $p_c = 1 - 3b_3$ or $p_c = \frac{R+G-2B}{R+G+B}$.

Summarizing the three cases, if we let X represent the smallest value among R, G, and B (i.e. $X = \text{MIN}(R, G, B)$) then the purity:

$$p_c = \frac{(R-X) + (G-X) + (B-X)}{R+G+B} = \frac{R+G+B-3X}{R+G+B}$$

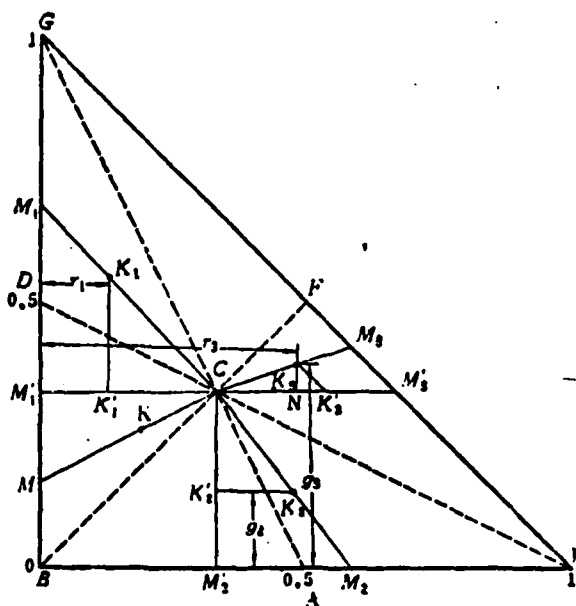


Figure 5. Method to Calculate Purity.

For the determination of the main wavelength, we are dividing the three sides of ΔRGB into BD, DG, GF, FR, RA, and AB six sections for examination.

Section BD, R is the smallest, B is the largest, main wavelength range $435.8 \text{ m}\mu \sim 496 \text{ m}\mu$. The ideal color M corresponding to point K can be defined solely by $b_o = \frac{B_o}{G_o + B_o}$.

It can be proved that $b_o = \frac{B-R}{G+B-2R}$ and $b_o \geq 0.5$ (because B is largest).

Similarly, in Section DG, R is the smallest and G is the largest. The main wavelength range is $496 \sim 546 \text{ m}\mu$. The ideal color in this section can be better designed by

$$g_o = \frac{G-R}{G+B-2R} (\geq 0.5)$$

In section GF, B is the smallest and G is the largest. The main wavelength range is $546 \sim 570 \text{ m}\mu$: it can be defined by

$$g_o = \frac{G-B}{G+R-2B} (\geq 0.5)$$

In Section FR, B is the smallest and R is the largest. The main wavelength range is $570 \sim 780 \text{ m}\mu$: it can be determined

$$\text{by } r_o = \frac{R-B}{G+R+2B} (\geq 0.5)$$

In Section RA, G is the smallest and R is the largest. The mainwavelength range is $496 \sim 546 \text{ m}\mu$: it can be defined by

$$r_o = \frac{R-G}{R+B-2G} (\geq 0.5)$$

In Section AB, G is the smallest and B is the largest. The main wavelength range is $546 \sim 570 \text{ m}\mu$: it can be defined by

$$b_o = \frac{B-G}{B+R-2G} (\geq 0.5)$$

Combining these six sections, if we let Y represent the largest value among R, G, and B (i.e. $Y = \text{MAX}(R, G, B)$) then the parameter determining the main wavelength is W

$$1 \geq W \geq 0.5, W = \frac{Y - X}{R + G + B - 3X}$$

In summary, one must carry out the following operation for any selected color:

1. Brightness $L = L_R R + L_G G + L_B B$

2... Purity $p = \frac{R + G + B - 3X}{R + G + B}$ where $X = \min\{R, G, B\}$

3. Main wavelength coefficient $W = \frac{Y - X}{R + G + B - 3X}$

where $Y = \max\{R, G, B\}$

If we define the upper and lower limits of brightness as L_m and L_n , the upper and lower limits of purity as p_m , p_n , and the upper and lower limits of the main wavelength coefficient as W_m , W_n , then for the input R, G, B three channel signals the one with the minimum value is used to choose the circuit. The one with the maximum value will select the circuit and four operational amplifiers to produce signal such as $X, Y, L_R R + L_G G + L_B B, R + G + B, R + G + B - 3X$. It is then followed by carrying out the following comparisons using six comparative amplifiers:

$$\begin{aligned} L_m - (L_R R + L_G G + L_B B) &\geq 0 \\ (L_R R + L_G G + L_B B) - L_n &\geq 0 \\ (R + G + B) p_m - (R + G + B - 3X) &\geq 0 \\ (R + G + B - 3X) - (R + G + B) p_n &\geq 0 \\ (R + G + B - 3X) W_m - (Y - X) &\geq 0 \\ (Y - X) - (R + G + B - 3X) W_n &\geq 0 \end{aligned}$$

Their accuracy requirement is not more than 1%. It is sufficient to distinguish a 24 color colorimetric card commonly used in foreign countries. Compared to the description in (§. 200) of "Theory of Optical Instruments" by A. N. Tutolovsky on the microscopic sensitivity of human color vision, the

color discrimination capability of the above equipment is at least comparable to human eyes.

V. CONCLUSIONS

In summary, using the theory of colorimetry we can separately distinguish the brightness, hue (main wavelength), and saturation level (purity) of the three basic color signals in a colorimetric system. The accuracy requirement of the entire equipment can be relaxed. In addition, a simpler circuit and an easier operating procedure can be adopted to read the necessary color. The function can approach the color discrimination capability of human eyes. Here it is particularly suitable to use the simulated solution apparatus (high operating speed, accuracy requirement not too high) to further simplify the colorimetric equipment without using an electronic computer. With slight modification (such as using a divider) the above method can be used economically in areas such as electronic colorimeters, color copiers, and electronic color discrimination, etc. For those multiple function or consolidated systems which require high color discrimination level, simultaneous multiple color reading, or even simulation of vision, boundary identification and pressed color identification, etc., a combination of the simulation and digital techniques should be adopted. The brightness and colority of the color are separated using the simulated solution equipment first and then the identification work is carried out by the digital equipment and its software. Such an arrangement is also very attractive.

REFERENCES

- [1] A. N. Dutlovskiy. "The Theory of Optical Instruments", Scientific Publishing House, 1975.
- [2] Xian Municipal Textile Institute, Information Laboratory "Introduction to Japanese Electronic Automatic Device which reads and draws".
- [3] Compiled by Xian Jiaotong University, Radio technology teaching and research laboratory "Color Television Fundamentals", 1976.
- [4] Xian Electronic Silk Jacquard weaving control system manufacturing group, "Analysis of the Principle of Photo-electric Scanning Electronic Color Scanner", Xian Science and Technology, 1978, No. 2, pp. 32-45.

Summary

Color Discrimination by a Color-Picture Reader

Chen Chenghang

Textile pattern design is one field where computer-aided design technique can be applied. As is acknowledged, a direct control of weaving loom or an automated punching of Jacquard cards is based on the reading of an artist's sketches or point paper manuscripts. For technicolored sketches or point paper manuscripts, processing methods in technology vary from one color to another. Therefore, the capacity of a reader to discriminate the different colors of a sophisticated sketch is essential to the effective use of the computer-aided textile pattern design technique in textile production.

This paper employs colorimetry in giving an outline of a convenient process for color discrimination which identifies the hue, purity and brightness of a color. Simple circuits are developed to separate twelve colors and produce the color code output for each color directly. Experiments have confirmed the stability and reliability of this process for color discrimination. No restrictions are imposed on the kinds of pigments used.

Another scope of this paper deals with the method for more accurate color recognition. Colors can be recognized accurately and easily through a simple operation to turn the three-color coefficients into signals of the hue, purity and brightness of a color. It is considered to be too expensive to carry out this operation with digital computers, because A/D converters must be incorporated to convert input signals into digital ones. Analog computers, however are characterized by their simplicity and high speed in this operation. They need only a few operational amplifiers and voltage comparators to carry out the operation in question with satisfactory accuracy of color recognition. By using an analog computer, the colors can be recognized nearly as accurately as by human eyes.

ON THE UNIQUENESS OF THE SOLUTION TO THE VELOCITY POTENTIAL INTEGRAL EQUATION ESTABLISHED BY USING GREEN'S THEOREM

Liu Qiangang

I. Formulation of the Problem

In using the singularity method to solve the potential flow problem around an object, one of the commonly used methods in current gas dynamic numerical computation is to establish the distribution of singularities on the surface of the object, by means of the Green theorem. Let S denote the surface of the object, and R' denote the flow field external to the object. Then according to Green's theorem, when point p is in R' , its potential function may be expressed as

$$\phi(p) = \frac{1}{4\pi} \iint_S \phi(q) \frac{\partial}{\partial n_q} \left(\frac{1}{r(p,q)} \right) ds - \frac{1}{4\pi} \iint_S \frac{1}{r(p,q)} \frac{\partial \phi}{\partial n_q}(q) ds. \quad (1)$$

and when point p is on S , the potential function is

$$\phi(p) = \frac{1}{2\pi} \iint_S \phi(q) \frac{\partial}{\partial n_q} \left(\frac{1}{r(p,q)} \right) ds - \frac{1}{2\pi} \iint_S \frac{1}{r(p,q)} \frac{\partial \phi}{\partial n_q}(q) ds. \quad (2)$$

where q is a point on s and is also the variable of integration. $r(p,q)$ is the distance between the points p and q , and n_q is the exterior normal at q .

The first integral on the RHS of (1) may be considered as the surface dipole with $\phi(q)$ as density, which covers the whole surface of S . The second

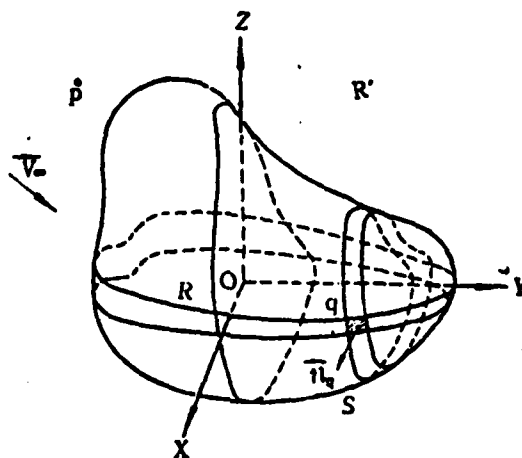


Figure 1

integral may be considered as a surface source, $\partial\phi/\partial n_i(q)$ which also covers the whole surface of S.

When the surface boundary condition (Neumann condition) is set,

$$\frac{\partial\phi}{\partial n_i} = V_{\infty} \cdot n_i \quad (3)$$

the second integral on the RHS of (2) is a known function of q . Therefore equation (2) becomes a Fredholm integral equation of the second kind with ϕ as the unknown function. This equation has been used in some of the reference material and literature as a fundamental equation to analyse and compute three-dimensional rotational flow problems.

However, in the discussions on the integral equation method for solving potential flow problems, in [7], it was stated that equation (2) had no unique solution and its application in numerical computations would cause difficulties. It was also stated that this might have been a possible reason why this equation has never been used as a base for general potential flow computation, and that a constant ϕ on S would not produce a velocity in R' . Hence the non-uniqueness was obvious.* Thus the following questions are raised: Does the integral equation (2) possess a unique solution? Can this equation be used as a base for analysing and computing the potential flow about an object? Is there any real meaning in the results obtained by using this equation as a base with the assumption that it does have a unique solution. All these questions need to be researched and clarified. In this

* To facilitate the discussion, the basic notations used in this paper essentially agree with those used in [7] in which R' denotes the external region of the curved surface S, and R denotes the interior of S.

paper we have made a preliminary investigation on this problem based on the fundamental theory of potential function and integral equations. Our opinion is that on this problem the opinion in [7] is not appropriate. Under a given surface Neumann boundary condition, the integral equation (2) has a unique solution, and it is entirely possible to use it as a base for numerical computations in solving the potential flow problems around an object.

We shall present our discussions in two aspects as follows:

II. Conditions used in Establishing Equations (1) and (2)

Let us first discuss the conditions used in establishing equations (1) and (2). This will be helpful in studying the uniqueness problem of equation (2). We, therefore, shall briefly explain the process in deriving equations (1) and (2).

Let S be a given boundary surface which satisfied the LYAPUNOV conditions. Draw a large sphere enclosing the object (spherical radius being A). Let S_1 be the spherical surface and R' be the region between S and S_1 . Let u, v be two arbitrary function with continuous second order partial derivatives in R' , and continuous first order partial derivatives in $R' + S$ and $R' + S_1$. Then according to Green's theorem, we have

$$\iiint_{R'} (v \Delta u - u \Delta v) dV = - \iint_S \left(v \frac{\partial u}{\partial n} - u \frac{\partial v}{\partial n} \right) ds - \iint_{S_1} \left(v \frac{\partial u}{\partial n} - u \frac{\partial v}{\partial n} \right) ds_1, \quad (4)$$

where

$$\Delta = \frac{\partial^2}{\partial x^2} + \frac{\partial^2}{\partial y^2} + \frac{\partial^2}{\partial z^2},$$

and n is the surface normal at the boundary pointing toward the interior of R' .

Let $u = \phi$, where ϕ is the perturbation velocity potential, satisfying the Laplace equation in R' , i.e.

$$\Delta\phi=0, \quad (5)$$

$v = 1/r$ where r is the distance between a point $p(x,y,z)$ in R' and a point $q(\xi,\eta,\zeta)$ on the boundary. It is equal to

$$r = \sqrt{(x-\xi)^2 + (y-\eta)^2 + (z-\zeta)^2}$$

With p as center and ϵ as radius, draw a small sphere ω in R' . Applying equation (3) in the Region $R' - \omega$, we get

$$\begin{aligned} \iint_{\sigma} \left(\phi \frac{\partial \frac{1}{r}}{\partial n} - \frac{1}{r} \frac{\partial \phi}{\partial n} \right) ds + \iint_{S_1} \left(\phi \frac{\partial \frac{1}{r}}{\partial n} - \frac{1}{r} \frac{\partial \phi}{\partial n} \right) ds, \\ + \lim_{\epsilon \rightarrow 0} \iint_{\sigma} \left(\phi \frac{\partial \frac{1}{r}}{\partial n} - \frac{1}{r} \frac{\partial \phi}{\partial n} \right) d\sigma = 0, \end{aligned} \quad (6)$$

where σ is the surface of ω .

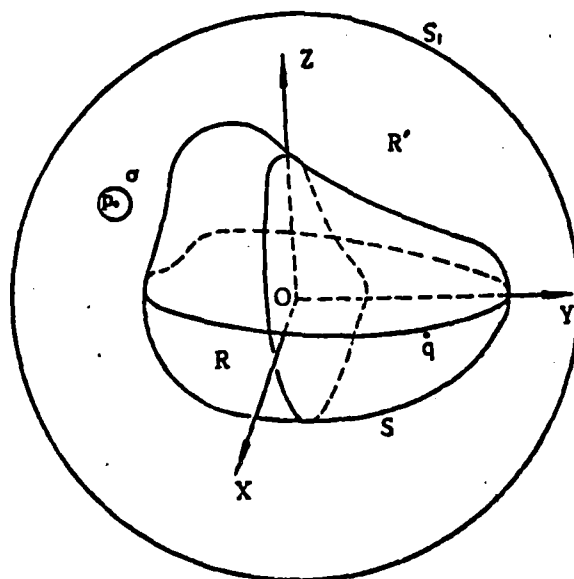


Figure 2

It is easy to show that

$$\lim_{\epsilon \rightarrow 0} \iint_{\sigma} \left(\phi \frac{\partial \frac{1}{r}}{\partial n} - \frac{1}{r} \frac{\partial \phi}{\partial n} \right) d\sigma = -4\pi \phi(x, y, z), \quad (7)$$

From (6) and (7) we have

$$\phi(x, y, z) = \frac{1}{4\pi} \iint_S \left(\phi \frac{\partial \frac{1}{r}}{\partial n} - \frac{1}{r} \frac{\partial \phi}{\partial n} \right) ds + \frac{1}{4\pi} \iint_{S_1} \left(\phi \frac{\partial \frac{1}{r}}{\partial n} - \frac{1}{r} \frac{\partial \phi}{\partial n} \right) ds_1. \quad (8)$$

Let the perturbation velocity potential at infinity $\phi=0$; then we can find a constant C such that on S_1

$$|\phi| \leq \frac{C}{A}, \quad \left| \frac{\partial \phi}{\partial n} \right| \leq \frac{C}{A^2},$$

Hence, when we let the radius A of the large sphere enclosing the object approach infinity, the second integral in (8) will approach zero. Thus

$$\phi(x, y, z) = \frac{1}{4\pi} \iint_S \left(\phi \frac{\partial \frac{1}{r}}{\partial n} - \frac{1}{r} \frac{\partial \phi}{\partial n} \right) ds, \quad (9)$$

This is equation (1)

When the point $p(x, y, z)$ is on S, we can still draw a small sphere ω with p as center and ϵ as radius. Substituting the surface S enclosed by ω with the spherical surface outside S and then applying Green's formula, we get

$$\phi(x, y, z) = \frac{1}{2\pi} \iint_S \left(\phi \frac{\partial \frac{1}{r}}{\partial n} - \frac{1}{r} \frac{\partial \phi}{\partial n} \right) ds + \frac{1}{2\pi} \iint_{S_1} \left(\phi \frac{\partial \frac{1}{r}}{\partial n} - \frac{1}{r} \frac{\partial \phi}{\partial n} \right) ds_1, \quad (10)$$

Introduce now the condition that the perturbation velocity potential at infinity $\phi=0$ and let A approach infinity. The second integral in (10) approaches zero and

$$\phi(x, y, z) = \frac{1}{2\pi} \iint_V \left(\phi \frac{\partial}{\partial n} \frac{1}{r} - \frac{1}{r} \frac{\partial \phi}{\partial n} \right) ds, \quad (11)$$

This is equation (2).

It is worth noticing that we have used the condition

$$\lim_{A \rightarrow \infty} \phi = 0, \quad (12)$$

in the derivation of (1) and (2). It is precisely this condition that reduces equation (8) and (10) to (1) and (2), changing the problem from a Neumann interior problem to a Neumann exterior problem. Under a given Neumann boundary condition, the latter has a unique solution. We shall prove this below.

III. Concerning the uniqueness of the solution to the integral equation (2).

Let ϕ be one solution of equation (2) and ϕ_2 another. Let

$$\phi_1 - \phi_2 = \mu,$$

Substitute ϕ_1 and ϕ_2 separately into equation (2) and subtract. Taking into account that they should both satisfy the same Neumann boundary conditions, we have

$$\mu(p) = \frac{1}{2\pi} \iint_V \mu(q) \frac{\partial}{\partial n_q} \left(\frac{1}{r(p, q)} \right) ds, \quad (13)$$

Now the question of whether the integral equation (2) has a

unique solution is reduced to that of whether the integral equation (13) has only ordinary solutions. Since

$$\frac{\partial}{\partial n_q} \left(\frac{1}{r(p, q)} \right) = - \frac{\cos(r, n_q)}{r^2},$$

equation (13) may be written as

$$\mu(p) = - \frac{1}{2\pi} \iint_R \mu(q) \frac{\cos(r, n_q)}{r^2} ds, \quad (14)$$

Introducing the kernel

$$K(p, q) = - \frac{1}{2\pi} \frac{\cos(r, n_q)}{r^2}, \quad (15)$$

equation (14) may then be written as

$$\mu(p) = \iint_R \mu(q) K(p, q) ds, \quad (16).$$

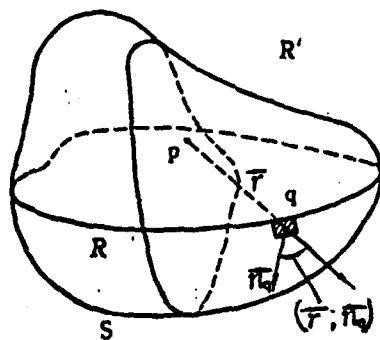


Figure 3

We transpose the kernel of equation (14) to obtain the transposed kernel $K_1(p; q)$:

$$K_1(p, q) = K(q, p) = \frac{\cos(r, n_p)}{2\pi r^2}, \quad (17)$$

Thus the transposed equation corresponding to equation (14) is

$$\mu_1(p) = -\frac{1}{2\pi} \iint_S \mu_1(q) \frac{\cos(r, n_q)}{r^3} ds, \quad (18)$$

From the Fredholm theorem we know that the transposed equation (18) and the original equation (14) have either only zero solutions or non-zero solutions simultaneously. Hence the investigation of whether the integral equation (2) has a unique solution may now be reduced to the investigation of whether equation (18) has only ordinary solutions.

Let $u_1(q)$ be the bounded solution of equation (18). $u_1(q)$ must be continuous due to the property of the integral operator with $K_1(p; q)$ as kernel. Consider the mono-layer potential function V

$$V = \iint_S \mu_1(q) \frac{1}{r} ds, \quad (19)$$

This monolayer potential function with continuous density has a regular normal derivative, and it is not difficult to prove that the limiting value of this normal derivative on S is

$$\left(\frac{\partial V}{\partial n} \right)_e = \iint_S \mu_1(q) \frac{\cos(r, n_q)}{r^3} ds - 2\pi \mu_1(p) \quad (20)$$

where the subscript "e" denotes exterior limit.

Comparing (18) and (20), we have

$$\left(\frac{\partial V}{\partial n} \right)_e = 0. \quad (21)$$

Since the function V is a harmonic function in R' , and vanishes at infinity and $\left(\frac{\partial V}{\partial n} \right)_e = 0$ on S , then according to the

uniqueness theorem of the Neumann exterior solution, $V = 0$ in R' . At the same time, as the mono-layer potential function V is a continuous function over all space, $V = 0$ also on S . Since V is harmonic inside S , then according to the uniqueness theorem of the Dirichlet interior solution, $V = 0$ too. Hence in all space,

$$V \equiv 0 \quad (22)$$

From this we may conclude that the interior limit of the normal derivative of the mono-layer potential function V on S also vanishes, i.e.

$$\left(\frac{\partial V}{\partial n}\right)_i = 0 \quad (23)$$

where the subscript "i" indicates the interior limit.

Therefore, according to the relationship between the density and the exterior and interior limits of the normal derivatives of the mono-layer potential function, we obtain the result that on S

$$\mu_i(q) = \frac{1}{4\pi} \left(\left(\frac{\partial V}{\partial n}\right)_i - \left(\frac{\partial V}{\partial n}\right)_e \right) = 0. \quad (24)$$

This proves that equation (18) has only ordinary solutions, and hence the integral equation (2) has a unique solution.

It can be seen that the opinion stated in [7] that the integral equation (2) does not possess a unique solution is groundless. With given boundary conditions (Neumann conditions), the solution of the integral equation (2) is unique. The opinion that "the non-uniqueness can be easily seen as a constant ϕ on S will not produce a velocity in R' ", as expressed in the same paper, also cannot be confirmed, since from (2) and (1), there is no constant ϕ solution on S or in

R' and if there is, it can only be $\phi = 0$.

It is worth pointing out that, besides the discussion on the integral equation (2), in [7] there is also a discussion on the integral equation obtained from the surface source flux density distribution.

$$2\pi\sigma(p) - \iint_S \frac{\partial}{\partial n_p} \left(\frac{1}{r(p,q)} \right) \sigma(q) ds = -n_p \cdot \nabla \varphi \quad (25)$$

where σ denotes the surface source flux density distribution.

The opinions in [7] on the existence and uniqueness of the solution to this equation and its practical solution are all correct. According to [7], the existence and uniqueness of the solution to (25) have been discussed in detail in [9], but there was no discussion on (2). From the practical problems treated in this book [9], this may appear to be the case. But if we transpose the kernel of the integral equation (2) (as was done in this paper), and then investigate the uniqueness of the solution to (2) according to the transposed equation, then all the methods and theory applied to (25) are also applicable to (2). In accordance with the stipulations of [7] (denoting the external normal of s by n , with exterior Neumann conditions as the boundary conditions and the region of investigation being the region R' exterior to S), the solution to both of these equations belongs to the Neumann exterior problem. From the discussion presented earlier in this paper, their solutions are both unique.

We notice that if the problem under discussion is not the external flow but the internal flow of the curved surfaces, then according to the velocity potential integral equation derived from Green's theorem or the integral equation of the singular source flux density distribution, the solutions are

AD-A115 866

FOREIGN TECHNOLOGY DIV WRIGHT-PATTERSON AFB OH
RECENT SELECTED PAPERS OF NORTHWESTERN POLYTECHNICAL UNIVERSITY--ETC(U)
AUG 81

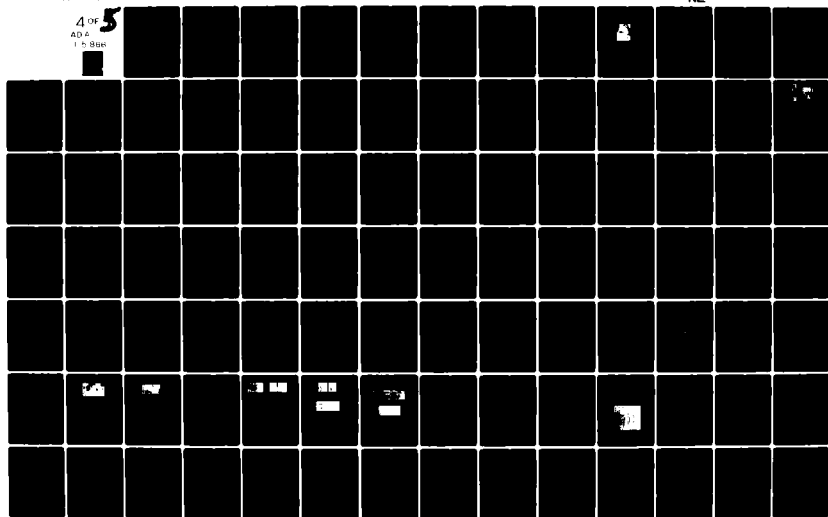
F/G 20/4

UNCLASSIFIED

FTD-ID(RS)T-0260-81-PT-2

NL

4 of 5
AD-A
1 of 866



indeed not unique. Their various solutions differ by a constant. We refer the reader to the related sections in [2,4,9,10] for detailed discussions on this problem.

From the above discussions we see that, given the Neumann boundary conditions, the surface velocity potential distribution function $\phi(q)$ is the unique solution to the integral equation (2). We may then substitute $\phi(q)$ in the integral on the RHS of (1), so that the integrals on the RHS of (1) are known functions and thus can be found. From this, we can then uniquely determine the value of the velocity potential at any point p in the flow field.

After the discussion of the uniqueness problem of (2), we must also point out that, if only the surface Neumann conditions are given, then from (2) we can only solve the problem of rotational flow of a three-dimensional body without circulation. Additional auxiliary conditions such as Kutta conditions are needed if we want to solve the problem of rotational flow of a three-dimensional body with circulation. For works in this area, the readers are referred to references [5,6].

In the references quoted above and in the other literature, the finite element method has been successfully used to apply (2) in solving rotational flow of a three-dimensional body with and without circulation. In these computations, no special methods have been introduced to take into consideration that (2) might have non-unique solutions, and no difficulties have been encountered, as mentioned in [7]. On the contrary, as the singularity distribution of this method is more reasonable and the formulation is relatively more simple, results in better agreement with reality have been obtained with fewer divisions and less computational time, thus demonstrating that the integral equation (2) can definitely be used as a base in solving the potential flow problem around an object.

IV. Conclusion

In this paper we have investigated the uniqueness problem of the solution to the velocity potential integral equation derived from Green's theorem, based on the fundamental theory of potential function and integral equations. We have pointed out the lack of validity of certain opinions in related references and proved that for given Neuman boundary conditions the solution to equation (2) is unique.

REFERENCES

- [1] Wu Xinmou, Mathematical physics equation teaching material, Higher Education Publishing House, 1956, pp. 169-189.
- [2] S. L. Sobolev, translated by Qian Min et al, Mathematical Physics Equations, People's Educational Publishing House, 1961, pp. 156-187.
- [3] V. I. Smirnov, translated by Chen Zhuanzhang, Four Volume Course in Higher Mathematics, Vol. 1, Higher Education Publishing House, 1958, pp. 15-67.
- [4] V. I. Smirnov, translated by Gu Chaohao and Jin Fulin, Four Volume Course in Higher Mathematics, Vol. 2, Higher Education Publishing House, 1960, pp. 584-601, 633-645.
- [5] Morino, L., Chen, L. T., Suciu, E. O., Steady and Oscillatory Subsonic and Supersonic Aerodynamics around Complex Configurations, AIAA Journal, Vol. 13, No. 3, Mar. 1975, pp. 368-374.
- [6] Morino, L., and Kuo, C. C., Subsonic Potential Aerodynamics for Complex Configurations: A General Theory, AIAA Journal, Vol. 12, No. 2, Feb. 1974, pp. 191-197.
- [7] Hess, J. L., Review of Integral Equation Techniques for Solving Potential-flow Problems With Emphasis on The Surface-Source Method, Computer Methods in Applied Mechanics and Engineering, Mar. 1975, p. 150.
- [8] Lamb, H., Hydrodynamics, Cambridge University press and The Macmillan Co., 1945, pp. 43-61.
- [9] Kellogg, O. D., Foundations of Potential Theory, Frederick Ungar Publishing Co. 1929, pp. 277-338.
- [10] R. Cran, D. Her-ert, translated by Qian Min and Guo Dui ren, Mathematical Physics Methods, Vol. 1, Scientific Publishing House, 1958, pp. 94-96

The Uniqueness of the Solution of the Velocity Potential Integral Equation Established by Using Green's Theorem

Liu Qiangang

Let S be a given boundary surface which satisfies the Liapounoff conditions. R' be the infinite region outside S . According to Green's Theorem, the Potential function at point P on the surface S can be expressed as

$$\phi(P) = \frac{1}{2\pi} \iint_S \phi(q) \frac{\partial}{\partial n_q} \left(\frac{1}{r(p,q)} \right) ds - \frac{1}{2\pi} \iint_S \frac{1}{r(p,q)} \frac{\partial \phi}{\partial n_q}(q) ds. \quad (1)$$

If the Neumann boundary condition

$$\frac{\partial \phi}{\partial n_q} = V_n \cdot n_q \text{ on } S \quad (2)$$

is applied, the second integral on the right-hand side of eq. (1) is a known function of position, and eq. (1) becomes a Fredholm integral equation of the second kind. This equation can be used as the basis of a general method of potential flow calculation⁽¹⁾⁽⁶⁾⁽⁸⁾.

In reference [7], however, Hess asserted that the integral equation (1) has a nonunique solution which can lead to numerical difficulties in applications⁽⁷⁾. This paper shows that Hess' assertion is not valid. In the following paragraphs, the essential steps in proving the uniqueness of the solution of the integral equation (1) are briefly summarized.

According to Fredholm's basic theorems of integral equation, if eq. (1) does have a unique solution, then the associated homogeneous equation

$$\mu(p) = - \frac{1}{2\pi} \iint_S \mu(q) \frac{\cos(r, n_q)}{r^2} ds \quad (3)$$

possesses only a trivial solution, and the "transposed" integral equation

$$\mu_1(p) = \frac{1}{2\pi} \iint_S \mu_1(q) \frac{\cos(r, n_p)}{r^2} ds \quad (4)$$

associated with eq. (3) also possesses only a trivial solution.

Let $\mu_1(q)$ be the bounded solution of eq. (4). Consider the potential of a simple distribution V with $\mu_1(q)$ as its density:

$$V = \iint_S \mu_1(q) \frac{1}{r} ds \quad (5)$$

This potential function has continuous derivatives in the region R' . The exterior limit of its normal derivative on S is given by

$$\left(\frac{\partial V}{\partial n} \right)_e = \iint_S \mu_1(q) \frac{\cos(r, n_r)}{r^3} ds - 2\pi\mu_1(p). \quad (6)$$

From eqs. (4) and (6), we have

$$\left(\frac{\partial V}{\partial n} \right)_e = 0. \quad (7)$$

Since V is harmonic in region R' and approaches zero at infinity and $(\partial V / \partial n)_e = 0$ on S , then, according to the Theorem of Uniqueness of the Neumann exterior problem, V is equal to zero in the region R' . V is also equal to zero on S , because V is continuous in the whole space. Since V is harmonic inside S , then according to the theorem of Uniqueness of the Dirichlet interior problem, we also have $V = 0$ inside S . Therefore in the whole space

$$V = 0. \quad (8)$$

Thus the interior limit of the normal derivative of the potential V on S is also equal to zero, i. e.,

$$\left(\frac{\partial V}{\partial n} \right)_i = 0. \quad (9)$$

Therefore

$$\mu_1(q) = \frac{1}{4\pi} \left(\left(\frac{\partial V}{\partial n} \right)_i - \left(\frac{\partial V}{\partial n} \right)_e \right) = 0. \quad (10)$$

This completes the proof that eq. (4) has only a trivial solution and hence the solution of eq. (1) is unique.

INITIAL EXPERIMENTAL RESEARCH
INTO THE RESPONSE
OF TURBOJET ENGINE COMPRESSORS
TO DISTORTION OF INTAKE PRESSURE

Chen Fu-qun, Tang Di-yi, Hu Zi-long, Id Wen-lan,
Yu Jin-di, Wu Xin-yuan, Zhao Jue-liang, Lin Qi-xun,
Wang Zong-yuan, Liu Si-hong, Yu Shaopkun, Cong Meng-zi,
et al.

SUMMARY

This article gives an introduction to the results of preliminary research into the influence which distortions in intake pressure have on the stability and characteristics of the compressors of turbojet engines. The research work which is being considered was carried out on the test bed of a turbojet engine with a nine-stage compressor, whose first stage is trans-sonic.

If one carries out a comparison between the results of experiments in which there were distortions of intake pressure and the results of experiments in which there were no such distortions, then one sees the following: distortions in the intake of turbojet engines have a very obvious influence on the characteristics of engine compressors; it not only influences the stall boundary, but it also influences the shape and location of the constant speed lines of the compressors involved. Distortions in the intake cause compressor constant speed lines to shift to the left

and become flat or level; moreover, these distortions also cause the operational lines to move toward the stall lines. The influence of a reduction in the exhaust areas of the first stage directional guidance devices in the turbine (This sort of reduced first stage exhaust area for the guidance devices will hereafter be called "Small Guidance I") is similar to those produced by the distortions in the intake of the compressors. Measurements taken of the various parameters which occur in the stages of compressors demonstrate the following: the degree of distortion in the intake is enlarged in the first stage of the compressor; in the later stages, it attenuates rapidly; this is particularly true in stages two, three and four. On the basis of an analysis of the course of pulsations in the flow parameters for the points of instability, it was discovered that in the case of a 3 x 36 mesh screen, the form of the instability is of a classical type in which the flow oscillates with large amplitudes, and that during a portion of the cycle there exists a rotating stall; in the case of "small guidance I", or a decrease in the turbine nozzle area, there is a surge [5].

The experiments also demonstrate that when one is dealing with a 3 x 36 mesh screen (for which the index of distortion is 16% if one assumes 90% of the design speed of the engine), then there is still no occurrence of instability when the engine is speeded up to 93.3% of the speed for which it was designed.

I. INTRODUCTION

The mutual tolerances between air intake and engine are very serious problems one encounters in the process of test production of aircraft for supersonic flight. In the

process of the use of an aircraft, it is common to run across the production of intake distortions caused by such things as violent maneuvering of an aircraft and a consequent lack of coordination in the operations of the intake/engine complex leading to the sucking in of gases which the engine has already expelled.

Intake distortions lower the stability margin of the compressor system, and, in extreme circumstances, they will lead to stall or engine surge; this can even lead to combustion chamber flame out, the stopping of the aircraft in mid-air, and even to the vibration of compressor blades, their shaking and even breaking off. Because of all this, intake distortions are always a decisive factor, limiting the total possible maneuverability of an aircraft.

The objective of the research which is discussed in this article falls into the following areas: measurement and analysis of the aerodynamic influences which turbojet engines have on intake distortions; observance and analysis of the characteristics which intake distortions have when viewed in terms of compressors, as well as observation and analysis of the influences which these distortions have on instability as it can appear in the stall lines of compressors (either rotating stall or surge); and minute observation and analysis of the passage of intake distortions through compressors.

II. EXPERIMENTAL EQUIPMENT AND EXPERIMENTAL METHODS

The experiments with which this article deals were carried out on the test bed of a nine-stage compressor turbojet engine, in which the first stage is of a trans-sonic

type. A diagram of the installed tube as well as a chart of the distribution of the measurement points are to be found in Figure 1. In the front of the intake of the engine, there was installed a measurement section to take readings of the amount of flow. At a place which was at a distance from the intake of the engine approximately equal to half the diameter of that intake, a supporting framework was installed, which was capable of rotating and which supported a mesh (1 eye, wire diameter 2); this mesh, which caused the disturbances in the flow we have been calculating and distortions covered over a supporting net, and it was fixed with stainless steel wires (Figure 2). Outside the rear jet exhaust of the engine, a movable, stopper-type conic body; the largest blocking area of this conic body was approximately 30% of the prescribed area of the jet exhaust.

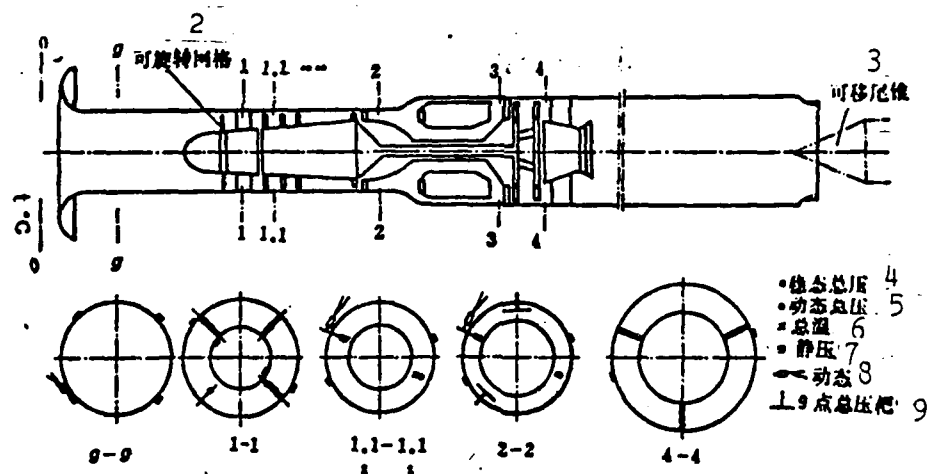


Figure 1. Diagram of test equipment and arrangement of measuring points.

2) rotatable mesh; 3) movable tail cone; 4) stable-state total pressure; 5) kinetic-state total pressure; 6) total temperature; 7) static pressure; 8) kinetic state; 9) total pressure at 9 points.

During the experiments, the operating speed of the engine was maintained at a constant rate of rotation; by use of fish scale-type plates and the gradual movement of the tail cone, both changes in the jet exhaust, itself, and reduc-

tions in the area of the jet exhaust were possible; these changes and reductions caused the operational point of the engine to move along the constant speed line of the compressor, until it reached the stall threshold; at this point, one saw the occurrence of a surge or a rotating stall.



Figure 2. Photograph of the distortion net or mesh capable of turning.

III. RESULTS AND ANALYSIS

1. Intake Flow Spectrum

Figure 3 is a stable-state pressure spectrum for a cross-section of the intake of the engine. From the figure we can see that the boundary lines between the high and low regions of the engine intake flow fields are fairly distinct.

NOTE: In research work discussed in this article, comrades who also took part included Zheng Li-zhi, An Ju-cai, Yang Hui-qin, Ma Dong-ming, Du Ge, Zhang Ji-hua and Li Feng-lan.

Figure 4 is the circumferential spectrum of total pressure of total pressure of engine intake cross-section. The points in the figure which are connected by a solid line go to make up a spectrum of the overall pressure produced by the interference of the 1 x 36 mesh net, the index of distortion D is 17.3% after the air flow is interfered with by the 3 x 36 mesh net. On the illustration, the tooth shape is caused by the influence of the supporting frame.

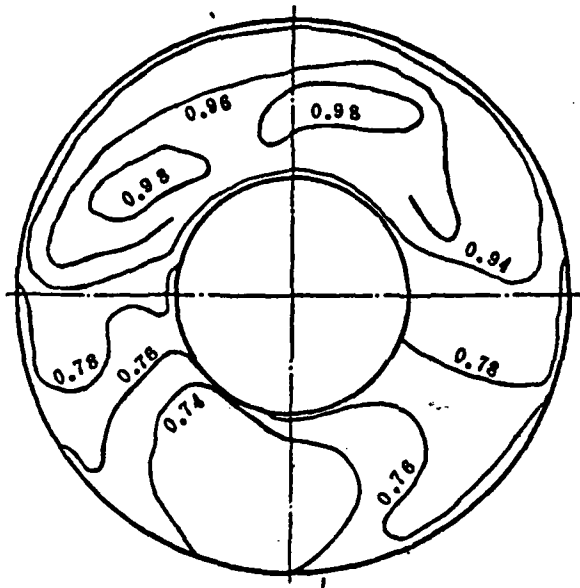


Figure 3. Pressure spectrum of the intake of the engine.

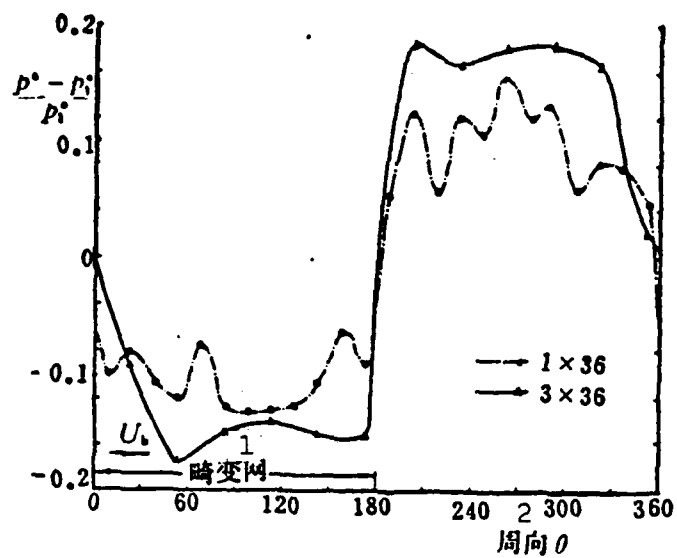


Figure 4. Circumferential spectrum of total pressure of cross-section of intake in engine:
1) distortion net; 2) circumferential angle θ .

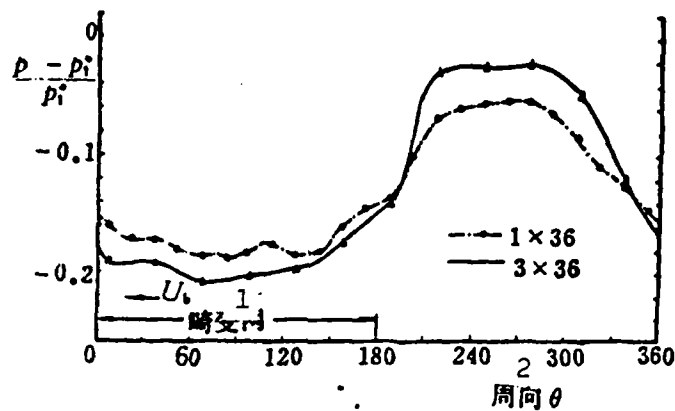


Figure 5. Static pressure distortion spectrum for a cross-section of intake of the engine: 1) distortion net; 2) circumferential angle θ .

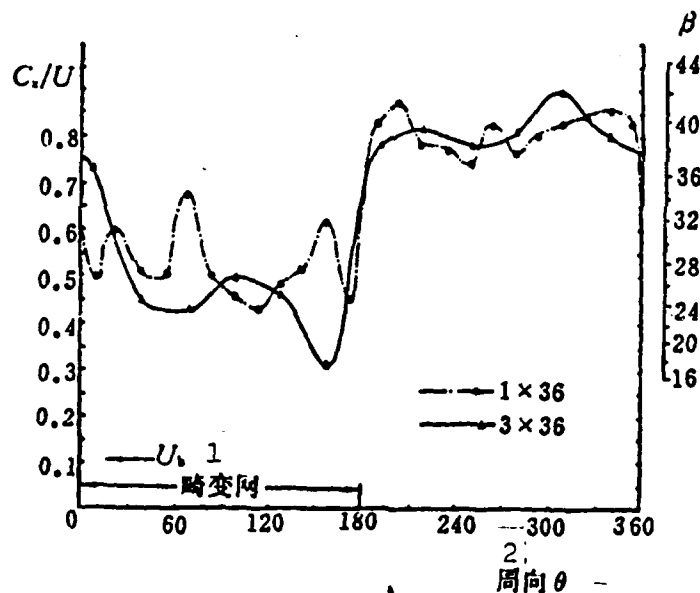


Figure 6. Circumferential distortion spectrum of the axial speed after mesh: 1) distortion net or mesh; 2) circumferential direction θ .

Figure 5 is a static pressure circumferential distortion spectrum for the intake of the engine. (This type of static pres-

sure circumferential distortion is caused by the tendency to homogenize the flow speeds of the two areas of flow that enter the intake of the engine compressor and are caused by the difference in the degree of suction which high pressure areas and low pressure areas have exerted on them by the compressor.) Air flow in low speed area of distortion increases in speed, and the static pressure falls; high speed "clean" or "pure" area of air flow reduces its speed, and its static pressure goes up; this set of changes forms a static pressure circumferential distortion.

Figure 6 is an axial speed circumferential distortion spectrum, taken after the distortion net has done its work. The values which are put out in the illustration are measured against the angle β of the intake air flow as it comes in contact with the blades of the compressor wheel or disc.

2. Passage of Distortions Through the Compressor

Figures 7, 8 and 9, respectively, present the circumferential distributions of total temperature, total pressure and wall surface static pressure for various average radii of compressor exhaust. It is possible to anticipate that the effects of the grid net or mesh will not produce total temperature distortions in the intake of the compressor; however, the distortions in total pressure which are produced after the net or mesh has done its work cause the compressor to add different amounts of power to different fan-shaped areas of the air flow, and this leads to various types of total temperature distortions in the exhaust (Figure 8.) From Figure 7 and Figure 8, it can be seen that after the air flow passes through the first stage of the compressor, the distribution of the total pressure becomes an asymmetrical one; when the temperature distribution curve on the blades of the compressor wheel or disc

leaves the area of low pressure, one obtains a "peak", and when the curve enters an area of low pressure, one obtains a "trough" or "valley." The appearance of the asymmetrical curves and the peaks and valleys or troughs we have just mentioned is primarily due to the effects of the lateral flow from areas of high pressure to areas of low pressure in the circumferential direction and to the effects of irregular flows of air. Because of the fact that in places where the blades of the compressor leave areas of low pressure the lateral flow and the circumferential speed of the compressor wheel or disc are in the opposite direction, there is a corresponding reduction in the size of the angle of the air flow; the attack angle is enlarged; the amount of power injected into the air flow from the compressor is enlarged; and the total temperature becomes relatively higher. To put it another way, in places where the blade of the compressor wheel or disc enters areas of low pressure, the direction of the flow of the lateral air currents and the circumferential speed of the wheel or disc are the same; the angle of attack is reduced in size; the amount of power which is added is reduced in size, and, therefore, the total temperature is relatively lower. Besides this, in a distorted flow field, what the blades of the compressor wheel or disc actually encounter is a periodically oscillating angle of attack of the air flow; moreover, the effect which the lift from the wing shape has on the oscillating angle of attack has in it what is called a "delayed" or "lagging" effect; this type of effect is even more pronounced in areas where high pressure and low pressure meet (where the angle of attack has been enlarged); the influence which these effects have on the amount of power which the compressor adds to the air flow going through it is very good, as is the influence of the lateral flows discussed previously; therefore, the influence or effects of irregular air flows may also be a possible reason for the appearance of peaks and troughs or valleys.

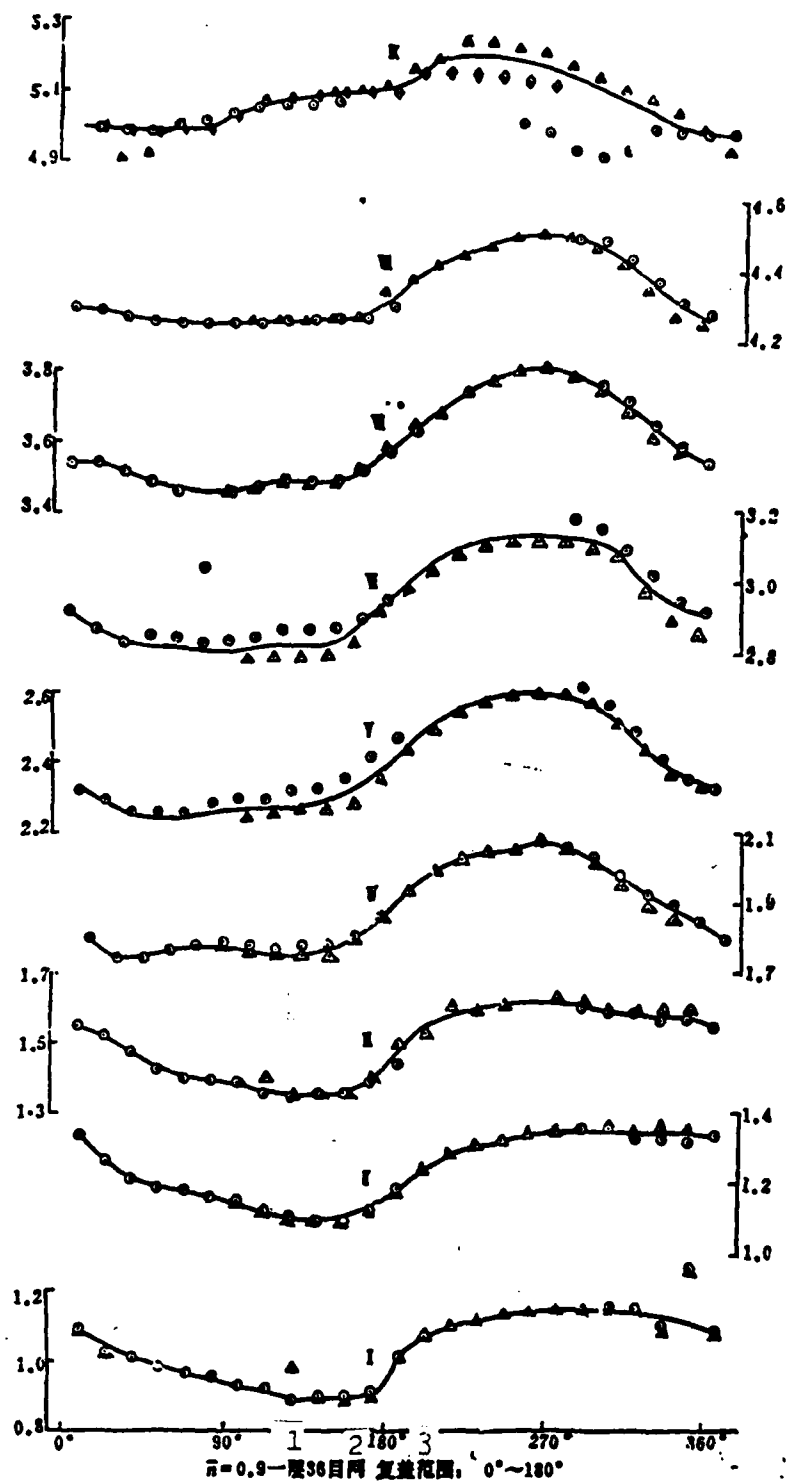


Figure 7. Circumferential distribution of total pressure for the exhausts of the various stages of the compressor: 1) layer; 2) eye mesh; 3) overload range or coverage.

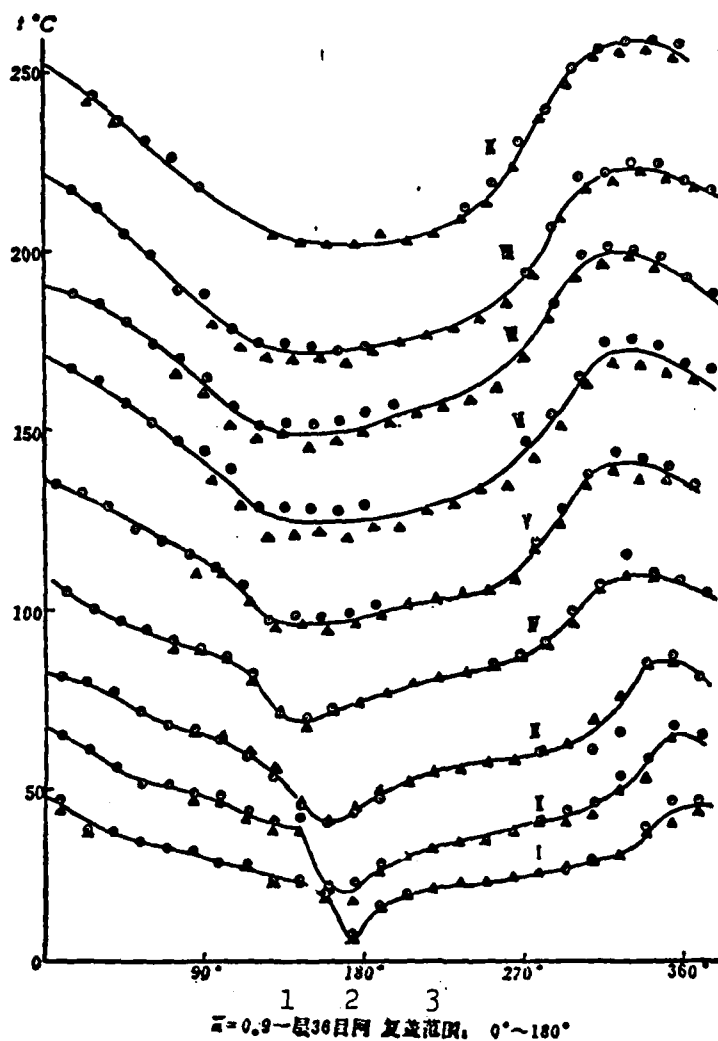


Figure 8. Circumferential distribution of the static pressure in the exhausts of various stages of the compressor: 1) layer; 2) eye mesh; 3) overload coverage of range.

From Figure 9, it can be seen that after the static pressure distortion in the intake of the compressor has passed through the compressor, the static pressure in the intake of the compressor has a tendency to even itself out. In the five types of representative situations which were measured in these experiments, the degrees of unevenness in the static pressure

readings in the intake of the compressor were all already within the range of deviation or error. If one considers the fact that there is a relatively large amount of free space behind the compressor, then it is possible to understand the principles behind the circumferential evenness in the static pressure of the intake.

Figure 8

on the basis of the location of the peak values in the total temperature curve for the exhausts of the various stages of the compressor, it is possible to see that in the compressor stages 1 - 7, when the air flow is passing through the various stages of the compressor there is an angular shift of a definite number of degrees in the same direction in which the compressor wheel or disc is turning. The direction and magnitude in the angular shift or turning in the air flow are primarily determined by the stopover time during which the air flow is passing through the compressor blades and the direction of the air flow in the interval between the various stages of the compressor; the former is the cause for the shifting or turning of the air flow in the same direction as the compressor wheel or disc is already turning, and the latter is related to the direction of the air flow in the intake and the exhaust of the compressor. In the engine used for these experiments, the installation angles for the stator blades in compressor stages 7, 8 and 9 were, respectively, $91^{\circ}16'$, $97^{\circ}43'$ and 90° . In the two compressor stages 7, 8 one finds a reverse deflection; on top of this, one can add the facts that several latter stages of the compressor have blade arc lengths which are relatively short, and that the encounter time during which the air flow is passing through the compressor blades is brief. Because of these factors, it is possible for the air flow not to be turned in the way we have described or even to twist around in the opposite direction. The location of the peak values for total pressure in

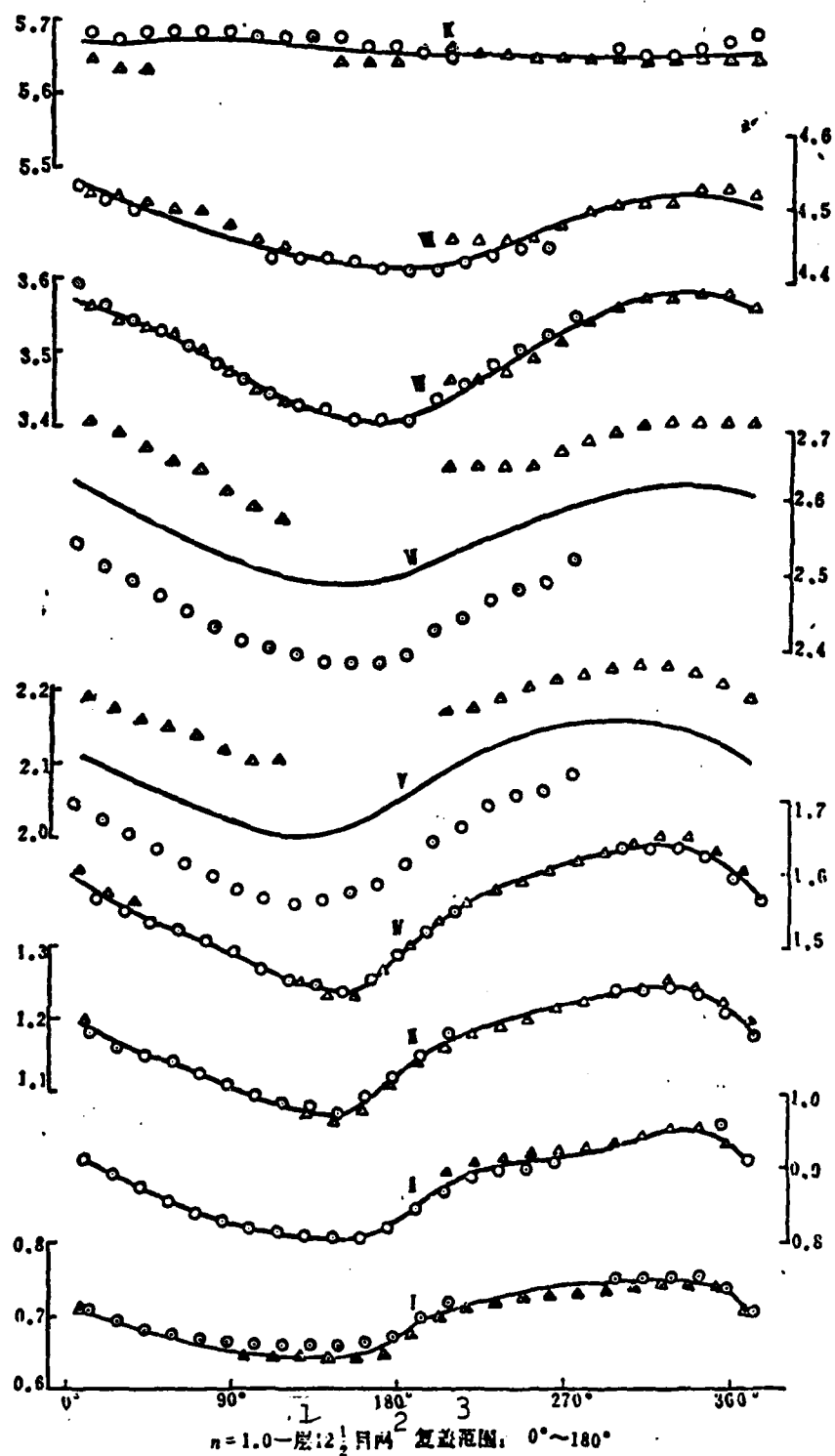


Figure 9. Circumferential distribution of total temperature for exhausts of various stages of the compressor: 1) layer; 2) eye mesh; 3) overload or coverage range.

the last two stages in Figure 8 seems to reflect the tendency to have a turning in the opposite direction to the one which had been the case before.

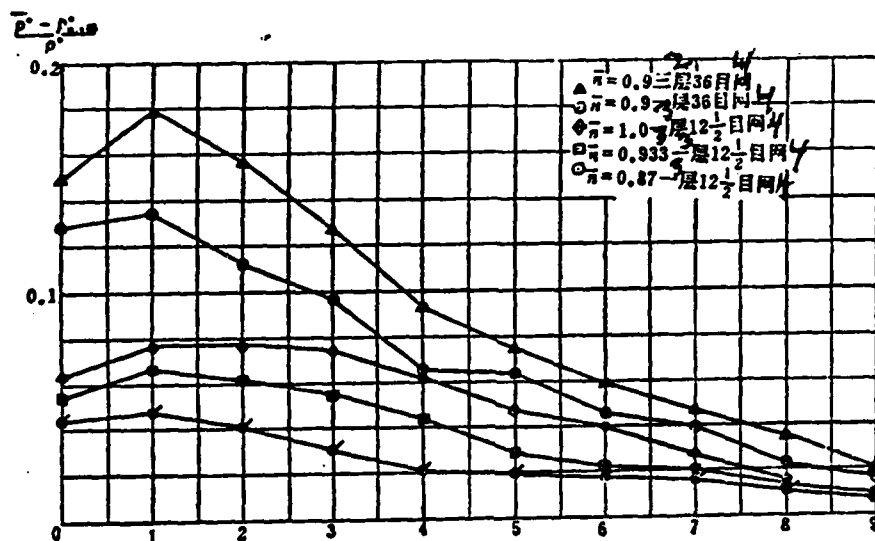


Figure 10. Degree of distortion in total pressure in exhausts of various compressor stages: 2) three layer; 3) one layer; 4) eye mesh.

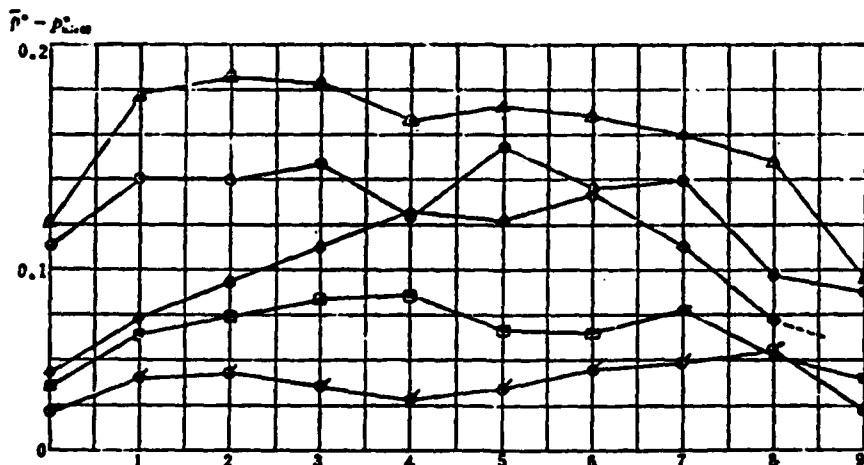


Figure 11. Amplitude of oscillations in total pressure for exhausts of various stages of the compressor.

Figures 10 and 11 show the changes in the degree of distortion of the total pressure and the amplitude of the oscillations in the circumferential direction occurring along the various stages of the compressor. If we analyze Figure 10, we discover that within our experimental range even though the degrees of distortion in the intake of the compressor are not all the same, after the air flow has passed through the numerous stages and has been attenuated, the degree of distortion in the total pressure in the exhaust of the compressor does not differ greatly from other exhaust values. (In all of five tries which were done on this experiment, the results for the degree of total pressure distortion were all within a 1 - 2% range.) If we carry this further, then, it can be seen that after the air flow has gone through the first several stages, the degree of distortion has already been greatly attenuated. Obviously, if these principles govern the attenuation of distortion in this engine, this sort of engine will have a relatively high capability for resisting distortion in medium and high operational (rotational) speed ranges.

Figure 11 shows a set of curves which are relatively complicated; as far as the amplitude of circumferential oscillation in the values for the total pressure is concerned, the first stage has an obvious enlarging effect; the middle stages have enlarging effects in some cases and reducing effects in others; the stages numbered eight and nine have relatively obvious attenuating effects.

III. INFLUENCE OF INTAKE DISTORTION ON PERFORMANCE OF ENGINE COMPRESSORS

Figure 12 deals with the influence that intake distortion has on the performance of engine compressors when the

compressors with so-called "clean" intakes). From the illustration, it can be seen that the pressure ratio for the operation of the secondary or sub-compressor with the deformed intake has already greatly exceeded the pressure ratio for the stable state stall speed. Moreover, the pressure ratios encountered in the operation of the secondary or sub-compressors with the clean or undeformed intake are all much, much lower than the operating pressure ratios which they alternately pass through areas of deformation and areas which are "clean" or "pure" of deformation, so to speak. The size of the angle of attack of the air flow as it passes over the blade of the turbine wheel or disc also alternates. In this sort of unstable or irregular situation, the interference with the dynamic stall speed causes the angle of attack for the dynamic stall speed to exceed the angle of attack for the stable state stall speed. This is precisely the main reason that the operating pressure ratios for secondary or sub-compressors with deformed intakes exceed the stable state stall speed pressure ratios.

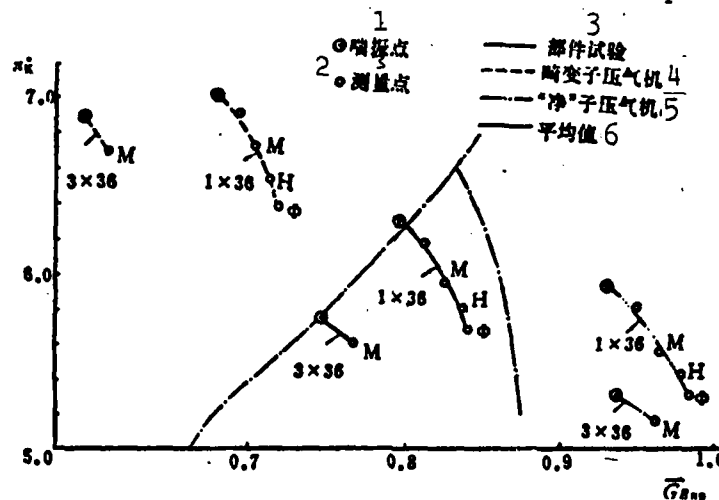


Figure 13. Compressor characteristics for engine with deformed intake and two secondary or sub-compressors: 1) surge point; 2) measurement point; 3) testing of the equipment as a whole; 4) secondary or sub-compressor with deformed intake; 5) secondary or sub-compressor with a "clean" or undeformed intake; 6) average values.

As it can be seen very clearly from Figures 12 and 13, the theoretical third stage for operation of parallel compressors (appendix 1) does not fit this example.

IV. INFLUENCE OF REDUCTION IN EXHAUST AREA OF THE TURBINE IN GUIDE CONFIGURATION I ON THE PER- FORMANCE OF COMPRESSORS INVOLVED

Figure 14 shows the changes in engine compressor performance for a 12% reduction in exhaust area of the turbine in guide configuration I. This reduction in the area in guide configuration I causes the operating point of the engine to move up, and, at the same time, causes the line defined by equal rotational speeds of the compressor to move to the left and to become flattened. The lower the rotational speed, the more severe the degree of flattening of the curve, and this trend continues even to the point where one sees a branching off to the left from a curve defined by equal speeds of rotation and with a rate of slope that is perpendicular.

Because one does see a movement to the left by the line or curve defined by equal values for the speed of rotation, and the operating point comes close to the stall curve, the stall speed margin for the compressor in question takes an obvious downturn. The stall speed margins which are figures on the basis of SM_2 changes as shown below:

| # | 1 | 2 | ΔSM_2 |
|------|-----------|----------------|---------------|
| | 原型 SM_2 | 减小 I 导后 SM_2 | |
| 1.0 | 18.7% | 8.7% | 10.0% |
| 0.9 | 15.6% | 9.4% | 6.2% |
| 0.87 | 15.2% | 10.0% | 5.2% |

Key: 1) Original form of SM_2 ; 2) SM_2 after reduced, Guide Configuration I.

One can see that the reduction in the area of the exhaust with guide configuration I causes the stall speed margin to be reduced, and the higher the rotational speed, the larger the losses in the stall speed margin.

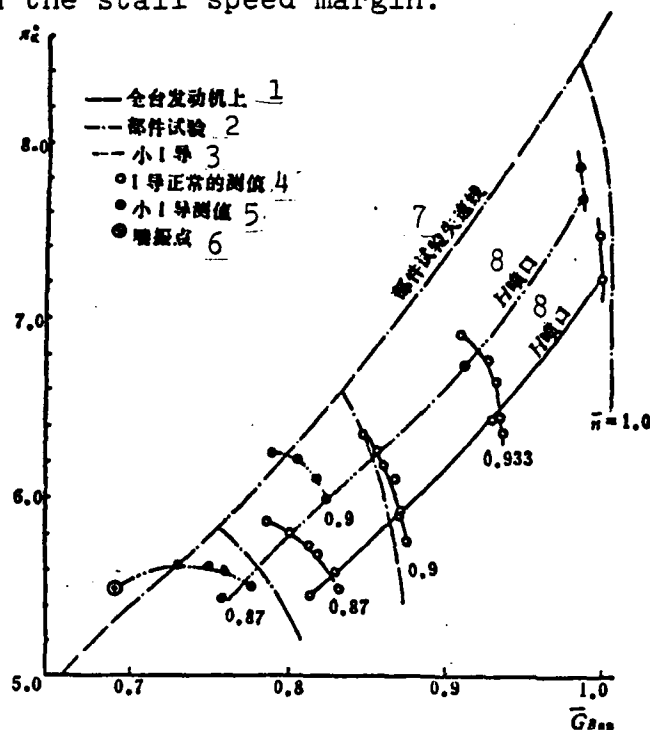


Figure 14. Influence of a reduction of 12% in an area of exhaust in guide configuration I on compressor performance: 1) engine, as a whole; 2) all-component test; 3) small vane I configuration; 4) regularly measured value for small vane or guide I configuration; 6) surge point; 7) stall line for an all-component test; 8) H jet nozzle.

V. INFLUENCE OF INTAKE DISTORTION ON UNSTABLE STATE OF ENGINE

Figure 15 is a history over time of certain quantities when the engine involved is operating at 87% of the rotational speed for which it was designed, the area of the exhaust in guide configuration I is reduced 12%, and there is no intake

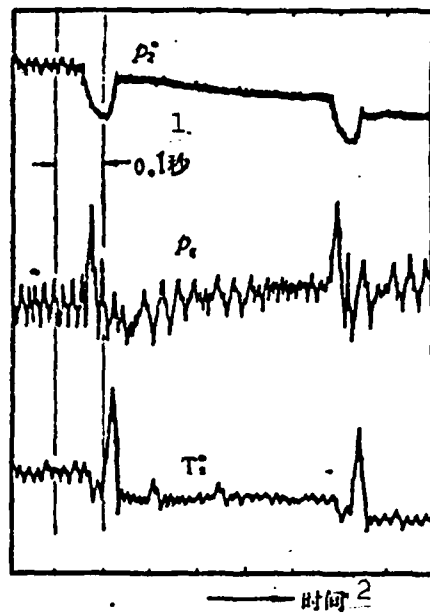


Figure 15. Record over time of p_2^* , p_g and T_2^* during a surge with the area of the exhaust of a guide I configuration reduced by 12%: 1) sec; 2) time.

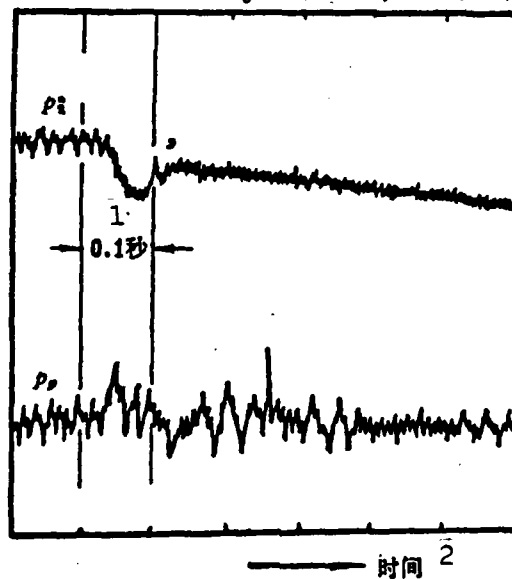


Figure 16. Record over time of the values of p_2^* and p_g during a surge with a 180° circumferential 1 x 36 eye mesh net in use. 1) sec; 2) time.

distortion. The engine in question also experiences a surge. The quantities measured under these conditions are: the overall pressure of the compressor exhaust p_2^* ; static pressure in the measured section of the flow p_g ; and the overall temperature of the compressor exhaust T_2^* . From the figure, it can be clearly seen that when surge begins, the sharply pointed wave which is produced reaches the measured section of the flow in a very short period of time (approximately 6 ~ 8 msec); when this happens, p_g reaches a peak value.

Figure 16 is a history over time of certain quantities when the engine involved is operating at 90% of the rotational speed for which it was designed. There is a standard area of exhaust for a guide vane I configuration. The intake being used is equipped with a 180° circumferential 1 x 36 eye mesh distortion net. The engine in question also experiences surge. Quantities measured under these conditions are the total pressure of the exhaust of the compressor p_2^* and the static pressure of the measured section of the flow p_g . Due to the drag of the distortion net, the sharply pointed wave which is produced when the surge occurs is already greatly attenuated by the time it reaches the measured section of the flow. The p_g curve still shows a reaction to the arrival of this wave. However, the peak has already disappeared. Figures 17a and 17b are photographs taken under the types of conditions described previously; i.e., the two measured quantities are $p_{1.2}^*$ and $p_{1.3}^*$. The sudden increase which takes place in the value of the curves of Figure 18 before these same curves suddenly dip is explained by the fact that the stage of the compressor which is involved here was in front of the stage which caused the surge.

Figure 19 is a record over time of certain quantities measured when the engine in question was operating at 90% of the rotational speed for which it was designed. There was a

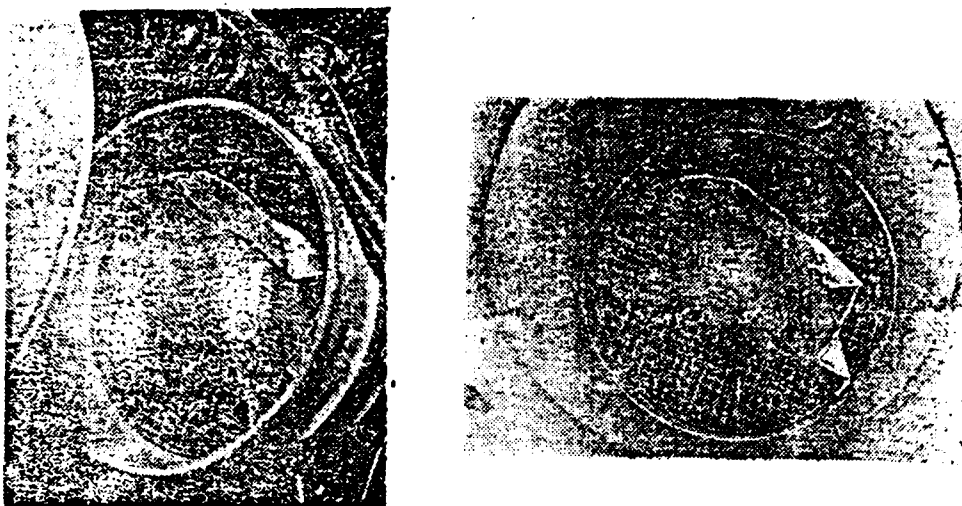


Figure 17. Photographs of the 180° circumferential 1 x 36 eye mesh distortion nets which were blown back by the sharply pointed wave which was generated during a surge.

standard area for the exhaust in a guide vane I configuration, and the intake was equipped with a 180° circumferential 3 x 36 eye mesh distortion net; the engine involved was experiencing a surge at the time of measurement in addition to the other conditions mentioned. The quantities measured were: overall pressure in the compressor exhaust p_2^* ; the static pressure p_g measured in the measured section of the flow; and overall temperature T_2^* in the exhaust of the compressor involved. Figure 20 is a record over time of the total pressure p^* between compressor (i.e., the exhausts of stages 1, 2, 3 and 4 of the compressor involved) stages. From the figure, it is possible to see clearly that when the engine involved experiences surging, then rotational stall occurs in parts of the cycle of the compressor. Concerning this point, the dynamic parameters between the different stages of the compressor point out even more clearly the following: in the range of low frequency amplitude values in the oscillation cycle, one finds rotational stall at approximately 70 Hertz (about 45% rotational speed). Concerning the record over time of the total temperature in the exhaust T_2^* after surging takes place, one also finds rotational

Page 310
not available

stall at a frequency of 70 Hertz. The overall pressure pulsations between the different stages of the compressor also very clearly show that the total pressure suddenly goes up before surging; this fact explains the fact that the surge begins in the rear stage of the compressor.

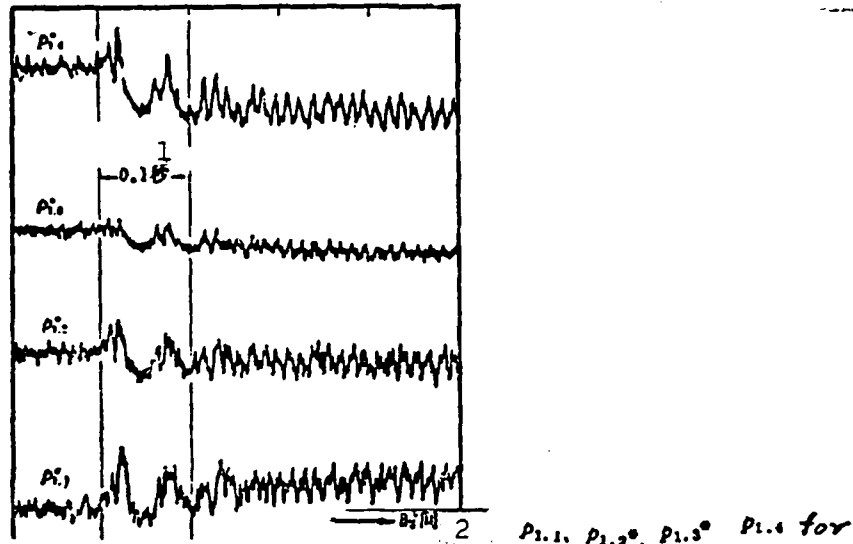


Figure 20. Record over time of the values of a 180° circumferential 3 x 36 eye mesh net and surge occurring: 1) sec; 2) time.

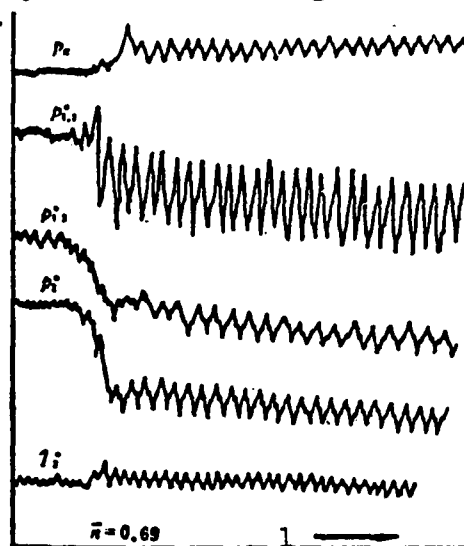


Figure 21. Record over time of the values of $P_{t,2}$, $P_{t,1}^*$, $P_{t,1}$, $P_{t,2}^*$ and $T_{t,1}$ when the upper stall point is experiencing stall. 1) time.

Figures 21 and 22 are respectively record over time the values of p_0 , $p_{1.1}^*$, $p_{1.2}^*$, p_2^* and T_2^* when there is no intake net and the rotational stall speeds are 69% and 49% (i.e., the upper and lower points at which stall occurs). Both are rotational stalls. According to what was shown by the results of a B& K 3347 frequency spectrum analysis and a JFF-8AJ-B real time numerical data analyzer analysis, the frequencies for the two respective cases were rotational speeds of 46% and 45% [6]. From the figures it is possible to see that the second stage is the one in which the stall for the whole compressor and engine begins.

[TRANSLATOR NOTE: Illegible foreign paragraph.]

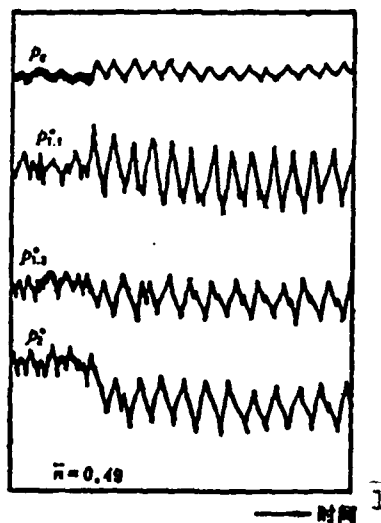


Figure 22. Record over time of the values of p_0 , $p_{1.1}^*$, $p_{1.2}^*$, p_2^* and T_2^* when there is a stall at the lower stall point. (1) time.

VI. CONCLUSIONS

1. Capabilities of compressors of this type of turbojet engine are not only determined by the capabilities or characteristics of the components of the compressor. They are also determined by the structural arrangement and actual situation of other components in the system of the compressor. Given that the rotational speeds stay the same, a distortion in the intake causes the line determined by equal values of rotational speed to move toward the left and flatten. The larger the distortion, the more severe the degree of the reduction in the exhaust area of a turbine in the guide vane. Configuration I also causes the line which is defined by equal values of rotational speed to move left and flatten. The degree of flattening which is the result of this cause is more severe than that which is caused by the influence of the intake distortion.

2. The appearance of unstable state conditions in the stall curve of the compressors of turbojet engines is not only dependent on the volumes of the combustion chambers of the engines involved and the rotational speed of those engines. It is also dependent on the actual set-up of the system of the compressor with which one is dealing. When one is dealing with moderate and low speeds of rotation values in the curves being examined (such as the upper and lower stall speed points mentioned in reference 6) then, even though one finds rotational stall, there is no accompanying surge. When one is dealing with high speeds of rotation (such as 90% of the rotational speeds for which the engines involved were designed), even though one observes surge, different systems give rise to different forms of surge. 3x36 eye mesh gives rise to surge with a classic form. A system in which the area of the guide vanes has been reduced by 12% will give rise to the appearance of a deep surging mode.

3. Intake distortions cause the engines in question to have their stall speed margins drop substantially and cause an increase varying directly with the degree of the distortion. The reason for this is the leftward movement of the line defined by equal values of the rotating speed curve and the effect that this movement has on the operating point of the engine in the experiment as that point and the rotating speed curve get close to the stall speed curve. A reduction in the area of the turbine wheel or disc also causes the stall margin of the engine to go down, similar to the distortion of the intake, when in a guide vane I configuration.

4. The 1 x 36 and 3 x 36 eye mesh intake distortion nets which were used in these experiments in a 180° circumferential mode successfully produced a close approximation to a square wave form in the overall pressure spectra involved. The rotatable interference net structures and the movable stopper-type tail cones which were used during these tests are all thoroughly workable in practical terms.

5. When engines involved in the tests were operated with a 3 x 36 eye mesh net for distortion purposes at 90% of the rotational speed for which the engines were designed, i.e., $\bar{D} = 0.173$, and the rotational speed was then increased to 93.3% of the design rotational speed, the engines involved still did not give rise to any instability phenomena.

REFERENCE WORKS

- [1] Roberts, F., et al., Insights into Axial Compressor Response to Distortion, AIAA paper No. 68-565, 1968.
- [2] Mikolajczak, A. A., The practical Importance of Unsteady Flow, AGARD cp-177, 1977.

[3] Korn, A., Estimated Effect of Circumferential Distortion on Axial Compressors Using Parallel Compressor Theory and Dynamic Stall Delay, AIAA paper No. 74-233.

[4] Greitzer, E., Surge & Rotating stall in Axial Flow Compressors. Pt. I, Theoretical Compression System Model. Trans. of ASME, April 1976.

[5] Greitzer, E., Surge & Rotating Stall in Axial Flow Compressors. Pt. II, Experimental Results & Comparison With Theory, Trans. of ASME, April 1976.

[6] Northwestern University of technology air intake distortion group. Initial experimental research on compressor stall on all engines. Unpublished.

[7] Robert, S. Mazzawy, Multiple Segment Parallel Compressor Model for Circumferential Flow Distortion, AGARD cp-177, 1977.

[8] Edwin, J. Graber, JR. and Willis, M. Braithwaits, Summary of Recent Investigations of Inlet Flow Distortion Effects on Engine Stability, AIAA paper No. 74-236.

APPENDIX

1. Basic Principles of Parallel or Coordinate Compressors [8].

Assumptions concerning parallel or coordinate compressors: (1) a compressor with a deformed intake can be seen to be made up from two secondary or sub-compressors unrelated to each other -- one with a "clean" or undeformed intake, and the other with a deformed intake; (2) the exhausts of the two secondary or sub-compressors are so arranged that their exhaust gases are evenly emptied into a common area or volume, and the static pressures of the exhausts of the two secondary or sub-compressors are equal; (3) both the secondary or sub-compressors obey the rules which are characteristic of stable state compressors; however, when the pressure ratio of the secondary or sub-compressor with the deformed intake reaches the pressure ratio which corresponds to a stall, the compressor as a whole stalls (or experiences a stall).

2. Stall Margin Formulas.

1. Stall margin as defined by the pressure ratio:

$$SM_1 = \frac{\pi_{R^*9} - \pi_{R^*0}}{\pi_{R^*0}} \times 100\%$$

2. Stall margin as defined by the pressure ratio and the ratio of the values for the amount of flow:

$$SM_2 = \frac{(\pi_{R^*}^*/G_B)^9 - (\pi_{R^*}^*/G_B)_0}{(\pi_{R^*}^*/G_B)_0} \times 100\%$$

In these equation, the subscript "9" represents the parameter for the operating point.

Summary

A Preliminary Experimental Investigation of the Response of a Turbojet Engine to Inlet Pressure Distortion

*Chen Fuqun, Tang Diyi, Hu Zilong, Li Wenlan, Yu Jindi,
Wu Xinyuan, Zhao Jueliang, Lin Qixun, Wang Zongyuan,
Liu Sihong, You Shaokun, Cong Mengzi, etc.*

In this paper, preliminary experimental results about the effect of inlet pressure distortion on the characteristics and instability of the axial compressor of a turbojet engine are presented. The experiments have been conducted on the test bed on a turbojet engine with a 9-stage compressor, whose first stage is transonic. The tests have been run for each of the following cases:

- (1) at 90% design speed with 180° triple-deck 36 mesh screen in front of the engine inlet, i. e., 3×36 mesh;
- (2) at 90% design speed with 180° single-deck 36 mesh screen, i. e., 1×36 mesh;
- (3) at 90% design speed with "clean" inlet;
- (4) at 87% design speed with a decrease of about 12% of the first stage turbine nozzle exit area, i. e., $\Delta A_{Tn} = -12\%$.

A comparison between the results from tests with or without inlet distortion shows that the inlet pressure distortion affects not only the stall line but also the shape and position of constant speed lines of the compressor. Inlet pressure distortion shifts the speed lines leftward and causes it to become flat in shape. The effect of the decrease in the first stage turbine nozzle exit area is similar to that of inlet pressure distortion.

The results from the interstage measurements in the compressor show that the degree of flow distortion increases in the first stage and decays rapidly in the following stages, especially in the 2nd, 3rd, and 4th stages.

From the analysis of the behavior of instability which occurs on the stall line of the engine compressor tested, it is found that in the case of 3×36

mesh screen, the surge produced is of a classical mode in which flow oscillates with large amplitudes and during a portion of the cycle there exists a rotating stall; and that in the case of decrease in turbine nozzle area, the surge produced is of a deep surge mode.

From the results it can also be seen that in the case of 3×36 mesh screen (distortion index $\bar{D} = \bar{p}_1^* - p_{min}^* / \bar{p}_1^* = 0.173$ at 90% design speed), there is no occurrence of instability when the engine is accelerated up to 93.3% design speed.

THE MEASUREMENT AND ANALYSIS OF STATION PARAMETERS OF A TURBOJET ENGINE

Dong Qui-ting, Zhao Jue-liang, Liu Si-hong, Wu Xin-yuan,
Hu Zi-long, Cong Meng-zi, Lin Qi-xun, Wang Zong-yuan, You
Shao-kin, Zheng Li-zhi

TABLE OF SYMBOLS

| | | | |
|----------|--|-----|---|
| T | Absolute Temperature | T | Turbine or fuel |
| t | Celsius Temperature | C | Jet Tail Pipe |
| P | Pressure | B | Air |
| n | Rotational Speed | F | Burned Gasses |
| G | Amount of Flow | cor | Recomputed for Standard Atmospheric Conditions |
| π | Pressure Increase Ratio or Expansion Ratio | in | Intake Nozzle |
| σ | Total Pressure Recovery Coefficient | K | Compressor or Specific Heat Ratio |
| η | Efficiency | max | Maximum |
| ζ | Coefficient of Thermal Radiation | min | Minimum |
| R | Thrust or Gas Constant | 1 | Cross Section of Compre- ssor Intake |
| C_r | Fuel Consumption Rate | 2 | Cross Section of Turbine Intake |
| D | Diameter | 3 | Cross Section of Turbine Exhaust |
| F | Area | 4 | Cross Section of the Jet Tail Pipe |
| q_t | Injection Angle for the Amount of Fuel Per Kg of Air Per Sec | 5 | (Critical Angle Markers) |
| O | Boundary Conditions | * | Blockage Values |
| a | Measured Cross Section of the Flow | - | Corresponding Values |
| KC | Combustion Chanber | | |

I. THE OBJECTIVES AND CONTENTS OF THE EXPERIMENTS

The objective of the experiments was, by means of measurements of the various characteristic cross sections of flow fields as well as of aerodynamic parameters, station parameters, the loss parameters for various components, and so on, to get a firm grasp of the station parameter flow states and characteristics of the engines concerned, to investigate the influence of aerodynamic states on the various types of parameters and the performance of the engines involved, to find effective means by which to raise the performance of the turbojet engines involved, and, at the same time, to take a step in the direction of improving the experimental or measurement technology available for the investigation of engines as they operate as a whole. The plan for the experiments was:

1. Measure the design states for the various characteristic cross sections of flow fields for an engine as well as the aerodynamic parameters, the process parameters for the engine and the loss parameters for the various components of the engine;

2. Measure the influence of intake conditions on the various types of parameters in the engine;

3. Measure the situation in which the various parameters being measured change with variations in the rotational speed, the air release or escape system or the adjustment of the cross sections of the engine under consideration.

II. THE ENGINES

The engine type which was used in these experiments was a standard type, single axis turbojet engine. During the entire

process of experimentation, the area of the turbine guide vane apparatuses was maintained invariable. During the entire process of experimentation, the capabilities of the engines were always up to standard. These engines included such features as a nine-stage axial flow compressor which also has mounted on it a two-stage turbine on the same axis, a tube combustion chamber composed of ten flame tubes, an afterburner or thrust augmentation combustion chamber and a jet tail pipe which can be operated in such a way that it can restrain the exhaust in certain ways. Aft of the fifth stage of the compressor, the engine type under consideration has an automatic air release structure. During when the engine is running at low rotational speeds, the air release automatically opens preventing the occurrence of a surge.

III. CHANGES IN THE EQUIPMENT ON THE ENGINES

In order to be suited to the needs of these experiments, the engines were changed in quite a few instances. In the intake, aft of the full flow cap or cover, there was installed a 100 mm long section of round tubing in order to measure the amount of flow in the engine. In the front edge of each of the eight hollow blades of the turbine guide vane apparatus in the first stage of the turbine, there were opened seven small holes, and in these holes there were installed needles for the measurement of the total pressure. Aft of the turbines, the ten pre-fuel jet nozzles and pre-combustion chamber which were found on the afterburner or thrust augmentation diffuser casing were all eliminated, and use was made of the cavities of rectification panels and diffusion apparatuses for the installation of gear wheel transmission structures, and these structures can be changed to function as rotational devices for measuring temperature and for the measurement of the temperature after the turbine in operating configurations which do not involve the afterburners.

IV. THE MEASUREMENT POINTS AND THE INSTRUMENTS TAKING THE MEASUREMENTS

The measurement point arrangement for the entire course of the flow through the engine is as shown in Figure 1.

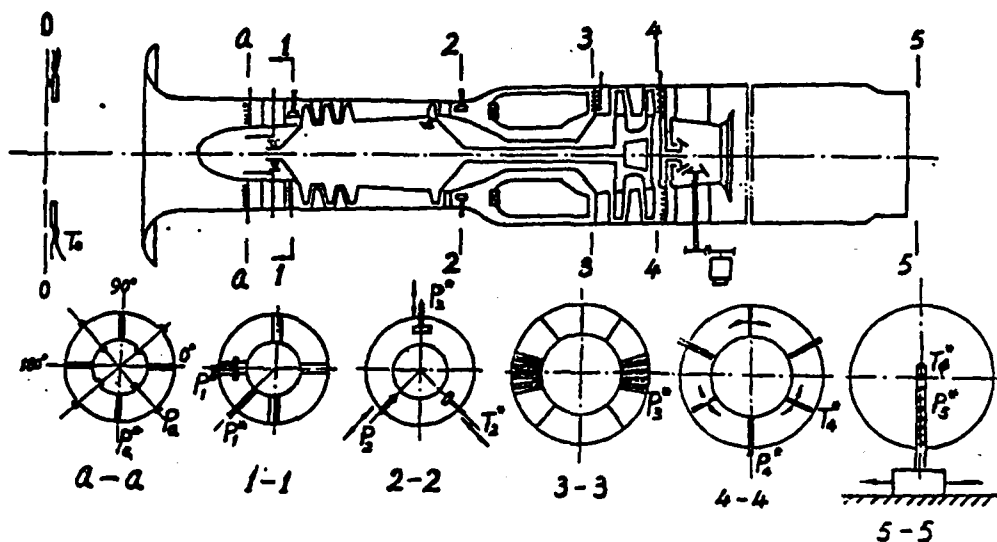


Figure 1. Arrangement of the Measurement Points Throughout the Entire Course of the Flow of This Turbinejet Engine.

The measurement sensors, the instrumentation, and the number of measurement points in the various characteristic cross sections of the engine are as shown in Table 1.

IV. RESULTS AND DISCUSSION

1. The Amount of Flow Through the Engine

The amount of flow through the engine is determined by the flow speed method. The total pressure field is measured and determined by the use of four comb-type total pressure

Table 1

The Number of the Parameter Measurement Points for the Various Cross Sections and the Sensors and Instrumentation Employed (key, previous page)

| 1 表 1 | | 2 各截面参数测点及传感器和仪表 | | 3 仪 表 | | 14 备 注 |
|-----------|---------------------------|------------------|-----------------|---------|---|------------------------------|
| 6 7 截面 参数 | 8 名 称 | 9 数量 | 10 方 式 | 11 测点 数 | 12 式 样 | 13 数量 |
| 0 | T: 15 铂电阻温度计 | 4 | 16 定点 | 4 | 17 自动平衡仪 XQC300, B.A ₂ -90~50℃ | 1 |
| | T: 18 热电偶 | 4 | 19 定点 | 4 | | 20 4支电偶并联后与T ₁ 反串 |
| | T: 21 大气压力计 | 1 | 22 定点 | 1 | 23 福廷式 | 1 |
| | P: 24 15点线状总压管 | 4 | 25 以22.5°间隔测量一次 | 210 | | 15 |
| 1 | P _外 : 26 外壁静压孔 | 4 | | 16 | 27 水柱U形管 | 1 |
| | P _内 : 29 内壁静压孔 | 4 | | 16 | | 1 |
| | P: 30 15点总压孔 | 1 | | 15 | 34 水柱U形管 | 15 |
| 2 | P: 32 15点线状总压管 | 1 | 33 定点 | 15 | | 15 |
| | T: 36 3点总压孔 | 1 | 37 径向移动4个位置 | 36 | 38 自动平衡仪 XWC104E 0~20mV 12点 | 1 |
| | P: 39 10点总压孔 | 1 | 40 径向移动4个位置 | 40 | 41 SYD-1 压力传感器 XJ-100 巡回检测仪 | 1 |
| | P ₃ : 42 三孔计 | 1 | 43 径向移动4个位置 | 4 | 44 同 上 | 1 |
| 3 | P _外 : 45 外壁静压孔 | 4 | 46 定点 | 4 | 44 同 上 | |
| | P _内 : 45 内壁静压孔 | 8×4 | 46 定点 | 32 | 44 同 上 | |
| | P: 49 一特前缘7点总压管 | 8 | 46 定点 | 56 | 50 XJ-100 巡回检测仪 | |
| 4 | T: 51 5点线状热电偶 | 3 | 53 每旋转6°测量一次 | 300 | 54 自动平衡仪 XWC200/A, XWC300, EU-2, 400~900℃ | 55 各1 |
| | P: 52 7点线状总压管 | 3 | 46 定点 | 21 | 50 XJ-100 巡回检测仪 | |
| 5 | T: 56 总压热电偶 | 1 | 57 直径方向横扫 | 57 | 58 模拟运算器, SE 2000 紫外线记录仪 | 59 各1 |
| | P: 59 6点线状总压管 | 1 | 60 定点(直径方向分布) | 60 | 50 XJ-100 巡回检测仪 | |
| | 61 边界热电偶 | 2 | 46 定点 | 2 | | |
| | 62 边界总压孔 | 2 | " | " | | |

Key: 1. Table 1, 2. The Number of the Parameter Measurement Points for the Various Cross Sections and the Sensors and Instrumentation Employed, 3. Objective of the Testing, 4. Sensors, 5. Instruments, 6. Cross Section, 7. Parameters, 8. Nomenclature, 9. Numerical Amount, 10. Method, 11. Number of Measurement Points, 12. Type, 13. Number, 14. Remarks, 15. A Platinum Electrical Resistance Temperature Gauge, 16. Specified Point, 17. Automatic Balance $\times \text{QC300.BA}_2 - 90 \sim 50^\circ\text{C}$, 18. Thermocouple, 19. Specified Point, 20. 4 Thermocouples and Two-Way Connections Between Those Thermocouples and T_2^* , 21. An Atmospheric Pressure Gauge, 22. Specified Point, 23. Fu Ting Type, 24. 15 Point Comb-type Overall Pressure Tube, 25. Taking an Interval of 22.5° Between Each Measurement, 26. Outside Wall Static Pressure Hole, 27. A U-shaped Tube with a Water Column, 28. Pressure Tubes of the Same Diameter Set Next to Each Other, 29. Internal Wall Static Pressure Hole, 30. 15 Point Overall Pressure Consumption, 31. Circumferential Distribution Behind the Rectifier Panels or Blades, 32. 15 Point Comb-type Total Pressure Tube, 33. Specific Point, 34. U-shaped Tube With a Water Column, 35. Radial Distribution Behind the Rectification Plates or Panels, 36. 9 Point Overall Temperature Consumption or Utilization, 37. Four Locations of Radial Movements, 38. Automatic Balance $\text{XWC104E } 0 \sim 20\text{mV } 12\text{ pt.}$ 39. 10 Point Overall Pressure Consumption or Use. 40. Four Locations of Radial Movement, 41. SYD-1 Pressure Sensor and Transmitter and XJ-100 Roving Test Instrument, 42. Three Hole Needle, 43. Four Locations of Radial Movement, 44. Same as Above, 45. External Wall Static Pressure Hole, 46. Specified Point, 47. External, 48. Between Stages, 49. 7 Point Total Temperature Tube on the Leading Edge of a Vane, 50. XJ-100 Moving Test Instrument, 51. 5 Point Comb Type Thermocouple, 52. 7 Point Comb-type Total Pressure Tube, 53. A Measurement Taken Every 6° of Rotation, 54. Automatic Balance $\text{XWC200/A.XWC300.EU-2.400} \sim 900^\circ\text{C}$ 55. Each 1, 56. Total Temperature Thermocouple, 57. Radial Horizontal Sweep, 58. Analog Computer, SE2000 Ultra-violet Recording Instrument, 59. 6 Point Comb-type Overall Pressure Tube, 60. Specified Points (Distribution Along a Diameter), 61. Boundary Thermocouple, 62. Boundary Overall Pressure Measurement Gauge, 63. Interior.

measuring tubes or needles with 15 points each. With consideration given to the boundary layers on the surfaces of the interior and exterior walls, the designers artificially took the pathway of the engine and divided it into three circular surfaces. The thicknesses of each of the interior and exterior surfaces were all taken as 15 mm, and each of these surfaces had distributed on it five measurement points. The five measurement points on the surfaces in the middle are all distributed on the basis of a numerical integration method. The circumferential field is measured and determined by measurements of sections of the flow which are measured each time the field is rotated another interval of 22.5° . The average total pressure for the entire cross section involved is solved for by using the basis of the area involved. The results of these measurements show that the degree of unevenness between the measured pressure values for single points and the average values is, at its circumferential maximum, not greater than 0.1%; the thicknesses of the boundary layers on the interior and exterior wall surfaces were respectively approximately 3mm to 10mm.

On the interior and exterior walls of the measured section of the flow, there were made at evenly separated intervals four holes for taking measurements of the static pressure on the wall. Due to interference between the rectifier guides or vanes and the intake cover, the static pressure field is twisted. Through the use of measurements made by the use of five comb-type three hole needles set at inclined angles, it was learned that the degree of unevenness in the circumferential static pressure on the exterior wall surface was 1.6%, and the corresponding figure for the interior wall was 1.2%; the degree of unevenness of the static pressure along a radial direction at a place on the panel involved was 1.6%, and the corresponding measurement at a place between two of the panels was 1.7%. The angles of deflection of the air flow in a shear direction and an axial direction were respectively capable of

reaching the values of 5° and 2.5° . Because of this fact, only making measurements of the static pressure on the wall surfaces is not usually enough. However, if one is considering the case of the sort of turbojet engine which is involved in these experiments, then, if one takes the static pressure holes in the surface of the walls and puts them between two of the rectifier panels, that is to say, if one carries out measurements at 45° , then, it is possible to get relatively satisfactory results. The measured values and the average static pressure values which were obtained by measurements using the three hold needles set at inclined angles only differed with each other by 0.05%.

II. THE EFFICIENCY AND PRESSURE INCREASE RATIO OF THE COMPRESSORS INVOLVED.

When one is making measurements to determine the total pressure of the intake of the compressors involved in these tests, fifteen point comb-type total pressure measurement needles are used in order to measure the boundary layers. Also a fifteen point total pressure rake is used to make measurements to determine the nature of the wake of the rectifier panels (see Figure 2).

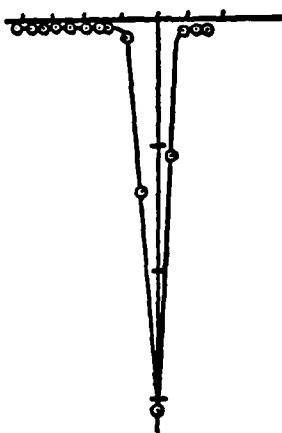


Figure 2. A Chart of the Wake of a Rectifier Panel in Cross Section.

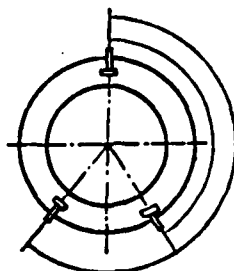


Figure 3. An Illustration of the Locations at which the Compressor Exhausts Were Measured.

The efficiency of the compressors involved is measured by the use of the temperature rise method. At the three locations A, B, and C in the exhaust of the compressor being measured as those locations are shown in Figure 3 which appears above, respective use is made of nine point total temperature rakes which are capable of automatically moving in the radial direction, ten point total pressure rakes as well as three hole needles in order to measure the distribution of the T_2^* , P_2^* , and P_2 values which correspond to grooves in the exhaust. The positions at which the measurement points are placed along the radial axis are determined by taking the exhaust cross-section of the compressor involved and dividing it up into four equal round surfaces. On the basis of a numerical integration method precise determinations are made for four of the measurements. Measurements of the rise in temperature in a compressor involve the use of four T_1^* thermoelectric thermocouples placed together which have the same return circuit resistances. A temperature measuring circuit from the conversion switch inside the instrument is used. Point-by-point correlation of the T_2^* temperature values from the temperature rake is performed.

The total temperature and pressure distributions which were obtained by measurements of the cross sections of the compressor exhausts are as shown in Figure 4 and Figure 5. It can be seen from the figures that the special characteristics of the temperature distribution of the exhaust of the compressor along the (one character unreadable) are that the area of the

wake is higher than the area of the main flow from the point of view of temperature, and the area of the blade "basin" is higher in temperature than is the back of the blades. The principles which govern the distribution of total pressure are the precise opposite of these. The maximum differential value between the wake area of flow and the main area of flow, in terms of total temperature, can reach 4% of the temperature rise of the compressor. The total pressure can reach 7% of the average pressure. The special characteristic of the distribution in radial direction is the fact that the blade tips and the blade bases have high total temperatures and low total pressures, but the middle portion of the blades have high total pressures and low total temperatures at the same times. These characteristics simply illustrate how the efficiency of the compressor changes as one moves in a radial direction. (See Table 2).

In order to make observations of the circumferential flow field of the exhaust of the compressor, one needs to make use, respectively, of three of the total pressure rakes or three of the total temperature rakes as shown in positions A, B, and C in Figure 3. These all need to be used at the same time to measure the total temperature and pressure. The results of such measurements show that, due to the situation in which the intake comes in through various troughs and the existence of defects in the precision of the workmanship, the fit of the various stages of the compressor in relationship to the stages in front and behind and such factors as the back pressure of the flame tubes, there can be a difference between the average values for the aerodynamic parameters along the grid distance of different troughs on the same blade. The largest deviation in the total temperature reaches 3% of the rise in temperature of the compressor, and the maximum deviation in the total pressure reaches 8% of the average total pressure. Because of this, when one is taking measurements of the average total temperature and average total temperature in the exhaust of a

compressor, besides the fact that one should, on the basis of wake theory, give very careful attention to the measurement of the total temperature and total pressure in the exhaust or exit of a trough, one should also give attention to the precise measurement and correction of the degree of unevenness in the circumferential direction.

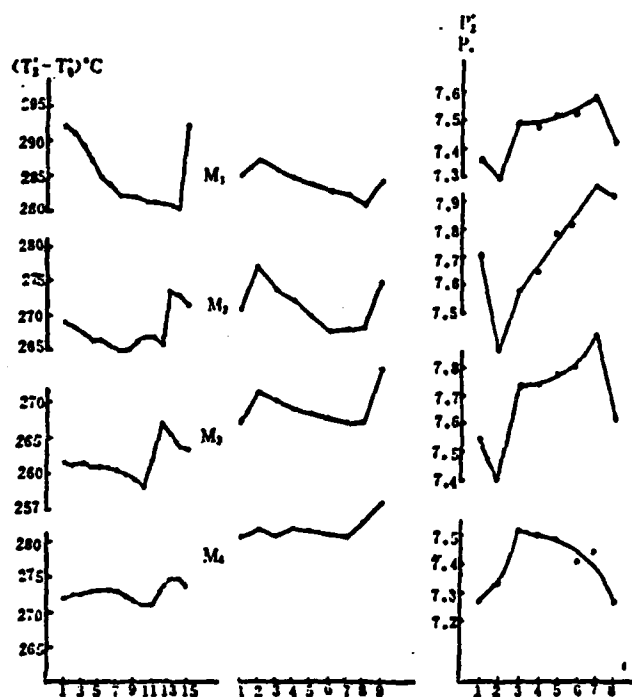


Figure 4. The Distribution of T_2^* and P_2^* along the Grid Distance.

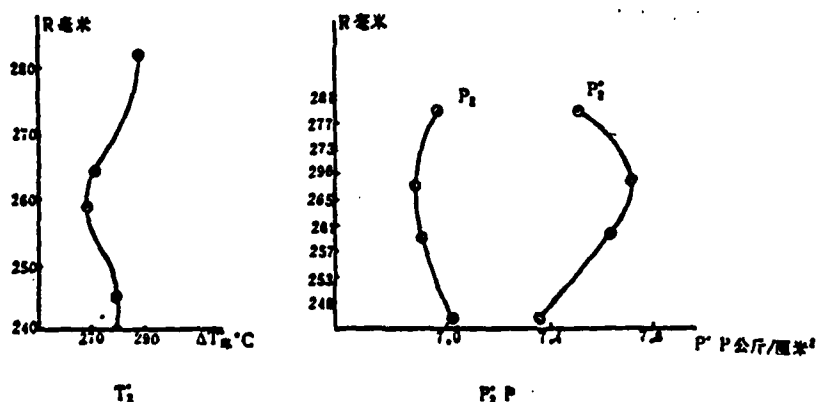


Figure 5. Radial Distribution of T_2^* and P_2^* .

Aft of the grid, sensors were installed which will form a stopper or blockage. In order to study the influence of the blockage of the total temperature rake and the total pressure rake, use was made respectively of single point thermocouples which are capable of moving in the circumferential and radial direction and of single point total pressure measurement needles in order to carry out comparative experiments. If we now take total temperature as an example, we may make use of the results of the comparative experiments which are shown in Table 3 and Table 4.

Table 2. Changes in the Efficiency of Compressors Along the Radial Direction

| Radial Direction Position | I | II | III | IV |
|---------------------------|-------|-------|-------|-------|
| 7% | 0.774 | 0.827 | 0.835 | 0.782 |

Table 3. The Influence of the Blockage on the Amount Value of T_2^*

| 2 径向位置 | $T_{\text{总}}^3 - T_{\text{单}}^4$ [°C] | 5 总温耙局部堵塞 | | | | 6 单点热电偶局部堵塞 | | | 7 通道堵塞 | |
|-----------|---|---------------------------------------|---------|----------|-------------------------------------|---------------------------------------|----------|-------------------------------------|-----------|----------|
| | | $(\frac{f_n}{F_0} \frac{d_i}{l_i})\%$ | | | $\Sigma(\frac{f_n d_i}{F_0 l_i})\%$ | $(\frac{f_n}{F_0} \frac{d_i}{l_i})\%$ | | $\Sigma(\frac{f_n d_i}{F_0 l_i})\%$ | $(f/F)\%$ | |
| | | 8 屏罩 | 9 壳体 | 10 支杆 | | 8 屏罩 | 10 支杆 | | 3 耙 | 11 单点 |
| I | -0.1 | 1.4 | 1.3 | 0.5 | 3.2 | 0.2 | 0.1 | 0.3 | 0.08 | 0.02 |
| II | 3.3 | 1.4 | 1.2 | 3.6 | 6.2 | 0.2 | 0.4 | 0.6 | 0.26 | 0.06 |
| III | 7.0 | 1.2 | 1.3 | 5.6 | 8.1 | 0.2 | 0.7 | 0.9 | 0.37 | 0.09 |
| IV | 8.4 | 1.2 | 1.2 | 9.0 | 11.4 | 0.2 | 1.0 | 1.2 | 0.63 | 0.16 |
| I | — | 12 | 20 | 38 | — | 12 | 60 | — | — | — |
| d/l | — | 0.25 | 0.23 | 0.26 | — | 0.25 | 0.07 | — | — | — |

Key: 2. Radial Direction Position, 3. Rake, 4. Single or Unit, 5. Local Blockage of the Total Temperature Rake, 6. Local Blockage of the Single Point Thermocouple, 7. Passage Block, 8. Cover, 9. Casing, 10. Rod, 11. Single Point.

From the tables it can be seen that the blockage of the total temperature rake will cause the value for the amount of T_2^* to go up, and there will also be tendencies to add to the width of the wake and to increase the twist of the distribution. This is because the blockage aft of the grid not only reduces the areas of passage, it also raises the corresponding back pressure in the exhaust of the trough; because of this, there is a reduction in the amount of flow through the corresponding trough and an increase in the amount of power added; there is also an increase in the value of the amount of T_2^* . Besides this, the reduction in the amount of flow causes an increase in the angle of attack at the location where the flow meets or enters the turbine wheel; at the same time, this points to the appearance of the slip speed of the dish of the stator blades and shows that the dish of the stator blades not only has a collecting effect on both the wheel wake and the main flow, but also, due to this, the blockage leads to an increase in the width of the wake and a twisting of the distribution.

The degree of the blockage is expressed as the ratio of the area of the cross section of the blocking object and the area of the corresponding passage, that is to say, the ratio of the passageway to the blockage. When one is concerned with local blockages, the simple use of the ratio of the area which meets the flow of the wind and the area of the trough is not sufficient. Beyond this, one needs also to reflect the influences of the distance between the trailing edges of the blocking objects and the blades. On the basis of the mechanism involved in local blockages, the degree of these blockages can be expressed by using the characteristic dimensions of the various sensors (such as rod diameter, thickness of shell or casing, and so on) and weighting the ratio of the areas and the ratio of the interval distances.

Due to the fact that the blockage ratio in the passageway for the various sensors is always smaller than 1%, it is possible to ignore the influence of this blockage of the passageway. However, the local blockages are not easy to ignore. Experimentation demonstrates that, following increases in the depth of insertion of the sensors, the values for the amounts coming from the total temperature rake increase. But this increase is not continuous. It can be seen that local blockages from rods have important influences on the situation.

In the same way, the blockage from the total temperature rake causes an increase in the values of P_2^* and a twisting of the distribution. When an engine is in a design state, the blockage causes increases in the amounts of these values whose numerical size can reach 0.8% of the average total temperature in the exhaust.

In view of the fact that the errors associated with these blockages belong to a system of errors, it follows that one should make use of control methods in order to take care of this defect. Making use of small single point sensors which are capable of multi-dimensional displacements is one effective way of reducing the error due to the blockages. However, one must make corresponding and considerable increases in the speed with which data is collected and processed in order to shorten the time required for experimentation.

In a cross section of the exhaust of a compressor, we can solve for the average values for each of the various rings by using the gradation method to figure the average along the grid distance and then multiply by the appropriate correction coefficients for circumferential unevenness. After this, for four ring sections, corrections can be made according to quantitative averages and blockage errors; it is then possible to solve for the average total temperature and not the average total pressure for the cross sections involved.

III. THE EFFICIENCY AND PRESSURE DROP RATIO OF TURBINES

The total pressure P_3^* in front of a turbine is measured by seven point comb-type total pressure measuring needles which are placed in position along the forward edges of the eight hollow blades of the guide vane devices of one stage of the engine. If one gives thought to the influence which the boundaries of the flame tubes have, one realizes that the blades of the eight guide vane devices are concentrated in their locations in the exhaust cross sections of two flame tubes.

The total temperature, T_3^* , in front of the turbine is not obtained by direct measurement, but is calculated on the basis of T_4^* , which is measured, and in accordance with the equal power method. The reason for this is that, on the basis of the principle of the error propagation, it is possible to lower the requirements for the measurement of temperature and to raise the precision of the measurement of turbine efficiency. For example, if we start with the fact that the error in the turbine efficiency is $\frac{d\eta_T}{\eta_T} \leq 3\%$, and, if we measure T_3^* directly, then, if the various errors in quantities are all distributed equally, the errors in the measurements of T_3^* and T_4^* will both be impermissible if they are larger than 0.4%. Obviously, this is very difficult to obtain. However, if one makes use of the method of figuring T_3^* on the basis of T_4^* , then the error in the measurement of T_4^* can be allowed to be as large as 2.1% and still be acceptable.

Figure 6 is the temperature field which was obtained by measuring T_4^* . The largest temperature differential in this field is 280°C. The largest temperature differential between the average temperatures in the flame tubes is 48°C; it can be seen from this that the temperature field is very uneven.

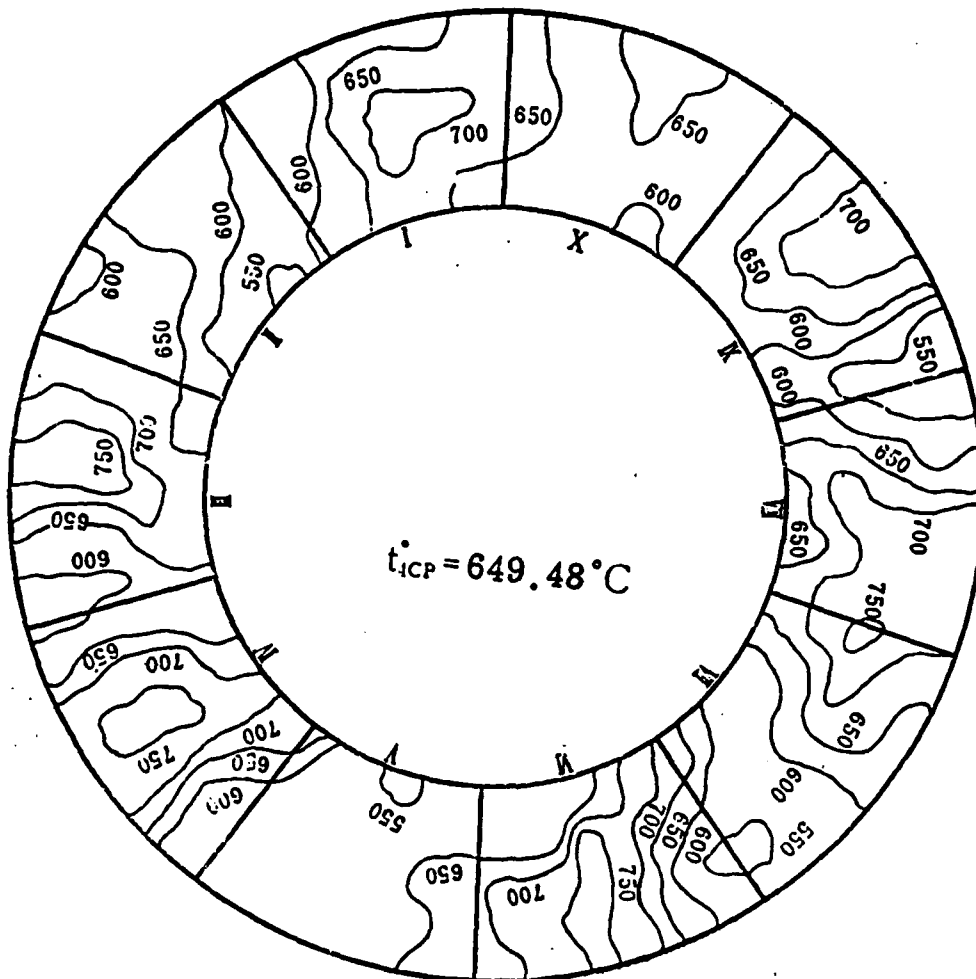


Figure 6. T_{II}^*

Because of this, in order to obtain relatively precise measurements of the average total temperatures in the various cross sections, it is necessary to have an adequate number of measurement points. However, if one uses too many sensors, this practice will cause a serious blockage. For example, if use a ten-arm-five-point comb-type thermocouple in order to carry out the measurements and we assume that this thermocouple has a diameter of 10mm, (the blockage ratio in the passageway is 5.7%). This will cause the temperature, T_{II}^* , to go up approxi-

mately 20°C. Because of this problem, if one makes use of rotating structures in order to measure the temperatures and takes as his instrument a three-arm-five-point comb-type thermocouple which takes one measurement of the temperature each time it rotates 6° so that measurements are taken at 300 points altogether when the device is put through one cycle, then, one can get relatively good solutions to this measurement problem. In order to guarantee the measurement accuracy of $T_{\frac{1}{4}}^*$, the thermocouples which are to be used to measure $T_{\frac{1}{4}}^*$ are designed on the basis of the best design methods for thermocouples used to measure total temperature. After having gone through static state testing as well as standard wind tunnel testing and hot wind tunnel testing, these thermocouples have the finest accuracy in measurement.

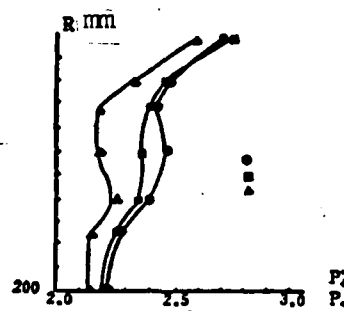


Figure 7. A Chart of the Distribution of $P_{\frac{1}{4}}^*/P_0$ in Cross Sections of the Exhaust of Turbines.

For measuring the total pressure, $P_{\frac{1}{4}}^*$, aft of the turbines, a seven-point comb-type pressure measurements needles are used evenly distributed circumferentially on three guide sleeves. In order to reduce blockage as well as pressure pulsation and other related phenomena, the total pressure measurement needles are installed at a point 40mm downstream from the exhaust of the turbine. If one is thinking about the influence of the gap between the blade tips, one can artificially divide the cross section of the exhaust into two rings. There are six measurement points positioned on the inner ring when using a

numerical integration method. On the outer ring, there is one measurement point intended for measuring the total pressure of the air flow which passes between the blade tips. Experimentation demonstrates that the blade tips have relatively high total pressures (see Figure 7). When one is measuring the average total pressure in the exhaust of a turbine, one should install appropriate measurement points in order to aid in the analysis of this type of phenomenon. Concerning the measurement of the quantity, T_4^* , due to the influence of cooled air which is still present, it is not necessary to take special precautions, as it is in the case of such quantities as P_4^* .

IV. THE RECOVERY COEFFICIENT OF TOTAL PRESSURE IN JET NOZZLES AND AFTERBURNER TEMPERATURES

The exhausts of jet nozzles have special characteristics such as high speeds, high temperatures and uneven flow fields. Due to its critical position, these exhausts are extremely sensitive to blockages. For example, a blockage ratio which reaches 2% is capable of causing an increase in the temperature, T_4^* , of about 20°C. Because of this fact, measurements in such areas use water-cooled, single point thermocouples which are capable of moving horizontally. Also six-point, water-cooled, sheathed total pressure measurement needles are used. Measurements of the boundary parameters of jet nozzles are made with boundary thermocouples and boundary total pressure measurement needles. In order to increase the response of the thermocouples, use is made of time-constant, adjustable, analog computers which carry out inertial compensations. The thermocouples of this type pass through a cooling passageway in which, periodically, there is cooling air sprayed out at the contact points which do the measuring. This sets up a temperature gradient or "step", so to speak, and this helps to make accurate measurements.

V. THE CHARACTERISTICS OF THE OPERATIONAL SPEED OF THE ENGINE WHICH IS USED IN THE COMPUTATIONS INVOLVED IN CONDUCTING THESE EXPERIMENTS

In order to maintain the dimensions of the engine as nearly invariable as possible, the experiments about which we have been talking were carried out under the condition that the rotational speed of the engine was $n = n_{\text{design}}$. During the testing, the atmospheric temperature changes from 37°C to 1.4°C, that is to say that there was a corresponding change in the rotational speed of the engine as it was used in calculations of $\bar{n}_{\text{cor}} = 0.96 \sim 1.023$. Within this range, data recordings for the design location of the jet nozzle were made 40 different times. Moreover, regression was taken into account.

The various parameters for the engines which were used in these experiments follow the same principles as those which govern the changes in the speed of rotation which is used in the calculations.

Concerning the aerodynamic parameters for the characteristic cross sections of the various design configurations of the engine used in the experiments, the principal parameters of the engine being tested at various points along the course of the air flow as well as the loss coefficients for the various components all obey the principles which govern the changes in the rotational speed of the engine as it is used in the calculations. These variations are as shown in Figures 8 - 13.

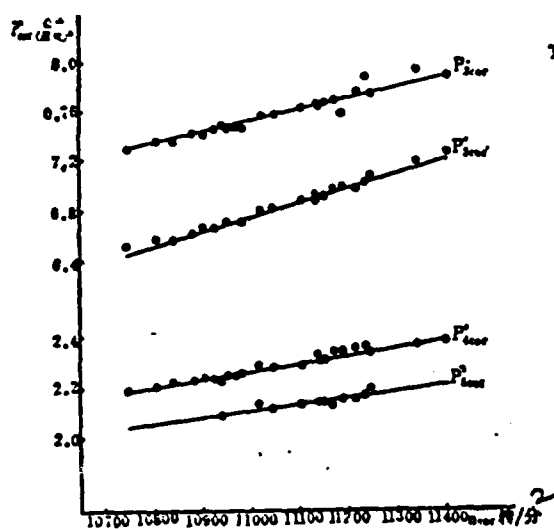


Figure 8. The Relationship between n_{cor} and the Design Configurations $\frac{P_{design}^1, P_{design}^2, P_{design}^3, P_{design}^4}{P_{design}^1}$ 2. rev/sec.

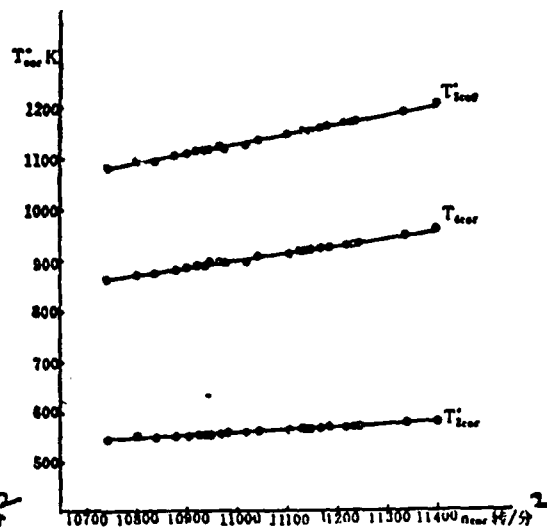


Figure 9. The Relationship Between n_{cor} and the Design Configurations $\frac{T_{design}^1, T_{design}^2, T_{design}^3, T_{design}^4}{T_{design}^1}$ 2. rev/sec.

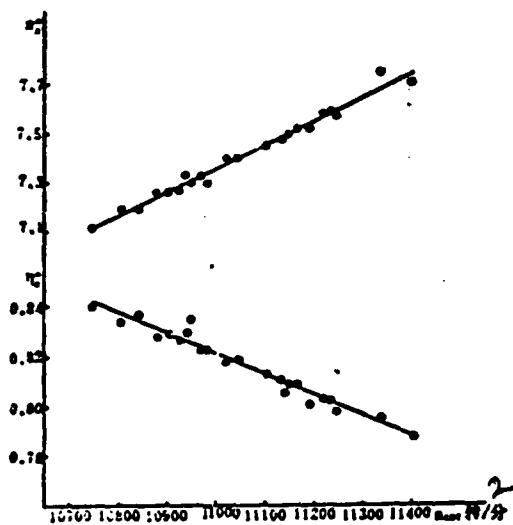


Figure 10. The Relationship Between n_{cor} and the Design Configurations π^1, π^2 2. rev/sec.

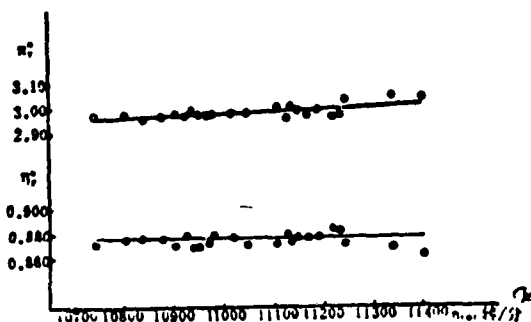


Figure 11. The Relationship Between n_{cor} and the Design Configurations η^1, η^2 2. rev/sec.

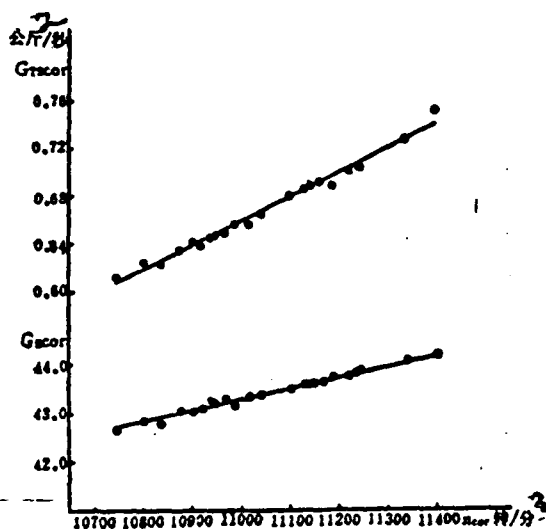


Figure 12. The Relationship Between n_{cor} and the Design

Configurations G_{cor} , G_{max}
2. kg/sec, 3. rev/sec.

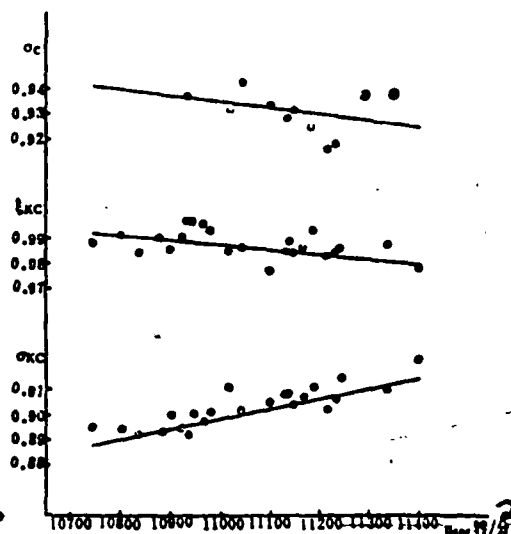


Figure 13. The Relationship Between n_{cor} and the Design

Configurations σ_{kc} , ϵ_{kc} , σ_c
2. rev/sec.

From Figures 8-13 it can be seen that:

(A) the principles which govern the changes in the parameters of the overall course of the flow as well as the aerodynamic or gasdynamic parameters for the various characteristic cross sections of the engine being tested are all consistent with a theoretical analysis of the same cross sections.

(B) The efficiency η_c of the compressors tested varied with increases and decreases in n_{cor} . When \bar{n}_{cor} increases from 0.96 to 1.023, then, η_c decreases from 0.847 to 0.789, that is to say, a drop of 6%.

(C) The exhaust gas temperature, T_4^* , and the temperature of the combustion gases in front of the turbine, T_3^* , follows the increases and decreases in the rotational speed which is used in the calculations. When \bar{n}_{cor} increases from 0.96 to

1.023, then, T_4^* falls from 930.7°K to 914°K , that is to say that there is a decrease of close to 17 degrees C.

(D) Within the range of these experiments, that is to say, within the range of $\bar{\pi}_{cor} = 0.96 \sim 1.023$, with the exception of the efficiency of the compressors, the loss coefficients for the various other components are basically maintained invariable or do not change to any great degree.

σ_{λ} basically does not change

η_T^* basically does not change

ξ_{λ} changes not more than 0.4%

σ_c changes not more than 1.7%

σ_{λ} changes not more than 2.5%

(E) The results of these experiments show that the pressure drop ratio of the turbines involved, π_T^* , remains basically unchanged within a relatively wide range of changes in the rotational speeds which are used in the calculations.

VI. THE THROTTLE CHARACTERISTICS OF THE ENGINES INVOLVED IN THESE EXPERIMENTS

Under conditions close to standard atmospheric temperature ($t_0 = 15.08 - 15.81^\circ\text{C}$), repeated tests were made of the throttle characteristics of the engines which were involved in the experiments. Careful measurements were taken and determinations were made of the principles by which the various types of parameter values of the engines involved vary with changes in the physical rotation speed. Careful determinations were also made concerning the air release systems and the influence which changes in the throttle cross section (that is, the area of the exhaust of the jet nozzle) have on the values of the various parameters mentioned before. The results of the experiments are as shown in Figures 14 - 19.

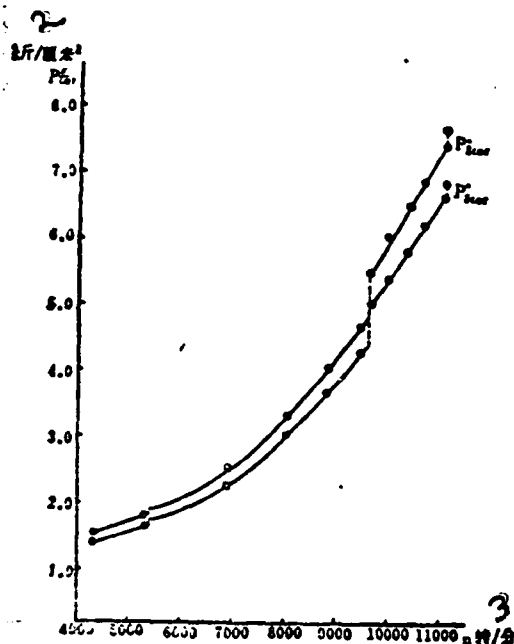


Figure 14. The relationship between n and P_{1scr}, P_{2scr} .
2. kg/cm^2 , 3. rev/sec.

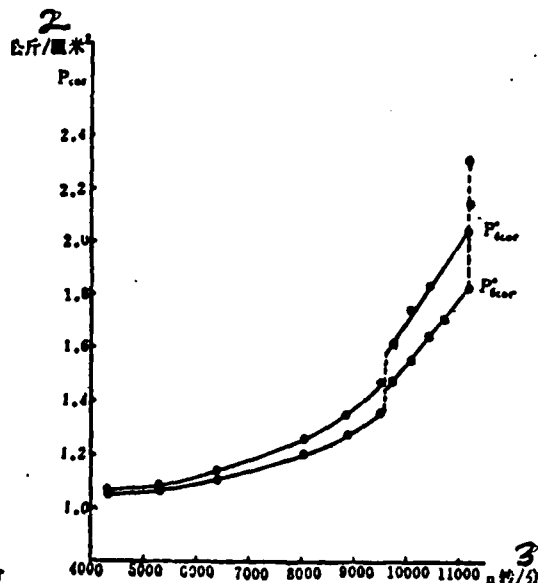


Figure 15. The relationship between n and P_{1scr}, P_{2scr} .
2. kg/cm^2 , 3. rev/sec

From Figures 14 - 19, we can see that:

(A) The principles by which the values of the various types of parameters in the engines involved vary with changes in the physical rotation speed are all consistent with a theoretical analysis of the same type of situation.

(B) In response to a decrease in the speed of rotation, the efficiency of the compressors involved first increases until it reaches the boundary of the area in which the efficiency is at its greatest ($\eta_c = 0.837$). In the interval of rotation speeds between $n = 9600 - 11000$ rev/sec, the efficiency of the compressors involved first rises and then falls. For $n = 8000$ rev/sec, the efficiency keeps right on dropping very fast.

(C) Under conditions in which $n = 10000$ rev/sec or less, the amount of air flow in the intake of the engine closely follows the increases in the speed of rotation and increases

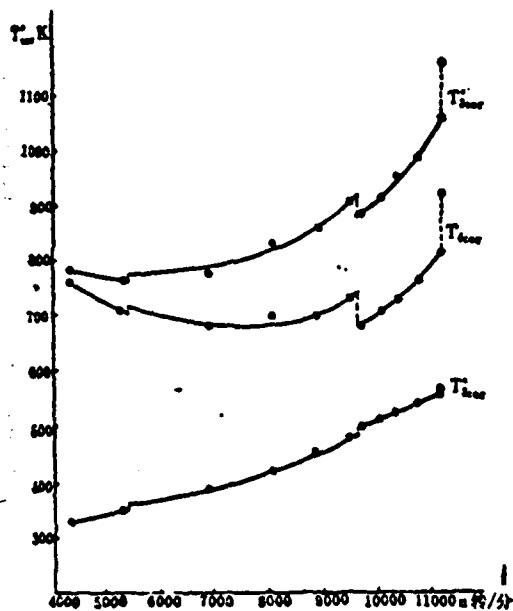


Figure 16 The relationship
between n and $T_{K_{top}}$, $T_{K_{middle}}$, $T_{K_{bottom}}$
1. rev/sec

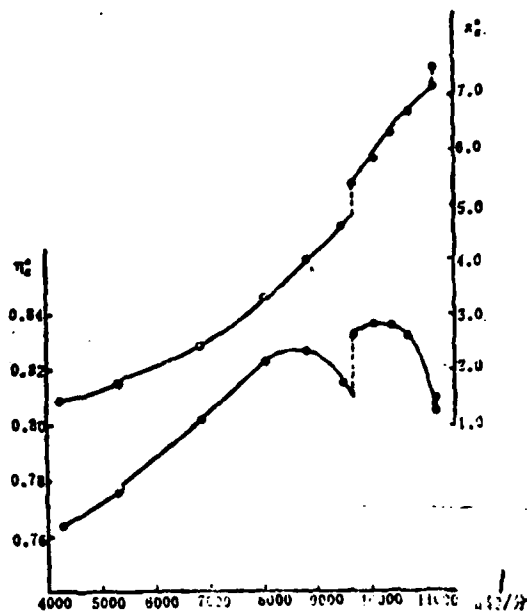


Figure 17. The relationship
between n and $\pi\%$, $\eta\%$
1. rev/sec

its own value in direct proportion to those increases. After one gets into the range in which $n > 10000$ rev/sec, the increase in the amount of flow slows down. This is due to the fact that the speed of axial flow in the intake increases, and the slowing down in the increase in the number $q(\lambda)$ is a result. The opening of the path along which the gases escape causes the flow rate in the intake to experience a slight increase.

(D) After one reaches the condition in which $n > 10000$ rev/sec, the parameters σ_{in} , σ_{ex} , ξ_{in} , and σ_e basically maintain their values unchanged.

VII. CONCLUSIONS

1. The methods of measurement which were employed during these experiments as well as the system used to handle the amounts of flow involved are all capable of satisfying the accuracy requirements which are involved in research into the values of the aerodynamic or gasdynamic parameters of turbine jet engines during the whole course of the air flow through these engines.

2. The flow fields, aerodynamic or gasdynamic parameters, and the principal process parameters which were measured during these experiments for the various characteristic cross sections of the design configurations of the engines being tested were all accurate and reliable.

3. Providing for engine flow parameters being measured both when at designed rotational speed and when air temperature is from 1.4 to 37°C and for changing the rules of the main process parameters and performance parameters will furnish reliable data by advancing analytical research a step further.

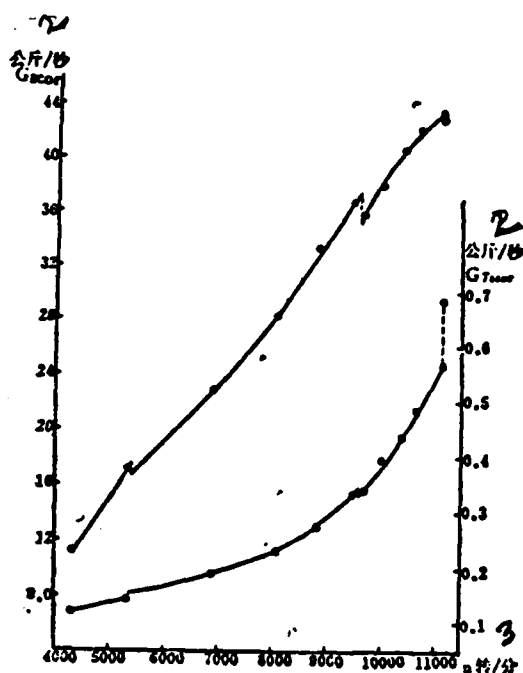


Figure 18. The relationship between n and G_{mec} , G_{mec}
2. kg/sec, 3. rev/sec.

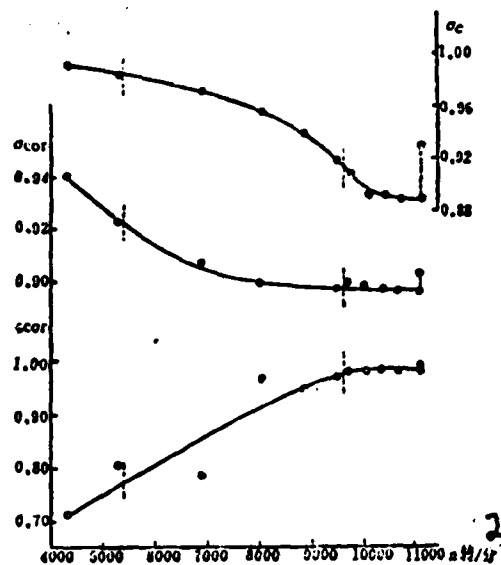


Figure 19. The relationship between n and σ_e , σ_m , E_m
2. rev/sec.

Note. The team chiefs for this project were Dong Qui-ting and Zhao Jue-liang. This article was written by Dong Qit-ting and Liu Si-hong. The plan for the experimentation was contributed by Lin Qi-xun, Liu Si-hong, Wu Xin-yuan and Fu Wei-de. The principal parts of the engine were taken care of by Dong Qiu-ting, Qu Xin-yuan, Hu Zi-long, Cong Meng-zi, Tang Ti-yi and Li Wen-lan. Temperature measurements were taken care of by Liu Si-hong and Zhao Jue-liang. Dynamic temperature measurements were taken care of by Wang Zong-yuan and Liu Ci-gong. Measurements of pressure were taken care of by Lin Qi-xun and You Zhao-kun. Experimentation was handled by Cong Meng-ci, Zheng Li-zhi, Miao Yong-rui, Dong Ze-ping, An Ju-cai, Ma Dong-ming, Du Ge, Zhang Qi-hua, Yang Hui-qin, and Li Feng-lan. Displacement structures and control lines were taken care of by An Ju-cai and Ma Dong-ming.

REFERENCES

- [1] Kerrebrock, J. L., Mikolajczak, A. A. Intrastator Transport of Rotor Wakelets and Its Effect on Compressor Performance. Trans. ASME Series A. Journal of Engineering for Power, October 1970.
- [2] Moffat, Robert J., Gas Temperature Measurement, Temperature, Its Measurement and Control in Science and Industry, Vol. 3, Part 2, 1962.
- [3] Glawe, G.E., Simmons, F.S., Stichnev, T. M., Radiation and Several Chromel-Alumel Thermocouple Probe in High-Temperature High-Velocity Gas Stream, NACA TN 3766, October 1956.
- [4] Temperature measurement, Northwestern University of Technology (1973).
- [5] Pressure flow rate and measuring amount of flow, Northwestern University of Technology (1973).
- [6] Zhang Suzhen, Liu Zhaoren, Zhu Hong. Pressure and temperature measurement techniques for engine as a whole and its components. Unpublished.
- [7] Li Chunfang, Engine temperature measurement, unpublished.
- [8] Wormser, A. F., Pfuntner, R. A., Pulse Technique Extends Range of Chromel-Alumel to 7000°F, SAE Paper 5245, 1962.
- [9] Dynamic thermocouple method for measuring high temperature air flow temperature. Qirghua [Tsinghua] University Engineering Mechanics Thermophysics Lab., 1973.
- [10] Yanagizawa Taxeshi. Together attaining total optical wall, design of active filter. Industrial Journal, 1973.
- [11] Zhang Shuhan, translator and editor, Theory of measurement error. Chinese Industrial Publishing House, 1966.

Summary

The Measurement and Analysis of Station Parameters of a Turbojet Engine

*Dong Qiuting, Zhao Jueliang, Liu Sihong, Wu Xinyuan,
Hu Zilong, Cong Mengzi, Lin Qixun, Wang Zongyuan,
You Shaokun and Zheng Lizhi*

This paper presents the experimental schedule, the results and analysis of parameter measurements of a typical turbojet engine. Firstly, the parameters of flow fields at the characteristic stations of the engine under design operating conditions are measured, and then by using the data so obtained, the gasdynamic parameters of the characteristic station, main process parameters, component loss coefficients, and performance of the engine are calculated. Furthermore the reliability and accuracy of the computed results are analyzed.

Secondly, the parameters of the characteristic stations of the engine at design operating speed are observed and recorded, with the relative corrected speed \bar{n}_{cor} varying from 0.96 to 1.023 as a result of changes in ambient temperature. The corresponding parameters and coefficients of each characteristic station of the engine are plotted as functions of relative corrected speed \bar{n}_{cor} .

Thirdly, the parameters of the engine under various throttle conditions are observed and recorded for different speeds, different nozzle areas, and with or without compressor bleeding. From these data, altitude-speed performance of the engine is calculated and compared with that of approximate estimation. These results appear to be satisfactory.

Besides, this paper discusses the rational selection of probe locations to take due consideration of the peculiarities of flow field and discusses the selection of the proper method of data processing for obtaining accurate average station parameters of the engine. In the measurement of engine airflow, the effects of boundary layers of outer and inner wall at the engine inlet and the effect of the distortion of static pressure field owing to the existence of nose and streamlined struts of the engine have been considered. After verification of the flow pattern of compressor exit, whose total pressure

and total temperature are to be measured, not only the total pressure and total temperature distributions of one blade channel are measured in accordance with the theory of wake, but also supplementary measurements and corrections are made for the circumferential non-uniformity of the flow field of the compressor exit. The blockage errors of total pressure and total temperature rakes are also investigated experimentally. In order to improve the accuracy of measurement of turbine efficiency and to make requirements of accuracy of temperature measurement less stringent, turbine inlet temperature T_3^* is not measured directly, but calculated by using measured turbine outlet temperature T_4^* . For making the T_4^* measurement, a rotating supporting mechanism and an optimum design procedure of total temperature thermocouple are used. In measuring the recovery coefficient of the nozzle and augmented temperature of the engine, the authors utilize a thermocouple probe with lag compensation and a movable supporting mechanism. Boundary parameters of engine jet stream at the nozzle exit are measured with boundary thermocouples and boundary total pressure probes.

AN EXPERIMENTAL INVESTIGATION OF THE ROTATING STALL, SURGE AND WAKE BEHIND THE ROTOR FOR A SINGLE STAGE AXIAL COMPRESSOR

Zhang Weide, Zhang Changsheng, Liu Zhiwei and Liu Jiafeng*

ABSTRACT

From experimental investigations with dynamic testing methods on the rotating stall, surge and wake behind the rotor of a single stage axial compressor, the relationship between the rotating stall and the total turbulence behind the rotor caused by the wake is obtained. The wave form of the wake behind the rotor shows marked changes when rotating stall approaches. The wake-induced degree of total turbulence increases sharply and, therefore, may be used as a way to predict rotating stall. The total process of rotating stall and surge as well as the difference between the two and their connection have also been compared.

I. FOREWORD

The rotating stall and surge of axial compressors is an important problem. The problem of stall and surge is more serious for compressors and fans with high pressure ratio and large flow rate. In order to enlarge the stable working range of the compressor, many measures have been taken, such as air release, rotating stabilizer blades, double and even triple rotators, etc. These measures usually bring about a great deal of structural complexity or the downgrading of the performance of the whole generator. This indicates that the mechanism of stall and surge has not yet been understood.

Since the phenomena of rotating stall and surge involve unsteady flow and viscous flow [1-7], the physical phenomena are so very complex that theoretical studies cannot satisfactorily resolve the

* Other comrades who participated in this experimental work are Zhang Shuzhen, Lin Qixuen, Wang Zhongyuan, Liu Si (illegible), Hu Bigang, Fan Feida, Shi Jingxuen and Huang Jiangong.

problems of instability encountered in real compressors, such as: the relationship between rotating stall and the wake behind the rotor, the developmental process from stall to surge, the prediction and monitor of stall and surge, the mechanism to enlarge the stability range of a compressor, etc. The solution to these problems relies on more in-depth experimental studies of the development of the wake behind the rotor, stall and surge and of the inter-relationship and differentiation between them.

In practical work, there is an urgent need to solve the problem of predicting and monitoring the rotating stall and surge of a compressor. This has resulted in the experimental investigation on the wake behind rotor as reported in this paper.

The purposes of our investigation are:

1. To study the development of the wake behind a rotor and its relationship to rotating stall and to find a possible way to predict stall.
2. To study the characteristics of rotating stall and surge and their relationship as well as differentiation.
3. To compare several means of measuring wake, rotating stall and surge.

II. EXPERIMENT SET UP AND MEASURING DEVICES

1. Experimental station for single stage axial flow compressor

(Referring to Figure 1). A 250 Kw DC motor with rotational speed specification of 1250 rev/min and acceleration ratio 12.15 provides the power. The torsional work gauge is mechanical (using optical methods for observation). The test sample is a K-70 single stage axial flow compressor. The exhaust section has a hole plate

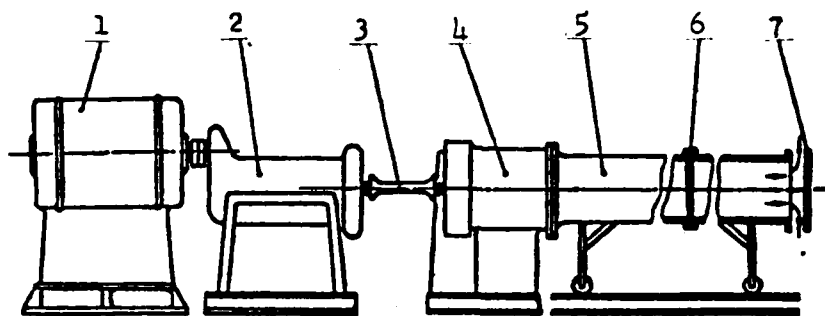


Figure 1. Experimental set-up of a single stage axial flow compressor.

1--DC motor; 2--accelerator; 3--torsional gauge 4--experimental compressor; 5--exhaust section; 6--flow hole plate; 7--regulating valve

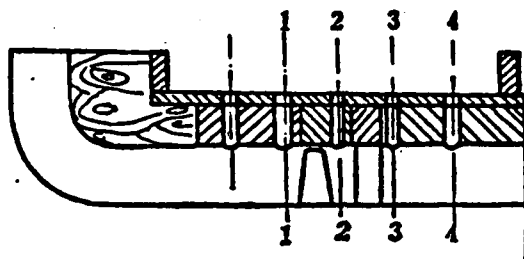


Figure 2. Arrangement of measuring cross-section

for measuring flow rate and the adjustment valve to regulate flow rate. There are five measuring cross-sections in the experimental section--namely, two before the work wheel, one behind the work wheel and two behind the stabilizer (Figure 2). At each cross-section, the static pressures of the internal and external wall at three points can be measured. There are also two stands set at a definite angle from each other. They are used to install coordinate frames to measure flow parameters. The major geometrical dimensions and characteristic parameters for the experimental sample are:

| | | | |
|-------------------------|--------|--|----------------|
| inlet external diameter | 298 mm | average total pressure ratio π^* | 1.25 |
| hub-tip ratio | 0.61 | average absolute thermal efficiency η^* | 0.9 |
| number of moving blades | 30 | design rotational speed n^* | 15,000 rev/min |
| | | air flow rate G | 5.6 kg/sec |

2. Measuring apparatus

a) Hot wire wind anemometer, one each of DISA 55A01 and 55D01 (55M01).

Affected part--two hot filaments or films installed in the 2-2 cross section behind the rotor with an angle of 45° and at a distance of $0.2 \sim 0.4b$ from the tail edge of the blade.

When measuring the rotating stall, because the propagation speed of the stall is relatively low, the requirement for the response frequency of the affected part, under the single stage situation, is not high, about $100 \sim 200$ hertz (it varies with the rotational speed). As the wake frequency is dozens of times higher than the stall frequency, we must carry out square wave experiments to ascertain the frequency response of the affected part. After adjustment, the frequency response of the 5μ hot element or the 55R type hot film both reach 5000 hertz or above satisfying the basic requirement.

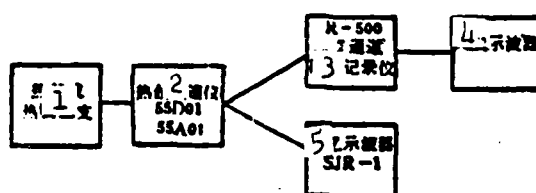


Figure 3. Block diagram of heating filament measurement
1--2 hot wires or films; 2--hot wire anemometer 55D01, 55A01;
3--R-500 7 track magnetic tape recorder; 4--8 trace oscilloscope;
5--memory oscilloscope SJR-1

b) GGKY-1 type solid piezoresistance transducer

Its range of measured pressure is $0 \sim 1 \text{ kg/mm}^2$ with maximum output 40-70 mV. The maximum diameter of the silicon film is 8 mm. Because

of its relatively large size, the frequency response is somewhat weak. It can satisfy the requirement when measuring the rotating stall but cannot be used for measuring the wake.

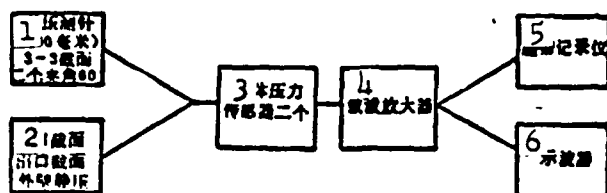


Figure 4. Block diagram of solid pressure transducer measurement.

1--total pressure detection pointer 400mm Two 3-3 cross-section;
2--inlet cross-section outlet cross-section external wall static pressure;
3--solid piezoresistance transducer; 4--carrier wave amplifier;
5--magnetic tape recorder; 6--oscilloscope

c) B&K4135 type microphone condenser

A microphone condenser may be affected by pressure pulse signals. Since the total pressure in the wake region is less than that of the principal flow region and the pressure pulsates with time, it can be used to receive wake pressure signals. The sensitivity is 0.2 mV/ μ bar, frequency response is 100 Hz \sim 100,000 Hz, maximum range 174 (equivalent to a pulse pressure of 0.1 bar). The microphone condenser is suitable for both wake and stall measurement but its size is still too large (6 mm).

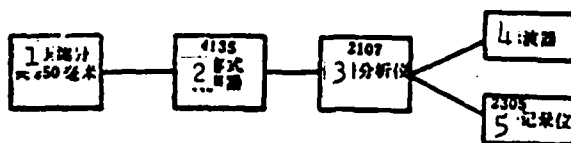


Figure 5. Block diagram of capacitive microphone measurement.

1--total pressure detection pointer 250 mm length; 2--4135 microphone condenser; 3--2107 frequency spectrum analyzer; 4--oscilloscope; 5--2305 electric recorder

d) Dynamic temperature measurement

Temperature is measured with relatively thin (0.15 mm) thermocouples with inertia compensation to increase its frequency response. Before compensation, a pre-amplifier (SF-72 data amplifier) amplifies the volt size signals by 100 times. Then an inertial circuit is used to compensate for its inertia. Noise is filtered with a low pass filter in the circuit, but because the cut-off frequency is too low, the response is not very good.

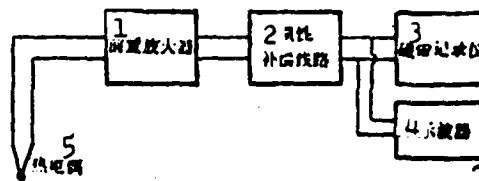


Figure 6. Block diagram of temperature measurement

1--preamplifier; 2--inertia compensation circuit; 3--magnetic tape recorder; 4--oscilloscope; 5--thermal couple

e) R500C magnetic tape recorder and SJR-1 memory oscilloscope

Five channel parameters (2 heating filament channels, two pressure channels and one temperature channel) are recorded during the stall experiment. In the wake experiment, because of the high wake frequency, the wake wave forms are actually photographed on an SJR-1 memory oscilloscope.

III. ANALYSIS OF EXPERIMENTAL RESULTS OF ROTATING STALL AND SURGE

The experimental investigation of rotating stall and surge was carried out at the rotational speeds of $n=5000$, 6500 and 8000 rev/min. Characteristic curves were obtained in all three cases, and the parameters for the starting points of stall and wave as well as the wave forms of the speed, pressure and temperature pulses were recorded. Measurement of the stall region was taken along the blade



Figure 7. Experimental apparatus

height. Detailed measurement of the processes from stability into stall and from stall into surge was also carried out. Experiment was also done on the processes of retreating from stall and surge.

1. The complete process from steady flow to stall,

At some constant rotational speed, the regulating valve was gradually closed off in steps to reduce the flow rate. For a long period in the beginning, there was no pulsing of the hot filament signal, the solid piezoresistance signal and the temperature signal, indicating that the compressor was working under stable conditions. When the valve position was at 69 (69 was a mark representing the degree to which the valve was closed, 0 for fully open, 76 for fully closed), sudden stall occurred. (At this point, the discharge coefficient C_{1a}/μ_{peak} was about 0.3).

The first and second channels are hot films, the third and fourth channels are pressure transducers and the fifth channel is temperature.



Figure 8. Process from stability to stall at rotational speed 8000 rev/min From top to bottom: the first and second channels are heating films, the third and fourth channels are pressure transducers and the fifth channel is temperature.

From Figure 8 (the time sequence of Figure 8-Figure 14 are all from right to left) it can be seen that:

(a) Once stall occurs, regular pulsating waves appear in speed pressure and temperature, and marked phase differences in the two film channels and the two pressure channels, indicating the formation of stall cells. The pressure is lower and temperature higher in stall cell regions. (Temperature curve and pressure curve has 180° phase difference).

(b) From the pressure signal, it can be seen that the average pressure drops markedly when stall occurs.

(c) From the photograph, it may be observed that the heating film (or filament) that receives the speed signals is the most sensitive. The solid piezoresistance transducer shows the stall wave form about 1.2 ms later than the heating film (may be due to the longer indicator of the total pressure, about 400 mm). Because the cut-off frequency of the low pass filter in the inertia compensation circuit is too low, the response for the temperature signal is insufficient and the temperature signal is later than the solid piezoresistance by about 35 msec.

d) One can see from the wave forms for speed and pressure, the peak is relatively flat, indicating that the region with large pressure and high speeds is large, while the valley is much sharper, indicating a relatively smaller region of low speed. This shows that at the onset of rotating stall, the region occupied by the stall cells is smaller than the normal region.

e) From actual observations at the experimental site, when going into stall from stability, the noise of the machine suddenly increases while a low humming sound appears. The total pressure p_s^* of the after stage drops abruptly, but the cotton balls at the inlet remain sucked to the dust screen without showing any to-and-fro motion, indicating the absence of a back flow phenomenon. According to measurement, the noise decibel value increased from 115 dB to 123 dB (when rotating stall occurred).

2. The developmental process of rotating stall

When the regulating valve continued to be closed beyond position 69, i.e., the valve position changed from 69+70+72+74, the discharge rate was reduced further and the corresponding discharge coefficient decreased from 0.3 to 0.2. It can be seen from Figures 9 and 10 that the high pressure region or high speed region (wave peak) changes from broad to narrow, indicating the diminishing of the normal region, and that the low pressure region or low speed region (wave valley) changes from narrow to broad, indicating the growth of the stall region. When the valve was closed to position 74 (approaching surge, with shrieking noise), the speed and pressure wave forms became irregular and the stall region became very broad.

3. The process of going into surge

Surge was entered when the regulating valve was further closed to position 75 (the discharge coefficient $C_a/u_{peak} = 0.15$ at this

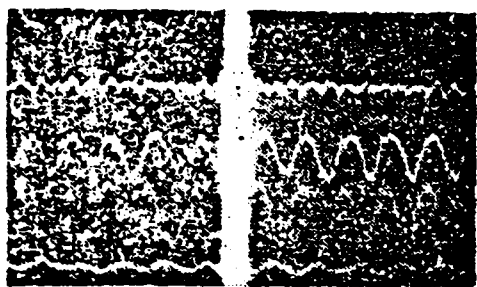


Figure 9. Rotating speed at 5000 rev/min. The figure on the right has valve position 70 with broad high pressure region; the figure on the left has valve position 72 with narrowing high pressure region and broadening stall region.

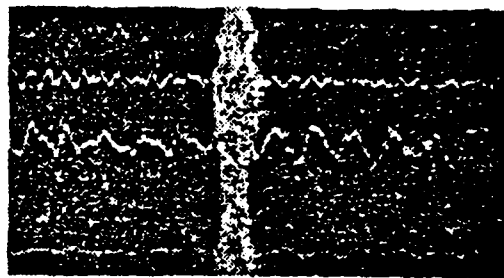


Figure 10. Rotating speed at 5000 rev/min. Valve position is at 74 for figure at left with the low pressure region (stall region) already very broad. Valve position for figure on right is at 72.

point) when the total pressure p_3^* at the outlet dropped suddenly. The water column reading pulsed (no such phenomenon at rotating stall) and the cotton balls at the inlet dust screen moved back and forth with sizable amplitude (indicating back flow phenomenon). There was also abrupt change in the noises.

From Figures 9, 10 and 11, it can be seen that: The transition from stall to surge is a gradual process. On entering surge, the wave forms are chaotic. No distinction can be made between the main flow region and the stall cell region. Apparently, surge is formed through the gradual growth of stall cells.

From Figure 12, it may be observed that during surge there are large low frequency pulsations in both pressure and temperature with frequency about 7 Hz. The phases of temperature and pressure are opposite.

Summarizing the above, during surge the total air flow enters unstable flow with a back flow phenomenon. There is an additional abrupt pressure drop relative to the stall pressure and there is very

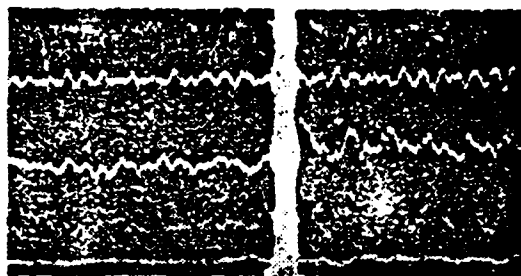


Figure 11. Rotational speed at 5000 rev/min. Valve position at 74 for right figure. Valve position 75 for left figure.

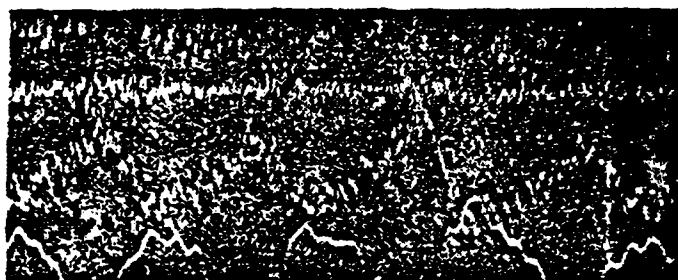


Figure 12. Wave form at surge for rotational speed 8150 rev/min.

low frequency pressure and temperature pulsation (which can be observed even in water column readings).

4. Process of receding from stall

Different situations from that of entering into stall arise when receding from stall.

(a) The receding from stall is gradual (Figure 13).

(b) There is often a non-steady stall process when receding from stall, i.e., we have the phenomenon of the splitting apart or combining together of stall cells. Two kinds of wave forms appear, one with small amplitude and high frequency (reflecting a situation

of high average pressure and many cells) and another with large amplitude and low frequency (reflecting a situation of low average pressure and diminishing number of cells) (Figure 14)

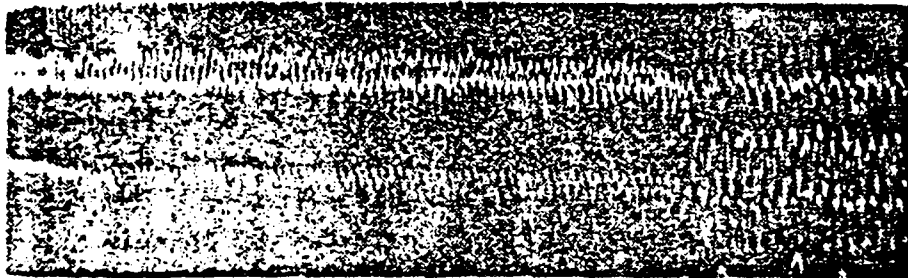


Figure 13. Process of receding from stall at speed 8150 rev/min.

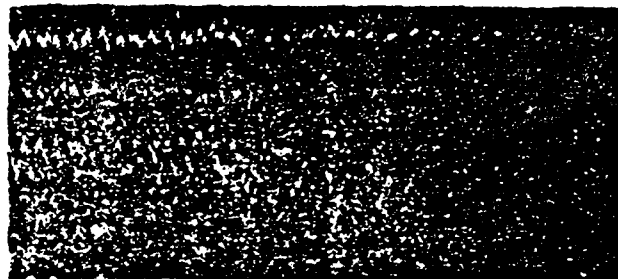


Figure 14. Phenomenon of instability during receding from stall at rotational speed 6500 rev/min.

(c) There is an obvious sluggishness when receding from stall. Onset of stall occurs at valve position 69 with discharge coefficient around 0.3, while receding from stall occurs with obvious sluggishness at valve position 67.5 with the discharge rate at about 0.4.

IV. RELATIONSHIP BETWEEN THE WAKE BEHIND THE ROTOR AND ROTATIONAL STALL

Macroscopically speaking, when the flow rate is gradually reduced so that stall is being approached, there does not seem to be any unusual change in the pressure and temperature. But in reality,

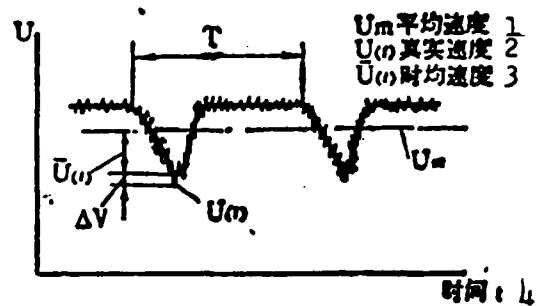
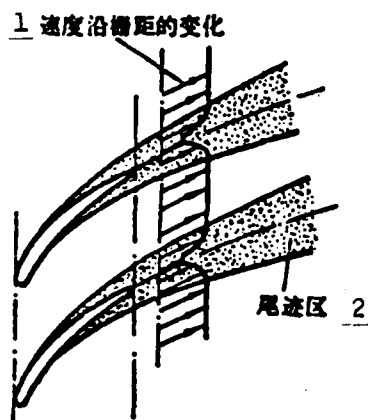


Figure 15. Velocity wake behind the rotor
1--variation of velocity along the grid distance; 2--wake region

Figure 16. Velocity wake signal detected by the hot wire
1--average velocity; 2--true velocity; 3--time average velocity; 4--time

because the angle of attack is increased, the wake region behind the rotor blades will increase, and when the wake region enlarges sharply so that serious separation results, rotational stall will then occur. Hence, measuring the wake region behind the rotor may enable us to predict the occurrence of stall.

It can be seen from Figure 15 that the air current forms the wake region at the tail edge of the blades after passing through the grid of the work wheel blades. Thus, the flow field behind the grid is divided into two regions: The wake region and the principal region. In the wake region the pressure is basically the same as that in the principal region; however, both the total pressure and the velocity are lower. Hence, the velocity field and the total pressure field are non-uniform behind the work wheel and they rotate with the wheel. Besides, the true velocity and true pressure of the air current in both the principal and the wake regions pulsate with time, i.e., with a degree of turbulence. The fixed heating filament detector behind the work wheel will be affected by two kinds of signals (Figure 16), one of which is formed at the filament by the alternating action of the different time averaged velocities in the principal

and the wake regions, and the other of which is a random signal due to the irregular pulsation of the deviation of the actual velocity from its time average. The filament is affected by the total turbulence.

In time interval T let the overall average velocity of the air current be U_m , the true velocity of the air current be $U(t)$ and the time average of the true velocity be $\bar{U}(t)$. The difference between the true velocity and its time average is $U(t) - \bar{U}(t) = \Delta v$ (Figure 17). Then the total degree of turbulence is

$$W_{\Sigma} = \frac{\sqrt{\frac{1}{T} \int_0^T [U(t) - U_m]^2 dt}}{U_m},$$

The regular degree of turbulence due to the variation of the time averaged velocity $\bar{U}(t)$ is

$$\bar{W}_{\Sigma} = \frac{\sqrt{\frac{1}{T} \int_0^T [\bar{U}(t) - U_m]^2 dt}}{U_m},$$

The irregular random degree of turbulence is

$$\hat{W}_{\Sigma} = \frac{\sqrt{\frac{1}{T} \int_0^T [U(t) - \bar{U}(t)]^2 dt}}{U_m}.$$

Therefore, $W_{\Sigma}^2 = \bar{W}_{\Sigma}^2 + \hat{W}_{\Sigma}^2$.

Strictly speaking, if the irregular velocity pulsation of the air flow is an unstable random signal, then it should be replaced by a global average. The degree of the total velocity turbulence may be determined by the average square root volt meter in the hot filament wind anemometer [9].

$$\text{Degree of velocity turbulence } W_{\Sigma} = 100 V_{RMS} \sqrt{\frac{4V}{V_0^2 - V_0^2}} \%,$$

where V_{RMS} -- average square root turbulence

V -- output potential of the hot filament wind speedometer (volt)

V_0 -- output potential of the hot filament wind speedometer at 0 wind velocity (volt)

The degree of regular turbulence \hat{W}_r is entirely due to the fact that the time-averaged velocity of the wake region is lower than that of the principal region. The degree of random turbulence \hat{W}_s is due to the fluctuation of the true velocity about its time average. According to the data of the stabilizer blade grid, [7], the degree of turbulence in the principal region behind the grid is very small, while the degree of turbulence of the wake region is nearly 10 times higher. Thus, it can be argued that \hat{W}_s is also basically formed by the wake region. The degree of total turbulence W_{um} behind the rotor is basically formed by the wake region and W_{um} is a sign for the strength and width of the wake region.

The total pressure of the wake region behind the rotor is less than that of the principal region. Hence, the variation of the pressure wake may be measured by connecting a total pressure-detecting needle to the microphone condenser. The average square root of the total pressure pulse $\sqrt{\Delta p'^2}$ may be computed with the following equation:

$$\sqrt{\Delta p'^2} = \sqrt{\Delta p_0'^2} \cdot e^{\frac{db}{20}},$$

where db—measured decibel value

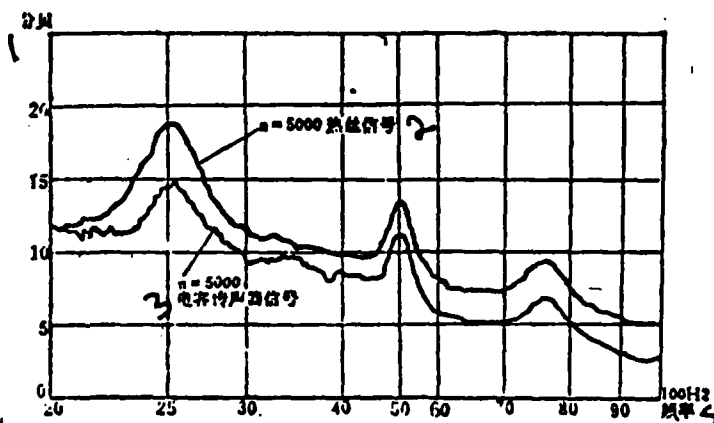


Figure 17. Result of the spectral analysis of the velocity wake and pressure wake signals behind the rotor
1--decibel; 2--hot wire signal; 3--microphone condenser signal;
4--frequency

$\sqrt{\Delta p_s}$ — average square root value of the standard pressure pulse at 0 decibel. It is 2×10^{-10} bar for the present transducer.

The hot wire signal and the microphone condenser signal were fed into a 2107 spectral analyzer and a 2305 electric recorder for spectrum analysis (see Figure 17). The decibel value had a marked peak at the rotational frequency of the blades which indicated that this was a wake signal. The spectra on either side of the blade rotational frequency indicated the random pulses of the air flow. There were also relatively high peaks at the first and second harmonics of the rotating frequency.

1. Wave forms at various discharge rates ..

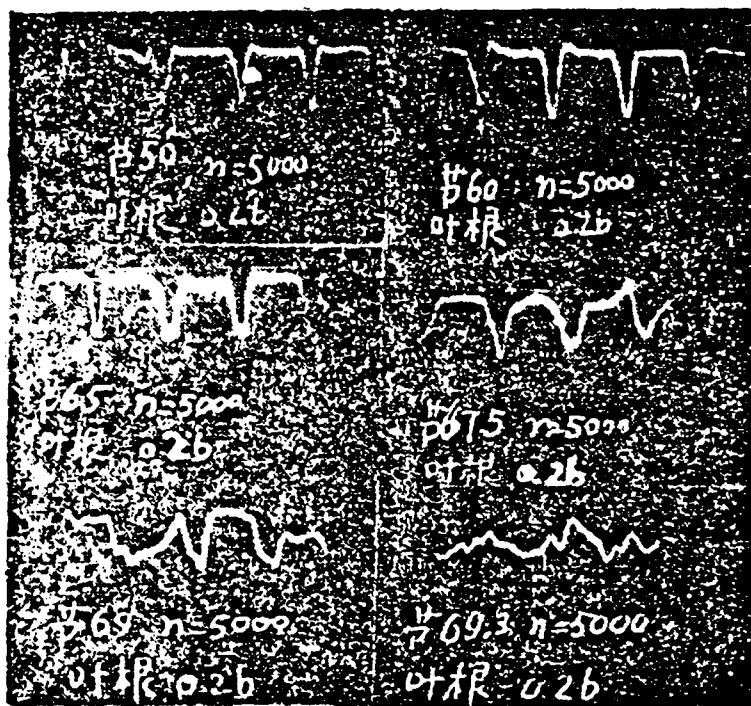


Figure 18. Wave forms of the wake behind the rotor at different regulating valve positions.

Figure 18 shows the changes in the wave form of the wake behind the rotor just before stall. The regulating valve position was gradually changed from 50 to 69 (discharge rate decreased from 0.6 to around 0.3). At larger values of the flow rate (valve position 50 to 60), the wake region was narrower and the principal region was wider with better wave forms. When the flow rate was reduced to a certain level (valve position 67.5), the wake region enlarged and the principal region diminished. There were manifest changes in the wave form of the wake. Just before stall (valve position 69), the change in the wake wave form was marked, and there were obviously sudden pressure changes in the wake region (serious separation). The principal region has by now vanished. Hence, from the wake wave form the approach to stall point can be determined.

2. Changes in the total pressure pulse and the degree of total turbulence behind the rotor due to the wake at various regulating valve positions

It can be seen from Figure 19 that within the normal working range (valve position 50~65) the degree of total turbulence due to the wake behind the rotor basically remains unchanged. Thus the size and amplitude of the wake region do not vary very much. When the flow rate is gradually reduced, so that rotational stall is approached, the degree of total turbulence begins a sharp rise. At the stall point, it may be a dozen or more times higher than the normal value.

Figure 20 shows the variation of the degree of total pressure pulse turbulence at various valve positions. Within the normal working range (valve position 50~65), the degree of total pressure pulse turbulence remains basically unchanged. When the flow rate is gradually reduced, the degree of total pressure turbulence begins to increase. When stall is approached, it rises sharply.

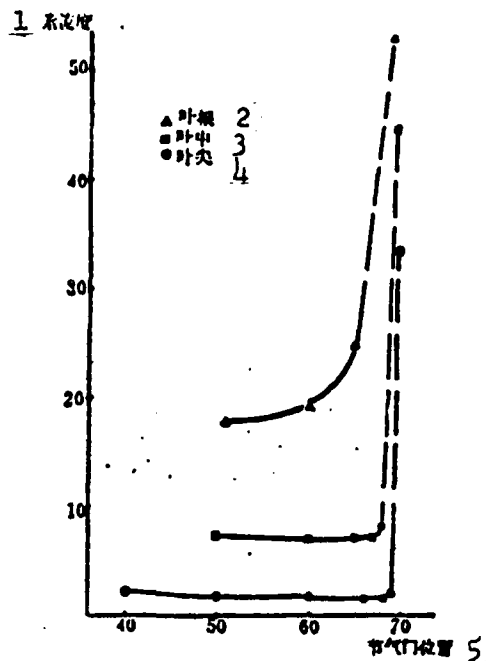


Figure 19. Degree of turbulence behind the rotor due to the wake at various valve positions.
 1--degree of turbulence; 2--root of blade; 3--middle of blade; 4--tip of blade; 5--valve position

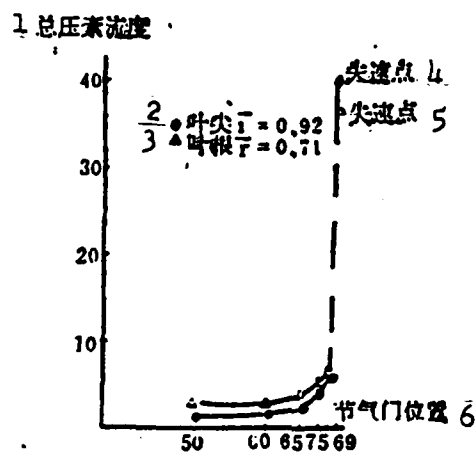


Figure 20. Variation of degree of total pressure turbulence behind the rotor with valve positions
 1--degree of total pressure turbulence; 2--tip of blade; 3--root of blade; 4--stall point; 5--stall point; 6--valve position

3. Degree of turbulence curve represented by the discharge coefficient $\overline{C}_{1a}(C_{1a}/u)$ peak

In order to relate to the compressor velocity triangle, we have calculated the flow rate and discharge coefficient at various valve positions and found how the degree of turbulence varies with the discharge rate.

As shown in Figure 21, when the discharge rate \overline{C}_{1a} changes from 0.6~0.4, the degree of turbulence W_{um} remains basically unchanged. When \overline{C}_{1a} becomes smaller than 0.4, W_{um} begins to rise sharply. Stall is reached when \overline{C}_{1a} is reduced to 0.3. It follows that we can tell that rotating stall is imminent when the degree of turbulence begins to rise sharply. This has pointed a way to predict rotating stall and surge.

Analysis indicates that the angle of attack is about $\pm 5^\circ$ when \overline{C}_{1a} is about 0.6~0.4, and that when \overline{C}_{1a} decreases, the size of the wake region increases somewhat, while the amplitude decreases (since the time averaged velocity drops). The degree of total turbulence will increase when the wake region is enlarged, but it will decrease when the time average velocity is decreased. Hence, the change in the degree of total turbulence is not large, the curve being flat. When the discharge coefficient \overline{C}_{1a} is reduced to less than 0.4, the angle of attack becomes larger than a constant value. Serious separation occurs and the wake region enlarges rapidly. The degree of irregular random turbulence increases sharply. Thus, the degree of total turbulence also increases sharply. When rotating stall is reached, the normal flow motion is destroyed with the formation of stall cells. Therefore, the degree of turbulence is increased by more than a dozen-fold.

V. SUMMARY OF CONCLUSIONS

1. Before rotational stall occurs in a single stage axial flow compressor, the wake region behind the rotor grows rapidly, the wake

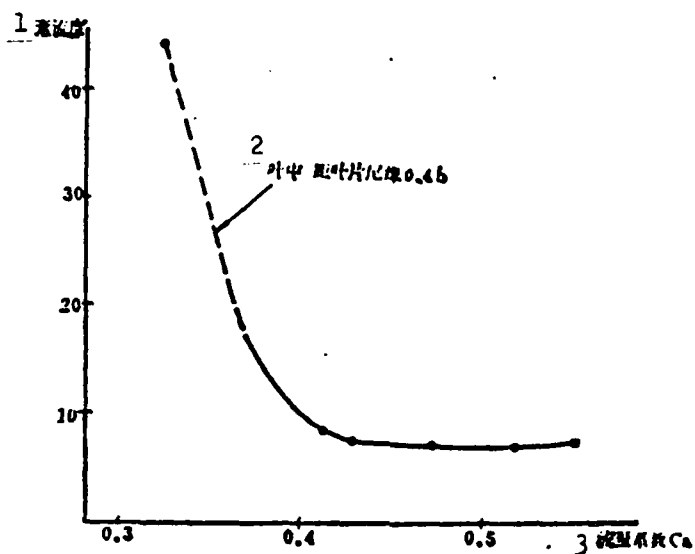


Figure 21. Variation of degree of total turbulence with discharge coefficient C_{1a}

1--degree of turbulence; 2--middle of blade from tail edge of blade; 3--discharge coefficient

wave form changes markedly and the degrees of total velocity and pressure turbulence due to the wake increase sharply. Within the normal work range, the degree of turbulence is relatively small. Its rate of change with the discharge coefficient approaches zero. When rotational stall is approached, the degree of total turbulence rises sharply, and its rate of change with the discharge coefficient also increases to some value. Hence, the wave form of the wake behind the rotor and the variational pattern of the degree of total turbulence may be used as a base to predict rotational stall.

2. Before the occurrence of rotational stall, the macroscopic values of the pressure, temperature and velocity do not show any clear changes, but the changes in the wake wave form and in the degrees of velocity and total pressure turbulence due to the wake are more pronounced. Therefore, the wave form of the wake behind the rotor and the degree of turbulence may be used as a major factor to measure the internal flow process of a compressor. As [6] pointed out, because of the effect of the wake behind the rotor, when stall

approaches, the angle of attack of the air current at the stationary blades will have greater changes. Hence, the wake behind the rotor should be further studied.

3. The experimental specimen developed abrupt rotational stall over the whole blade, while its receding from stall was gradual, with marked delay. There is a development from quantitative change to qualitative change in the process of changing from rotational stall to surge. The gradual enlargement of the stall cell region leads to surge. There is a close correlation between surge and stall. As soon as surge appears, periodic stall cells disappear, and there is a marked back flow phenomenon in the air flow. The pulse frequency of the air flow is very low (a few cycles per second) and the whole air flow is in an unstable state. Judging from the structure of the air flow, surge and rotational stall are completely different.

4. The hot wire, microphone condenser, solid piezoelectric transducer, thermocouple with dynamic compensation can all be used to measure rotational stall and surge. The hot wire and the microphone condenser must be used to measure the wake behind the rotor.

REFERENCES

- [1] Huppert, M. C., Preliminary Investigation of Flow Fluction During Surge and Blade Row Stall in Axial-Flow Compressors, NACA RHE25E28, 1952.
- [2] Grabam, R. W., and Prian, V. D., Rotating Stall Investigtition of 0.72 Hab-Tip Ratio Single-Stage Compressor, NACA RME53L17a, 1954.
- [3] Fabri, J. and Suruge, J., Unstable Operation and Rotating Stall in Axial-Flow Compressors, Preceedings of the Second International JSME Symposiam Fluid Machinery and Fluidics, Vol. 2 Fluid-Machinery-II.
- [4] Alan, H. Stenning, Anthony, R. Kriebel and Stephen, R. Montgomery, Stall propagation in Axial-Flow Compressor, NACA TN 3580, 1956.
- [5] Takata, H., and Nagano, S., Nonlinear Analysis of Rotating stall, ASME Gas Turbine and FluidsEngineering Conference and Products Show, Vol. 1, 1972.
- [6] Evans, R. L., Turbulence and Unsteadiness Measurements Downstream of a Moving Blade Row, Trans. ASME, Series A, Vol. 97, Jan. 1975, p. 131.
- [7] Kiock, R., Turbulence Downstream of Stationary and Rotating Cascade, ASME Gas Turbine Conference and Products Show, 1973
- [8] Miao Yongmiao, Jiang Peizheng, Investigation of the Rotational Separation of Axial Flow Compressor Air Flow.

Summary

An Experimental Investigation of The Rotating Stall, Surge, and Wake behind the Rotor for a Single Stage Axial Compressor

Zhang Weide, Liu Zhiwei,

Zhang Changsheng and Liu Jiafeng

In order to meet the needs arising from actual practice, this paper studies mainly the problems of predicting rotating stall and of discriminating between the rotating stall and surge.

Experimental equipment used includes a single stage axial compressor; driven by a 250 kw D. C. motor. The design speed of the compressor is 15000 rpm.

By means of dynamic measurements, the wake of rotor, rotating stall and surge of a single stage axial compressor are investigated. The rotating stall is found to be related to the total turbulence caused by the wake behind the rotor. Experiments show that before rotating stall takes place, the wake range of rotor widens, the shape of wake changes markedly, and the total turbulence caused by the wake increases sharply. These measurements are made possible by the hot-wire anemometer. At the same time the total pressure pulse also sharply increases. Its measurement is made possible by the microphone condenser. Thus the above-mentioned wake-related phenomena may serve as clear signs that rotating stall is impending.

Experiments also show that, as a result of continuous expansion of the rotating stall cell, surge takes place. As soon as surge occurs, distinct reverse flow appears. The flow pulse frequency of surge is far less than that of rotating stall.

In order to take measurements on the rotating stall and surge, the hot-wire, microphone condenser, solid piezoresistance transducer, and thermocouple with dynamic compensation can be used. The sensitivity of hot-wire is excellent, therefore its use is to be preferred for measuring the wake.

EXPERIMENTAL INVESTIGATION OF A VAPORIZING
COMBUSTION WITH DOUBLE COMBUSTION SPACES

Tang Ming, Zhu Huiling, Du Qinfang

EXPERIMENTAL INVESTIGATION OF A VAPORIZING COMBUSTION WITH DOUBLE COMBUSTION SPACES

ABSTRACT

This paper is the research report on a new type of oil film, vaporizing combustor with double combustion spaces. The combustor is to be used in a high temperature, hot wind tunnel to provide a steady uniform hot gas stream.

The special design features of the pre-vaporizing installation in the head section and the combustion chamber are introduced first in this paper. The flow model of the head section of this combustor with double combustion spaces is obtained through a water visualization technique. During the experimental process, the burning is good with short flames; the flame stays a pale blue even when the combustor is working under oil-rich conditions with an excess air coefficient of 2.8. The combustion efficiency varies little with changes in the fuel-air ratio. A large quantity of work has been done to make the blow-out characteristics of the inner and outer spaces the same. An effective method to control the double space stability is finally found. Studies have also been carried out on the position of the igniter and the manner of torch ejection, and good ignition characteristics are obtained. The highest working temperature of the combustor is close to 1100°C . When the outlet temperature is 950°C , the temperature variation over the entire outlet cross-section is no more than $\pm 45^{\circ}\text{C}$, and the temperature field coefficient is not larger than 0.07.

Our paper provided a practical combustor design for the above mentioned purposes. At the same time, the experience gained in the experiment is also helpful for the development of similar combustion systems of a gas turbine.

I. DESIGN FEATURES OF THE COMBUSTOR

This vaporizing combustor with double combustion spaces is designed for the heating process of a hot wind tunnel. According to

the requirements of the hot wind tunnel, the combustor should satisfy the following conditions:

1. Combustor outlet temperature should be 400-1100°C; the highest temperature rise of the gas in the combustor should be 800-900°C.

2. The requirements for uniformity and stability of the outlet temperature field are: When the burning fuel temperature reaches 1000°C, the largest temperature variation should not exceed $\pm 50^\circ\text{C}$ and the temperature pulsation should not exceed $\pm 25^\circ\text{C}$.

3. Ignition of the combustor should be safe and reliable and the flame should not extend beyond the combustion chamber. This requires that the combustor possess such characteristics as the uniform distribution of the fuel concentration, steadiness of burning, shortness of the flame, etc. To achieve this, we have designed the oil film vaporizing single tube combustor with double combustion spaces, as shown in Figure 1.

The combustion chamber is composed of the outer shell, the flame tube, the pre-vaporizing head section and the igniter. The outer shell of the combustor, the tube body of the flame tube and the igniter are all adapted from available combustor parts with only minor changes to facilitate manufacturing. Our main mission is to design the pre-vaporizing head section, to arrange the fuel inlet and to carry out necessary adjustments through experimentation.

A roll of the principal combustion orifices and a roll of mixing orifices are opened along the flame tube wall. The air that enters into the inner combustion space through the central inlet cone is counted in the inlet air volume through the principal combustion orifices. Five air film cooling slots, three of which have a corrugated strip structure, are provided to cool the firing tube wall.

The pre-vaporizing head section consists of the fuel ejection ring and the vaporizing tube. There are two inter-connecting concentric rings in the fuel ejection ring, installed respectively on the edge of the two vaporizing wall inlets of the vaporizing tube. The fuel oil is ejected into the prevaporized air stream through the small holes on the two fuel rings and enters the vaporizing tube space with the air stream to form an oil film along its internal and external walls. On the hot wall, the film continues to evaporate to form the combustion fuel--air-fuel mixture. The pre-vaporized air-fuel mixture is ejected in a reverse direction through the ring orifices of the inner and outer outlets of the vaporizing tube into the first combustion space.

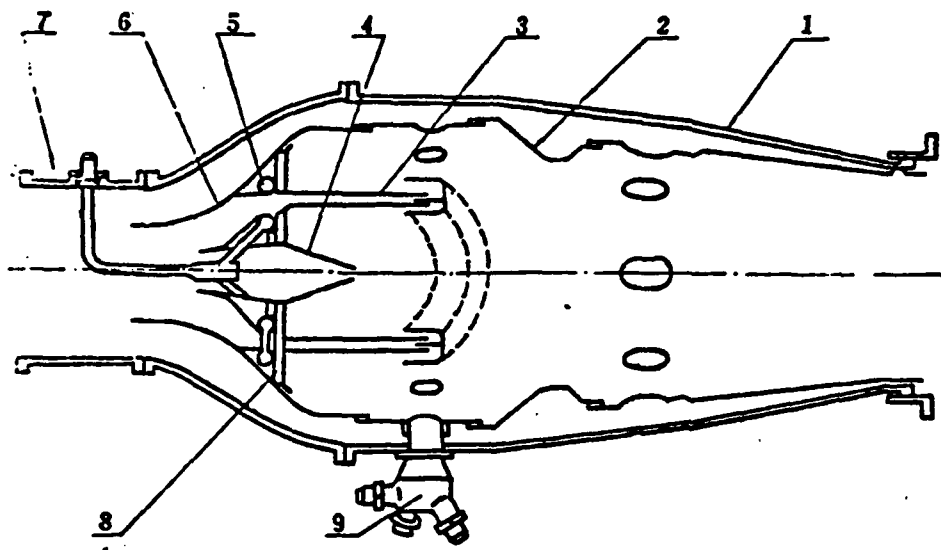


Figure 1. Oil film vaporizing single tube combustor with double combustion spaces.

- | | | |
|----------------------------|------------------------|-------------------------|
| 1. combustor outer housing | 2. flame tube | 3. vaporizing ring tube |
| 4. central air inlet cone | 5. fuel injection ring | 6. air inlet cap |
| 7. inlet section | 8. installation plate | 9. igniter |

The major characteristic dimensions of the vaporizing annular tube consist of the outlet area, the area ratio of the inner and

outer outlet annular orifice, the length of the vaporizing wall and the height of the vaporizing chamber, etc. The size of the outlet area is determined by the principle that the excess-air coefficient of the pre-vaporized mixture should be maintained at a value close to 1. The ratios of the areas of the inner and outer outlets and the ratio of the cross-sectional areas of the inner and outer combustion spaces are basically kept the same, so that the space of the head section may be optimally utilized. The length of the vaporizing wall (the distance from the inlet of the vaporizing annular tube to the outlet cross-section) is designed based on the empirical data of the evaporation rate of the fuel oil on unit area of the vaporizing wall [2] so that the oil film will be vaporized completely. The number II vaporizing annular tube is shorter by 10 mm than the number I tube in order to maintain a good match between the ejected flow from principal combustion orifice and the first combusting space.

As for the determination of the number of ejection orifices, the number should be large if we consider the uniformity of the temperature angle, but consideration must also be given to the phenomenon that during fuel supply at low pressure, the upper orifices and the lower orifices of the fuel ring inject fuel at markedly different rates owing to the effect of gravity. Hence, we experimented on the fuel injection ring and came up with the current, satisfactory design.

The combustor design parameters are as follows:

| dimensions, overall | Name | Unit | No. I | No. II |
|---------------------|-----------------------------|-----------------|--------------|--------|
| | combustor inlet area | cm ² | 149.6 | 149.6 |
| | maximum combustor area | cm ² | 697.6 | 697.6 |
| | maximum area of flame tube | cm ² | 483.6 | 483.6 |
| | incoming air cap inlet area | cm ² | B44.2; C26.4 | C'22.8 |
| | degree of inlet opening (1) | | B0.30; C0.18 | C'0.16 |

| | | | | |
|---|--|--------------------|-----------------------|----------------------|
| dimensions of vaporizing annular tube | length of vaporizing plate | mm | 120 | 110 |
| | height of vaporizing ring space | mm | 14 | 12 |
| | outlet annular gap area A_1 | cm ² | 58.8 | 54.1 |
| | outer space area/inner space area (2) | | 2.63 | 2.68 |
| area of air orifices | principal combustion orifices area A_2 | cm ² | 49.6 | 49.6 |
| | mixing orifice area A_3 | cm ² | 48.0 | 48.0 |
| | air film orifice area A_c | cm ² | 36.8 | 36.8 |
| | total area of open orifice A_2 | cm ² | 175.6 | 170.9 |
| | A_1/A_2 | | 33.3% | 31.7% |
| dimensions of fuel injection ring | diameter x wall thickness of fuel injection tube | mm | $\phi 10 \times 0.5$ | $\phi 10 \times 0.5$ |
| | diameter of fuel injection tube | mm | 0.4 | 0.4 |
| | number of fuel injection orifices | ↑ | 46 | 46 |
| | distance between fuel injection orifices | mm | 外 17; 内 20 | 外 17; 内 20 |
| air and fuel parameters | flow rate of air G_a | kg/sec | 1.1 | |
| | inlet total pressure P_A^* | kg/cm ² | 1.3 | |
| | inlet temperature t_2^* | °C | 200 | |
| | average flow velocity at maximum | M/sec | 17 | |
| | fuel flow rate cross section | kg/sec | 26.2×10^{-3} | |
| | total combustor excess-air coefficient α | | 2.8 | |

NOTE (1) Air inlet cap area/combustor inlet area

NOTE (2) Ratio of inner and outer combustion space area of the flame tube at the outlet cross-section of the vaporizing annular tube.

III. EXPERIMENTAL SET UP

The air in this experiment is supplied by a centrifugal pressurizer (pressure 2 kg/cm^2 , flow rate 2 kg/sec) and enters the experimental section after preheating in the fuel-mixture direct pre-heater. The fuel is domestic aeronautic kerosene from Daqing. It enters the evaporizing annular tube through the fuel injection ring after being pressurized by a gear pump. Figure 2 is the diagram of the experimental section.

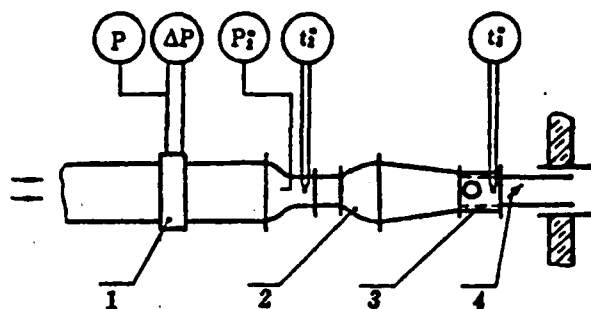


Figure 2. Diagram of the experimental section
1--double hole plate 2--experimental combustion chamber 3--outlet measurement section and observation port 4--butterfly valve

III. FLOW AND COMBUSTION SITUATIONS

1. Flow model of the flame tube

In order to understand the flow situation in the head section of the double combustion spaces, a water flow observation has been made (see Figure 3) with a simplified one tenth, fan-shaped transparent tester (the scale is 1:1 but there are not two streams of gas). Observations indicate that the pre-vaporized air stream, which enters the combustion region in the reverse direction from the vaporizing annular tube outlet, forms vortices in the inner and outer combustion spaces. The vortices are strong and regular but the inner space and outer space vortices are different. The outer space

vortex is strong with the center close to the upstream of the head

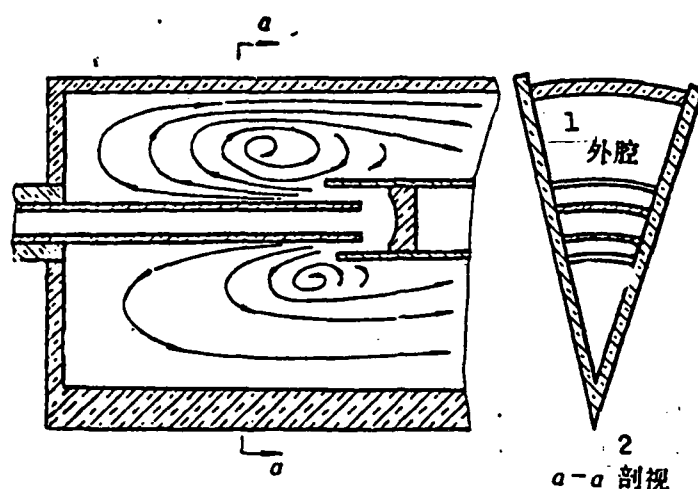


Figure 3. Water flow model of the head section
1--outer space; 2--inner space

section while the inner space vortex is weak with the center close to the edge of the injection outlet. Hence, the space in the outer chamber is fully utilized, but the inner chamber is not. Observations also show that the length of the outlet directional section of the vaporizing annular tube has a marked effect on the strength and size of the vortices. An increase in its length will strengthen the vortices and make them more stable. This is advantageous to both the combustion and the outlet temperature field.

2. The combustion situation

The flame color is a direct indicator of the vaporization situation of the fuel oil in the vaporizing chamber. As computed and measured in [2], the length of the oil film in the vaporizing chamber is strongly affected by the inlet air temperature. When the inlet temperature is $40\sim 80^{\circ}\text{C}$, no matter what steps are taken structurally, there are red flames flickering at the outlet of the vaporizing annular tube. This indicates that oil film still exists at the end of the vaporizing wall. This oil film irregularly enters the combustion region as oil droplets, forming a flickering red flame.

But when the inlet air temperature is raised to $150\sim 200^{\circ}\text{C}$, the fuel oil vaporizes completely in the vaporizing chamber, so that even in the fuel-rich state, the temperature in the combustion chamber reaches 840°C and the flame remains pale blue and confined to the interior of the combustion chamber.

Shortening the height of the vaporizing chamber leads to the increase of air flow velocity in the vaporizing chamber which is advantageous for the oil film to vaporize. Thus the vaporizing wall of No. II vaporizing tube is 10 mm shorter than that of No. I, yet the vaporization characteristics are improved.

IV. COMBUSTION CHARACTERISTICS

1. Ignition characteristics

The reliable air flow rate for ignition is 0.7 and 1.1 kg/sec, and the total excess air coefficient is $3.4\sim 7.0$.

Since the igniter is installed on the external wall of the outer chamber, decreasing the mixture ratio and air flow velocity of the outer chamber combustion region is more advantageous to ignition.

Raising the inlet temperature definitely aids ignition. When the inlet temperature $t_2^* = 40\sim 60^{\circ}\text{C}$, we find such phenomena as long ignition time, extension of flame beyond the combustion chamber, etc. When t_2^* is increased to $130\sim 150^{\circ}\text{C}$, the flame at ignition is confined in the combustion chamber. When the position of the igniter is shifted forward 17 mm and appropriate changes are made in the manner the flame is blown in (see Figure 4), experimental results show that the ignition characteristics are much improved.

It may be considered that the firing chamber of the original igniter is easily affected by the flow of the cool, combustible mixture. After the modification, the firing chamber is not affected

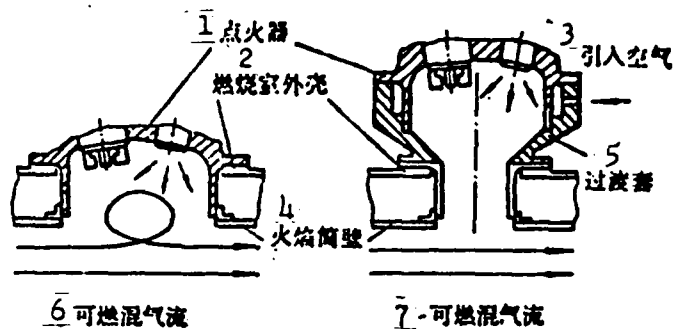


Figure 4. The igniter and the change in its position.

1--igniter; 2--outer shell of combustion chamber; 3--inlet air; 4--flame tube wall; 5--transition sheath; 6--flow of combustible mixture; 7--flow of combustible mixture

by the flow of the cool combustible mixture so that a strong enough torch is produced to ignite the gas mixture. Observations during the experiment indicate that when the igniter is started without supplying the principal fuel oil, the torch cannot be seen at the outlet of the original igniter while it definitely exists for the improved igniter.

2. Quenching limit for poor fuel mixture

At the onset of our experiment, the situation of a narrow quenching range for poor fuel mixture and that of mis-matched inner and outer chamber quenching characteristics with the inner chamber more easily quenched than the outer chamber, are encountered. Some structural changes have been made to improve the quenching characteristics in the testing process.

(1) The effect of the volume of pre-vaporized air

We used such methods as reducing the inlet area of the cap in the head section, reducing the annular gap area of the vaporizing annular tube outlet and enlarging the air-intake area of the mixing orifice, etc., to reduce the volume of pre-vaporized air.

AD-A115 866

FOREIGN TECHNOLOGY DIV WRIGHT-PATTERSON AFB OH
RECENT SELECTED PAPERS OF NORTHWESTERN POLYTECHNICAL UNIVERSITY--ETC(U)
AUG 81

F/6 20/4

UNCLASSIFIED

FTD-ID(RS)T-0260-81-PT-2

NL

5 OF 5
AD A
115 866



| | | | | | | | | | | | | | | |
|--|--|--|--|--|--|--|--|--|--|--|--|--|--|--|
| | | | | | | | | | | | | | | |
| | | | | | | | | | | | | | | |
| | | | | | | | | | | | | | | |

END

DATE

FORMED

07-82

DTIC

Experiments show that changing the area of the air-intake cap does not greatly affect the quenching limit for poor fuel mixtures and, in particular, will not alter the premature quenching of the inner chamber.

The effect of reducing the area of the mixing orifice or changing the gap of the vaporizing tube outlet is also not obvious on the stability of the inner chamber but is more pronounced on the outer chamber (see Figures 5 and 6).

Decreasing the height of the vaporizing chamber from 14 to 9 mm markedly increases the quenching range of the inner and outer chambers, and completely satisfies the requirement of the combustion chamber working range.

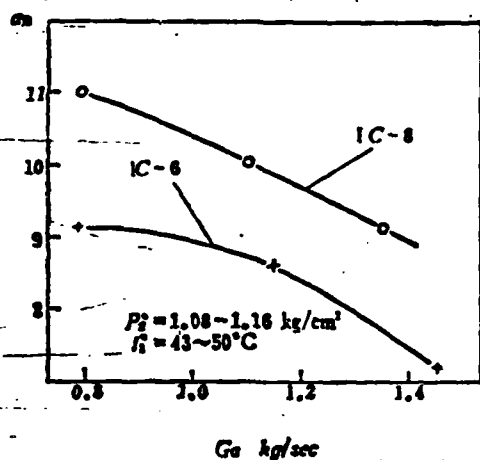


Figure 5. Effect of enlarging the mixing orifice on quenching characteristics. (note) the area of the mixing orifices of IC-8 is 21% larger than that of IC-6.

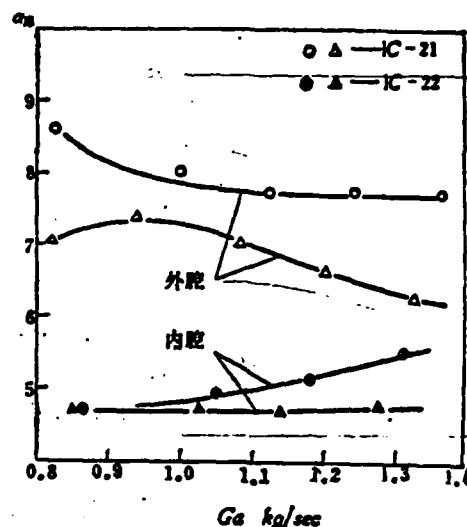


Figure 6. Effect of the outlet area of the vaporizing annular tube on the quenching characteristics. (note) the outlet area of IC-22 is smaller than that of IC-21 by 14%.

(2) The effect of the separation ring

Installation of a separation ring in the vaporizing annular tube (see Figure 7) brings marked changes to the stability of the

inner and outer chambers: The separation rings with smaller diameters will even give a better stability characteristics for the inner chamber than for the outer chamber, as shown in Figure 8.

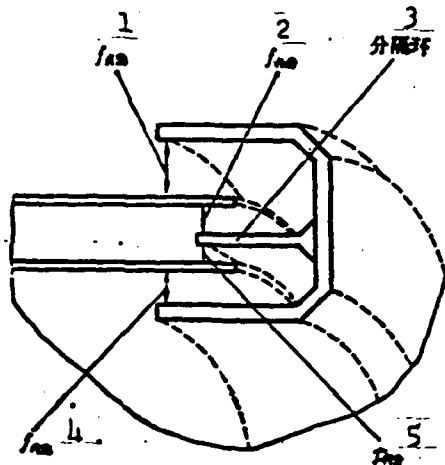


Figure 7. Diagram showing the position of the separation ring in the vaporizing annular tube.
1--outer outlet; 2--outer separation ring; 3--separation ring; 4--inner outlet; 5--inner separation ring

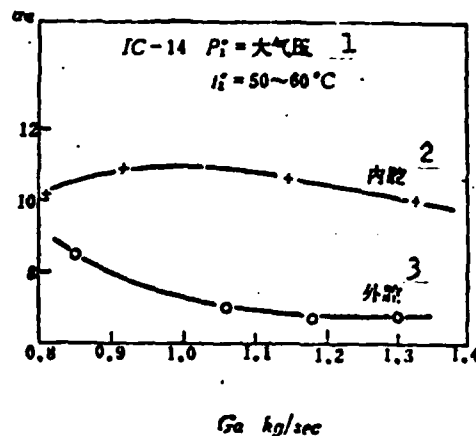


Figure 8. Effect of the separation ring on the stability characteristics
1--atmosphere; 2--inner chamber;
3--outer chamber

Several separation rings of different diameters have been tested in an effort to find one with appropriate dimensions to make the stability of the inner and outer chambers approach each other. The conditions for obtaining the optimal dimensions of the separation ring are provided by these experiments as shown in Figure 9. The optimal area ratio ($f_{\text{outer}}/f_{\text{inner}}$) for air flow rate 0.9 kg/sec is 2.3 and for air flow rate 1.2 kg/sec is 2.1. They are very close to the ratio of the inner and outer outlet areas $f_{\text{outer outlet}}/f_{\text{inner outlet}} = 2.3$.

The function of the separation ring may be explained from the following aspects:

(a) Since the separation ring has a definite thickness, the circulation area of the vaporizing annular tube is reduced which

then reduces the volume of pre-vaporized air. When the thickness of the separation ring is increased to 2.5 mm, the circulation area is reduced by 21%. Experiments indicate that the stabilities of both the inner and outer chambers are very improved.

(b) The inner and outer surfaces of the separation ring may form oil films which cause the fuel to mist poorly. Although this improves the stability when the inlet air temperature is low, it is accompanied by the phenomenon of two-phase combustion. However, when the inlet air temperature is raised to above $150\sim 200^{\circ}\text{C}$, this effect is drastically reduced.

(c) The separation ring changes the distribution of the flow rates in the inner and outer chambers of the vaporizing annular tube and, therefore, also changes the ejection speed of the pre-mixed gas. This is the main cause for the improvement of the stability of the inner chamber.

(3) The mutual interference of the inner and outer chambers

It is pointed out in [4] that mutual interference exists for composite injected flames. When they are too close to each other, the stability of the injected flame at the center will deteriorate. Hence, it is difficult to make the ^{flame}stabilities of the inner and outer chambers of this combustor the same.

3. Combustion Efficiency

The combustion efficiency hardly changes with the total excess-air coefficient of the combustion chamber, except when the state of quenching is approached. As shown in Figure 10, when the quenching range at a poor fuel mixture is widened, the combustion efficiency for the poor fuel mixture is increased. When the inlet air temperature is increased, there exists an optimal inlet temperature for a maximum combustion efficiency.

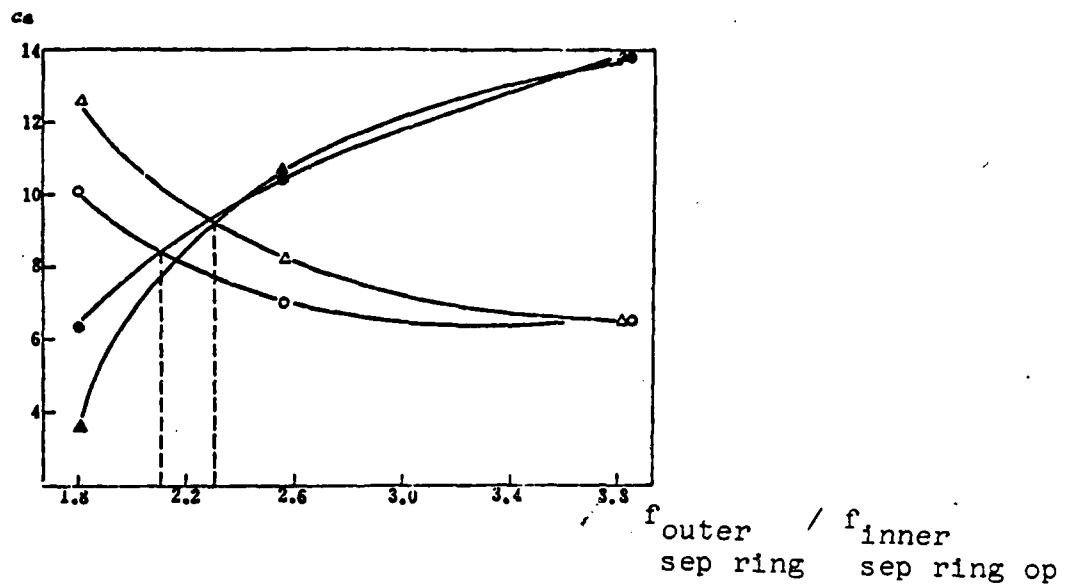


Figure 9. Graphic solution for the optimal dimensions of the separation ring.

● and ○ are respectively the inner and outer chamber quenching points at $G_a = 1.2$ kg/sec.

▲ and Δ are respectively the inner and outer chamber quenching points at $G_a = 0.9$ kg/sec.

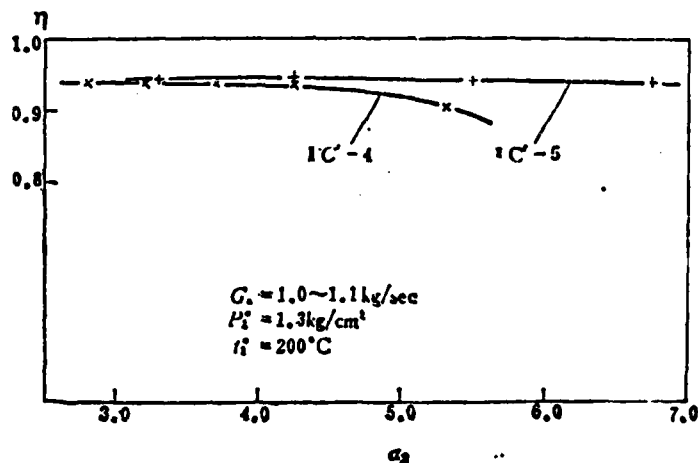


Figure 10. Variation of combustion efficiency characteristics

4. Outlet temperature field

As predicted, after tuning and adjustment, this combustor yields very good results in the uniformity of the outlet temperature field. The maximum temperature variation over the outlet cross-section decreases drastically. The largest non-uniformity coefficient $\delta_{TM}(\delta_{TM} = (t_{3max}^* - t_{3min}^*) / (t_{3m}^* - t_2^*))$ reaches 0.12~0.13 with the corresponding temperature field coefficient 0.06~0.07. The distribution of temperature is also reasonable. The effects of various factors on the temperature field are:

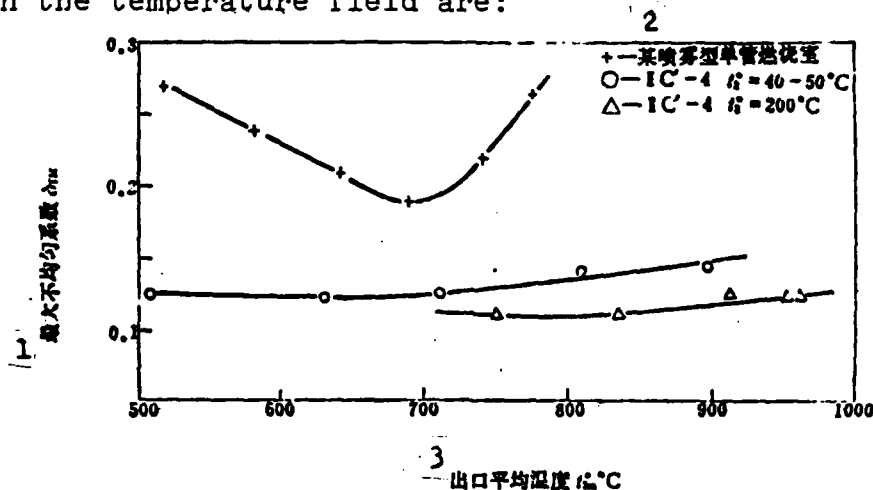


Figure 11. Maximum non-uniformity coefficient of outlet temperature
1--maximum non-uniformity coefficient δ_{TM} ; 2--+—A certain fuel spray single space combustor; 3--average outlet temperature t_{3m}^* °C

(1) Effect of inlet air temperature

When the inlet air temperature is increased from 50°C to 200°C, the outlet temperature field of the combustor is obviously improved as shown in Figure 11. Raising the temperature of the inlet air vis-à-vis combustion, mixing and wall-cooling all tend to make the temperature field more uniform. But when the separation ring is not installed in the vaporizing annular tube, raising the inlet air temperature does not visibly improve the uniformity of the temperature field.

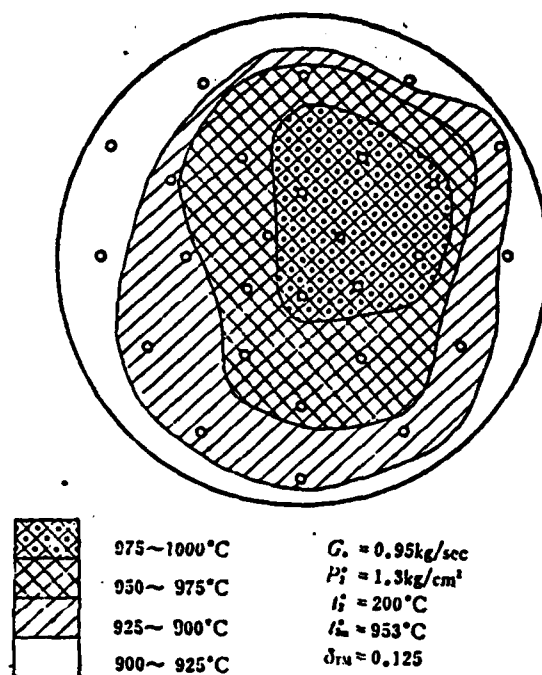


Figure 12. Outlet temperature field of the combustor

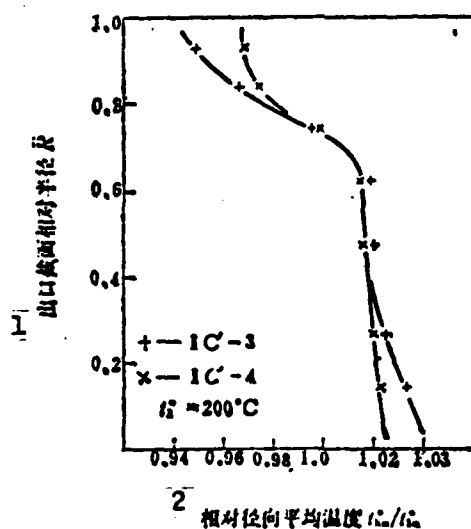


Figure 13. Effect of enlarging the mixing orifice on radial temperature distribution.

(NOTE: The mixing orifice of IC'-4 is increased by 17% over that of IC'-3.

1--relative radius \bar{R} of the outlet cross-section; 2--relative radial average temperature

(2) Effect of enlarging the mixing orifice

Enlarging the mixing orifice not only improves the temperature field not only when the inlet air temperature is increased, but also at normal temperatures.

Enlarging the mixing orifice (but keeping the number of orifices the same) has the direct effect of increasing the strength and depth of mixing. It tends to improve the mixing process. Also when the volume of mixed air is increased, the volume of pre-vaporized air correspondingly decreases and hence more fuel is burnt behind the vaporizing annular tube. This will improve the radial temperature distribution (see Figure 13).

(3) Effect of the diameter of the separation ring on the temperature field

Changing the diameter of the separation ring will change the fuel distribution of the inner and outer chamber, and hence the temperature distribution of the outlets. Experiment shows that separation rings with smaller diameters make the temperature distribution worse with generally a larger maximum temperature variation and an increased central temperature.

V. CONCLUSIONS

(1) When the inlet temperature of the combustor is $150^{\circ}\text{--}200^{\circ}\text{C}$, the outlet temperature is $400\text{--}1100^{\circ}\text{C}$. When the average outlet temperature is 950°C , the maximum temperature variation over the outlet cross-section does not exceed $\pm 45^{\circ}\text{C}$, and the temperature variation does not exceed $\pm 20^{\circ}\text{C}$. The improved ignition installation is effective in guaranteeing a safe start-up. Thus, a practical, usable design has been provided for a hot wind tunnel combustor.

(2) Experiment indicates that the fuel pre-vaporization characteristics of the oil film vaporizing combustor are good and that

the vaporizing annular tube, cooled by the oil film, does not over-heat. At the same time, the vortex flow in the head section of the double chamber combustor is strong and regular so that the volume of the combustor head section can be fully utilized. This is exactly what is required of a smokeless, short annular combustor.

(3) Experiment also shows that the single tube double chamber combustor has inner and outer chambers with large geometrical differences which result in obvious difference in flame stability. Installation of a separation ring in the vaporizing annular tube will sensitively change the stabilities of the inner and outer combustion chambers and make them approach each other.

(4) Experiment further indicates that changing the size of the separation ring will drastically change the radial distribution of the outlet temperature.

REFERENCES

[1] Moffat, R.J., A Stable High Temperature Thermometry Rig, S.A.E. Paper 158E, April 1960, p. 14.

[2] 辻正一, A Study on A Vaporizing Combustor for Gas Turbines, NASA TTF-13272.

[3] Lefebvre, A.H., Combustion in Advanced Gas Turbine System, Cranfield International Symposium Series, Volume I, Pergamon Press, 1968, pp. 3-19.

[4] Beer, J.M., and Chigier, N.A., Combustion Aerodynamics, Applied Science Publishers, Ltd., 1972, p. 46.

[5] Parnell, E.C., and Williams, M.R., A Survey of Annular Vaporizing Combustion Chambers, Pergamon Press, 1969, pp. 91-104.

EXPERIMENTAL INVESTIGATION OF A VAPORIZING COMBUSTION WITH DOUBLE COMBUSTION SPACES

Tang Ming, Zhu Huiling and Du Qinfang

A Vaporizing Combustor with Double Combustion Spaces

Tang Ming, Zhu Huiling and Du Qinfang

This paper deals with a tubular combustor with a novel type of pre-vaporizing tube, which is of annular cross-section. It divides the dome of the combustor into two combustion spaces. Fuel is injected under moderate pressure into the annular space of the pre-vaporizing tube, through the orifices on the two fuel-distribution rings. The injected fuel forms oil films on the two walls.

This combustor is designed to be used as an air heater for the test setup of a hot wind tunnel. It is required that the combustor furnish a steady uniform hot gas stream at a temperature of 400-1100°C and that the flame should not extend beyond the exit of the flame tube.

Contrary to the usual practice in pre-vaporizing systems, a lean fuel-air mixture with an excess-air coefficient of nearly unity is adopted in the design of the pre-vaporizing tube. This requires the entrance area of the air to be pre-vaporized to make up about 30% of the total air entrance area. Air film cooling technique is adopted by using corrugated strips to form a number of cooling slots. The area of the cooling slots is selected to be about 20% of the total air entrance area. It is found that the cooling effect is satisfactory.

A centrifugal supercharger is used to supply the air for the tests. The air flow mass rate is measured with a dual orifice metering system. The combustor exit temperature profile is plotted from data obtained simultaneously with 27 nickel-chromium/nickel-aluminum thermocouple probes. Two quartz glass windows are provided for observation purposes on the wall of the combustor. For most of the test runs, the air flow rate is 1.10 kg (Mass)/sec and the inlet air pressure is 1.30 kg (force)/cm².

In the process of making adjustments to attain smooth functioning the following measures have been taken. First water visualization technique was used on a simplified model of the combustor to study qualitatively the size, strength and position of the recirculating vortices in the primary combustion zone. This experiment significantly helps to predict the flame stabilization tendencies.

Secondly, during the firing tests of the combustor, the position of the igniter and the manner of torch ejection were repeatedly adjusted until the flame is kept within the combustor.

Finally, a number of tests were run to study flame stabilization. At first, blowout of the flame always occurred earlier in the inner space than in the outer space. The pre-vaporizing air entrance area and the area of dilution holes were then varied in turn without noticeable success in synchronizing the blow-outs in the two spaces.

It was then suggested that a partition-ring of certain dimensions be placed in the pre-vaporizing tube to control the mixture ejection velocities at the inner and outer annular exits. This proves to be effective in controlling the blow-out characteristics of the flame in the two combustion spaces, and by varying the size of the partition ring, it is possible to make the blow-outs in both spaces occur almost simultaneously. The influence of the size of the partition ring on the blow-out characteristics of either combustion space was then studied and the test results are given in the form of curves, whose ordinate is the overall excess-air coefficient corresponding to the blow-out in either space and whose abscissa is the ratio of areas of the annular spaces separated by the partition ring. The point of intersection of the two blow-out characteristic curves gives the optimum size of the partition ring which makes the blow-out of both spaces occur simultaneously.

As is expected, by using a combustor with the above-mentioned pre-vaporizing system, the burning is stable, the flame is kept within the combustor, and its color is light blue in the whole range of the following operating conditions:

Overall excess-air coefficient—2.8-10;

Exhaust gas temperature—400-1100°C.

The curve of combustion efficiency versus the overall excess-air coefficient is flat except in the neighborhood of the blow-out point.

The uniformity of the exit temperature distribution is quite satisfactory. The maximum variation of temperature over the entire exit section is less than 45°C, when the exhaust gas temperature is as high as 950°C. Furthermore, it is not necessary to preheat the inlet air to a high temperature; a temperature of 150-200°C is usually high enough to satisfy the requirement of uniformity.

It may be concluded that a satisfactory tubular combustor with pre-vaporizing tube of annular cross-section has been developed for the test setup of a hot wind tunnel. Besides, the experience gained may also be helpful in the development of a similar combustor for the combustion system of a gas turbine.

THE COMBUSTION INSTABILITY IN SOLID PROPELLANT ROCKET MOTORS WITH TUBULAR GRAIN

Wu Xinping

ABSTRACT

This paper discusses the problem of combustion stability of solid propellant rocket motors with tubular grain, including the discernment, analysis and suppression of combustion stability, from certain design considerations. In decision techniques, apart from confirming that the most reliable method is to measure the oscillatory pressure in the combustion chamber, we also introduce the experience of discerning the existence of unstable combustion in a motor from the results of ordinary tests (average pressure curve, copper column pressure, test appearance, etc.). In theoretical analysis we derive in this paper the criteria for linear combustion stability (Equations 20-22) of solid propellant rocket motors with tubular grain using the energy balance theory. It is also pointed out that suitably distributing the local gas flow parameter and reducing the parameter for metal containing propellant will increase combustion stability. This conclusion agrees with experimental experience, thus pointing out a way to adjust design parameters to suppress the combustion instability that may arise in tests producing such motors. In addition, other suppression procedures are also introduced and evaluated. It is also pointed out that combustion instability should be divided into the strong and the weak kinds and that it is not necessary to eliminate completely the weak instability of combustion.

I. INTRODUCTION

Unstable combustion is a difficult technical problem frequently encountered in the design and manufacture of solid propellant rocket motors with tubular grain. In many countries, there have been some solid propellant motors which had to be redesigned or even abandoned

because of the occurrence of unstable combustion. Because of this, in the past three decades a large amount of research work has been done on this topic but practical problems are still recurring constantly.

Taking the requirement of engineering applications into consideration, what is urgently needed is a set of methods and principles that may be used to guide the design, development and production directly. Although we understand that the research in combustion instability has not yet matured to such a stage that the unstable combustion in a motor may be reliably predicted or prevented, yet it is still possible and profitable by taking advantage of current scientific theory and practical experience and focusing on motors with different propellant loading methods to study as well as raise some opinions which may be used to guide the design work. The work in [1] belongs to this category. Its author expressed various fundamental research (including theoretical as well as empirical) results on acoustical instability of combustion with simple mathematical formulae and derived from them some general principles concerning the combustion stability of propellant motors with end surface combustion and with circular or star-shaped internal orifice combustion, which may be used for design considerations. This paper is written with similar goals, but it emphasizes the discussion on acoustic instability of combustion for propellant motors with tubular grain (including single tubular, multitubular and double tubular).

The problems discussed in this paper are concerned with aspects of discernment, analysis and suppression of combustion instability. The effect on the linear acoustic instability of combustion of some design parameters for propellant motors with tubular grain is investigated primarily through theoretical analysis, while various methods to discern unstable combustion are summarized based on practical experiences. Some opinions on how to suppress the combustion instability of this type of solid rocket motor are then offered by using as a basis theory unified with experience.

II. DISCERNMENT

As is generally known, the most obvious sign of unstable combustion in a solid rocket motor is the irregularity in the pressure-time curve. Explosions may result in serious cases. On the other hand, there are many causes which can lead to abnormality in the pressure or even explosion while testing a newly designed solid motor. If the cause(s) cannot be properly determined in time, then the R & D work will not be able to proceed smoothly.

In the following we will first discuss some experience in the analysis of normal testing results. A more rigorous method to discern acoustic instability of combustion will then be described.

1. Analysis of normal test result .

The special item of monitoring combustion instability is generally not included in the static firing tests at ordinary rocket testing stations. Yet the functional abnormality of some new rockets is often discovered first in these static firing tests. Thus, how to analyze the regular testing results (average pressure curve, copper column pressure and test observations, etc.) to determine whether combustion instability exists in the rocket motor is often a meaningful technique. From our observation and understanding, the following noticeable characteristics are associated with rocket motors with combustion instability during static tests.

(1) In repeated testing of the same type of motors, the time at which irregularities in the average combustion chamber pressure appear, or at which the motor explodes due to excess pressure, is generally about the same, but the repeatability of the changes and shapes of the pressure-time curve is rather poor. This is because, although there is regularity in the production of combustion instability, yet there exists a complexity of factors affecting the initiation and development of combustion instability, such as the composition and characteristics of the propellant, the geometrical

dimensions of the loaded propellant and its condition of loading, the combustion environment, etc., which cannot be rigorously repeatable even though they are basically invariant.

(2) For relatively weak acoustic instability of combustion, the effect of the acoustic field on the average rate of propellant combustion in most motors is negative (this is more obvious for many double base propellants) so that the average pressure is lower than the normal value (Figure 1a).

For strong, acoustically unstable combustion, owing to the reinforcement of acoustics, the effect of the acoustic field to the average rate of combustion is always positive. Thus the so-called "secondary pressure peak" will appear (Figure 1b).

Sometimes, accompanying the development of pressure oscillations from weak to strong, the corresponding pressure curve will show a change from being concave to being convex (Figure 1c). To facilitate comparison, the average pressure curves under normal combustion conditions and the oscillatory pressure (the AC part

after straightening) during unstable combustion as recorded by high frequency dynamic pressure recording system are shown in dotted lines.

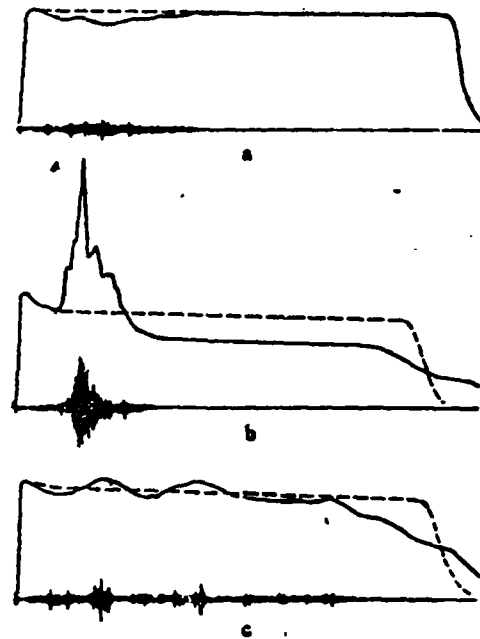


Figure 1

(3) The copper column pressure gauge has definite values in indicating combustion instability. When oscillatory pressure exists in the combustion chamber, the copper column will deform more under the oscillatory pressure. Therefore, the pressure obtained from it may be higher than that under normal conditions and may also be

higher than the maximum pressure on the average pressure curve. In the experimental results of some motors undergoing unstable combustion, the copper column pressure exceeds the maximum curve pressure by more than 1 fold. At the same time, due to the non-uniform spatial distribution of the oscillatory pressure field, the copper column pressures at different testing points in an experiment may differ widely. But when the combustion instability is weak, if the average pressure decreases with the pressure oscillation and the average pressure together with the peak value of the oscillatory pressure is still less than the maximum pressure under normal conditions, then the copper column pressure will also not be on the high side. In other words, the copper column pressure gauge is not sensitive to weak acoustic instability of combustion.

(4) During static testing of a motor under unstable combustion, sometimes one can hear the noise produced by the abnormal combustion or smell the abnormal odor produced by incomplete combustion. If the motor should explode, by examining the propellant remnant after explosion, one can often discover wavy lines, marks or pits. A directional wavy line is often produced by the oscillation of the acoustic wave motion normal to it.

2. Measurement of oscillatory pressure and identification of the vibrational modes.

The most fundamental characteristic of the appearance of unstable combustion in a solid propellant rocket motor is the existence of acoustic frequency pressure oscillations in the combustion chamber. Therefore, the most direct proof of its discernment is to measure the pressure oscillation in the combustion chamber. The dynamic pressure measuring system used for this purpose is usually required to have a frequency response of 0-20 KHz and more. The system usually consists of such major components as high frequency dynamic pressure transducer, amplifier, magnetic tape recorder and dynamic spectral analyzer.

The acoustic instability of combustion in a solid propellant rocket motor is the result of the interaction between the combustion process and the pressure oscillation in the combustion chamber. The space left in the propellant-loaded combustion chamber is equivalent to an acoustic chamber that can easily generate spontaneously excited oscillations. From the theory of acoustics, we know that any acoustic chamber has a series of normal modes. The most easily excited modes in a solid propellant motor are usually the various fundamentals, but sometimes some low-lying, high level modes and secondary harmonics may also appear. During the testing of a motor, if transducers can be placed at many positions to rigorously measure the frequency, amplitude and phase, then it will not be difficult to identify the vibrational modes of the instability. Compared to motors with propellant filled along the walls, it is more convenient to install transducers on motors with tubular grain. It is not only easier to make the film of the transducer parallel to the empty chamber wall, but there is also more freedom in choosing the measuring positions.

To identify the vibrational modes of the instability, some knowledge of acoustics is needed. The most important thing is the calculation of the characteristic frequencies of the empty chamber. The geometric shape of the chamber of motors with tubular grain is fairly simple. Their characteristic frequencies may be calculated with formulae.

(1) Longitudinal characteristic frequencies: Usually we can use the formula for a tube with both ends closed, i.e.,

$$f_n = \frac{na}{2L} \quad (1)$$

where a represents the sound speed in the burning gas; L represents the internal length of the combustion chamber; $n = 1, 2, 3, \dots$ is the longitudinal frequencies. If we are to take into consideration the effect of the gas flow velocity, then according to some experimental data [2], we propose that Equation [1] be multiplied by the

correction factor $(1-0.57J)$. J is the ratio of the instantaneous throat area of the motor to the area of the grain air passage. The J value decreases as the air passage area increases after the motor with tubular grain is fired; therefore, the value of f_c may increase somewhat during the operation of the motor.

(2) Tangential characteristic frequencies. The typical geometric shape of the cross-sectional area of the empty chamber of a motor with tubular grain is a circle or a circular ring (Figure 2).

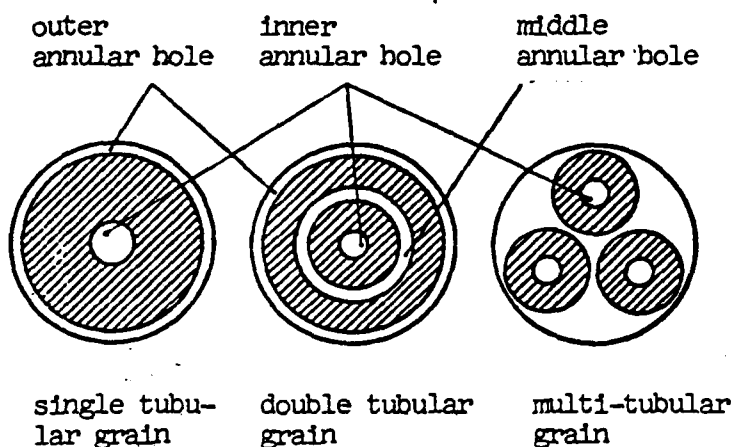


Figure 2

Since the combustion instability usually does not appear in radial vibrational modes, we are primarily interested in tangential modes.

For a cylindrical chamber, the tangential modes are calculated from the formula

$$f_{t,m} = \frac{\eta_m a}{2R} \quad (2)$$

where R is the radius of the circle, $m = 1, 2, 3, \dots$ is the tangential mode order number, η_m is the characteristic value. The η_m values of the 1-3 order modes $m = 1, 2, 3$ are listed in Table 1. More data may be found in [3, page 395] if needed. Obviously, the inner hole of the tubular grain will gradually increase in the combustion process so that correspondingly $f_{t,c}$ will steadily decrease.

TABLE 1. VALUES OF β , F AND η_m CHARACTERISTIC VALUES OF THE TANGENTIAL MODE FOR A CYLINDRICAL CHAMBER

| m | η_m | β | F |
|-----|----------|---------|-------|
| 1 | 0.588 | 1.84 | 0.702 |
| 2 | 0.972 | 3.05 | 0.571 |
| 3 | 1.337 | 4.20 | 0.490 |

For an annular cylindrical chamber, a similar formula may be used for the tangential characteristic frequencies:

$$f_{t,a} = \frac{\xi_m a}{2R} \quad (3)$$

where the characteristic values ξ_m are already provided by [4]. The values of ξ_1 are listed in Table 2. The outer annular hole--the empty space between the inner wall and the loaded propellant, will have R_1 decreasing and R_2 constant as combustion progresses. Therefore, $f_{t,a}$ will gradually increase. The middle annular hole --with combustion surfaces on either side, will have a constant \bar{R} during the combustion process. Although R_2/R changes, if we take $R = \bar{R}$, then it can be seen that ξ_1 varies very little so that $f_{t,a}$ is nearly constant. It may be approximated as $\xi_1 = 0.322$.

TABLE 2. VALUES OF ξ_1 , THE FIRST ORDER TANGENTIAL CHARACTERISTIC FREQUENCIES FOR AN ANNULAR CYLINDRICAL CHAMBER

| R_2/R_1 | | 1.1 | 1.2 | 1.5 | 2.0 | 2.5 | 3.0 | 3.5 | 4.0 | 4.5 | 5.0 |
|-----------|-------------|-------|-------|-------|-------|-------|-------|-------|-------|-------|-------|
| ξ_1 | $R=R_1$ | 0.304 | 0.290 | 0.258 | 0.215 | 0.186 | 0.163 | 0.145 | 0.131 | 0.119 | 0.108 |
| | $R=R_2$ | 0.334 | 0.348 | 0.384 | 0.431 | 0.466 | 0.491 | 0.509 | 0.523 | 0.534 | 0.543 |
| | $R=\bar{R}$ | 0.319 | 0.319 | 0.320 | 0.323 | 0.326 | 0.326 | 0.326 | 0.326 | 0.326 | 0.326 |

In the table, R_1 represents the inner wide radius; R_2 the outer circle radius $\bar{R} = (R_1 + R_2)/2$.

Analysing the measured principal vibrational frequency values (also taking into account their time variation) according to the

above and comparing them with the values computed from Equations (1-3), the vibrational modes can be basically discerned in many situations. Of course, the vibrational mode of the combustion instability of a motor may be singular or composite. The composite vibrational modes must be distinguished in the analysis.

III. ANALYSIS

According to the linear theory of the combustion instability of a solid repellant rocket motor, the motor may be regarded as an acoustic spontaneously excited oscillator. On one hand, the combustion surface of the solid propellant drives with a very small portion of the released energy, one or several acoustic oscillational modes of the combustion chamber space. On the other hand, acoustic energy is expelled through the exhaust and the acoustic oscillations of the burning gas are retarded by the acoustic absorption of the suspended or colloidal particles in the burning gas of the metal containing propellant, the absorption of the visco-elastic grain and the dissipation on the inner wall surface of the housing, etc. For an ordinary motor, among the many damping factors, usually only the exhaust tube and the damping from the suspended particles are large enough to be of the same order of magnitude as the combustion surface enhancement damping. The interaction between the average flow field and the acoustic field may have different effects under different conditions--enhancement or damping--but the value is usually much smaller than the combustion surface enhancement.

Whether the combustion in a solid rocket motor is linearly stable or not is determined by the balance between the enhancement and damping of the acoustic energy in the combustion chamber. If we assume that the various factors of damping and enhancement are independent (i.e., they may be super-imposed) then according to the energy balance theory, the criteria for combustion stability of the motor may be expressed as

$$\Sigma \alpha_i < 0$$

(4)

where α_1 represents the enhancement or damping constant ($\beta = \beta_0 e^{\alpha_1}$) of the acoustic wave amplitude when that enhancement or damping factor acts alone. Since the acoustic energy density is proportional to the square of the acoustic pressure amplitude, from the energy point of view, α_1 is equivalent to half the value of the relative growth (or decay) of the acoustic energy density produced by the enhancement (or damping).

From a qualitative point of view, to expose the true nature of the problem in the simplest way, we grasp the major contradiction and neglect the secondary factors, to write Equation (4) concretely as

$$\alpha_b + \alpha_n + \alpha_p < 0 \quad (5)$$

where α_b is the combustion surface enhancement constant, α_n is the exhaust tube damping constant and α_p is the colloidal damping constant.

In the following we concretely discuss these three constants.

1. Combustion surface enhancement constant

α_b is primarily determined by the combustion surface response characteristics of the propellant and the distribution of the combustion surface in the acoustic field. For a particular propellant, its combustion surface response characteristics is a function of the acoustic wave frequency and the average pressure. There is as yet no suitable theoretical method of computation for the combustion surface response characteristics of solid propellants. It is mainly dependent upon experimental measurements. The most widely used method currently is to measure the response characteristics of a propellant by using the T-shaped combustor. We equate the cross sectional area of the combustor to the combustion surface of the test sample in the T combustor and let the combustion surface enhancement constant--as measured under the condition (if the experimental condition is different, then it may be converted to this condition)

that the combustion surface is completely under the pressure wave-- be the combustion surface enhancement constant of the T combustor, denoted by a_{bT} . We also define the dimensionless quantity $k = a_m/f$ (f being the frequency) as the relative amplification of the propellant. k is still a function of the frequency and pressure. Parameters a_{bT} and k both reflect the response characteristics of the propellant. For convenience of expression, we will use the dimensionless parameter k in our discussions.

If the relative amplification k of the selected propellant is known within the ranges of variation of the acoustic characteristic frequency and the combustion chamber pressure of the motor, then it is not difficult to find the a_b of the motor. In [1], the formulae have been derived already for the cases of end surface combustion and inner hole combustion. We will derive the formula for tubular grain (with both ends enveloped) in a similar way below and also relate the problem of combustion instability to the fundamental design parameters of the motor.

According to acoustic theory [3, page 299], a_b 's relation with the pressure field may be written as

$$a_b = \Phi (\bar{p}_A / \bar{p}_V)^2 (A/V) \quad (6a)$$

where

$$\bar{p}_A^2 = \frac{1}{A} \int_A p^2 dA \quad (6b)$$

$$\bar{p}_V^2 = \frac{1}{V} \int_V p^2 dV \quad (6c)$$

In the above, A is the combustion surface, V the volume of the acoustic cavity, \bar{p}_A^2 and \bar{p}_V^2 are respectively the average values of the square of the acoustic pressure amplitude over the whole combustion surface and over the whole volume. They are determined by the vibrational mode. Φ is the parameter related to the acoustic response characteristics of the combustion surface. If Equation (6) is used to analyze the T combustor, then $\Phi = ka/4$ (a being the sound velocity of the burning gas). Substituting into Equation (6a) we get

$$\alpha_s = \frac{ka}{4} \left(\frac{p_s}{p_v} \right)^2 \left(\frac{A}{V} \right) \quad (7)$$

Equation (7) will now be specialized for the various vibrational modes of the motor with tubular grain.

The longitudinal pressure distribution is

$$P = \bar{p} \cos(n\pi z/L) \quad (8)$$

where the origin of coordinate z is set at the end surface of the head section of the inner cavity of the combustion chamber, with the direction of the coordinate axis the same as the longitudinal axis of the motor. From Equations (8) and (6b,c) we may get

$p_s/p_v = 1$. Substituting it into Equation (7), the combustion surface enhancement constant for the longitudinal mode may be obtained as

$$\alpha_{s,0} = \frac{ka}{4} \frac{A}{V} = \frac{kas}{4L} \quad (9)$$

where s is the port parameter (ratio of combustion surface area to port area). Since the combustion chamber cavity in the longitudinal direction is sectioned into several parts by the tubular grain, we should discuss $\alpha_{b,z}$ for each part separately. If the assumption is made that the partial cavities are acoustically isolated from one another, then s in Equation (9) should be replaced with s_1 (inner cavity port parameter), s_2 (middle cavity port parameter) and s_3 (outer cavity port parameter) in the calculation of $\alpha_{b,z}$ in each partial cavity. If the assumption of acoustic shorting, then $\alpha_{s,0}$ may be calculated from the overall s value of the motor. Since there is generally only a small gap between the end of the combustion chamber and the ends of the tubular grain, the real situation lies somewhere between the two assumptions. A safer result may be obtained by using the acoustic isolation assumption.

The pressure distribution for tangential modes of the cylindrical cavity is

$$P = \bar{p} \sin m\theta J_n(\beta r/R) J_n(\beta z) \quad (10)$$

where the origin of the polar coordinates θ , r is taken to be at the center of the circle. J_m represents the m th order Bessel function $\beta = \eta_m \pi$. Substituting Equation (10) into Equation (6b,c) will yield approximately $(p_A/p_B)^2 = 1/F$, where $F = 1 - (m/\beta)^2$. As in the derivation of Equation (9) the combustion surface enhancement constant for tangential vibrational modes of a circular hole is

$$a_{1, \dots} = \frac{k a x_1}{4FL} \quad (11)$$

where

$$x_1 = 2L/R \quad (12)$$

Table 1 gives the value of β and F at $m = 1, 2, 3$.

When R_2/R_1 is not too large, the tangential mode pressure distribution in the cylindrical cavity may be approximated by

$$P = p \sin m\theta \quad (13)$$

Similarly, the combustion surface enhancement constant for tangential mode in an annular hole is

$$a_{1, \dots} = \frac{k a x}{4L} \quad (14)$$

The annular cylindrical cavity of practical motors may be divided into two categories as shown in Figure 2. One category is the "central annular hole" with combustion surfaces on both sides. The x in Equation (14) should be taken as x_1 . Apparently,

$$x_1 = 2L/B \quad (15)$$

The other category is the "outer annular hole" with combustion surface on the inside while the outside is the motor housing. The x in Equation (14) should be taken as x_2 while

$$x_2 = L(d - 2B)/(d - B) \quad (16)$$

In both equations above, B represents the "width" of the corresponding annular ring, i.e., $B = R_2 - R_1$. The d in Equation (16) represents the inner diameter of the combustion chamber.

2. Exhaust pipe damping constant

Concerning the research on exhaust pipe damping, for a long time the experimental value of a_n was generally higher than the theoretical result. The results of different experiments also vary widely. The usual explanation for these discrepancies is that additional damping exists because the gas flow separates far beyond the entrance of the exhaust tube due to the sharp geometric shape of the tube or to the fact that the inlet cross sectional area of the exhaust tube is smaller than the cross sectional area of the combustion chamber. Also other damping factors may have been neglected to various degrees in the many experiments. There have been comparisons of the results of several experimental methods recently which further supports the above view and which emphasize the importance of the shape of the exhaust tube inlet on the estimation of a_n .

For problems like this with complicated practical factors which have not been resolved theoretically, empirical formulae are usually used in engineering. Here we shall use the following empirical equations to calculate the exhaust tube damping constant.

For longitudinal vibrational modes:

$$a_{n,l} = -\epsilon_n a J / L \quad (17)$$

For tangential vibrational modes

$$a_{n,t} = -\epsilon_n a J / 2L \quad (18)$$

The ϵ_n in the two equations above corresponds to the various empirical coefficients used in the various references. For example, some take $\epsilon_n = 1$ and some take $\epsilon_n = 1.58$. We write down coefficient ϵ_n in Equations (17), (18) so that more appropriate data may be used to distinguish between different cases in the future. Equations (17), (18) indicate that $a_{n,l}$ is twice $a_{n,t}$. This is because, for a longitudinal mode exhaust tube, acoustic energy is expelled by means of both convection and radiation. The radiation term is as important as the convection term, while for the tangential

mode, acoustic energy is expelled only by convection with a negligible radiation term.

3. Colloidal damping constant

Colloidal damping is produced by the exchange of the momentum and energy between the condensed phase and the gas phase. Through viscous force and thermal exchange, acoustic energy decays as heat. Satisfactory theoretical analysis already exists for the damping effect of a uniform spherical colloid in an acoustic field. The problem now is that it is difficult to ascertain the distribution of colloidal size of the combustion products in practical motors.

For simple calculations, we may assume that the magnitude of the colloidal damping constant α , is approximately in direct proportion to the acoustic frequency f and to the ratio Z of the colloidal mass per unit volume to the gas mass per unit volume, i.e.,

$$\alpha = -\epsilon_p f Z \quad (19)$$

Here we have again introduced an empirical constant ϵ_{po} . According to theoretical analysis, if the colloidal size is uniform and if the optimal dimension is attained for a given acoustic frequency, then the maximum damping constant that can be obtained is equivalent to $\epsilon_p = 1.57$. In practice, the situation may deviate widely from the ideal situation. In [1], no distinction is made between the types of motors and propellants. $\alpha_p = -0.34fZ$ is used for preliminary analysis. This is rather rough. As in Equations (17), (18), we write down the coefficient ϵ_p in Equation (19) with no concrete data substituted for it.

4. Criteria for linear stability

Now, substituting Equations (9), (17), (19) and Equations (11) or (13), (18), (19) separately into Equation (5), we can obtain the following criteria for linear stability of unstable combustions in a rocket motor with tubular grain as follows:

Longitudinal mode

$$2(2e_s J + n e_s Z) / \alpha_i > k \quad i = 1, 2, 3 \quad (20)$$

Tangential mode for circular hole

$$2F(e_s J + n e_s Z L / R) / \alpha_i > k \quad (21)$$

Tangential mode for annular hole

$$2(e_s J + \xi_s e_s Z L / \bar{R}) / \alpha_i > k \quad i = 2, 3 \quad (22)$$

It must be emphasized that when applying the above criteria it is to be understood that k not only changes for different propellants, but that it is a function of both the frequency and the pressure for a given propellant. The value of k lies generally between 0.01-0.1. For most propellents, k 's value tends to decrease with increasing frequency and to increase with decreasing pressure. Hence, the effect of frequency on k for different vibrational modes must be remembered. Generally, the longitudinal modes have much lower frequencies than the tangential modes. Their k values may be very different. When the design parameters J or α for a motor are changed, the working pressure of the motor under most circumstances will also change. Thus k value will also change.

After analyzing the above criteria, we may offer the following opinions concerning the problem of acoustic instability of combustion of a solid propellant rocket motor with tubular grain. These opinions agree in general with our practical experiences.

(1) Reducing the port parameter of the motor is advantageous to increasing combustion stability. But α is not an independent design parameter. It is limited by the relation $\alpha = J/K$ where K represents the ratio of combustion surface area to cavity area. If K 's value is to be kept constant (corresponding to keeping the pressure of the combustion chamber constant), the value of J must vary directly with that of α . For motors with uniformly distributed inner, middle and outer local port parameters using propellant not containing any metal ($Z=0$), the design parameter contained

in the LHS of Equations (20)-(22) is just K. For propellents containing metal ($Z > 0$), under the condition of K being kept constant, the combustion stability will be increased provided J and α values can be simultaneously reduced.

(2) From the criteria of longitudinal mode stability, distributing local port parameters uniformly will aid combustion stability. For the tangential mode, as the annular cylindrical cavity is generally less stable than the cylindrical cavity, it is appropriate to choose larger α_1 than α_2, α_3 . From the point of view of combustion stability, it is never reasonable to choose α_1 much smaller than α_2 or α_3 .

(3) For rocket motors with tubular grains using metal containing propellents or using non-metal-containing propellents but with unreasonably distributed port parameters, acoustic combustion instability occurs more often during the early period when α is large or BJ product is small.

(4) From the appearance of the stability criteria, it seems that reducing K value will aid combustion stability. However, it may not be so in reality. For example, the k value of some double-based propellant increases rapidly with decreasing pressure so that as a result the increase of the LHS in Equations (20)-(22) due to lowering K value cannot compensate the increase of k on the RHS. Decreasing K value, therefore, will make the motor more unstable.

(5) Generally speaking, first order modes (fundamentals) are less stable than higher order modes. This is because the colloidal damping term is generally smallest when $n = 1$ and $m = 1$. Also the other secondary damping effects not included in the above criteria nearly all have positive rates of frequency change.

Finally, it must be stated that motors with tubular grain are usually loaded free-handedly. If the positions of the grains are

not strictly fixed, the actual geometric shape of the combustion chamber cavity may not be regular. Even so, the above analysis may be approximated and the basic feature of the problem probably will not be lost. For motors with multiple grain, the above opinions may still be taken as advice.

V. SUPPRESSION

Our opinion is that, from an engineering technique point of view, the acoustic combustion instability may be divided into the strong and the weak categories. The unstable combustions in some motor leads to obvious pulsation of the average pressure, or even the secondary pressure peak that may produce explosion. They may be called "strong instability". Comparatively, combustion instabilities in some motors have small pulsation in average pressure (less than a few per cent) with small vibrational pressure (not more than a few atmospheres). They generally do not affect the reliability of the motors. We may call them "weak instabilities".

Obviously, strong combustion instability cannot be allowed for any motor. It must be suppressed or weakened by using suppression procedures. The weak instability should be analyzed concretely. Some motors with weak combustion instability may still be accepted in the industry.

Much experience has been accumulated over the years on how to suppress unstable combustion in solid fuel rocket motors. These experiences are being gradually understood theoretically. The following are some of our experiences.

1. The design parameters α and J of a tubular grain motor affect its combustion stability. The above analysis has already shown the general direction in which the parameters may be selected or adjusted. For example, if a motor using aluminized propellents starts to show signs of combustion instability and in its original

design the difference between the inner and outer port parameters is large, then we suggest that they may be adjusted to be more uniformly distributed. If a tangential instability vibrational mode is discovered for a motor that uses non-metal containing propellents, then we suggest that one may try to widen the gap a little in the corresponding cavity along the transverse direction.

2. The combustion instability of a solid propellant motor tends to move toward the critical state; therefore, it is obviously insufficient to only pay attention to the design parameters discussed in the above analysis when we are considering the suppression measures. It is necessary that we not only consider all the factors that will affect the magnitude of the empirical parameters included in Equations (20)-(22), but also consider those factors not included in the above-mentioned equations. For instance, changing the geometric shape of the grain by installing a number of ledges to break up the vibrational modes and damp acoustic energy will increase combustion stability. Another way is to choose the propellant with appropriate visco-elasticity as a replacement for some propellant that is too hard (high elastic modulus) so as to increase the absorption and damping of acoustic energy by the grain. This may also facilitate the solution of the combustion instability problem.

3. Metal-containing propellents (the most common one contains aluminum powder) have better acoustic stability because of the existence of colloidal damping during combustion. But there are motors using aluminized propellant that are unstable, especially when the motor dimensions are large so that the acoustic characteristic frequencies are lower. Besides, combustion stability may not improve and sometimes even become worse when the aluminum powder content is increased. Superficially, this seems to contradict Equations (20)-(22) but if we notice that the ϵ_p and k in the equations may also change, then the situation becomes understandable.

Incidentally, here is an opinion not limited to motors with tubular grain nor even primarily related to motors of this kind.

Colloidal damping is important in suppressing acoustic combustion instability. It is related to the colloid size in the combustion products and is not a simple problem of increasing the metal content. Thus, in developing medium and high power metal-containing solid propellant rocket motors, it is not only important to investigate the combustion mechanism of metals from the point of view of increasing power, but also from the point of view of increasing the combustion stability--i.e., to maximize the colloidal damping.

4. It is rare for motors in the tubular grain to use mechanical devices to suppress combustion instability because structural simplicity is often the goal in this type of motor. Besides, their structure is not really suitable for the installation of center rod or separation panels. It is also rare to use methods of drilling transverse holes in the grain (which do not show obvious effects) because of the complexity they bring about in the grain production technique.

V. CONCLUSIONS

The current status of research work on combustion instability of solid propellant rocket motor is not yet developed to a stage where reliable prediction and prevention of instability may be achieved during the product design period. However, it is definitely profitable and certainly necessary to actively apply current research results to identify and analyze the various phenomena of combustion instability that have arisen during product R & D.

The investigations in this paper on motors with tubular grain indicate:

1. Ordinarily, there is no problem in discerning the existence of combustion instability in rocket motors with current knowledge and methods. The characteristic irregularity in the pressure-time curve and the obvious excess of the copper column pressure over the

maximum curve pressure in a static firing test are often the important signs for the existence of combustion instability. High frequency dynamic pressure measurement and analysis is a reliable method for making clear-cut determination.

2. The effect on combustion stability of the trend of variation in design parameters as shown by the criteria for linear stability (Equations (20)-(22)) derived from linear theory basically agrees with experiments. The main points are: rational distribution of local port parameters will increase combustion stability; under the condition that the ratio K of a motor using metalized propellant is kept constant, the smaller the port parameter (μ) the better; for motors using non-metalized propellant, if the K value is kept constant, the stability is not sensitive to variations in μ 's value; the acoustic combustion instability of this kind of motor frequently occurs in the beginning of the working period, the lower order vibrational modes being less stable than the higher order modes.

3. From an engineering technology point of view, acoustically unstable combustion may be categorized as the strong and the weak kinds. The weak combustion instability with small average pressure pulsation and low vibrational pressure amplitude may be tolerable for some motors. Steps must be taken to suppress or eliminate the destructive strong combustion instability.

4. The possible steps to take to solve the problem of unstable combustion for motors with tubular grain are: adjusting the design parameters, changing the geometric shape (adding ledges) of the grain, and switching propellant.

Linear theory can only be applied to analyze combustion instability with small perturbations. Once instability occurs, the limiting amplitude that may be reached and its effect on the average combustion rate are controlled by non-linear factors. Hence, the second

point in the foregoing conclusions is limited to answer only the question of whether unstable combustion will occur and not the question of how strong the unstable combustion will become. Besides, the gas flow near the head or top section of a motor with tubular grain is strongly affected by the distribution of local port parameters. It is also necessary to investigate further what is the result of neglecting the effect of the average flow field on the acoustic field to the conclusions above.

REFERENCES

- [1] Coates, R. L., and Horton, M. D., Design Consideration for Combustion Stability, JSR, Vol. 6, No. 3, 1969.3.
- [2] Buffum, F. G., etc., Acoustic Attenuation Experiments on Subscale Cold-Flow Rocket Motors, AIAA J., Vol. 5, No. 2, 1967.2.
- [3] P. M. Morse. Nanking University "Vibration and noise translation, Vibration and noise Scientific Publishing House, 1974.
- [4] Bridge, J. F. and Angrist, S. W., An Extended Table of Roots of $J'_0(x)Y'_0(\beta x) - J'_0(\beta x)Y'_0(x) = 0$, Mathematics of Computation, No. 16—17, 1962—1963.
- [5] Janardan, B. A., and Zinn, B. T., Rocket Nozzle Damping Characteristics Measured Using Different Experimental Techniques, AIAA J., Vol. 15, No. 3, 1977.3.
- [6] Temkin, S. and Dobbins, R. A., Attenuation and Dispersion of Sound by Particulate-Relaxation Process, J. Acoust. Soc. of Amer., Vol. 4, No. 2, 1966.

Summary

The Acoustic Instability of Combustion in Solid Propellant Rocket Motors with Tubular Grain

Wu Xinpeng

Combustion instability is an ever recurring problem in the design, development, and production of solid propellant rocket motors. Although at the present stage of technology development, it is still impossible to predict or to preclude this problem at the start of a project, many research results and much engineering experience are now available to make the solution of the problem easier than before. The present paper deals with certain design considerations (including discernment, analysis and suppression) regarding combustion instability of solid rocket motors with tubular or multi-tubular grain, which burn both internally and externally.

Although the most reliable way to ascertain combustion instability is to take measurements of the oscillatory pressure in a combustion chamber and compare them with the theoretical acoustic modes of the chamber, yet some signs of combustion instability which can be detected from ordinary static firing tests may be very useful to engineers. It has been found that, in addition to the secondary peaks appearing in the pressure-time curves, the abnormal concavity in the curves, which usually appears when double-based propellant is used and the instability is weak, is another visible sign of the occurrence of combustion instability. When the combustion chamber pressures measured by the copper-column pressure pick-ups are higher than usual and show very large differences between different points of measurement, the presence of instable combustion is also indicated.

On the basis of the energy balance theory, some linear stability criteria for tubular grain motors have been derived (see formulae 20-22). The criteria indicate that combustion stability can be increased by so distributing the port areas as to make the parameters α_i (ratios of local burning surface to local port area) as nearly equal as possible and by reducing the values of α_i (mainly for grains with aluminized propellants). The criteria also give the indication that the instable combustion of motors of this kind, if it happens, always

starts shortly after firing. These conclusions are in fairly good agreement with engineering experience.

From the engineering point of view, it is suggested that weak combustion instability is permissible in certain designs, while strong combustion instability must always be suppressed. In order to preserve the feature of structural simplicity, mechanical damping devices are seldom employed in solid propellant rocket motors with tubular grain. Therefore, proper adjustment of design parameters is a very important method to suppress the unstable combustion. Otherwise it may be necessary to change the grain configuration or the propellant.

ATE
LMED
7-8